UC Davis
UC Davis Electronic Theses and Dissertations

Title

3D Printing of Soil-based Cementitious Materials

Permalink

https://escholarship.org/uc/item/2544f3jb

ISBN

9798276020815

Author

Nodehi, Mehrab

Publication Date

2025-12-06

Peer reviewed|Thesis/dissertation

eScholarship.org Powered by the California Digital Library
University of California

3D Printing of Soil-based Cementitious Materials

By

MEHRAB NODEHI

DISSERTATION

Submitted in partial satisfaction of the requirements for the degree of

DOCTOR OF PHILOSOPHY

in

Civil and Environmental Engineering

in the

OFFICE OF GRADUATE STUDIES

of the

UNIVERSITY OF CALIFORNIA

DAVIS

Approved:

_____

Michele Barbato, Chair

_____

Boris Jeremic

_____

John Bolander

_____

Somayeh Nassiri

Committee in Charge

2025

Abstract

The construction sector accounts for a significant share of global energy use and embodied CO_2 emissions. It is estimated that a 10-20% embodied carbon reduction in buildings can be achieved by utilizing cement substitutes and other low-impact materials. One method that could potentially minimize industrial processing and transportation is the use of locally available earthen construction materials. Earthen materials generally use locally available soil to produce durable structural solutions, particularly for family dwellings and other low-rise buildings. This practice has been a successful construction method for centuries across different climates and cultures. Although producing earthen blocks provides a low-energy alternative to fired bricks and other construction materials, the process of making the blocks and installing them is still time-consuming and labor-intensive. Variations in local soil conditions or manufacturing techniques may also lead to uncontrolled variations in material quality. Yet, an increased interest in incorporating automation technologies in the construction industry, such as robotics and 3D printing, can offer innovative solutions to addressing these challenges.

3D printing follows a layer-by-layer placement of materials that eliminates the need for manually installing each block. It can also reduce the need for formwork and minimize the waste generated during construction. 3D printing with earthen materials (hereinafter referred to as 3D-printed soil-based materials) can not only increase the production speed of masonry units compared to conventional methods, but it can also provide greater control over geometry, layer consistency, and material composition. This integration of 3D printing into the construction process can have the potential to increase productivity and efficiency by reducing manual material placement.

Nonetheless, the most current 3D printing applications within the construction industry are largely focused on cement-based materials. These approaches remain heavily dependent on high volumes of ordinary Portland cement, processed aggregates, and a growing number of chemical admixtures, such as viscosity-modifying agents, retarders, plasticizers, and accelerators. These specialized requirements make the process of 3D printing less appealing in terms of cost competitiveness, environmental benefits, also material availability. In contrast, the application of 3D printing to soil-based materials represents a distinct pathway that emphasizes reduced labor and material processing, especially by removing processed sand and often using lower cement content (e.g., about 10% volumetric). Additionally, since 3D printing of cementitious materials is a new practice in the construction industry, standards regarding testing 3D-printed products are lacking. A lack of standardized procedures for testing 3D-printed materials introduces considerable uncertainty and variability into performance evaluation and the design process, ultimately challenging the perceived benefits of this technology.

This dissertation is organized into seven chapters that outline the research objectives, motivation, scope, and technical investigations. The emphasis is placed on the development, characterization, and environmental assessment of soil-based mixtures for 3D printing applications. The first two chapters outline the use of innovative technologies, such as 3D printing, and highlight the benefits of integrating soil-based materials into modern construction technologies. In addition, the first two chapters emphasize the potential of 3D printing in soil-based construction to enable the mass production of efficient and functional building components.

The third chapter presents a comprehensive experimental investigation into the development, characterization, and performance evaluation of sustainable soil-based construction materials produced through both conventional and 3D printing methods. It starts with the development of Compressed and Stabilized Alkali-activated[1] Earth Blocks (CSAEBs), which incorporate various precursors (e.g., glass powder, fly ash classes F and C) and activators (e.g., sodium silicate and sodium hydroxide). The results of extensive mechanical, durability, and microstructural tests performed for each mixture are then presented. Finally, a cradle-to-gate life cycle assessment (LCA) is performed to evaluate the environmental impacts of the developed mixtures. Results indicate that when glass powder is used in CSAEBs, it can at least provide the same level of compressive strength performance or acid resistance as those produced with class F fly ashes. In terms of environmental impacts, it is found that CSAEBs' impacts depend strongly on the choice of locally available activators and SCMs. For example, on average, mixtures produced with sodium silicate had a global warming of 118.2 CO_2 eq, compared to 103.9 CO_2 eq for sodium hydroxide-based mixtures. Similarly, on average, fly ash class F, class C, and glass powder produced an average CO_2 eq of 98.0, 103.7, and 131.49, respectively.

In chapter four, the dissertation shifts toward investigating properties of 3D-printed soil-based materials through two sustainability strategies: first, to use Portland cement- and geopolymer-based binders, and second, to evaluate the impacts of replacing the commonly used processed sand with natural, locally sourced soil. Four mixtures, each combining different binders (e.g., Portland cement-based or alkali-activated) and filler types (e.g., soil- and sand-based), are tested for their fresh and hardened properties. A strength-adjusted LCA approach is also developed to quantify

[1] Throughout this dissertation, alkali-activated systems are regarded as a general class of binders, while geopolymers are recognized as a narrower subset within that class.

the environmental impacts of a functional unit produced using the four mixtures, in two different locations (different supply distances), with and without strength normalization of the results. Findings show that soil-based mixtures can offer mechanical and environmental performance comparable to that of traditional mixtures under specific curing and mixture design conditions. For example, in terms of environmental impacts (e.g., global warming potential, acidification, smog formation, and total energy use), soil-cement samples recorded lower energy use (242.42 MJ) and lower acidification (0.09 kg SO_2-eq) than crushed sand-cement mixtures (292.58 MJ and 0.11 kg SO_2-eq, respectively). Similarly, geopolymer-soil mixtures exhibited lower smog formation (1.61 kg SO_2-eq) than geopolymer-sand mixtures (2.34 kg SO_2-eq). However, after applying a strength normalization factor, the trends shift in favor of mixtures based on their 28-day compressive strength.

In chapter five, a third study is conducted to evaluate how different specimen-sampling techniques, including coring, cutting, rodding, and vibrating, affect the mechanical behavior of 3D-printed cementitious components. In this work, more than 670 specimens were made, tested, and statistically analyzed to isolate any influence of different sampling techniques on the tested properties. The tests conducted include water absorption, compressive strength, modulus of elasticity, and splitting tensile strength. The results showed statistically significant differences in measured properties, originating from different sampling methods. The study also takes the first steps toward standardizing testing procedures and highlights their importance for providing reliable data in 3D printing research.

Finally, the sixth chapter discusses a rheology-based design framework to identify the printable boundaries of soil-based mixtures. In that study, over 100 soil-based mixtures with low cement and fly ash contents (e.g., 0-30% of the total solid mass as fly ash, and 5-30% of the total solid mass as Portland cement) were produced without any chemical admixtures. The mixtures were then evaluated for (a) dynamic viscosity, (b) yield stress, and (c) shear stress to establish a rheological printability boundary. Printable mixtures meeting the established rheological boundaries were then further tested for mechanical and environmental performance. Results confirm the possibility of printing structurally sound components with minimal binder content. The printability limits identified in this dissertation are defined by upper and lower bounds for three governing rheological parameters. Printable mixtures exhibited dynamic viscosity values ranging from a lower bound of $4.70\times10^{3} \pm 1.47\times10^{3}$ Pa·s to an upper bound of $1.48\times10^{4} \pm 1.22\times10^{3}$ Pa·s. The shear stress ranged from 0.846 ± 0.070 N/m^2 to 4.28 ± 1.29 N/m^2, while the yield stress fell between $1.36\times10^{2} \pm 1.47$ N/m^2 and $7.66\times10^{2} \pm 23.0$ N/m^2. Together, these limits define a practical rheological window for sustainable, soil-based 3D-printing mixtures. Additionally, the role of mixture optimization in balancing printability, strength properties, and environmental impacts is then discussed.

Together, these four studies form a unified experimental and environmental framework for sustainable soil-based and alkali-activated cementitious materials. Chapter seven integrates the findings by (a) comparing the mechanical and durability performance of CSAEBs with different precursors and activators; (b) synthesizing the fresh-state, hardened-state, and strength-normalized LCA behavior of 3D-printed soil- and sand-based mixtures using Portland cement and geopolymer binders; (c) evaluating how specimen-sampling methods influence measured mechanical

properties and establishing the need for standardized testing of 3D-printed materials; and (d) consolidating the rheology-based printability limits for low-binder soil mixtures, defined by the quantitative viscosity, shear stress, and yield stress boundaries. Together, these results provide a foundation for performance-based mixture design, specimen preparation, and environmental assessment tailored to 3D-printed soil-based construction. They also highlight pathways toward reliable, automated construction practices using locally available materials and minimal binder content.

Acknowledgments

I would like to acknowledge and express my deepest gratitude to everyone who made this work possible. Professor Christopher Cappa, Professor Miguel Jaller, Professor Boris Jeremic, Professor John Bolander, Professor Somayeh Nassiri, and Professor Michele Barbato have been essential to this work.

I would also like to offer a brief piece of advice to future generations of graduate students. Through adversity and experience, I have learned that there are many paths to success, but they share two fundamental elements: (a) believing in yourself and (b) taking proactive, deliberate action. If you understand what it takes to achieve your goals, begin now, one step at a time. It is equally important to remember that our time is finite. We are not promised unlimited opportunities, and someday each of us must leave our work behind. With that in mind, avoid meandering without purpose.

Stay focused, stay disciplined, and remain confident in your abilities. With persistence and intentional effort, meaningful accomplishments will follow.

Table of Contents

Abstract ii

Acknowledgments viii

Table of Contents ix

List of Tables xiii

List of Figures xv

1. Significant Original Features of Developed Work 1

1.1. Material Development for Low-Impact Masonry and 3D Printing 1
1.2. A Performance-linked Sustainability Method for 3D-printed Materials 1
1.3. First Comprehensive Quantification of Fabrication/Sampling Effects in 3D-printed Cementitious Testing 2
1.4. Rheology-driven Printability Boundaries for Low-binder, Soil-based Systems 2

2. Introduction 3

2.1. Objectives and Motivation 12
2.2. Scope 14
2.3. Research Novelty and Significance 15
2.4. Organization of the Dissertation 17
2.5. Journal Publications Derived from this Dissertation 19

3. Effect of Various Supplementary Cementitious Materials (SCM) and Activators in the Production of Compressed and Stabilized Alkali-Activated Earth Blocks (CSAEBs) 20

3.1. Introduction 20
3.1.1. Motivation and Significance 25
3.2. Materials 26
3.2.1. Soil 26
3.2.2. SCMs and Portland Cement 27
3.2.3. Alkaline Activators 30
3.3. Methods 31
3.3.1. Earth Block Fabrication 31

3.3.2. Mixture Proportions 33
3.3.3. Testing Matrix 34
3.3.4. Physical Properties of the Activators 35
3.3.5. LCA 36
3.3.6. Statistical Analysis, Quality Assurance, and Quality Control 42
3.4. Experimental Results and Discussions 44
3.4.1. Hardened Density 44
3.4.2. Water Absorption 47
3.4.3. Dry and Wet Compressive Strength 49
3.4.4. Flexural Strength 55
3.4.5. Wire Brush Test 56
3.4.6. Acid Resistance 58
3.4.7. Oxide Composition of Hardened Materials Using XRF 62
3.4.8. SEM Imaging of Hardened Materials 63
3.4.9. Statistical Analysis Done on Test Results 65
3.4.10. LCA Results 70
3.5. Conclusion 79
4. Comparative Properties of Soil-Based 3D-Printed Cementitious Materials Produced with Ordinary Portland Cement and Geopolymer Binders 85
4.1. Introduction 86
4.1.1. Novelty and Relevance 89
4.2. Materials 90
4.2.1. Soil and Crushed Sand 91
4.2.2. Fly Ash and Portland Cement 92
4.2.3. Alkaline Activators 94
4.3. 3D Printer and Methods 95
4.3.1. 3D Printer 95
4.3.2. Mixture Selection 96
4.3.3. Testing Matrix 97
4.4. Statistical Analysis, Quality Assurance, and Quality Control 99
4.5. Experimental Results 101
4.5.1. SEM Imaging of Hardened Materials 101
4.5.2. Oxide Composition of Hardened Materials Using XRF 104
4.5.3. Fresh Mixture Properties 106

4.5.4. Penetration Resistance and Initial Set Time 109
4.5.5. Water Absorption 111
4.5.6. Mechanical Properties of Hardened Mixtures 112
4.5.7. Life Cycle Analysis (LCA) 122
4.6. Conclusion 135
5. Effects of Specimen Preparation on Mechanical Properties of 3D-Printed Cementitious Materials 141
5.1. Introduction 142
5.1.1. Novelty and Relevance 146
5.2. Materials 147
5.2.1. Soil 147
5.2.2. Fly ash and Portland Cement 148
5.2.3. Mixing Water 150
5.3. 3D Printer 150
5.4. Mixtures and Methods 150
5.4.1. Mixture Proportions 151
5.4.2. Specimen Preparation and Testing Matrix 152
5.4.3. Statistical Analysis, Quality Assurance, and Quality Control 155
5.5. Experimental Results 158
5.5.1. Absorption 158
5.5.2. Compressive Strength 160
5.5.3. Modulus of Elasticity and Poisson's Ratio 173
5.5.4. Splitting Tensile Strength 173
5.6. Statistical Analysis of Test Results 175
5.7. SEM Imaging of Hardened Materials 178
5.8. Conclusion and Future Study Recommendations 183
6. Mechanical Properties and Printability Window of Low-Cement, Low-Fly-Ash, Soil-Based 3D-Printed Mixtures 191
6.1. Introduction 191
6.1.1. Novelty and Relevance 197
6.2. Materials and Equipment 198
6.2.1. Soil 198
6.2.2. Fly ash and Portland Cement 200
6.2.3. Mixing Water 201

6.2.4. 3D Printer 201
6.2.5. Viscometer 202
6.3. Mixtures, Methods, and LCA 204
6.3.1. Mixture Proportions 204
6.3.2. Testing matrix 209
6.3.3. Statistical Analysis, Quality Assurance, and Quality Control 211
6.3.4. Life cycle analysis (LCA) 212
6.4. Experimental Results 218
6.4.1. Flow Table, Fresh Density, and pH 218
6.4.2. Printability Limits 221
6.4.3. Mechanical Properties 229
6.4.4. LCA Results 238
6.5. Conclusion 246
7. Conclusions and Recommendations for Future Work 251
7.1. Conclusions 251
7.2. Limitations and Constraints of the Research 254
7.3. Future Research Work 256
References 258

List of Tables

Table 1. Physical properties of soil. 27
Table 2. The XRF result of cementitious materials used in this study. 28
Table 3. Properties of the activators used in this study. 30
Table 4. Mixture proportions were used in this study (normalized for 1000 g). 33
Table 5. Tests conducted and the standards that were followed. 34
Table 6. Distances considered from the supplier to the construction site (kilometers). 37
Table 7. GWP of all materials used in LCA calculations. 39
Table 8. Presenting the XRF result on all mixtures. 62
Table 9. Result of statistical analysis (p-values). 68
Table 10. Property characterization of natural soil and crushed sand. 91
Table 11. XRF results for fly ash and natural soil. 93
Table 12. Result of mill certificate supplied by Nevada Cement Inc. 93
Table 13. Tested properties of tap water and sodium hydroxide solution used in this study. 94
Table 14. Mixture proportions used for 3D printing, expressed per thousand grams. 97
Table 15. Tests and corresponding standards used in this study. 98
Table 16. XRF results from 3D-printed samples after 28-day curing. 105
Table 17. Measured properties of fresh mixtures. 108
Table 18. The quantity needed for the functional unit between two locations. 125
Table 19. GWP of all materials used in LCA calculations. 125
Table 20. Result of LCA per functional unit of 1 m (height) × 1 m (length) wall with a variable width (per strength) on the two different locations with the strength-normalization factor. 131
Table 21. Result of LCA per functional unit of 1 m (height) × 1 m (length) wall with a width of 0.1 m on the two different locations without the strength-normalization factor. 132
Table 22. Physical properties of soil and sand. 148
Table 23. The result of mill certificate provided by Nevada Cement, Inc. 149
Table 24. Compositions of supplementary cementitious materials and soil filler used in this study, according to XRF analyses 149
Table 25. Mixture proportions used for 3D printing expressed per standardized 1000 grams 151
Table 26. Tests conducted and the standards that followed 155
Table 27. Compressive strength of cubic samples produced with different manufacturing methods 165
Table 28. Compressive strength of cylindrical samples produced with different manufacturing methods 169

Table 29. The result of the strength coefficient (k), calculated based on the compressive strength between cylinder/cube samples, on different curing days 173
Table 30. Result of modulus of elasticity and Poisson's ratio tests 173
Table 31. Result of two-way ANOVA for cubic samples 177
Table 32. Result of the EDS analysis 183
Table 33. Physical properties of soil. 199
Table 34. The result of mill certificate provided by Nevada Cement Inc. 200
Table 35. The XRF result of cementitious materials used in this study 200
Table 36. The total of 100 mixtures tested in this study for printability (normalized per 1000 g mass) . 205
Table 37. Mixture proportions found to be printable (normalized per 1000 g mass). 208
Table 38. Tests and the standards that followed in this study. 210
Table 39. Materials quantity needed for the functional unit of each mixture. 214
Table 40. GWP of all materials used in LCA calculations. 215
Table 41. Kilometer distances from suppliers to the construction site considered in this study 218
Table 42. Chemical and fresh properties of mixtures used in this study 220
Table 43. The viscosity limits of printable mixtures, with ± standard deviation and COV in parentheses. 226
Table 44. The upper and lower limits of printable mixtures, ± standard deviation and COV in parentheses. 227
Table 45. Result of LCA per functional unit of 1 m (height) × 1 m (length) wall with a variable width (per strength) with the strength-normalization factor. 239
Table 46. Results of LCA on all mixtures without the strength-normalization per functional unit of 1 m (height) × 1 m (length) wall with a width of 0.1 m. 242

List of Figures

Figure 1. Showing (a) deformation of the lower 3D-printed layers from the (b) original shape outlined in yellow color. 10
Figure 2. SEM images of (a) glass powder with angular particles, (b) fly ash class F with spherical particles, (c) fly ash class C with spherical particles similar to class F, and (d) Portland cement with distinct morphologies and particle sizes. 29
Figure 3. Showing the preparation of earth blocks with (a) a sequence of block production, and (b) a few of the earthen blocks were made and put in the oven for curing. 32
Figure 4. The scope of the LCA study, cradle to gate, as indicated in A1-A3..... 38
Figure 5. Hardened density of various mixtures. 47
Figure 6. Water absorption (%) in different mixtures. 49
Figure 7. Compressive strength results, with (a) and (b) images of two samples broken under dry compression from SH-GP mixture, and (c) compressive strength at 7 and 28 days, (d) compressive strength at 56 and wet 28 days. 54
Figure 8. Flexural strength of various mixtures. 56
Figure 9. Result of the wire brush test on mixtures. 58
Figure 10. Physical shape of earthen blocks after exposure to 2 hours of nitric acid: (a) PC, (b) SS-GP, (c) SS-FF, (d) SS-FC, (e) SH-GP, (f) SH-FF, (g) SH-FC. 59
Figure 11. Acid exposure results with (a) mass loss, and (b) compressive strength before and after exposure. 61
Figure 12. SEM images with (a) PC, (b) SS-GP, (c) SS-FF, (d) SS-FC, (e) SH-GP, (f) and (g) SH-FF, (h) and (i) SH-FC..... 65
Figure 13. Impact categories of CSAEBs per functional unit of 1 m^3 of earth blocks, with (a) GWP (in kilograms of carbon dioxide equivalent), (b) acidification (in kilograms of sulfur dioxide equivalent), (c) smog formation (in kilograms of ozone equivalent), and (d) fossil fuel depletion (in megajoules (MJ)). . 72
Figure 14. Impact categories of strength-normalized CSAEBs per functional unit of 1 m^3 of earth blocks, with (a) GWP (in kilograms of carbon dioxide equivalent per 17.23 MPa compressive strength), (b) acidification (in kilograms of sulfur dioxide equivalent per 17.23 MPa compressive strength), (c) smog formation (in kilograms of ozone equivalent per 17.23 MPa compressive strength), and (d) fossil fuel depletion (in megajoules per 17.23 MPa compressive strength). 77
Figure 15. Contribution analysis of individual mixture constituents to different environmental impact categories with (a) PC, (b) SS-GP, (c) SS-FF, (d) SS-FC, (e) SH-GP, (f) SH-FF, (g) SH-FC..... 79

Figure 16. The device used to measure the pH, electrical conductivity, total dissolved solids, salinity, and resistivity of the fresh mixtures. 94
Figure 17. SCARA Elite printer. 96
Figure 18. SEM results: (a) C-Sa at 80× magnification, (b) C-Sa at 3500× magnification, (c) C-So at 80× magnification, (d) C-So at 3500× magnification, (e) G-Sa at 80× magnification, (f) G-Sa at 3500× magnification, (g) G-So at 80× magnification, (h) G-So at 3500× magnification. 104
Figure 19. Results of the penetrometer test. 111
Figure 20. Water absorption test results. 112
Figure 21. Compressive strength of samples with (a) 7, 14, and 28 day cured samples, and (b) 56 and 91 day cured samples 115
Figure 22. Compressive strength of cubes in two different directions (a) along printing direction, (b) perpendicular to printing direction 118
Figure 23. Splitting tensile strength. 119
Figure 24. Presenting (a) testing set up per ASTM C1425-19, and (b) results of shear test. 121
Figure 25. Comparison of the relative contributions from different components to the different environmental impact categories with (a) C-Sa in Sacramento, (b) C-Sa in Philadelphia, (c) C-So in Sacramento, (d) C-So in Philadelphia, (e) G-Sa in Sacramento, (f) G-Sa in Philadelphia, (g) G-So in Sacramento, and (h) G-So in Philadelphia. 135
Figure 26. (a) Scara Elite Printer in operation and (b) a printed sample. 150
Figure 27. The coring procedure used to extract samples from freshly printed elements with (a) and (b) coring of cubic specimens, while (c) and (d) coring of cylindrical specimens. 153
Figure 28. Absorption results of different samples 160
Figure 29. Splitting tensile strength of cylindrical samples produced with different manufacturing techniques. 175
Figure 30. SEM images of samples produced with different manufacturing techniques including: (a)-(b): C-So cored, (c)-(d): C-So rodded, (e)-(f): C-So vibrated 15s, , (g)-(h): C-So vibrated 30s, (i)-(j): C-Sa cored, (k)-(l): C-Sa rodded, (m)-(n): C-Sa vibrated 15s, (o)-(p): C-Sa vibrated 30s. 182
Figure 31. Showing (a) Scara Elite Printer and (b) a printed sample. 202
Figure 32. Compressive strength, including the 7, 14, and 28-day cured samples with (a) including 0F10P0.2W, 0F20P0.2W, 5F5P0.2W, 5F10P0.2W, and 5F30P0.3W, (b)10F5P0.2W, 10F10P0.2W, 10F30P0.3W, 20F20P0.3W, and 20F30P0.3W, and (c) 30F5P0.3W, 30F10P0.3W, 30F20P0.3W. 233
Figure 33. Clarifying the directions for testing samples. 236
Figure 34. Compressive strength of cubes in two different directions, including the 28-day cured samples with (a) including 0F10P0.2W, 0F20P0.2W, 5F5P0.2W, 5F10P0.2W, and 5F30P0.3W, (b)10F5P0.2W,

10F10P0.2W, 10F30P0.3W, 20F20P0.3W, and 20F30P0.3W, (c) 30F5P0.3W, 30F10P0.3W, 30F20P0.3W, (d) failure mode in printing direction, and (e) failure mode in perpendicular to printing direction. 238
Figure 35. Comparison of the relative contributions from different components to the different environmental impact categories of: (a) 0F10P0.2W, (b) 0F20P0.2W, (c) 5F5P0.2W, (d) 5F10P0.2W, (e) 5F30P0.3W, (f) 10F5P0.2W, (g) 10F10P0.2W, (h) 10F30P0.3W, (i) 20F20P0.3W, (j) 20F30P0.3W, (k) 30F5P0.3W, (l) 30F10P0.3W, and (m) 30F20P0.3W. 246

1. Significant Original Features of Developed Work

This dissertation advances the intersection of soil-based construction and 3D printing by developing, validating, and environmentally benchmarking low-binder, soil-based cementitious systems suitable for 3D printing. Its originality lies in four integrated contributions of (a) materials development, (b) sustainability assessment, (c) testing and standardization, and (d) printability design, brought together within a single, coherent framework.

1.1. Material Development for Low-Impact Masonry and 3D Printing

a) Introduces and systematically evaluates Compressed and Stabilized Alkali-activated Earth Blocks (CSAEBs) using diverse precursors (e.g., glass powder; class F and C fly ash) and activators (sodium hydroxide, sodium silicate).

b) Demonstrates that glass-powder–based alkali-activated systems can improve compressive strength and acid resistance while lowering environmental burdens relative to Portland cement-stabilized CSEBs, providing an alternative pathway when conventional SCMs are scarce or variable.

c) Extends materials development to 3D-printable mixtures pairing two binder families (Portland cement vs. geopolymer) with two filler types (processed sand vs. locally sourced natural soil), designed without chemical admixtures, thereby foregrounding locally available resources and minimizing processing.

1.2. A Performance-linked Sustainability Method for 3D-printed Materials

a) Proposes and links a strength-normalized life-cycle assessment (LCA) to the size of the functional unit to compare mixtures with different mechanical capacities on an equalized basis, complementing conventional volume-based LCAs.
b) Shows that, under appropriate curing and mixture-design conditions, soil-based mixtures can match the mechanical performance of traditional sand-based 3D-printed mixtures while improving environmental metrics, while clarifying when and how soil substitution is advantageous.

1.3. First Comprehensive Quantification of Fabrication/Sampling Effects in 3D-printed Cementitious Testing

a) Produces and analyzes >670 specimens to isolate the influence of coring, cutting, rodding, and vibration on measured properties (compressive/tensile strength, modulus, porosity) of 3D-printed materials.
b) Provides statistical evidence of significant variability introduced by specimen preparation methods, establishing a foundation for standardized test protocols tailored to the layer-wise nature of printed components.
c) Bridges a critical gap between the current practice of relying on different non-printing-specific standards and the need for reproducible, comparable data to support future design codes.

1.4. Rheology-driven Printability Boundaries for Low-binder, Soil-based Systems

a) Establishes a rheological printability framework for mixtures produced without admixtures by mapping yield stress, dynamic viscosity, and shear stress across >100 mixture designs with varying cement/fly-ash contents and water-to-solids ratios.
b) Identifies operational windows that ensure continuous extrusion, layer stability, and reduced clogging, and links these thresholds to mechanical performance and environmental outcomes, enabling practical mixture optimization and quality control.

Collectively, these contributions provide a unified pathway for sustainable, locally adaptable, and robotically enabled construction in which: (a) material chemistries that reduce Portland cement reliance; (b) an LCA approach that is fair to mixtures with differing strengths; (c) statistically grounded guidance to standardize testing of 3D-printed cementitious materials; and (d) actionable rheological limits to design printable, low-binder soil-based mixtures without specialized admixtures. By integrating material science, rheology, mechanics, and environmental assessment, the work delivers a scalable evidence base for low-carbon soil-based construction and supports the evolution of codes, specifications, and automated construction practices that leverage locally available soils.

2. Introduction

The construction sector accounts for a significant share of global energy use and embodied CO_2 emissions [1], [2]. It is estimated that at least 10–20% of embodied carbon in buildings can be reduced by using cement substitutes and other low-impact materials [3]. One method that could potentially minimize industrial processing and transportation is the use of locally available, low-carbon construction materials [4]. As a result, there is growing interest in decarbonizing the

construction sector by using local, low-impact materials that require minimal industrial processing or transportation. Among these, soil-based construction has gained renewed attention in academia [5], [6] and industry [7] as a historically proven, resource-efficient, and low-impact structural solution [8].

Building on this context, masonry and soil-based structures consist of a group of classical construction components generally produced with local materials. A good example of such construction components is the numerous heritage structures that were built at various historical periods, many of which remain significant to this day. Examples range from adobe buildings in the American Southwest [9] to rammed earth temples in Asia [10] and cob settlements across Europe [11]. Due to the cultural importance of such architecture, as well as their relatively high compatibility with the built environment, soil-based materials are still widely used today [12]. As a result, masonry construction is highly advocated because of its simplicity [13], low ecological footprint [12], fire resistance [14], and high compatibility with the living environment [15].

To better understand their technical basis, masonry units are defined as various forms of blocks and bricks produced with clay (as classified in ASTM C62-13 [16], ASTM C216-16 [17], and ASTM C652-15 [18]), concrete (as in ASTM C55-16 [19]), stone, and even ceramic tile, among others [20]. The mentioned parts are commonly assembled by various forms of patterns, such as interlocking bonds, reinforcing (e.g., prestressed sections) [21], and cementitious bonds [22].

Beyond their practicality, masonry structures commonly utilize local materials, minimizing resource demands, as well as the environmental impacts associated with transportation and

processing [23]. This characteristic is well-aligned with the recent social movement toward sustainability, sustainable design, and greener construction life cycles [24]. In addition, masonry structures offer strong performance attributes. For instance, hollow clay masonry walls are known for high thermal and acoustic insulation, with studies reporting up to a 45% reduction in thermal conductivity compared to ordinary walls (e.g., [25] and [26]). Similarly, better fire performance has been reported for masonry and earthen structures, compared to their concrete counterparts [27].

Despite these advantages, traditional earthen construction methods such as adobe, rammed earth, cob, and compressed earth blocks (CEBs) face some performance and durability challenges [28], including low performance under weathering and water impacts [29], [30], as well as variability of properties (e.g., physical, mechanical, and even durability) [31], [32]. To address these, compressed and stabilized earth blocks (CSEBs) have evolved to incorporate machinery for improved performance and dimensional consistency. While effective, these benefits typically rely on stabilizing agents, such as Portland cement, which reduces sustainability and limits alignment with emerging climate objectives, and international decarbonization targets. Therefore, there is a growing need to explore alternative binders, fillers, and production strategies that preserve the performance benefits of CSEBs while minimizing their carbon footprint and labor requirements. In response to this need, this dissertation investigates the use of alkali-activated materials as eco-friendly substitutes, selected along with different precursors and activators, to produce Compressed and Stabilized Alkali-activated Earth Blocks (CSAEBs). It builds on extensive experimental work [33], [34], [35] to establish mixture-proportioning methods, assess material properties, and compare the environmental impacts of CSAEBs with those of conventional CSEBs.

Another major shortcoming of masonry and earthen structures is the high labor needs and scaffolding costs (which are estimated to be up to 60% of total construction costs [17]). In addition, setting up scaffolding and repeatedly assembling masonry units can be very time-consuming [36]. Recent advances in 3D printing, robotics, and drone technologies present promising solutions to the scaffolding needs and repetitive assembly of earthen and masonry construction. These technologies can manufacture (3D printers [33] and robots [37]), assemble (drones [38] and robots [39]), and maintain (robots [40]) masonry structures while reducing construction time, human error, and ecological impact [38]. They also offer significant cost savings, especially in repetitive labor. For example, drones can transport materials and masonry units to construction sites [38], or even detect cracks [41] (or defects [42]) on masonry structures. Robots[2] can place masonry units [45], [46], [47], and 3D printers can produce masonry materials or units on site, eliminating the need for formwork and repeated assembly [48]. Among these technologies, the present dissertation focuses on 3D printing. According to previous studies [49], [50], [51], 3D printing of cementitious materials can significantly reduce construction duration (by about 95% excluding prefabricated modular concrete per [50]) compared to conventional methods.

Over the past several decades, various construction systems have been developed to accelerate the erection of concrete and masonry structures while maintaining structural performance. Notably, prefabricated and precast concrete panel systems [52], [53], including tilt-up wall construction [54], large-panel buildings [55], and modular precast elements [56], have been widely adopted in high-rise and mid-rise construction in the last decades. These systems enabled rapid assembly, improved quality control, and reduced on-site labor, contributing to the rise of

[2] For capital expenditure information and recent studies in that area, please refer to [43], [44].

industrialized housing and large residential units in Europe, the Soviet Union, and Asia [57], [58]. More recent advances include precast sandwich panels [59], stay-in-place formwork [60], and hybrid concrete wall systems [61], all designed to combine structural efficiency with construction speed.

3D printing can be viewed as a continuation of this trajectory toward automation and prefabrication, but with far greater geometric freedom and reduced need for molds or cranes. Instead of casting panels in controlled facilities, 3D printing allows the direct, additive fabrication of structural or infill elements on-site using locally sourced materials, potentially extending the principles of modular and panelized concrete construction into a fully digital manufacturing paradigm [62], [63].

In masonry applications, 3D printing can significantly increase the production efficiency of components with complex forms and geometries, such as cantilevers, vaults, and domes [64], [65]. These components are built with high geometrical freedom and precision. In the 3D printing area, previous studies (e.g., [66], [67]) have recorded the benefits of using clay materials in the rheological and thixotropic behavior of cementitious mixtures. Some studies have also used clay as the main 3D printing material [68], and have highlighted the endless recyclability of 3D-printed clay-based materials [69].

However, current 3D-printed cementitious mixtures require nearly twice the binder content of conventional concrete [49]. They also heavily rely on a growing list of chemical admixtures, such as viscosity-modifying agents, plasticizers, and retarders, to ensure shape retention and quality

printability [49], [70]. Securing chemical additives, used with high Portland cement and finely sieved sand content, makes 3D-printed cementitious materials (as a whole practice) less sustainable, because cement production is associated with high environmental impact per previous studies [71], [72] This can be seen from the results of previous studies (e.g., Han et al. 2021 [73]), which conducted Life Cycle Analysis (LCA) on a 3D-printed structure and noted that the environmental impact caused by 3D printing concrete construction is generally larger than traditional cast-in-situ concrete construction. This is seen in all indicators assessed in the mentioned study, including global warming potential, acidification, petrochemical pollution, and eutrophication. In general, it can also be difficult to secure some chemical additives on a global scale, especially since one of 3D printing's main advantages is obtaining materials locally and working in remote locations. In response, this dissertation has explored two sustainable approaches: the use of alkali-activated binders derived from industrial byproducts (e.g., coal fly ash), and the substitution of processed fine aggregates with locally available natural soils. Both approaches are designed and executed without any rheology modifiers or 3D printing-specific admixtures. Nevertheless, studies evaluating these strategies in combination remain scarce, and the performance implications of low-binder, soil-based systems in 3D printing applications are not yet well understood. This point can be seen in recent studies (e.g., [33], [35], [74], [75], [76]).

Additionally, although 3D printing parts have been shown to have acceptable performance both in industry (e.g., [77]) and academically (e.g., [78], [79]) to date, no set of regulatory or national codes for fair testing and comparison has been established. Many studies in this area are currently applying other industry standards or test methods to evaluate the fresh and hardened properties of 3DPC materials. Some have developed their testing methods based on layer-by-layer

construction (e.g., [80]), while others have followed the same procedure as in ordinary concrete areas (e.g., [81]). As a result, a major inconsistency in the results of previous works is identified, which makes any comparison efforts difficult. For example, in cited literature, 3D-printed components are tested for compressive strength by cutting larger printed parts into smaller sections (as in [82], [83]), or printing the parts to the size and shape of a cylinder or cubes discussed in [84], [85]. Some studies have even tried printing components inside molds [86]. The problem with cutting samples (or extracting from larger samples), is the large size variation that can result from human error. Similarly, printing the entire sample can cause precision issues since 3D-printed layers often do not develop high strength upon immediate printing and can deform when more layers are printed on top. This can cause a significant warping and deforming effect that can lead to a semi-triangular shape (e.g., bulging effect), as shown in **Figure 1**. The same can be discussed regarding printing specimens inside molds, which is similar to mold casting concrete and may not represent 3D printing. Such inconsistencies contribute to a high degree of uncertainty in interpreting mechanical behavior and present a significant challenge for the future development of design codes. A standardized set of tests can help with the following: compare the results of different studies that have used different materials and mixture proportions, allow the development of regulatory compliance codes, allow for better quality control of 3D-printed specimens, and assist in the reproducibility of the results.

In 2023, the International Standardization Organization (ISO) and the American Society for Testing and Materials (ASTM) introduced ISO/ASTM 52939-23 [87]. The mentioned standard thus far provided preliminary concepts regarding 3D printing structures, rather than implementing major qualitative or quantitative measures. This lack of quantitative measures indicates the need

for a gradual development of methodologies and testing procedures that are unique to 3D printing of cementitious materials.

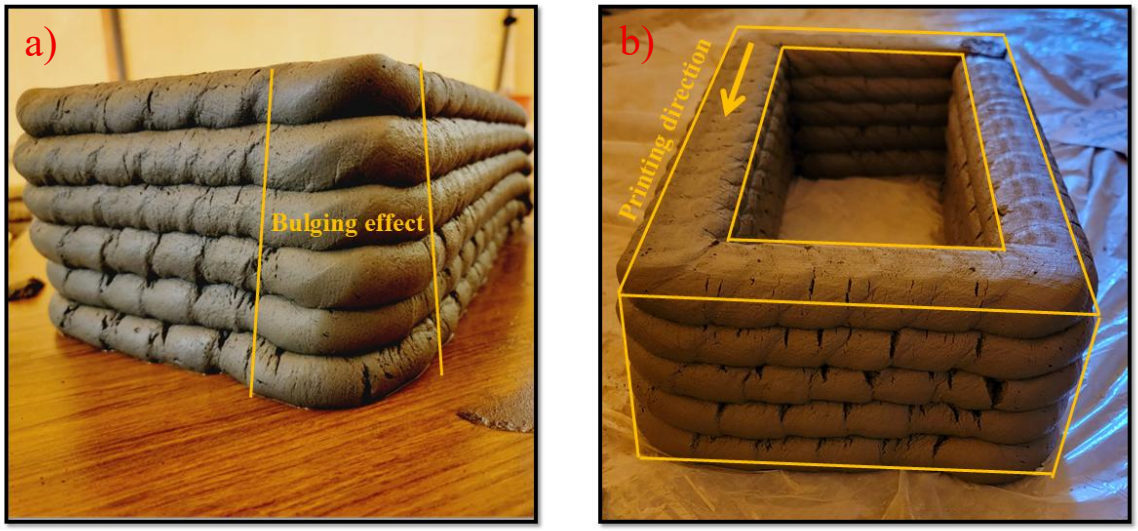


Figure 1. Showing (a) deformation of the lower 3D-printed layers from the (b) original shape outlined in yellow color.

In addition to the mentioned issue of lack of standardized tests, another major problem with 3D printing is the heavy reliance on fly ash for consistent and high-quality prints. Generally, printability defines a mixture's ability to be continuously extruded and retain its shape after deposition without significant deformation or collapse. However, achieving this balance requires a careful design of particle size and fresh-state rheology. Previous studies have defined the optimum and maximum particle size to be between one-fifth (1/5) to one-tenth (1/10) of the actual nozzle orifice [88] to avoid nozzle clogging. However, defining the rheology of the fresh state for 3D printable cementitious materials is difficult because its properties do not remain constant, as

described by Newtonian rheology models. As a result, cementitious materials are best described by Bingham or Herschel–Bulkley models, due to their yield stress and shear-thinning behavior, as well as time-dependent thixotropic rebuild [89], [90]. Unlike the angular and hard sand-based mixtures, soil particles are generally more cohesive and have different frictional and moisture contents, all of which can contribute to printability. To account for such factors, and if the maximum particle size of one-fifth (1/5) to one-tenth (1/10) rule is followed [91], the printability can be established by three main parameters: (1) yield strength, (2) dynamic viscosity, and (3) shear stress.

In general, yield stress governs the start of flow, and plastic or dynamic viscosity influences both extrusion pressure and layer stability [90], [92], [93]. If the yield stress is too low, layers may slump or deform under their own weight, while a high yield stress may result in clogging or difficulty pumping. Similarly, dynamic viscosity and shear stress can have a significant impact on nozzle clogging, extrusion, and buildability of the printed layers. Both dynamic viscosity and shear stress can represent flow resistance and shape retention [90], [94], [95]. Another useful piece of information relating to shear stress is the interlayer bonding at the fresh state, which, if low, can lead to the drifting or slipping of layers [96], [97]. As a result, and to account for the mentioned, this dissertation establishes printable boundaries by quantifying the values of all three for approximately one hundred mixture proportions with varying cement and fly ash contents, as well as different water-to-solid ratios. These thresholds are then linked to mechanical performance and environmental impacts.

In summary, to advance sustainable, printable, and structurally reliable earthen construction through 3D printing, the present study addresses four interconnected topics: (1) the development of alkali-activated earthen blocks using different precursors and activators; (2) the comparative performance and life cycle assessment of 3D-printed cementitious mixtures combining Portland cement/geopolymer binders with sand/soil fillers; (3) the assessment of the influence of specimen preparation and sampling techniques on the measured mechanical properties of 3D-printed materials; and (4) the determination of rheological thresholds and printable limits for low-cement and low-fly ash, soil-based cementitious systems, designed without chemical admixtures.

2.1. Objectives and Motivation

The primary objective of this dissertation is to establish a comprehensive experimental and environmental framework for the sustainable application of soil-based and alkali-activated cementitious materials in both conventional and 3D-printed construction. This is achieved through four main research chapters: to develop and evaluate compressed and stabilized alkali-activated earth blocks (CSAEBs) using a range of precursors (glass powder, fly ash class F and C) and activators (sodium silicate and sodium hydroxide), and to assess their mechanical, durability, microstructural, and environmental performance (as stated in Chapter 3). The outcomes include: (a) identification of effective precursor-activator combinations and (b) demonstration of enhanced performance and sustainability of CSAEBs compared to their Portland cement-based CSEBs counterparts.

This study comparatively investigates the fresh-state behavior, mechanical properties, and life cycle impacts of four 3D-printed cementitious mixtures made using two binder systems (Portland

cement and geopolymer) and two filler types (crushed sand and low-plasticity silt natural soil), as described in Chapter 4. This includes the development of a strength-normalized LCA methodology to better interpret the advantages and disadvantages between strength performance and environmental burden across different binder-filler combinations.

In addition, cementitious components for over 670 samples were made with soil and sand fillers (as stated in Chapter 5), to quantify the impact of fabrication and sampling methods, including coring, mold casting with rodding or vibration, as well as cutting, on the measured mechanical properties of 3D-printed concrete. Advanced statistical evaluation of all samples is also provided to highlight the necessity of standardized procedures for reliable material assessment.

To systematically determine the rheological boundaries of printable, low-binder, soil-based mixtures, over 100 combinations of Portland cement, fly ash, and water-to-solid ratios (as stated in Chapter 6) are studied. Parameters, such as yield stress, dynamic viscosity, and shear stress, are characterized to define printability limits. In this context, printability can be defined as the material's ability to be successfully extruded and deposited layer by layer without defects, such as clogging, tearing, or segregation. Additionally, the mechanical and environmental performance of successful mixtures is also evaluated, which can help provide practical guidance for sustainable mixture design without chemical admixtures.

These research efforts are motivated by the urgent need to decarbonize construction materials through the promotive use of local, underused materials. It can also establish robust design and testing methodologies compatible with the 3D printing of cementitious materials. Together, these

studies contribute to the broader goal of enabling sustainable, structurally reliable, and digitally integrated earthen construction.

2.2. Scope

This dissertation examines alternative cementitious systems incorporating both soil- and sand-based materials, developed in block-based and 3D-printed forms. The study focuses on mixtures prepared with a locally sourced, low-plasticity silt soil and crushed sand, used as fillers in combination with Portland cement and alkali-activated binder systems. To isolate the role of raw materials, no chemical admixtures are included. The research scope intentionally excludes clay-rich soils, as well as long-term durability considerations such as weathering, seismic response, and fire resistance.

The experimental program evaluates fresh-state rheology, printability, and hardened properties under controlled laboratory conditions. Printability trials are limited to extrusion-based 3D printing with a two-inch nozzle. Rheological behavior is assessed using a rotational viscometer, while mechanical performance is characterized by standardized specimens, including 50×50×50 mm cubes and 76.2 mm (diameter) × 152.4 mm (height) cylinders. In this dissertation, the focus is primarily on printability, defined as the successful extrusion and placement of mixtures. While some aspects of buildability, such as interlayer stability and shape retention, are inherently connected to rheological behavior, a comprehensive evaluation of layered structural performance is beyond the present scope.

Similarly, although durability is a critical performance factor for construction materials, this dissertation does not include durability testing of the 3D-printed mixtures produced. The exclusion is due to the exploratory nature of this study, which is focused on establishing rheological boundaries, mechanical properties, and environmental impacts. Durability aspects such as resistance to moisture ingress, freeze–thaw cycles, or long-term degradation remain essential for practical applications, and are recommended as important directions for future research.

Beyond the laboratory-scale experimental study, the dissertation extends to life cycle assessment (LCA) of the mixtures. This integration of performance testing with environmental impact analysis provides a comprehensive evaluation of soil- and sand-based cementitious systems, offering insights into their feasibility as low-impact alternatives for sustainable construction.

2.3. Research Novelty and Significance

This dissertation's novelty lies in combining the two research areas of earthen construction and 3D printing, both of which have been advanced in parallel. While earthen construction has a long history of using local soils to produce low-impact structural components, 3D printing has shown its ability to reduce labor, avoid formwork, and waste. As a result, the integration of these two methods for low-binder, soil-based systems is significant to be explored. The novelty of this work lies in developing, characterizing, and environmentally assessing the properties of both systems individually and combined.

From a material development perspective, this research is among the first to systematically evaluate compressed and stabilized alkali-activated earth blocks (CSAEBs) using a diverse range of precursors (such as glass powder and class F and C fly ash), and activators (such as sodium hydroxide and sodium silicate). Glass powder is introduced as a waste materials that can substitute class F and C fly ash in this application, and has the potential to improve strength, durability, and environmental performance, compared to conventional Portland cement-stabilized CSEBs.

In the domain of additive manufacturing, this dissertation is distinctive in jointly evaluating binder type (Portland cement vs. alkali-activated) and filler type (processed sand vs. natural soil) under identical mixture design, printing, and testing conditions. The application of a strength-adjusted LCA can provide a more realistic measure of environmental performance in sustainability evaluations of 3D-printed materials.

The work also makes a methodological contribution by being the first comprehensive study to quantify, through statistical analysis, how specimen fabrication and sampling techniques (coring, cutting, rodding, vibration), affect the measured hardened properties of soil- and sand-based 3D-printed cementitious materials. By isolating manufacturing-induced variability, the study lays the groundwork for standardizing testing protocols in the field of 3D printing cementitious materials.

Finally, this research establishes rheological boundaries for printability in low-cement, low-fly ash soil-based mixtures produced without chemical admixtures. By following a specific framework of varying mixture proportions and measuring key rheological parameters, such as yield stress, dynamic viscosity, and shear stress, this work identifies the operational limits for

successful extrusion and correlates these thresholds with mechanical and environmental performance. This integrated rheology, mechanical, and LCA framework provides an essential reference for future mixture optimization and quality control (buildability).

Taken together, the significance of this dissertation lies in its integration of earthen construction with additive manufacturing, as well as evaluating earth-based (a) material chemistry and microstructure, (b) rheology, (c) mechanical performance, and (d) life cycle impacts. The findings have significant practical implications for future studies to develop more sustainable, scalable, and locally adaptable construction practices. It also helps the development of both the standardization of testing protocols for 3D-printed materials and the design of low-carbon building systems that use locally available resources. By bridging gaps between traditional earthen construction and modern semi-automated 3D printing, this work supports the transition toward a low-carbon, resource-efficient, and robotically enabled construction industry.

2.4. Organization of the Dissertation

Chapter 3 introduces the development of compressed and stabilized alkali-activated earth blocks (CSAEBs). It investigates the effects of various precursors and activators on mechanical strength, durability, and sustainability. Glass powder is also introduced as a novel precursor for earthen block applications, and then a cradle-to-gate LCA is used to compare performance across multiple mixture proportions.

Chapter 4 presents a comparative evaluation of four 3D-printed mixtures produced with Portland cement and geopolymer binders with either crushed sand or natural soil as filler. Fresh, mechanical, microstructural, and environmental impacts are then evaluated under consistent printing and testing conditions. A strength-correction factor is applied in the LCA to standardize the results with mechanical performance.

Chapter 5 addresses the variability in test results caused by differences in sample preparation and collection methods. Over 670 specimens are tested to statistically assess the influence of coring, cutting, and mold casting (rodded and vibrated) on compressive strength, tensile strength, modulus of elasticity, and porosity. Results highlight the gap and the need for standardized sample preparation in 3D printing research to avoid unforeseen variabilities and inconsistencies.

Chapter 6 defines the rheological printability limits of soil-based mixtures produced with minimal cement and fly ash content for sustainability purposes. Using a printability-rheological approach, over 100 mixtures are evaluated for printability and then rheological properties, such as dynamic viscosity, yield stress, and shear stress. Successful printable mixtures are tested for mechanical performance and evaluated for their environmental impacts. The findings establish a foundational rheological database for sustainable soil-based mixture design.

Chapter 7 concludes the findings provided in other chapters and identifies other insights and implications made in different chapters for sustainable construction, in addition to opportunities for future research. The implications of research for future of sustainable construction, 3D printing

standardization, and design optimization are discussed. Directions for future work include scaling up for field applications, incorporation of different soil type databases, and long-term durability assessments.

2.5. Journal Publications Derived from this Dissertation

Journal article based on chapter 3 (in preparation):

- Nodehi, M.[3], Kumar, N.[4], Barbato, M.[5] (2025). "Effect of various supplementary cementitious materials (SCMs) and activators in the production of Compressed and Stabilized Alkali-activated Earth Blocks (CSAEBs)"

Journal article based on chapter 4 (in preparation):

- Nodehi, M.[1], Barbato, M.[3] (2025). "Comparative Properties of Soil-Based 3D-Printed Cementitious Materials Produced with Ordinary Portland Cement and Geopolymer Binders"

Journal article based on chapter 5 (in preparation):

- Nodehi, M.[1], Barbato, M.[3] (2025). "Effects of Specimen Preparation on Mechanical Properties of 3D-Printed Cementitious Materials"

Journal article based on chapter 6 (in preparation):

- Nodehi, M.[1], Barbato, M.[3] (2025). "Mechanical Properties and Rheological Boundaries of Low-Cement and Low-Fly Ash Soil-based 3D Printing Mixtures"

---

[3] Ph.D. Candidate, Department of Civil & Environmental Engineering, University of California, Davis; Email: mnodehi@ucdavis.edu; ORCID: https://orcid.org/0000-0001-5896-6375
[4] Assistant Professor, Department of Civil & Environmental Engineering, Indian Institute of Technology, Patna; Email: ntnkumar@iitp.ac.in; ORCID: https://orcid.org/0000-0002-4045-300X
[5] Professor, Department of Civil & Environmental Engineering, University of California, Davis; Email: mbarbato@ucdavis.edu; ORCID: https://orcid.org/0000-0003-0484-8191

3. Effect of Various Supplementary Cementitious Materials (SCM) and Activators in the Production of Compressed and Stabilized Alkali-Activated Earth Blocks (CSAEBs)

In this study, compressed and stabilized alkali-activated earth blocks (CSAEBs) using various types of precursors (e.g., glass powder, coal fly ash class F and C) and activators (e.g., sodium silicate and sodium hydroxide) are produced and compared to ordinary Portland cement-based CSEBs. A series of tests, including unit weight, water absorption, compressive and flexural strength, wire brush test, acid resistance, and life cycle analysis (LCA) have been conducted in accordance with standards to evaluate the physical, mechanical, durability, and sustainability of CSAEBs. Results show that the activators' overall pH and the precursors' chemical composition can determine the rate of strength development and the performance of each block specimen. In this study, a molarity of 3.0 with a pH of 12.37 for sodium hydroxide is found to surpass premixed 40:60 (sodium silicate to water) with a pH of 10.8 by a rate of approximately four times higher compressive strength values. Life cycle analysis (LCA) revealed that the availability of local materials, the optimization of mixture proportions, and the developed strength are significant contributing factors. For instance, sodium silicate mixtures averaged global warming potential (GWP) of 118.2 kg CO_2-eq, compared to 103.9 kg CO_2-eq for sodium hydroxide mixtures. After strength-normalization to 17.23 MPa, sodium silicate systems showed much higher GWP (average of 374.1 kg CO_2-eq), whereas sodium-hydroxide mixtures were lowest (74.83 kg CO_2-eq).

3.1. Introduction

Earthen construction represents one of the oldest methods of construction, which has been used for centuries based on local materials. Earthen construction is generally considered a resilient and resource-efficient method that includes adobe, rammed earth, cob, and compressed earth blocks (CEBs) [14], [98], [99], [100]. Although each method has evolved in response to specific climatic, geological, and cultural conditions, compressed and stabilized earth blocks (CSEBs) remain in use in many regions worldwide [101]. Since the building and construction sector is responsible for roughly 36% of global energy use and approximately 39% of energy- and process-related CO_2 emissions [2], the use of earth as a primary building material remains a sustainable alternative [102]. It is because CSEBs are produced by using natural and local materials, which avoids significant manufacturing processes and long transportation [103], [104], [105]. CSEBs are made by compressing soil blended with a stabilizing agent, such as cement or lime, where the stabilizer hydrates and gradually develops strength. Although CSEBs incorporate sustainable techniques through the addition of stabilizing agents, this strategy alone remains insufficient to meet ambitious climate goals outlined by policymakers [106], [107], [108]. This is because the commonly used stabilizers, such as cement and lime, are highly carbon-intensive, which limits the potential for reductions in embodied emissions.

Another promising alternative, primarily used as an alternative to common Portland cement-based materials, is the use of alkali-activated binders. Recent studies that have conducted Life cycle assessments (LCAs) have extensively shown that for a given volume of concrete, alkali-activated binders can reduce environmental impacts (i.e., CO_2 per m^3) by at least 45% [109]. Alkali-activated materials (AAMs) are aluminosilicate-based materials produced by activating a precursor, such as coal fly ash, with an alkaline solution [110]. Studies have reported that AAMs

not only lower the environmental impact of cementitious materials but also offer improved resistance to fire, acids, and other forms of chemical deterioration [111], [112]. Such better durability performance is especially valuable in earthen construction, where materials are exposed directly to outdoor conditions. Despite the advantages of using CSEBs as a locally sourced material, there are clear benefits to combining CSEBs with alkali-activated binders. Past research has shown that earthen materials have low abrasion and weathering resistance, experience brittle fracture, have a poor seismic performance, and are vulnerable to acid rain [113], [114], [115]. In reality, these shortcomings are often addressed by increasing the stabilizer content, in this case Portland cement, which again undermines the environmental benefits of CSEBs.

To overcome the limitations of earthen components, while also reducing the environmental impact of stabilizers, this study investigates the combined use of CSEBs with AAMs to produce compressed and stabilized alkali-activated earth blocks (CSAEBs). CSAEBs were produced using different precursors, including glass powder, coal fly ash class F and class C, and activated with sodium silicate and sodium hydroxide. While fly ash class F and class C have been used as supplementary cementitious materials (SCMs) for decades, glass powder is a more recently introduced SCM that has been highlighted as a viable alternative filler in cementitious systems [116]. Glass products have a global annual production of over 150 million metric tons [117]. It is reported that waste glass has a very low recycling rate, ranging from 21% [118] to 26% [119], despite its ability to be continually recycled [119]. One major issue in recycling glass is the significant energy demand required to remelt glass during the recycling process [119]. Reusing glass in powdered form can avoid the high-energy process of remelting it, and recent studies have achieved this practice [116], [120], [121].

The production of CSAEBs can obviously offer several benefits, including improved sustainability, enhanced mechanical performance, and higher resistance to chemical deterioration. However, the inclusion of glass powder can further enhance these benefits. For example, CSAEBs already rely on locally available materials [122], but finding a suitable local precursor similar to fly ash class F or class C can be challenging. Also, alkali-activated binders are known for their high acid and deterioration resistance, making CSAEBs particularly attractive for construction in various regions [123]. Since glass powder is an industrial byproduct with high chemical stability, its use is believed to enhance both the sustainability and durability of CSAEBs.

However, the properties of CSAEBs, particularly in combination with glass powder, have been studied in only a few studies to date. Idriss et al (2022) [124], for example, studied blocks made from calcined clay activated with sodium silicate and sodium hydroxide, but did not evaluate the influence of different precursors. Diop et al. (2011) [125], also made a similar attempt to substitute regular soil with calcined clays, activated with sodium silicate. However, while the calcination of clay requires less energy than the production of Portland cement, it still carries notable environmental impacts, particularly from fuel consumption and CO_2 emissions during firing [126]. Other studies (e.g., [127], [128]) have focused primarily on basic compressive strength, without providing a comprehensive evaluation of durability or microstructural characteristics. Additionally, in the mentioned studies, a full-scale evaluation of different properties and materials has not been made. Despite the major potential benefits of producing glass powder-based CSAEBs, only a handful of studies have been directly conducted in this research focus. For instance, Aluko et al. [129] examined the inclusion of glass powder as a cement replacement but did not evaluate

its properties with an alkali-activated binder. Rivera et al. [130] used glass powder as a partial replacement of coal fly ash, activated with an alkaline solution from the aluminum industry. Their analyses established the optimum ratio of the activator to precursor using that specific activator. Similar attempts to optimize the mixture proportions by using local byproducts and waste materials were presented by Larbi et al. [131]. The mentioned research gaps highlight the need for a more comprehensive study, including glass powder as a precursor in CSAEBs' production, to evaluate the physical, mechanical, and durability properties of the resulting blocks.

Based on the literature review mentioned, there is a need to investigate the impact of various precursors and activators on the production of CSAEBs. Given this research gap, there is a clear need to investigate the effect of various precursors and activators on the performance of CSAEBs. This study provides one of the first comprehensive experimental and environmental evaluations of CSAEBs (distinct originality) incorporating multiple supplementary cementitious materials (SCMs) and activators, establishing direct links between mixture design, mechanical performance, and life-cycle impacts. As a result, the objectives of this study are as follows:

- Developing a clear understanding of CSAEBs' mixture proportioning and their properties with those of conventional Portland cement-based CSEBs.
- Evaluating the physical, mechanical, and durability characteristics of CSAEBs produced with different alkaline activators and precursors, so that the most effective material combinations can be identified.
- Evaluating the environmental impacts of CSAEBs and providing each mixture's comparative impact for future mixture optimization studies in this area.

3.1.1. Motivation and Significance

Three main motivations drive this research: first, to identify and compare the impacts of different SCMs and their properties on producing CSAEBs; second, to determine the feasibility of producing alkali-activated glass powder-based blocks; and third, to evaluate their environmental benefits.

Both the first and second motivations compare the properties of CSAEBs made with different SCMs and activators. Since the production of fly ash is being substantially reduced, evaluating different SCMs for their properties in CSAEBs is a crucial step in identifying a suitable substitute. The findings provide guidance on selecting optimal material combinations and contribute to advancing the development of sustainable, high-performance earthen construction materials. In doing so, this work extends beyond prior studies by integrating mechanical, microstructural, and life-cycle assessments into a unified framework, offering a replicable methodology for designing low-carbon, high-performance earthen blocks.

The third motivation stems from the growing interest in reducing the environmental impact of conventional construction materials, such as ordinary concrete. For instance, it has been reported that producing 1 m^3 of conventional Portland cement-based concrete generates approximately 597.54 kg of CO_2 equivalent, whereas an equal volume of alkali-activated concrete (AAC) produces only about 148 kg of CO_2 equivalent [106]. As a result, a combination of environmentally friendly CSEBs with alkali-activated stabilizers has the potential to reduce the ecological impacts.

3.2. Materials

In this section, the following types of materials are discussed: natural soil, SCMs, Portland cement, and alkaline activators.

3.2.1. Soil

The natural soil used in this study was sourced from Ace Hardware in Davis, California. It was reported by the supplier that, the soil was extracted from subsurface layers several meters below ground level. The soil was then mechanically sieved using a TS-1 Gilson shaker to achieve a maximum particle size of 1.18 mm (No. 16 sieve), per ASTM C136-14 [132]. The coarser materials were discarded. The size of 1.18 had been chosen by the authors based on trials conducted on the mixtures and the small hydraulic machine used to produce the blocks in this study. Following sieving, all of the sieved materials were oven-dried at 110°C for 24 hours to minimize residual moisture within the remaining soil and to also remove any organic content per ASTM C136-14 [133] and ASTM D2216-19 [134]. The materials were then placed in a sealed dry bucket until used. The results of additional characterization, including particle size distribution, Atterberg limits, and compaction behavior (Proctor test), is presented in **Table 1**. Based on these results and classification under ASTM D2487-11 [135] and Unified Soil Classification System, the soil was identified as a low-plasticity silt (ML). In this study, sieve analysis was conducted in accordance with ASTM C117/C136 to characterize soil and sand, and the soil was washed per ASTM D6913-17 [136]. The original dry mass of the sample was 1336.30 g, and the wash mass was 521.90 g, resulting in a wash loss of 60.9%.

Table 1. Physical properties of soil.

Laboratory tests	Standards	Property	Value
Particle-size analysis	ASTM C117-17 [137] , C136-14 [132], D6913-17 [136]	Cumulative % Retained #4 (4.75mm)	0.0
		Cumulative % Retained #8 (2.36mm)	0.0
		Cumulative % Retained #10 (2mm)	0.0
		Cumulative % Retained #16 (1.18mm)	0.0
		Cumulative % Retained #30 (0.6mm)	8.2
		Cumulative % Retained #40 (0.425mm)	14.0
		Cumulative % Retained #50 (0.3mm)	19.0
		Cumulative % Retained #100 (0.15mm)	29.4
		Cumulative % Retained #200 (75µm)	38.1
		Pan	100.0
Atterberg limits	ASTM D4318-10 [138]	Liquid limit LL (%)	20.8
		Plastic limit PL (%)	13.9
		Plasticity index PI (%)	6.8
Soil compaction tests	ASTM D698-21 [139]	Optimum moisture content (%)	13.0
		Maximum dry density (kg/m^3)	1,873.3

3.2.2. SCMs and Portland Cement

In this study, glass powder was supplied by Vitro-minerals, located in Tennessee, USA, under the commercial name ACAS and with a specific gravity of 2.50. Based on the information provided by the supplier, the glass powder was recycled from glass plates (e.g., windows or auto windshields) and then ground to finer sizes. It is produced with a minimum fineness of 95%

passing a 325 mesh, corresponding to a Blaine fineness of 4000-4500 cm^2/g. Furthermore, the glass powder was rated at a reactivity index of 85% and 95% at 7 and 28 days of curing, respectively, when used as a 20% replacement of Portland cement in general-purpose mortar. The reactivity index reflects the relative strength contribution of the replacement material compared to plain Portland cement-based mortar [140].

In addition, fly ash class F and class C were supplied by Salt River Materials Group (SRMG) in Stockton, California. Additionally, the Portland cement type I/II was supplied by Nevada Cement, sourced from their main plant located in Reno, Nevada. The supplier's mill certificate indicated a phase composition of 58% tricalcium silicate (C_3S), 8% dicalcium silicate (C_2S), 7% tricalcium aluminate (C_3A), and 9% tetracalcium aluminoferrite (C_4AF). **Table 2** provides the X-ray fluorescence (XRF) results of the three SCMs used in this study. The XRF was conducted using the Rigaku Super Mini-200 model and then analyzed using the manufacturer's provided software, called ZSX. The method for calculating the oxides was recommended by the manufacturer [141], which involves a semi-quantitative XRF (also referred to as SQX). **Figure 2Error! Reference source not found.** presents SEM images of raw glass powder, fly ash class F, class C, and Portland cement taken by Thermo Fisher Quattro S ESEM at magnifications ranging from 50 μm to 5 μm.

Table 2. The XRF result of cementitious materials used in this study.

Chemical compounds and properties	Glass powder (%)	fly ash class F (%)	fly ash class C (%)
SiO_2	71.2	59.33	33.68
Al_2O_3	0.36	23.78	16.81
Fe_2O_3	0.44	6.22	8.61

CaO	9.33	3.86	27.27
MgO	3.86	1.39	3.29
SO_3	0.00	0.18	2.12
Na_2O	13.2	0.35	1.87
K_2O	0.04	0.00	0.92
Loss on ignition (LOI)	0.50	0.36	0.36

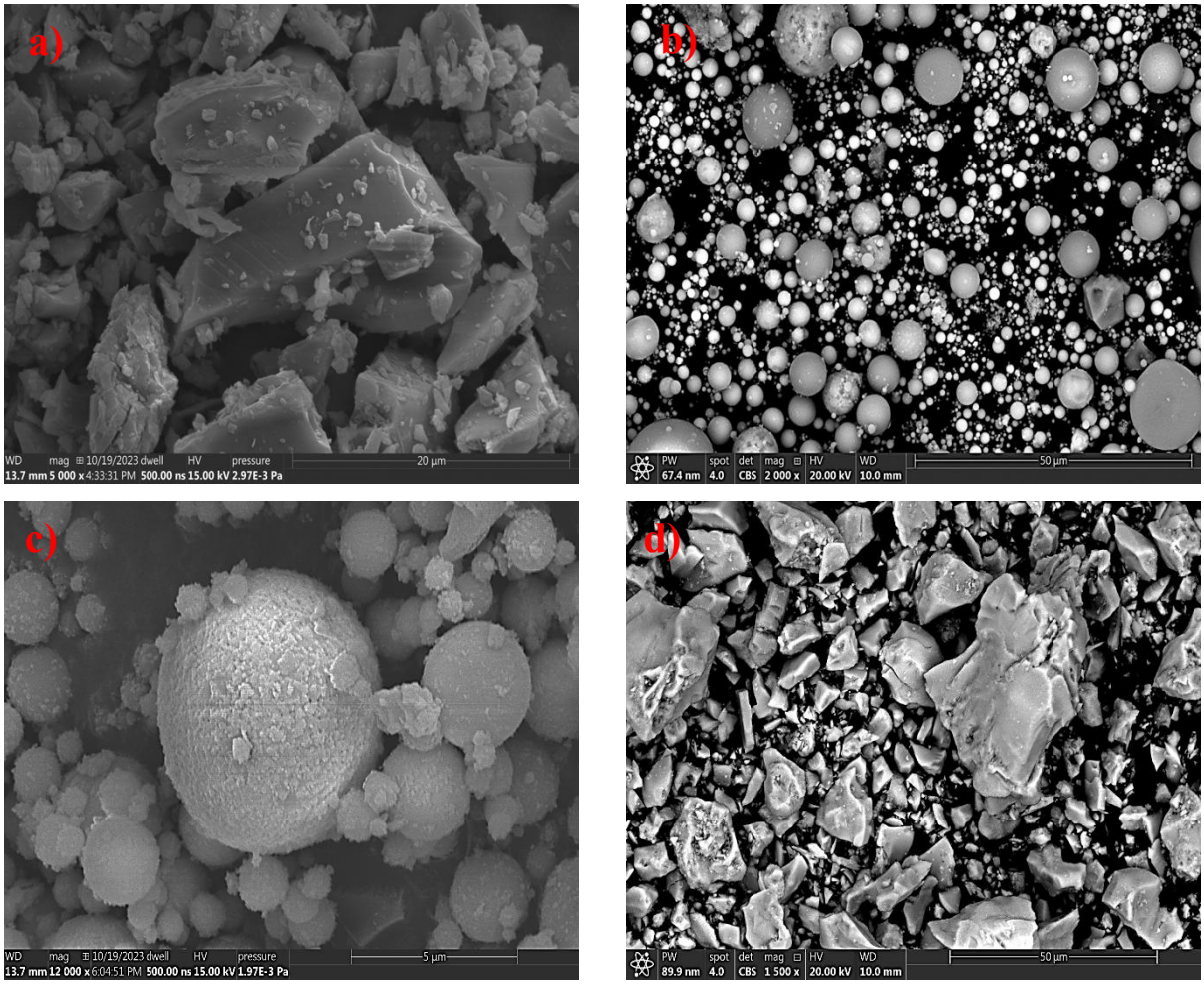


Figure 2. SEM images of (a) glass powder with angular particles, (b) fly ash class F with spherical particles, (c) fly ash class C with spherical particles similar to class F, and (d) Portland cement with distinct morphologies and particle sizes.

3.2.3. Alkaline Activators

In this study, reagent-grade sodium silicate and sodium hydroxide were supplied by Thermo Fisher Scientific and Duda Energy, respectively. The sodium silicate was supplied with a premixed ratio of 40% sodium silicate and 60% water, and a boiling temperature of 100.6°C). The sodium hydroxide supplied had a molecular weight of 39.99 g/mol, a pH of 11-14, and a relative density of 2.13, supplied in solid flakes. After mixing the flakes with water in a fume hood, the sodium hydroxide-water mixture was left at lab temperature (25±2 ºC) for at least 24 hours to cool. Based on the initial trials conducted and a sustainability perspective, a low molarity of 3.0 was extrapolated.

Table 3 presents the measured physical and chemical properties of the activators. The pH of the sodium silicate solution was determined to be 10.8, while the pH of the sodium hydroxide solution, with a very low molarity of 3.0, was 12.37. In AAMs, it is generally believed that the higher alkalinity of the solution or the overall mixture can substantially impact the strength development of materials [142]. In addition to the pH values, the conductivity, TDS, and resistivity values of the two activators are found to be largely different. This difference can be attributed to their chemical compositions. For instance, sodium silicate is known to be a compound containing sodium oxide and silica (Na_2O & SiO_2), while sodium hydroxide is composed of sodium and hydroxide ions (Na^+ & OH^-). As a result, the TDS and salinity values are found to be higher in sodium hydroxide because of its higher concentration of dissociated (sodium) ions.

Table 3. Properties of the activators used in this study.

Activators	pH	Conductivity (mS/cm)	TDS (g/L)	Salinity (ppt)	Resistivity (Ω)

Sodium silicate	10.8	32.2	22.7	16.1	31.1
Sodium hydroxide	12.3	203.0	100.0	98.1	5.1

3.3. Methods

This section describes the equipment used in this study and the methodology followed in sampling and testing standards.

3.3.1. Earth Block Fabrication

Earth blocks with a dimension of 88.9 mm × 63.5 mm × 30.48 mm, were manually made by a small hydraulic press, supplied by Advanced Earthen Construction Technologies Inc., located in San Antonio, TX. The blocks were fabricated using a hydraulic pressure of 26.20 MPa (fluid pressure), resulting in an average pressure of approximately 8.00 MPa applied to the blocks during fabrication. The mixing time to production was less than 5 minutes, ensuring that hydration starts almost simultaneously from mixing to block production. After the blocks were produced, they were placed in an oven at a temperature of 110°C for a duration of four hours. These temperatures and curing durations were chosen based on trials conducted by the authors and applied to all samples, including the reference and Portland cement-based blocks. After four hours in the oven, the samples were removed from the oven and placed in a lab environment at 25±5°C and a relative humidity of 50±10% until testing. **Figure 3** (a) shows the sequence of earth block production and **Figure 3** (b) shows a few of the earthen blocks that were made and put in the oven.

a)

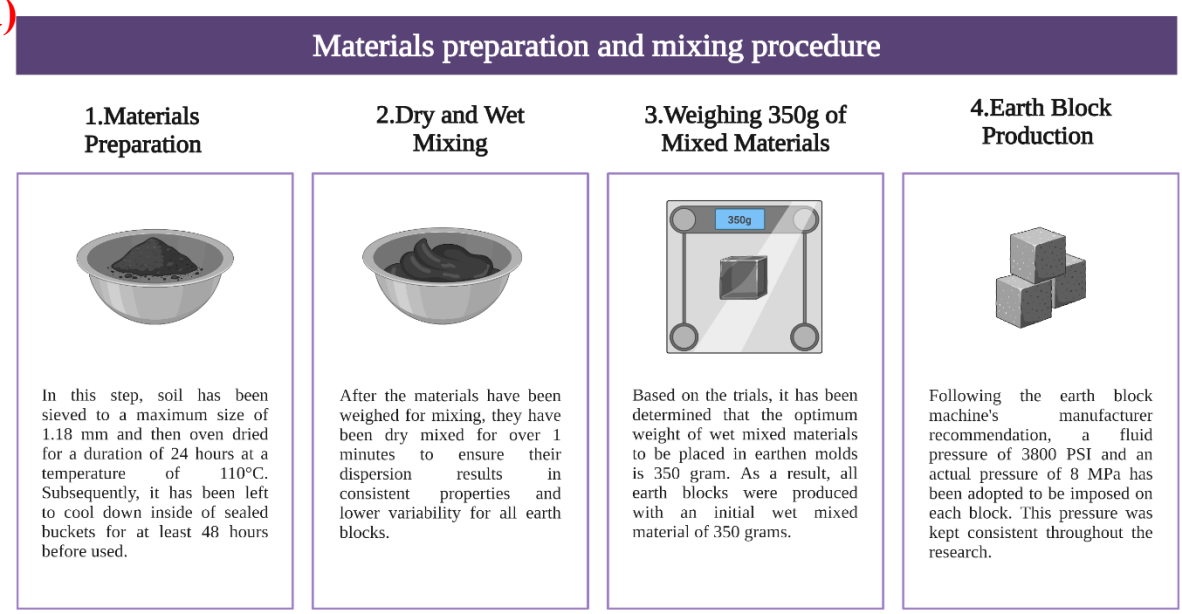




Figure 3. Showing the preparation of earth blocks with (a) a sequence of block production, and (b) a few of the earthen blocks were made and put in the oven for curing.

3.3.2. Mixture Proportions

A total of seven mixtures were manufactured, comprising one based on Portland Cement, three based on sodium silicate, and the other three based on sodium hydroxide. The alkali-activated mixtures were produced using fly ash class F and class C, as well as glass powder (one mixture per SCM, three mixtures per activator). It is important to note that this study does not evaluate the effect of combined sodium silicate and sodium hydroxide, as commonly used in ordinary alkali-activated concrete applications. The decision to evaluate each activator independently was deliberate. The aim was to isolate and better understand the distinct roles of each activator with the given SCM, where the literature is limited.

Table 4 presents the mixture proportions adopted in this study. The labeling of each mixture represents an acronym chosen based on the materials used in that mixture. For instance, PC refers to the use of Portland cement in the mixture, SS refers to sodium silicate, and SH refers to sodium hydroxide. Similarly, GP, FF, and FC represent glass powder, fly ash class F, and class C, respectively.

Table 4. Mixture proportions were used in this study (normalized for 1000 g).

Mixture	**Soil**	**Water**	**Sodium silicate**	**Sodium hydroxide**	**Molality**	**Portland cement**	**fly ash class C**	**fly ash class F**	**Glass powder**
(-)*	(g)	(g)	(g)	(g)	(mol/L)	(g)	(g)	(g)	(g)
PC	804.54	115.01	0.00	0.00	–	80.45	0.00	0.00	0.00
SS-GP	656.17	118.11	28.87	0.00	–	0.00	0.00	0.00	196.85
SS-FF	656.17	118.11	28.87	0.00	–	0.00	0.00	196.85	0.00
SS-FC	656.17	118.11	28.87	0.00	–	0.00	196.85	0.00	0.00

SH-GP	598.80	194.97	0.00	26.59	3.00	0.00	0.00	0.00	179.64
SH-FF	598.80	194.97	0.00	26.59	3.00	0.00	0.00	179.64	0.00
SH-FC	598.80	194.97	0.00	26.59	3.00	0.00	179.64	0.00	0.00

3.3.3. Testing Matrix

Table 5 presents the tests conducted in this study and the standards followed. Based on the table, for each testing procedure, at least 5 samples have been produced using the same construction method and crew members to minimize potential variability in the results. The five samples were then tested according to the standard, and their mean value and standard deviation were reported. Error bars in bar graphs also show the standard deviation of results across the five tested samples.

Most of the tests conducted are standard, and their roles are self-explanatory. For completeness, however, it is worth noting that electrical resistivity and salinity tests were performed on the activators (sodium silicate and sodium hydroxide). These tests helped characterize the ionic concentration and electrical conductivity (hereinafter conductivity) of the activating solutions, which are directly related to their effectiveness in initiating binder reactions. Also, in the acid test, 28-day cured samples were placed in reagent grade nitric acid with 70% purity and a density of 1.413 g/mL at 20 °C, for two hours. This duration was selected based on the authors trials and to ensure that the blocks would not disintegrate after exposure to acid.

Table 5. Tests conducted and the standards that were followed.

Test*	Standard	Curing age (day)

Sieve analysis	ASTM C117-17 [137] , C136-14 [132], D6913-17 [136], D7928-21 [143]	–
pH	ASTM D4262-18 [144]	–
Electrical resistivity	–	–
Salinity	–	–
Hardened unit weight	ASTM C20-22 [145]	0, 28
Water absorption	ASTM C20/C642-22 [146]	28
Flexure test	ASTM C293-16 [147]	28
Compressive strength (dry and wet)	ASTM C109-21 [148]	7, 28
Wire brush test (wet & dry)	ASTM C944-12 [149]	28
Acid test	–	28
SEM	–	28
XRF (Rigaku model Super mini-200)	–	28
LCA	ISO 14040-08 [150]	–

*In this study, sieve analysis was conducted on the soil, while pH, electrical resistivity, and salinity were conducted on sodium hydroxide. All other tests, including hardened unit weight, water absorption, compressive and flexural strength, wire brush, acid resistance, SEM, and XRF were conducted on the blocks.

3.3.4. Physical Properties of the Activators

To measure the properties of the activators, a dedicated device with the commercial name PC400S portable meter kit supplied by APERA instruments was used. The device features two separate probes for measuring pH, conductivity, total dissolved solids (TDS), salinity, and resistivity of liquids. The probes have been calibrated before and after each test to ensure data accuracy, and each test has been repeated 5 times to ensure consistent results.

3.3.5. LCA

To evaluate the environmental impacts of the produced earthen blocks, a cradle-to-gate life cycle analysis based on ISO 14040 [150] has been conducted. The LCA is conducted to assess how changes in the proportions of binders and fillers affect the environmental performance of each mixture, with emphasis on GWP, energy consumption, and resource depletion. This would then allow a better understanding and identification of the main contributions to environmental impacts.

3.3.5.1. Goal and Scope Definition of the LCA

To evaluate the environmental impacts of different mixtures, a declared unit of 1 m^3 of finished blocks is adopted, consistent with ISO 14040-08 [150] provisions for cradle-to-gate assessments, and has also been adopted previously [151], [152], [153], [154]. This choice ensures that (i) the geometric volume remains constant, while the mass and density differences among mixtures are properly reflected in the material and transport burdens, and (ii) the results are directly comparable to Environmental Product Declarations (EPDs), where impacts are typically reported per unit volume or mass of product. Adopting 1 m^3 as the reference quantity also facilitates future comparisons and scaling to wall assemblies or other building components without dependence on specific block dimensions or configurations. To ensure that the results also reflect the mechanical performance of each mixture, the environmental impacts are further expressed as a strength-normalized impact, with all results normalized to a reference compressive strength of 2500 psi (17.23 MPa). The reasons for selecting this value are provided in section 4.11, along with further explanations. This approach follows the methodology proposed in [155], [156], in which compressive strength is treated as an indicator of functional performance to facilitate performance-

based comparisons among mixtures. However, recognizing that several authors (e.g., [157]) have cautioned against defining the functional unit solely on material properties (and since this may not fully represent the material's intended function in a specific end-use or structural context), both the declared-unit results (per 1 m^3 of blocks) and the strength-normalized results are presented and discussed in parallel to provide a comprehensive assessment.

The construction site is assumed to be at coordinates 38°41'31.5" N, 121°30'54.8"W, in Natomas Central (northern Sacramento, CA). **Table 6** shows the distances of material distributors in kilometers to the specified location.

Table 6. Distances considered from the supplier to the construction site (kilometers).

Location	Water	Portland cement	Sodium hydroxide	Sodium silicate	Fly ash class F	Fly ash class C	Glass powder	Soil
Sacramento (CA)	0	263	146	146	1368	1368	14.8	0

Figure 4 shows the system boundary adopted for this study (i.e., cradle-to-gate) that includes (a) raw materials supply, (b) transportation, and (c) manufacturing of the blocks.

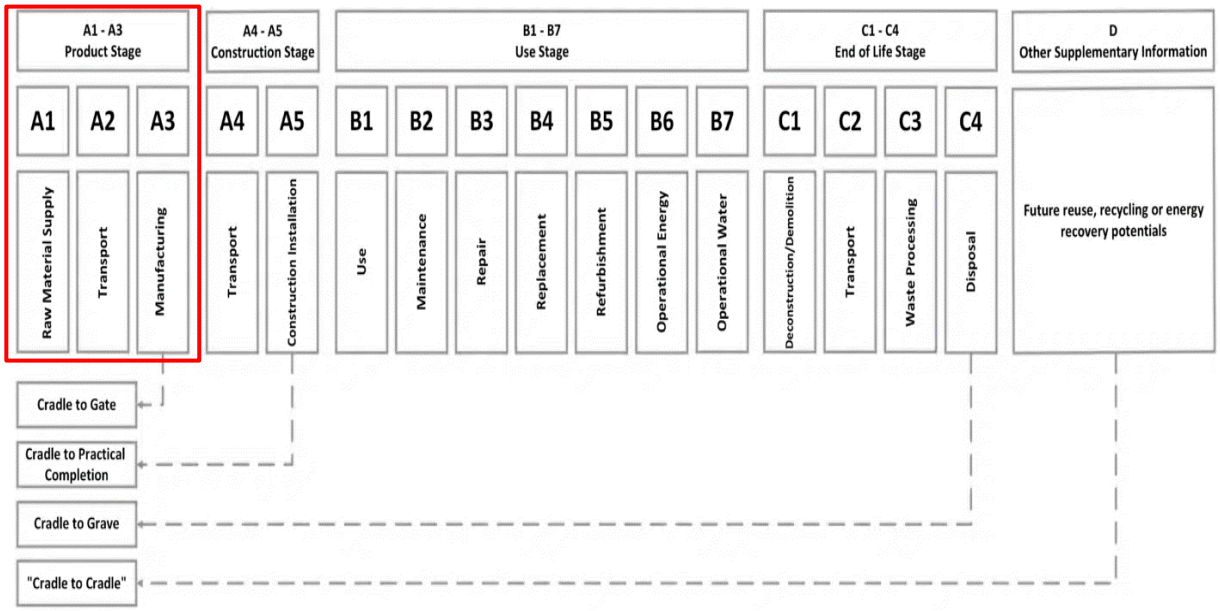


Figure 4. The scope of the LCA study, cradle to gate, as indicated in A1-A3.

3.3.5.2. Life Cycle Inventory (LCI)

In this study, the LCI was developed using TRACI v2.1 (Tool for the Reduction and Assessment of Chemical and other Impacts) [158], which provides midpoint-level impact categories relevant to U.S.-based assessments. **Table 7** provides the GWP of all materials used in this study. Notably, the GWP of the glass powder produced in this work (after the grinding process described in Section 3.3.2.5) is comparable to that reported in the environmental product declaration (EPD) of a similar commercial material (VCAS 200), which lists a GWP of 0.15 kg CO_2-eq per kilogram of glass. This framework was selected to ensure consistency with established methods and comparability with previous research. The following subsections present the operations, assumptions, and system boundaries adopted in the LCA modeling.

Table 7. GWP in CO_2 eq. of all materials used in LCA calculations.

Diesel combusted in industrial equipment (per kg diesel used)	Sodium hydroxide (per 1 kg)	Sodium silicate (per 1 kg)	Electricity; at user; consumption mix - 2022 US (per 1 MJ)	Portland cement (Type I/II), (per 1 kg)	Combination diesel powered truck transport (per 1 kg-km)	Grinding per kg of glass (kg)
3.88E+00	1.04E+00	1.29E+00	1.39E-01	9.19E-01	9.40E-05	2.25E-01

3.3.5.3. Soil Excavations

To supply soil for the masonry production, local soil is excavated using a diesel-powered 20-ton excavator (model Deere 210G LC) with a fuel consumption of approximately five gallons of diesel per hour (MPG 5), equivalent to 16.2 kg h^{-1} assuming a diesel density of 0.85 kg L^{-1}. Based on consultations with industry professionals, the excavator's production rate is estimated at 25 m^3 h^{-1}. With an assumed bulk density of 1500 kg m^{-3}, this corresponds to 37500 kg of soil excavated per hour. The soil is assumed to be taken from about 1 m below the surface to minimize organic matter content; however, since this depth is typical for foundation preparation, no additional energy is assigned for digging below ground level.

To account for the environmental impacts of soil excavation, a diesel-to-soil productivity ratio was calculated to relate the mass of soil excavated to the amount of diesel combusted. The excavator's productivity corresponds to 2314.8 kg of soil per kg of diesel, derived from the ratio of 37500 kg soil h^{-1} to 16.2 kg diesel h^{-1}. Accordingly, for every kilogram of soil used in the mixtures, the diesel requirement was determined as:

$$\text{Diesel required (kg)} = \frac{\text{Soil mass (kg)}}{2314.8} \quad \text{Eq. 1}$$

This calculated diesel mass was then multiplied by the corresponding unit impacts of diesel combustion in each environmental category to obtain the total contribution of soil excavation to the life-cycle results.

3.3.5.4. Transportation

For transportation, a heavy-duty truck with a gross vehicle weight rating of approximately 32 metric tons was assumed for transporting secondary materials, covering the distance from the supplier to the construction site. Fuel consumption of five miles per gallon (MPG) is considered for transporting materials. The energy required for transportation was subsequently calculated based on the weight of the materials. Since transporting the equipment and the machinery for CSAEB production is similar across different mixtures, they are not calculated in this LCA.

3.3.5.5. Grinding of Glass Powder

Glass powder is supplied as a waste material at a size of 4 mm. This size is chosen based on discussions the authors had with local waste managers, where it was mentioned that they conduct initial processing and provide such a size of glass. Similar to fly ash, which carries no upstream burden because its formation is allocated to electricity generation, recovered waste glass is treated as a burden-free secondary material at the point where it is supplied at 4 mm. Washing, sorting, and initial crushing to 4 mm was assumed in this study to be part of the municipal waste-

management regular activities and therefore were assumed to fall outside the system boundary of this study. Only the additional processing required specifically for this product, namely, grinding from 4 mm to 100 µm, is included. The energy required for grinding glass to a smaller size of 100 micrometers is then calculated based on Rittinger's formula (eq. 2) with an assumed Rittinger's constant of 50 kWh·mm^2/ton [159], [160], [161]. The final energy required for grinding glass is found to be 1.62 MJ per kg of glass.

$$E = C_R \times \left(\left(\frac{1}{P}\right) - \left(\frac{1}{F}\right)\right) \quad \text{Eq. 2}$$

With E referring to the energy required per unit mass (kWh/metric ton or MJ/metric ton), F representing initial particle size (4 mm), and P representing the final size (100 µm). The size of 100 µm was chosen from previous studies (e.g., [162], [163], [164], [165]) where the authors mentioned that glass powder with a particle size of around or lower than 100 µm can have enough reactivity to be used as a supplementary cementitious materials.

3.3.5.6. LCA Calculations

For the LCA calculations, the following four impact categories were selected for the LCA due to their relevance to construction materials: First, GWP (kg CO_2-eq) has been chosen since it captures greenhouse gas emissions related to climate change. TEC (MJ) reflects the total energy required across the life cycle, which is an important parameter given the high energy intensity of activators used in geopolymer binders. Smog formation (kg SO_2-eq) has also been selected to

account for pollutants that contribute to urban air quality degradation. Finally, acidification (kg SO_2-eq) measures emissions that lead to acid rain and ecosystem damage have been chosen.

After establishing the wall size with and without a strength correction factor, based on the hardened density (28-day) of each mixture, the amount of materials needed for each mixture is normalized. Based on that and the unit impact of each material, the amount of each material's impact in each mixture is then calculated. In doing so, the amount of materials needed is multiplied by their corresponding impacts for each mixture proportion. After calculating all the materials for all the mixtures with and without the strength factor, transportation is calculated based on the distances noted in **Table 6**. Finally, all the corresponding impacts of materials production and shipment are summed up and analyzed.

3.3.6. Statistical Analysis, Quality Assurance, and Quality Control

All experimental results were statistically analyzed to assess consistency, variability, and significance across different mixtures. For each group, the mean, standard deviation (SD), and coefficient of variation (COV) were computed using Microsoft Excel 2024. To perform a detailed pairwise comparison, MATLAB R2024a, developed by MathWorks Inc., was used. In the analysis, the Shapiro-Wilk test was first used to assess normality within each group. If both groups were found to follow a normal distribution, Levene's test was applied to determine variance homogeneity. Based on the outcomes, either a standard two-sample t-test (for equal variances) or a Welch's t-test (for unequal variances) was used. When normality was not met in either group, a nonparametric Mann-Whitney U test was conducted. All tests were performed at the $\alpha = 0.05$

significance level. Results are consistently reported throughout the manuscript as mean ± standard deviation, alongside their corresponding p-values, regardless of statistical significance. More details on the statistical analyses are provided in section 4.10. All results, whether statistically significant or not, are reported explicitly throughout the manuscript whenever comparisons are made. Similarly, for a fair comparison between different mixtures, the standard deviations and coefficient of variation (COV) are reported throughout the manuscript whenever comparisons are made.

For quality assurance, this study strictly followed the standardized tests and procedures established by the American Society for Testing and Materials (ASTM). All equipment used for preparing, curing, and testing was recalibrated according to the manufacturer's specifications before use. In cases of non-standardized procedures, reference materials and previous research studies were reviewed and cited, and credible justifications were provided in the methodology sections.

In terms of quality control, all the tests were conducted with the same crew members and instruments to minimize other sources of variability in the data collection stage. Generally, for each test, more than five specimens were prepared to ensure that no outlier in the reporting data would exist to impact the results. Specimens that exhibited signs of physical damage or had been subject to handling errors were identified as outliers and excluded from the analysis. Such outliers were then also removed from the final statistical analysis to prevent them from impacting the results. This approach ensured that the reported findings would reflect the actual behavior of the

CSAEB specimens under investigation. Also, in each figure, the reported mean is followed by ± calculated STD. A similar reporting method is used to explain the results.

3.4. Experimental Results and Discussions

In this section, the testing results, including fresh, mechanical, and durability properties, are discussed.

3.4.1. Hardened Density

The result of the hardened density tests after 28 days of curing is presented in **Figure 5.** The lowest hardened density was recorded for SS-FF, at 1662.20 ± 21.33 kg/m³, and the highest value was documented for SH-FC, at 1896.50 ± 3.91 kg/m³. The higher bulk density of SH-FC results from both the greater specific gravity of fly ash class C and its higher reactivity, which promotes more extensive reaction products and reduces porosity. As noted in [166], fly ash class C improves particle packing and promotes denser microstructural development. Furthermore, when mixtures are averaged by the activator type, sodium hydroxide-based blocks showed a higher average hardened density of 1828.70 ± 59.4 kg/m³, compared to 1704.20 ± 70.0 kg/m³ for their counterparts produced with sodium silicate. This trend was statistically supported by pairwise comparisons, where eight out of the nine sodium hydroxide-to-sodium silicate mixture combinations showed significant differences in hardened density with $p \leq 0.008$ in all cases. Only the comparison between SH-FF and SS-GP was not statistically significant ($p = 0.173$), which can be attributed to the homogeneity of the mixture introduced by glass powder. The higher density of sodium hydroxide-based mixtures is also consistent with observations made in sections 2.1.3 and 3.1.1,

where sodium hydroxide was noted to produce higher pH environments and lead to quicker reaction kinetics compared to sodium silicate. As a result, the blocks activated with sodium silicate tend to have lower final density values.

In terms of precursors used, fly ash class C-based blocks showed the highest average hardened density value of 1838.77 ± 86.0 kg/m³, which compares to SS-FC with 1733.70 ± 17.21 kg/m³ and 1896.50 ± 3.91 kg/m³ for SH-FC. These values are higher than those of glass powder-based mixtures that averaged 1742.90 ± 94.4 kg/m³, with SS-GP at 1690.70 ± 16.33 kg/m³ and SH-GP at 1784.10 ± 25.96 kg/m³. The lower hardened density of glass powder-based mixtures is consistent with previous sections and is likely due to the angularity of glass powder, resulting in a higher void content and less efficient particle packing within the matrix. Other combinations of SH-FC vs. SS-GP ($p = 0$), SH-FC vs. SH-GP ($p = 0.008$), and SH-FC vs. SS-FC ($p = 0.001$) were also statistically significant. These results confirm that the use of glass powder has reduced the overall density compared to fly ash class C. When compared to fly ash class F-based mixtures, including SS-FF (with 1662.20 ± 21.33 kg/m³) and SH-FF (with 1765.40 ± 10.29 kg/m³), the differences were again statistically significant. For example, SH-FC (with 1896.50 ± 3.91 kg/m³) was significantly denser than SS-FF (with 1662.20 ± 21.33 kg/m³) and SH-FF (with 1765.40 ± 10.29 kg/m³), with p-values of 0.000 and 0.003, respectively. Similarly, SS-FC's density also exceeded SS-FF (with 1662.20 ± 21.33 kg/m³, and $p = 0.000$) and even SH-FF (with 1765.40 ± 10.29 kg/m³ with $p = 0.008$). These findings confirm that fly ash class C-based mixtures consistently outperform glass powder and then fly ash class F-based counterparts in terms of hardened density. The denser microstructure of fly ash class C-containing mixtures is likely due to their higher calcium content and quicker initial reactivity, as reported in previous studies [167].

It is worth noting that glass powder-based blocks also exhibited higher densities than fly ash class F-based ones. For instance, SH-GP had a density of 1784.10 ± 25.96 kg/m³, while SS-FF had a density of 1662.2 ± 21.33 ($p = 0.000$). It also compares to SH-FF with 1765.4 ± 10.29 kg/m³, and $p = 0.173$. These differences are consistent with the higher specific gravity of ground glass powder (as discussed in section 2.1.2), and the results are statistically significant, except for SH-GP vs. SH-FF.

In terms of variability, hardened density values showed relatively low COV, ranging from 0.21% in SH-FC to 1.46% in SH-GP. One main reason for low variability is that they were all molded at a given mass before production, which reduced variability in results. For instance, SH-FC, which recorded the highest average density of 1896.5 ± 3.91 kg/m^3, had the lowest variability with a COV = 0.21%. In contrast, SH-GP had a higher COV of 1.46%, which confirms the assumption that glass powder can cause difficulty in mixing because of its angularity [168]. These findings are consistent with the density trends discussed earlier and underscore the impact of the early reaction on the results.

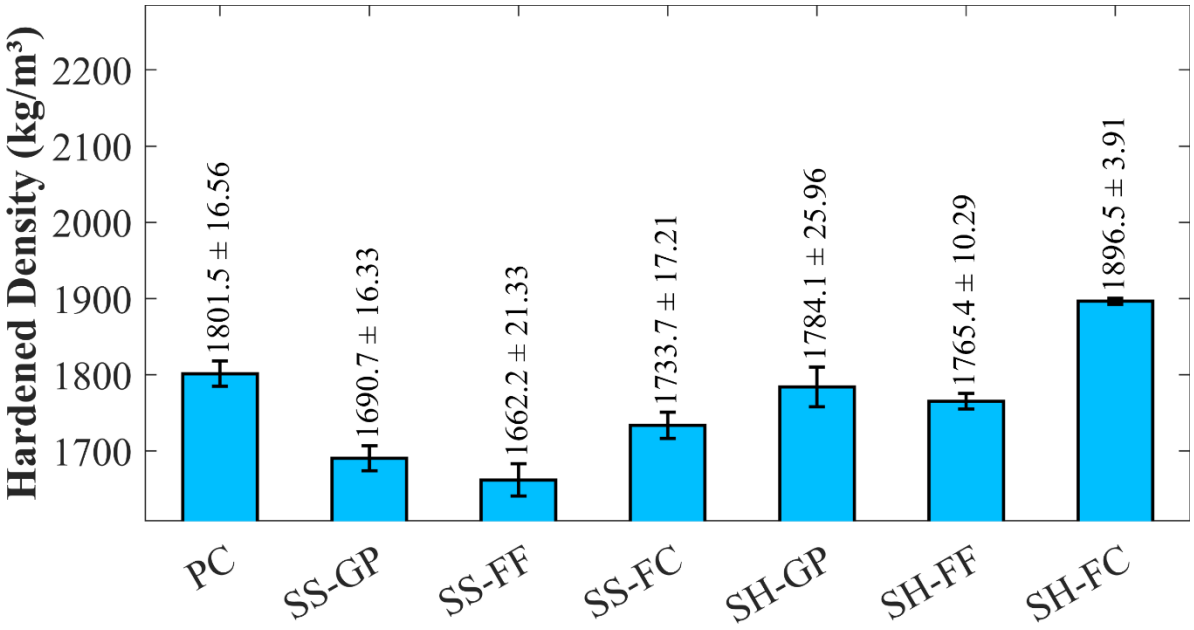


Figure 5. Hardened density of various mixtures.

3.4.2. Water Absorption

Figure 6 presents the result of the water absorption test. Among all mixtures, SS-GP recorded the highest absorption with 17.46 ± 0.16% (and a COV = 0.94%). SS-FF followed it at 16.80 ± 0.24% (and COV = 1.43%). The difference between SS-GP and SS-FF was statistically significant with a p = 0.001. PC also showed high absorption at 15.27 ± 0.24% (with COV = 1.54%), which is significantly higher than all sodium hydroxide-based mixtures (with p = 0.000 for all combinations of PC vs. SH-FC, SH-FF, and SH-GP). sodium hydroxide-activated systems exhibited a lower average absorption value of 13.78 ± 1.02%, compared to their sodium silicate-based counterparts, which had an average absorption value of 15.90 ± 2.16%. For example, SH-FC recorded the lowest overall value of 13.07 ± 0.52% (with COV = 3.95%), followed by SH-FF at 13.33 ± 0.13% (with COV = 0.94%) and SH-GP at 14.95 ± 0.48% (with COV = 3.20%). All

pairwise statistical analyses were significant with $p = 0.000$, except for SH-FC and SH-FF with $p = 0.306$.

Also, statistical analyses confirmed that the differences between sodium silicate- and sodium hydroxide-activated mixtures were generally significant (e.g., SH-FC vs. SS-GP ($p = 0.000$) and SH-FC vs. SS-FF ($p = 0.000$), except for SH-FC vs. SS-FC with a $p = 0.169$. Other pairwise comparisons, such as SH-GP vs. SS-GP ($p = 0.000$) and SH-GP vs. SS-FF ($p = 0$), and SH-GP vs. SS-FC were also significant ($p = 0.000$). These results are consistent with observations in Section 4.2, where sodium hydroxide-activated blocks also exhibited higher density values. The lower absorption values in sodium hydroxide mixtures can be attributed to the higher pH of the activating solution. A higher pH promotes faster dissolution of reactive alumina and silica in the precursor. This leads to denser gel formation and reduced capillary porosity, as also reported in earlier studies (e.g., [169]). As for the higher absorption of the sodium silicate-based system, it is possible that a substantial portion of the activator water does not contribute to the hydration and instead evaporates during the thermal curing done in this study [170], [171].

The type of SCM also influenced water absorption, with glass powder-containing blocks showing the highest average absorption, $16.21 \pm 1.77\%$, followed by fly ash class F-based blocks with an average of $15.07 \pm 2.45\%$. Finally, fly ash class C-based blocks had an average value of $13.25 \pm 0.26\%$. All pairwise analyses also yielded statistically significant results with $p < 0.05$. The elevated absorption in glass powder mixtures is probably related to the angular shape of glass particles, which can promote interparticle bridging and clustering. It can also result in difficulty mixing and an increased trapped air and pore volume [165].

In terms of variability, all COV values remained under 4.00%. Low COV values indicate low variability within each group and consistency in results. SH-FF and SS-GP had the lowest variation with COVs, with 0.94%. In turn, SH-FC had the highest COV value of 3.95%, which can be attributed to minor deviations in specimen preparation and possible microstructural differences.

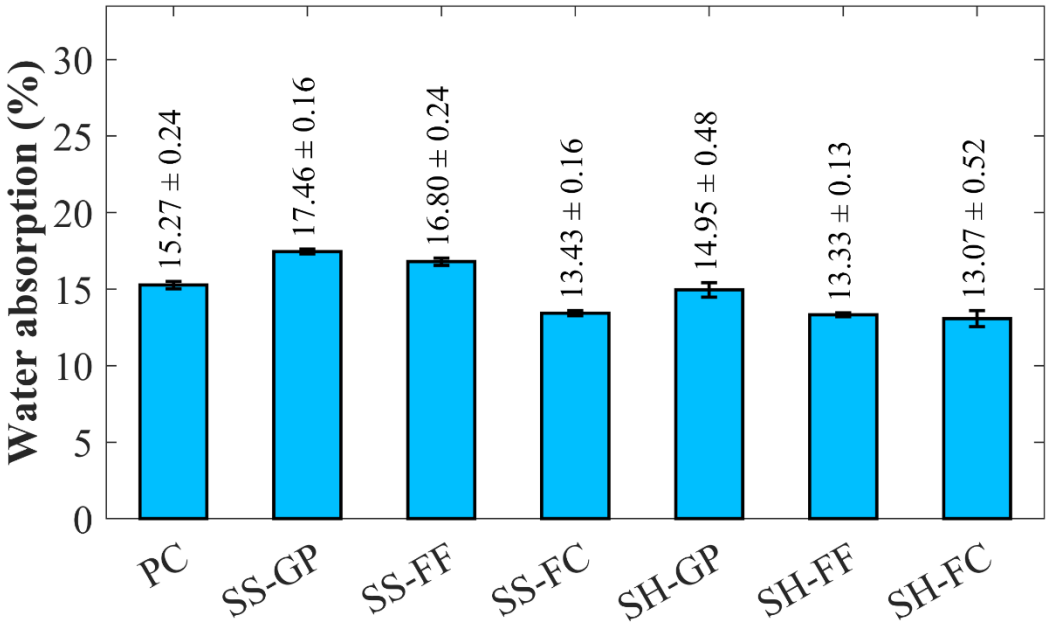


Figure 6. Water absorption (%) in different mixtures.

3.4.3. Dry and Wet Compressive Strength

The results of the compressive strength test evaluated at 7, 28, and 56 days are shown in **Figure 7**. Wet compressive strength tests were performed only on 28-day samples, whereas dry compressive strength tests were conducted at multiple ages. At 7 days, SH-FC developed the highest strength at 24.07 ± 1.40 MPa (COV = 5.8%), followed by SH-FF at 21.84 ± 0.79 MPa (COV = 3.6%) and SH-GP at 17.29 ± 1.78 MPa (COV = 10.3%). These values were statistically

significant for all comparisons involving sodium hydroxide mixtures vs. sodium silicate and Portland cement, with p = 0.000. Among the sodium silicate-based mixtures, SS-GP developed the highest strength at 9.56 ± 0.24 MPa (COV = 2.5%), which was higher than SS-FF with 3.70 ± 0.20 MPa (COV = 5.4%), and SS-FC with 3.89 ± 0.24 MPa (COV = 6.2%). The p-value was also equal to zero for both comparisons. However, the difference between SS-FF and SS-FC was not statistically significant (p = 0.221) at 7-day results. Portland cement-based blocks also achieved a 7-day strength of 8.36 ± 0.79 MPa (COV = 9.4%), which was lower than that of SS-GP (p = 0.025) but higher than that of SS-FF and SS-FC (p = 0.000 for both comparisons).

At 28 days, SH-FC again developed the highest strength at 30.95 ± 1.16 MPa (COV = 3.8%), followed by SH-FF at 22.23 ± 1.16 MPa (COV = 5.2%) and SH-GP at 21.35 ± 0.84 MPa (COV = 3.9%). The difference between SH-FC and SH-FF was statistically significant (p = 0.000), while the difference between SH-FF and SH-GP was not (p = 0.208). SS-GP and PC showed comparable values of 9.64 ± 0.82 MPa (COV = 8.5%) and 8.69 ± 0.31 MPa (COV = 3.6%), respectively, with a statistically significant difference (p = 0.041). These results show that the inclusion of glass powder has at least developed similar strength to Portland cement-based blocks, while SS-FF and SS-FC remained much lower at 4.18 ± 0.23 MPa (COV = 5.5%) and 4.31 ± 0.16 MPa (COV = 3.7%), with no significant difference between them (p = 0.332).

On average, sodium hydroxide mixtures developed a 28-day compressive strength of 24.84 ± 4.59 MPa, which is significantly higher than the average value of 6.04 ± 2.67 MPa. All results were also significant, with a p-value of 0.000. Similarly, the average 28-day strength with glass powder, fly ash class F, and class C was 15.50 ± 6.22 MPa, 13.21 ± 9.54 MPa, and 17.63 ± 14.06

MPa, respectively. The high standard deviations result from the significant difference between the sodium silicate-based and sodium hydroxide-based results that are grouped. Overall, fly ash class C has performed best since its calcium content is relatively higher than that of the other two materials and contributes to its hydration [166]. However, despite the common mixing or dispersion issues associated with glass powder particles [172], they have developed comparable strength to the two types of fly ash. Additionally, all sodium hydroxide mixture results were found to be statistically significant compared to sodium silicate and Portland cement-based mixtures ($p < 0.001$). The lower strengths developed for sodium silicate-mixtures can result almost entirely from a lack of alkali activation, which essentially results from the lower pH value of the mixture. Previous study [142] showed that a pH of 14.00 can develop up to 50 times higher strength than a mixture with a pH of 12.00. Partly, the pH can result from the activator used in their production, which is outlined in **Table 3**. For instance, from the average results discussed for sodium silicate vs. sodium hydroxide, it can be concluded that sodium hydroxide's pH of 12.37 has developed over four times higher compressive strength than samples produced with sodium silicate and a pH of 10.8. Similar results, where higher pH leads to higher strength development, are also reported in [173]. However, other studies also suggest that the chemical composition of particles, particularly calcium [174], plays a crucial role in the development of these properties. As mentioned by Rossi et al. (2022) [175], varying amounts of CaO, reactive fractions, and amorphous phases in the precursors can also be responsible for the different performance results, which could be a topic for future investigations.

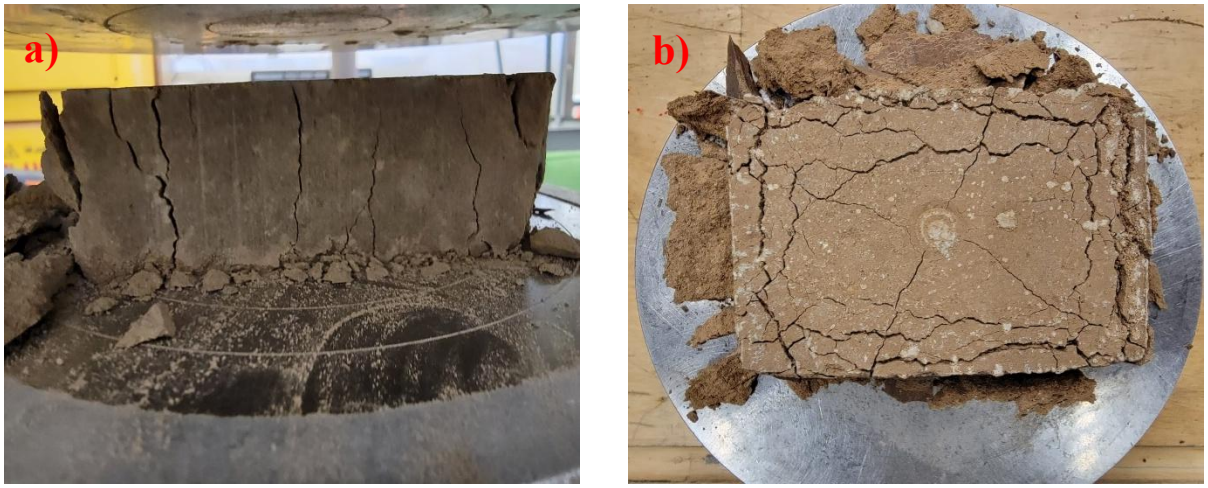
At 56 days, SH-FC again achieved the highest compressive strength at 38.12 ± 4.08 MPa (COV = 10.7%), followed by SH-FF at 24.43 ± 0.81 MPa (COV = 3.3%) and SH-GP at 24.19 ± 1.02

MPa (COV = 4.2%). These mixtures significantly outperformed all sodium silicate-based and PC mixtures with $p < 0.001$ for all mixtures containing sodium hydroxide versus sodium silicate or Portland cement comparisons. PC reached a strength value of 10.75 ± 0.47 MPa (COV = 4.4%), which was slightly higher than SS-GP at 10.31 ± 0.20 MPa (COV = 1.9%), but the difference was not statistically significant with $p = 0.089$. SS-FF and SS-FC again recorded the lowest values at 4.89 ± 0.37 MPa (COV = 7.6%) and 5.00 ± 0.55 MPa (COV = 11.0%), respectively, with a statistically significant difference between them ($p = 0.000$). Similarly, both mixtures were significantly weaker than PC and SS-GP ($p = 0.000$ for all comparisons).

Wet compressive strength measured at 28 days followed similar trends. SH-FC achieved the highest value at 25.06 ± 1.45 MPa (COV = 5.8%), significantly outperforming SH-FF with 19.26 ± 0.34 MPa (COV = 1.8%) ($p = 0.001$), and SH-GP at 11.38 ± 0.83 MPa (COV = 7.3%) (with $p = 0.000$). SS-GP and PC showed lower strengths at 9.05 ± 0.99 MPa (COV = 10.9%) and 7.70 ± 0.41 MPa (COV = 5.3%), respectively, with their difference being statistically significant ($p = 0.034$). SS-FF had a strength of 3.27 ± 0.25 MPa (COV = 7.6%), and SS-FC developed a higher strength of 3.72 ± 0.39 MPa (COV = 10.5%) (with $p = 0.06$). All sodium hydroxide mixtures outperformed PC, and all sodium silicate-based systems with all pairwise comparisons were significant (all $p < 0.001$). SS-GP remained stronger than both SS-FF and SS-FC ($p < 0.01$). This is aligned with the dry compressive strength values, which show better performance of sodium hydroxide. The slightly lower wet compressive strength compared to dry strength values confirms that soil particles become saturated and tend to expand when exposed to water [176]. This swelling introduces internal stresses within the binder matrix and at the soil–binder interphases, where crack initiation and growth are more likely to occur. Consequently, the observed strength loss is

attributed primarily to cracking within the binder and interphases, rather than failure of the soil particles themselves. Lowered wet compressive strength values (compared to dry compressive strengths) are also reported in [177]. Another point that the results show is also the fact that glass powder has performed comparable and often even better strength values, especially in sodium silicate-based blocks. One explanation is that glass powder particles may have retained moisture on their surfaces or within fine pores during curing, thereby prolonging the availability of water for reaction compared to other fly ash particles.

In terms of variability, SH-FF consistently showed the lowest COV across all curing ages, with 3.6% at 7 days and 5.2% at 28 days. SS-FC showed the highest variability at 56 days (COV = 11.0%), possibly due to slight differences in microstructure formation. SH-FC and SS-FF at 56-day compressive strength also demonstrated higher variability (COV > 7.0%). Overall, sodium hydroxide mixtures developed higher and more consistent strengths than sodium silicate- and Portland cement-based counterparts.



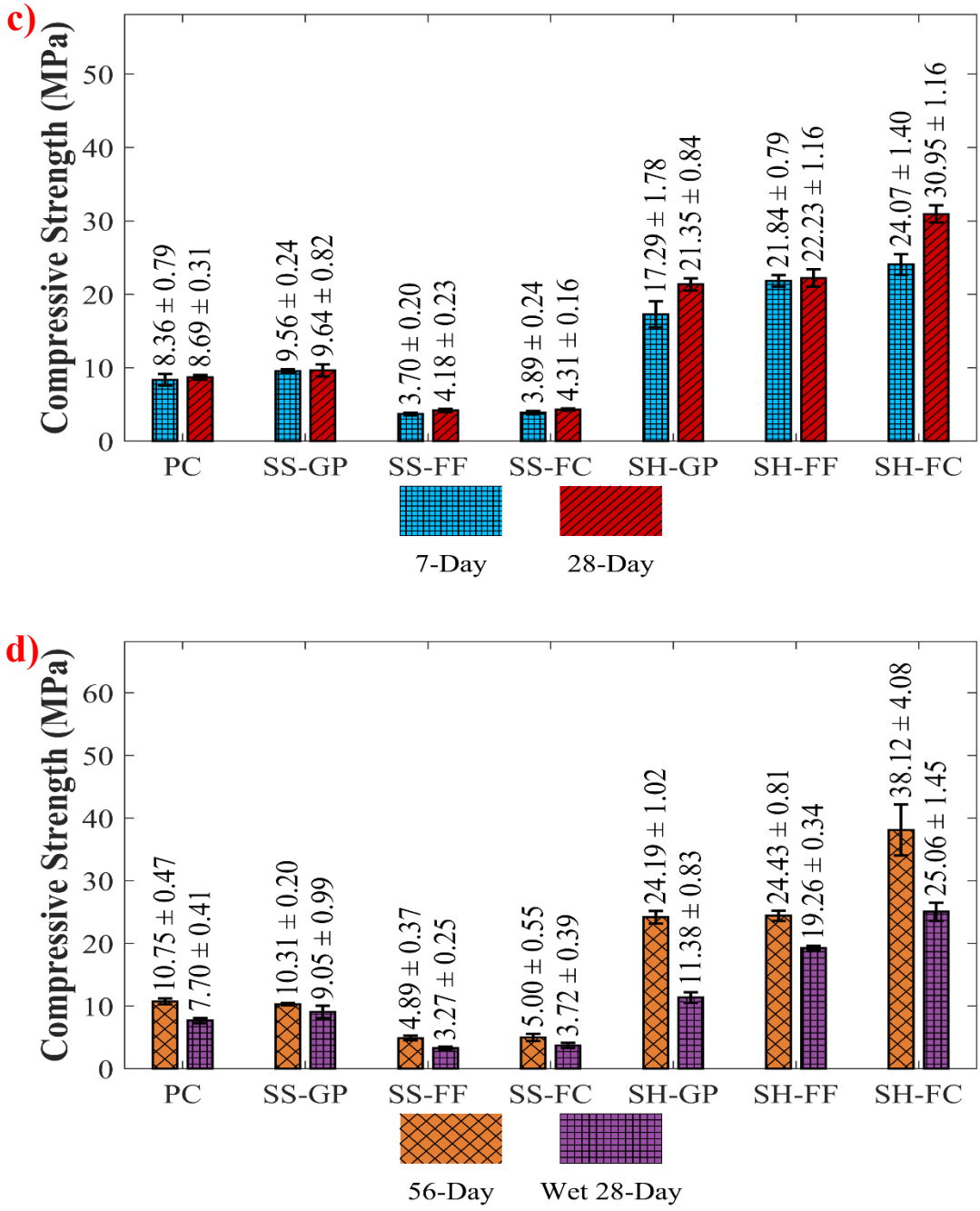


Figure 7. Compressive strength results, with (a) and (b) images of two samples broken under dry compression from SH-GP mixture, and (c) compressive strength at 7 and 28 days, (d) compressive strength at 56 and wet 28 days.

3.4.4. Flexural Strength

Flexural strength results at 28 days, with average values and standard deviations, are presented in **Figure 8**. SH-GP developed the highest flexural strength of 0.47 ± 0.006 MPa (with COV = 1.37%). SS-FF recorded the lowest value at 0.07 ± 0.004 MPa (COV = 5.22%). SH-FC and SH-FF followed with strengths of 0.42 ± 0.014 MPa (COV = 3.24%) and 0.33 ± 0.011 MPa (COV = 3.33%), respectively. Among the sodium silicate-based mixtures, SS-GP had the highest strength among other samples with 0.20 ± 0.005 MPa (and COV = 2.51%), while SS-FC yielded 0.10 ± 0.002 MPa (and COV = 2.45%). The control Portland cement-based samples showed a flexural strength of 0.12 ± 0.006 MPa with a COV = 4.61%. All pairwise comparisons also showed that the results were statistically significant with $p = 0.000$.

Compared by activator type, sodium hydroxide mixtures produced a substantially higher average flexural strength (at 0.41 ± 0.02 MPa, COV = 5.05%) compared to sodium silicate mixtures (at 0.12 ± 0.05 MPa, COV = 42.77%), similar to the results of compressive strengths and the impact of higher pH in section 5.6.1 [110].

In terms of precursor type, the average flexural strength of glass powder-based mixtures was highest at 0.34 ± 0.18 MPa, followed by fly ash class C-based at 0.26 ± 0.23 MPa, and fly ash class F-based blocks at 0.20 ± 0.18 MPa. The superior performance of glass powder can be due to its angular shape and filler effect, which contribute to crack-bridging and microstructural reinforcement. Similar to the compressive strength results, fly ash class C mixtures also performed well due to their higher calcium content, which promotes strength development [166]. fly ash class F-based blocks generally produced lower values, consistent with their compressive strength

results. In terms of COV values, all the values remained below 5.30%. The lowest variability was observed for SH-GP with 1.37%, while the highest was found for SS-FF at 5.22%.

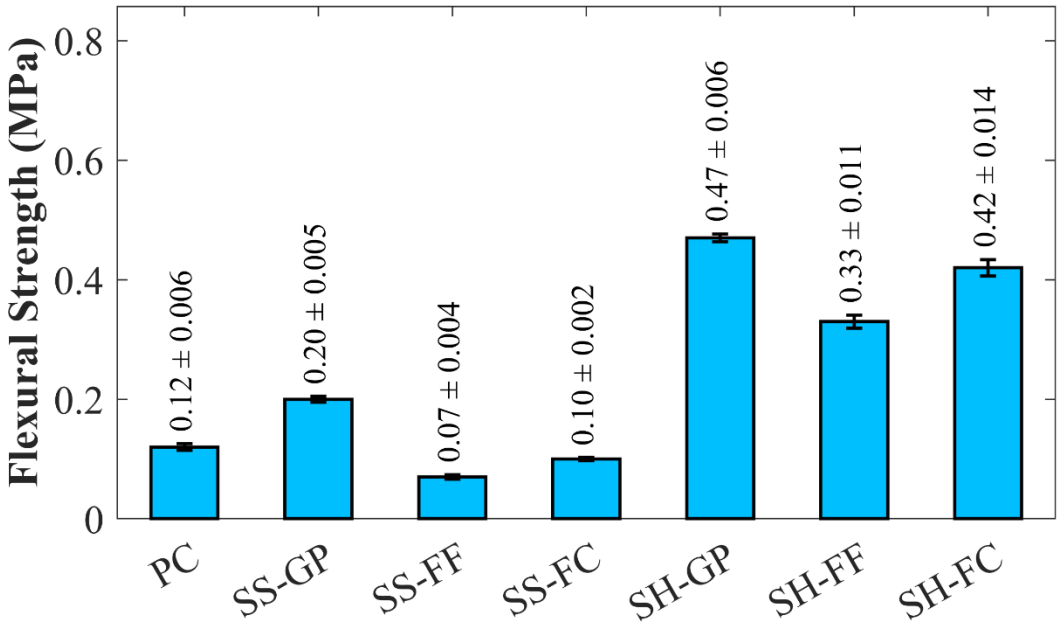


Figure 8. Flexural strength of various mixtures.

3.4.5. Wire Brush Test

The results of the wire brush abrasion test, conducted per ASTM D559-15 [178], are summarized in **Figure 9**. Among all mixtures, SS-FF and SS-FC failed to complete the full twelve brushing cycles and were excluded from the results. Among the remaining samples, the highest dry weight loss was recorded for PC blocks, with an average mass loss of 6.84 ± 1.44 g and a COV = 21.1%. In contrast, SS-GP had the lowest dry weight loss at 3.90 ± 0.73 g and a COV = 18.6%. sodium hydroxide-based blocks showed comparable performance, with SH-GP, SH-FF, and SH-FC recording dry losses of 4.60 ± 0.78 g (COV = 16.8%), 4.69 ± 0.23 g (COV = 4.95%), and 4.40 ± 0.72 g (COV = 16.4%), respectively. SS-GP appears to have had the

lowest dry weight loss, while mixtures SH-GP, SH-FF, and SH-FC have had rather comparable results. One major takeaway from the figure can be the better performance of almost all alkali-activated mixtures as compared to Portland cement-based blocks in dry weight loss. This is evident in the statistical analyses as well, with PC having a significantly higher loss than that of SS-GP ($p = 0.004$), SH-GP ($p = 0.016$), SH-FF ($p = 0.011$), and SH-FC ($p = 0.010$). The reason for this can be the higher strength of alkali-activated binders. However, in the case of glass powder-containing mixtures, the better performance can originate from the higher hardness of glass powder. Similar findings are also documented in [165], [179], whereby glass powder has outperformed other SCMs when under abrasion. However, under saturated conditions, Portland cement-based blocks showed better resistance. The saturated weight loss of PC was 20.56 ± 2.59 g (with a COV = 12.6%), which was lower than that of alkali-activated blocks. For example, SH-FF and SH-FC showed higher saturated losses of 23.91 ± 4.69 g (with COV = 19.6%) and 23.69 ± 4.13 g (with COV = 17.4%), respectively. SS-GP and SH-GP followed with losses of 20.93 ± 7.47 g (and COV = 35.7%) and 20.56 ± 3.67 g (and COV = 17.9%), respectively. However, statistical comparisons under saturated conditions indicated that the differences between PC and the alkali-activated blocks were not significant ($p > 0.15$ for all comparisons). Furthermore, no significant differences were detected among the SH-based or between SH and SS-GP mixtures in saturated weight loss. These results align with previous literature [180], which suggests that alkali-activated binders may be more susceptible to damage under cyclic wetting or freeze-thaw conditions, leading to increased mass loss when saturated.

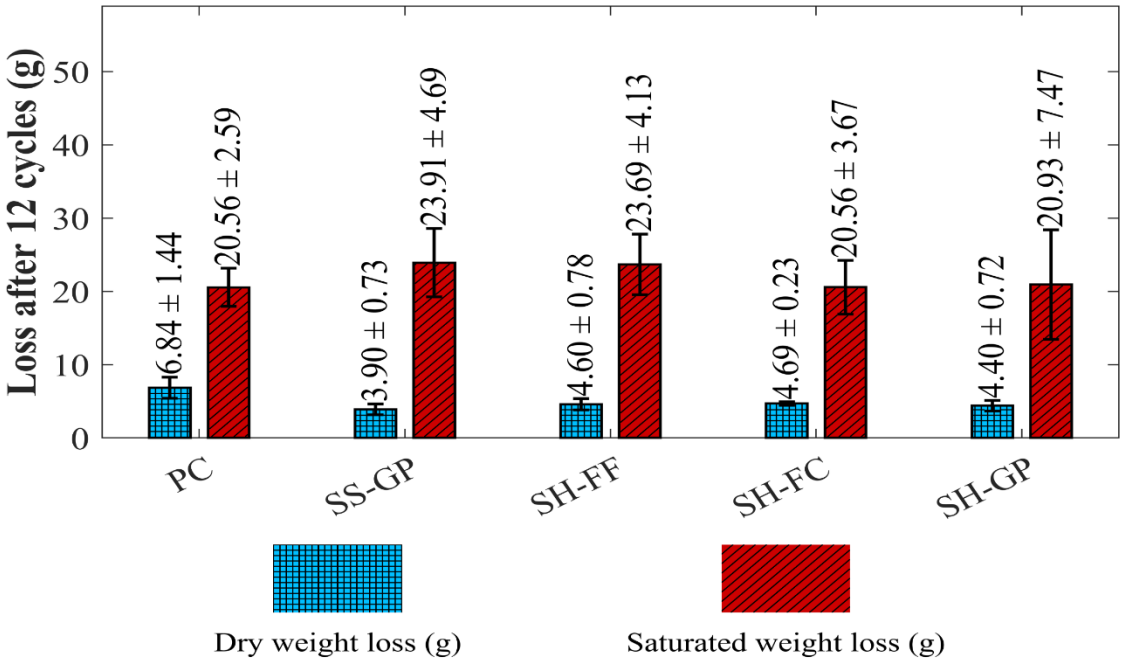


Figure 9. Result of the wire brush test on mixtures.

3.4.6. Acid Resistance

To evaluate the properties of the produced earth blocks, each mixture's samples were exposed to nitric acid for two hours. **Figure 10** presents the visual deterioration of blocks after exposure to nitric acid. **Figure 10** (a) shows the deterioration of the Portland cement-based block, which can be noted as severe. However, all alkali-activated mixtures appear to have been damaged less than the Portland cement-based block. This is aligned with previous studies (e.g., [181], [182]) that noted a significantly better performance of AAMs, as compared to their Portland cement counterparts, especially in acidic environments. According to literature, the unique chemical composition of aluminum-dominated microstructural products (specifically the Si-O-Al bonds) appears to have higher resistance to acid-induced degradation, as compared to calcium silicate hydrate (C-S-H) [183], [184], [185].

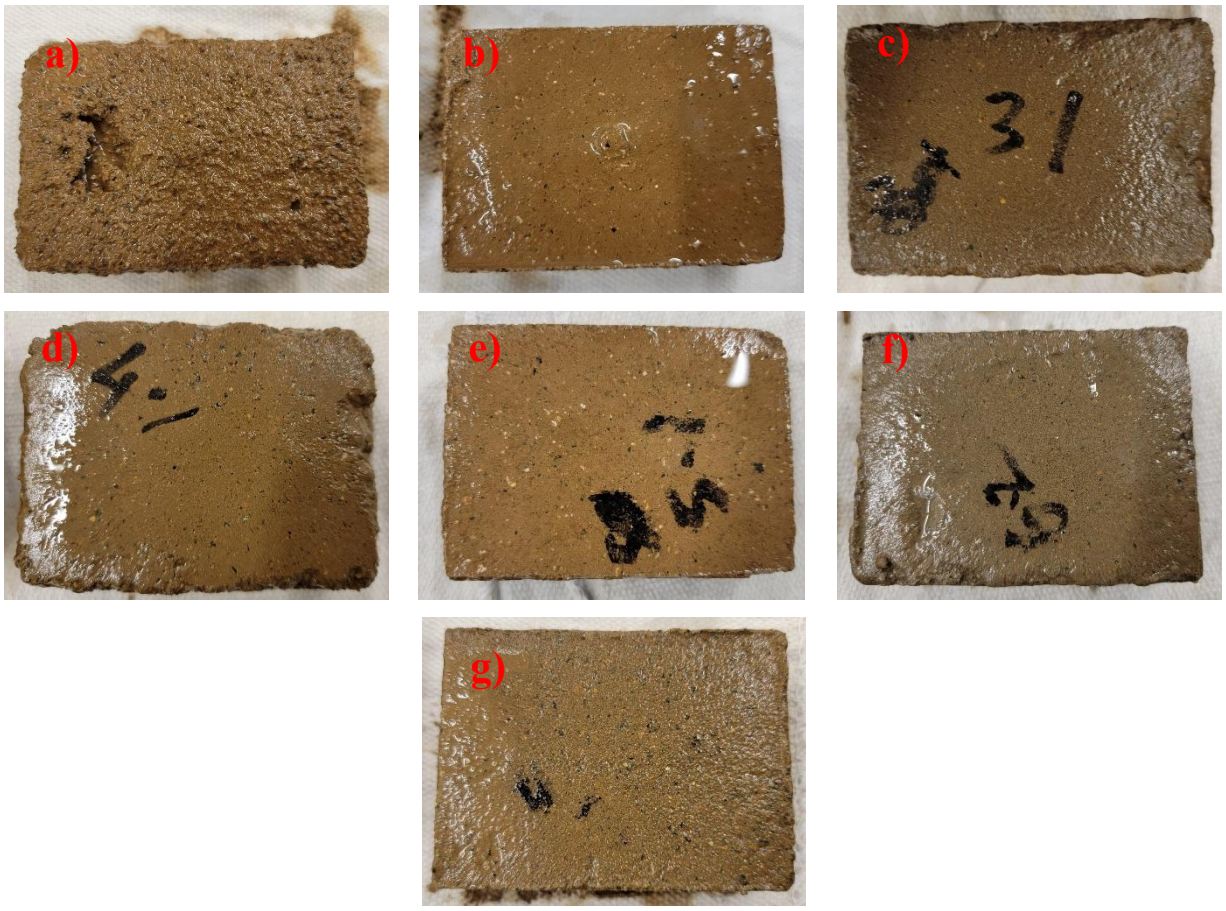


Figure 10. Physical shape of earthen blocks after exposure to 2 hours of nitric acid: (a) PC, (b) SS-GP, (c) SS-FF, (d) SS-FC, (e) SH-GP, (f) SH-FF, (g) SH-FC.

Figure 11 (a) and (b) show the mass loss and compressive strength after exposure to acid. The Portland cement-based blocks show the highest mass loss at 8.39 ± 0.45 g, significantly greater than all alkali-activated mixtures except for SS-FC with 8.21 ± 0.22 (with $p = 0.440$). Among the alkali-activated mixtures, SS-FF and SS-FC showed losses of 7.36 ± 0.40 g and 8.21 ± 0.22 g, respectively. Although SS-FC's mass loss was statistically comparable to PC (both insignificant with $p = 0.440$), SS-FF showed significantly lower mass loss than PC with $p = 0.005$. It is interesting to note that despite the lower compressive strength of blocks made of SS-FF and SS-FC, their performance upon exposure to acid is considerably better than PC. Similarly, sodium

hydroxide-based mixtures showed better performance over PC ones. For example, SH-GP recorded a mass loss of 7.46 ± 0.62 g, SH-FF had 6.73 ± 0.52 g, and SH-FC had the lowest value of 6.03 ± 0.52 g. All sodium hydroxide-based blocks were statistically significant, compared to PC (with all $p < 0.026$). The better performance of alkali-activated blocks confirms that their binding system does not easily break down under acidic conditions. A previous study in [110] associated this performance with the reduced amount of calcium present in the alkali-activated microstructure and the better resistance of SCMs to acids, as opposed to PC. In addition, the highest mass loss belonged to SH-FF, falling behind the glass powder-containing mixtures. The reason for the lower strength value of SH-FF can be that the greater number of unreacted fly ash particles are susceptible to acidic environments and tend to destabilize and form Si-OH and Al-OH group of bonds, resulting in a significant loss of performance [110].

Furthermore, the highest loss in strength values after exposure to acid is for samples made with sodium hydroxide, with a mean value of 67.95%, as compared to sodium silicate and Portland cement-based samples with 36.72% and 39.89%, respectively. These differences were statistically significant, with $p < 0.002$ for all sodium hydroxide vs. Portland cement and sodium hydroxide vs. sodium silicate comparisons. The reason behind this higher loss can be the higher Na^+ & OH^- in the sodium hydroxide, which results in higher strength loss [110].

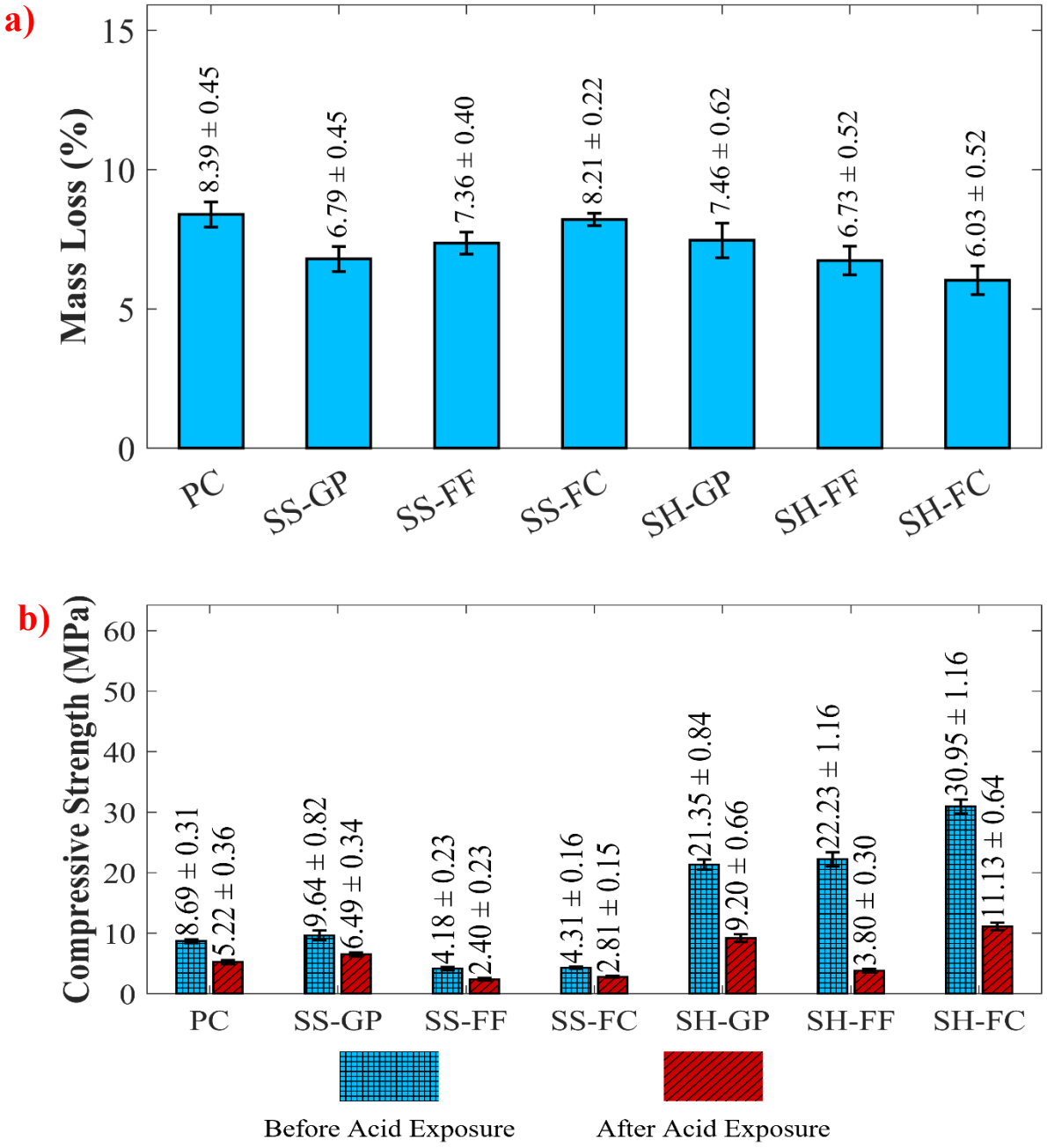


Figure 11. Acid exposure results with (a) mass loss, and (b) compressive strength before and after exposure.

3.4.7. Oxide Composition of Hardened Materials Using XRF

Table 8 presents the results of XRF conducted on all samples. As seen in the table, the average aluminum content is the lowest when glass powder is used in the blocks, while it is the highest when fly ash class F is used. In contrast, samples produced with glass powder are found to have a slightly higher SiO_2 content, with a mean value of 63.23%, as compared to fly ash class F and class C, with values of 61.08% and 52.63%, respectively. These results are aligned with the information shared in section 3.1.2. The glass powder used in this study had the highest SiO_2 and the lowest Al_2O_3 among the SCMs. The same goes for the fly ash particles (both fly ash class F and class C), their hardened blocks show similar XRF results to the raw materials. However, it is interesting to note that the soil used in the production of blocks does not seem to alter the overall ratios of the chemical composition in the blocks. This is because the hardened composition is mainly controlled by the SCMs added to the mixture. Upon a closer look at the table, similar conclusions can be made for the activators. For instance, blocks made with sodium silicate are found to have average aluminum, silicon, and calcium oxides of 10.79%, 60.50%, and 9.54% respectively. This compares to 9.71%, 57.46%, and 11.51%, respectively, for samples made with sodium silicate, which is not significantly different from sodium hydroxide-based samples.

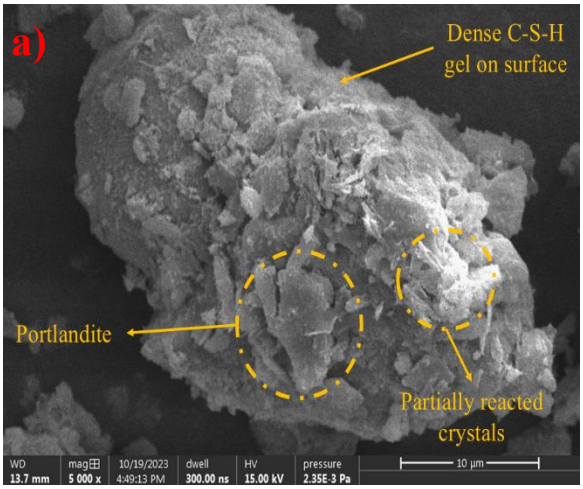
Table 8. Presenting the XRF result on all mixtures.

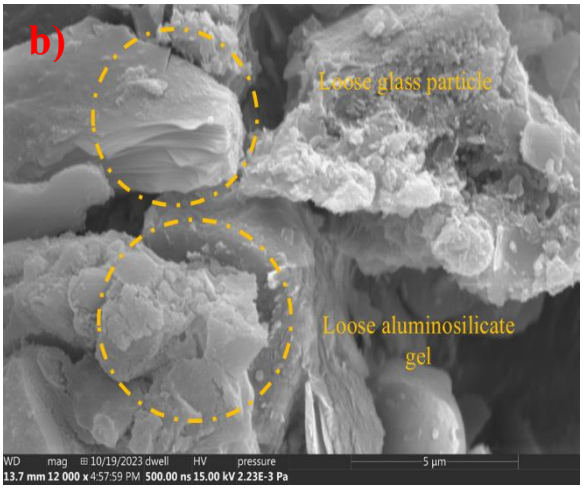
Component	PC	SS-GP	SS-FF	SS-FC	SH-GP	SH-FF	SH-FC
Na_2O	0.95	0.00	3.78	4.73	4.67	2.80	3.06
MgO	1.71	0.94	2.25	2.70	1.79	1.43	1.95
Al_2O_3	10.81	4.95	13.72	10.47	7.48	13.17	11.73
SiO_2	58.96	60.91	61.94	49.52	65.56	60.21	55.74
P_2O_5	0.22	0.00	0.47	0.47	0.18	0.53	0.60
SO_3	0.66	0.20	0.43	1.23	0.23	0.43	1.00

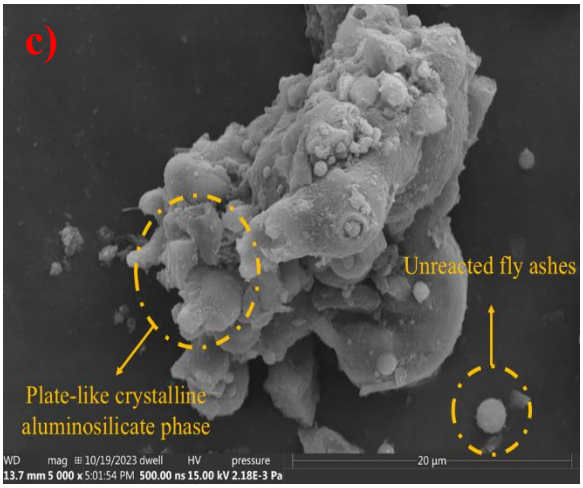
Cl	0.04	0.12	0.04	0.07	0.04	0.04	0.04
K_2O	2.47	3.27	1.92	2.40	1.93	2.20	2.04
CaO	11.95	13.78	6.46	14.30	8.73	7.62	12.28
TiO_2	0.85	1.08	0.79	1.42	0.67	0.90	1.08
MnO	0.18	0.25	0.12	0.19	0.14	0.17	0.14
Fe_2O_3	11.07	14.50	7.95	12.31	8.49	10.26	10.13
ZnO	0.04	0.00	0.03	0.00	0.00	0.04	0.06
SrO	0.08	0.00	0.10	0.19	0.03	0.14	0.14
ZrO_2	0.00	0.00	0.00	0.00	0.00	0.00	0.00

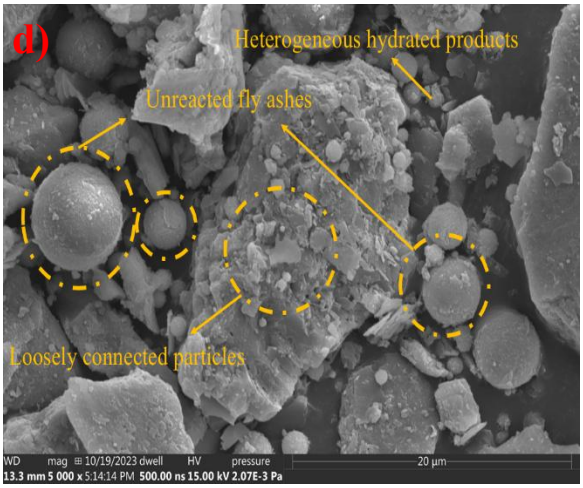
3.4.8. SEM Imaging of Hardened Materials

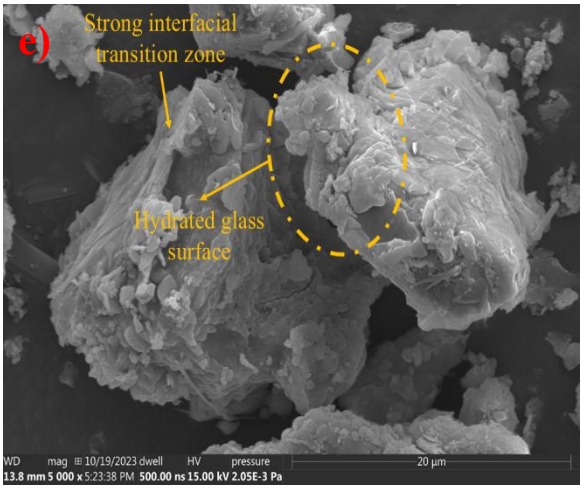
Figure 12 presents the SEM images of hydrated blocks after 28 days of curing. Based on **Figure 12** (a), A relatively dense and interconnected C-S-H gel is visible, which is attached to a soil particle. Furthermore, smaller hexagonal-style crystals are also seen on top of a granular particle that has partially reacted and formed a calcite crystal. Commonly, rhombohedral or hexagonal shapes represent calcite and portlandite crystals in cementitious materials [186], [187]. **Figure 12** (b), (c) and (d) present rather loosely connected particles, including fly ashes and angular glass powder particles, that seem to be unreacted. This is consistent with the results outlined in Section 3.2, which indicate that sodium silicate-containing mixtures did not achieve very high strength values, primarily due to the lack of alkali-activation. In contrast, **Figure 12** (e), (f), (g), (h), and (i) show earthen blocks produced with sodium hydroxide, which contain numerous interconnected clusters, resembling a complex arrangement of fibrous hydrated products, platelets, or globular features that represent the calcium and sodium silicate hydrate (C-A-S-H or N-A-S-H) gels. Notably, **Figure 12** (h) and (i) show a partially hydrated fly ash, which on its surface has features of surface dissolution, as a result of exposure to the high pH of the sodium hydroxide.

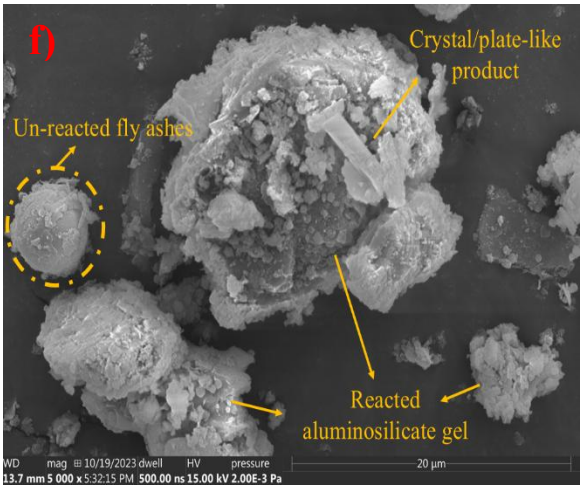

a)
Dense C-S-H gel on surface
Portlandite
Partially reacted crystals
WD 13.7 mm | mag 5 000 x | 10/19/2023 4:49:13 PM | dwell 300.00 ns | HV 15.00 kV | pressure 2.35E-3 Pa
10 µm


b)
Loose glass particle
Loose aluminosilicate gel
WD mag 10/19/2023 dwell HV pressure
13.7 mm 12 000 x 4:57:59 PM 500.00 ns 15.00 kV 2.23E-3 Pa
5 µm


c)
Unreacted fly ashes
Plate-like crystalline aluminosilicate phase
WD mag 10/19/2023 dwell HV pressure
13.7 mm 5 000 x 5:01:54 PM 500.00 ns 15.00 kV 2.18E-3 Pa
20 µm


d)
Heterogeneous hydrated products
Unreacted fly ashes
Loosely connected particles
WD mag 10/19/2023 dwell HV pressure
13.3 mm 5 000 x 5:14:14 PM 500.00 ns 15.00 kV 2.07E-3 Pa
20 µm


e)
Strong interfacial transition zone
Hydrated glass surface
WD mag 10/19/2023 dwell HV pressure
13.8 mm 5 000 x 5:23:38 PM 500.00 ns 15.00 kV 2.05E-3 Pa
20 µm


f)
Crystal/plate-like product
Un-reacted fly ashes
Reacted aluminosilicate gel
WD mag 10/19/2023 dwell HV pressure
13.7 mm 5 000 x 5:32:15 PM 500.00 ns 15.00 kV 2.00E-3 Pa
20 µm

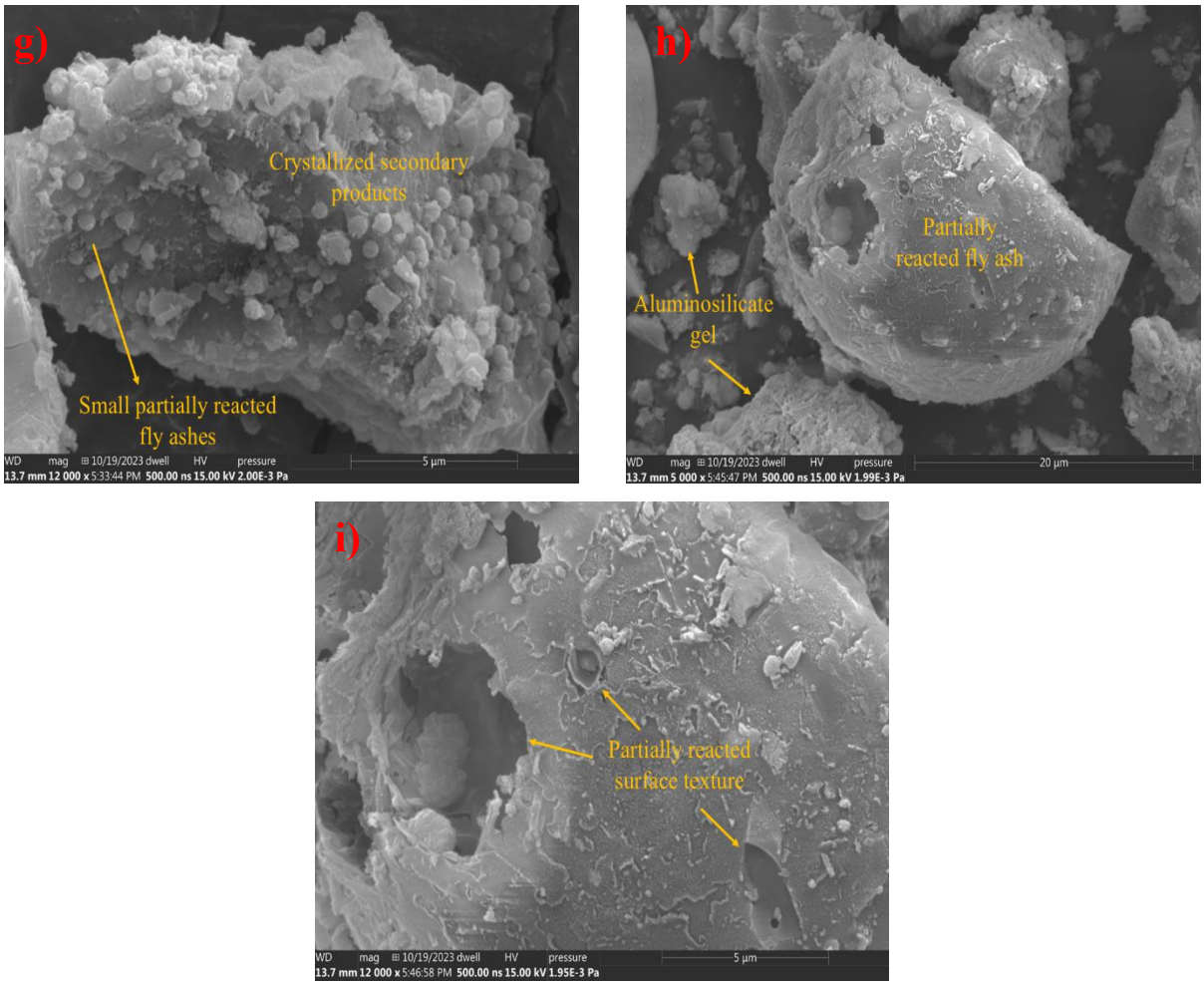


Figure 12. SEM images with (a) PC, (b) SS-GP, (c) SS-FF, (d) SS-FC, (e) SH-GP, (f) and (g) SH-FF, (h) and (i) SH-FC.

3.4.9. Statistical Analysis Done on Test Results

To ensure that the observed differences between test results were statistically significant, a comprehensive pairwise comparison framework was implemented in this study. For each test category and pair of mixtures, the analysis began with the Shapiro-Wilk test to assess whether the data were normally distributed. If both groups met the normality criterion, Levene's test [188] was then used to evaluate variance homogeneity. For data with equal variances of $p > 0.05$, a standard two-sample t-test [189] was conducted. For groups with unequal variances, Welch's t-test [190]

was applied. If either group failed the normality test, the Mann–Whitney U test [191] was used instead. A threshold of $\alpha = 0.05$ was adopted for all comparisons to determine statistical significance.

This approach eliminated the need for traditional Analysis of Variance (ANOVA) or post hoc tests by directly comparing each pair of mixtures using the most appropriate test for the underlying data characteristics. All p-values are explicitly reported in **Table 9**. Each row corresponds to a specific mixture comparison (e.g., PC vs. SS-GP), while each column represents a different test category.

The results show statistically significant differences ($p < 0.05$) for most comparisons involving mechanical testing results, including 7-day, 28-day, 28-day wet, and 56-day compressive strengths, as well as acid-exposed compressive and flexural strengths. These findings indicate that the mixture design had a pronounced and statistically reliable influence on strength development under both standard and acidic curing conditions.

For durability-related parameters, such as dry and saturated weight loss after wire brush testing, and mass loss under acid exposure, more variability was observed across mixture comparisons. In several cases, especially those involving glass powder, the p-values exceeded 0.05. It indicates that group differences were not statistically significant. This was most evident in the saturated weight loss test, where six comparisons yielded $p > 0.05$, and in the acid-induced mass loss category, where non-significant results were again more frequent among glass powder-based formulations. These results suggest that glass powder inclusion may contribute to greater

heterogeneity in acid resistance or surface degradation behavior. It is possible that, due to the angularity of the glass particles and the difficulty in dispersing glass powder during the mixing process, variable reaction kinetics or increased microporosity are produced in the samples.

In general, most pairwise statistical analyses confirm that binder type and filler selection have a statistically significant influence on most test results. The few exceptions, mainly concentrated in durability and absorption-related tests, appear to be associated with the complex behavior of glass powder-based mixtures.

Table 9. Result of statistical analysis (p-values).

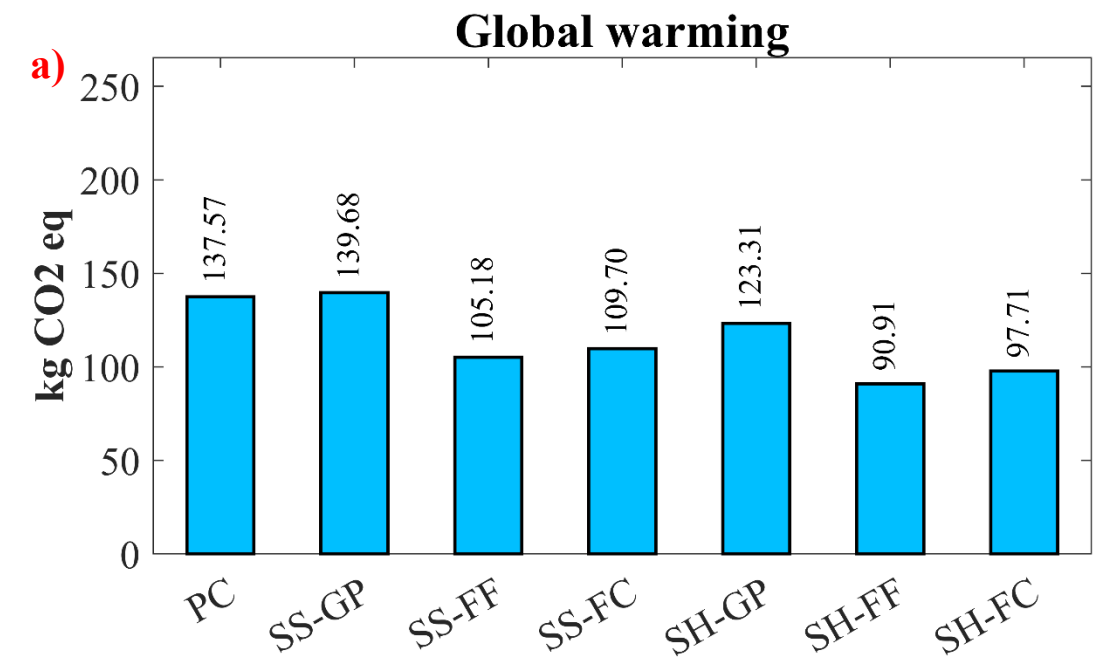
Group 1	Group 2	Hardened Density	Water Absorption	7D Comp	28D Comp	56D Comp	28D wet comp	Flex	Dry weight loss (wire brush)	Saturated weight loss (wire brush)	Loss in mass acid	28D acid comp.
PC	SS-GP	0	0	0.025	0.041	0.089	0.034	0	0.004	0.151	0	0
PC	SS-FF	0	0	0	0	0	0	0	–	–	0.005	0
PC	SS-FC	0	0	0	0	0	0	0	–	–	0.44	0
PC	SH-GP	0.241	0.22	0	0	0	0	0	0.016	0.188	0.026	0
PC	SH-FF	0.003	0	0	0	0	0	0	0.011	0.998	0.001	0
PC	SH-FC	0	0	0	0	0	0	0	0.01	0.918	0	0
SS-FF	SS-GP	0.045	0.001	0	0	0	0	0	–	–	0.067	0
SS-FC	SS-GP	0.004	0	0	0	0	0	0	–	–	0	0
SH-GP	SS-GP	0	0	0.001	0	0	0.004	0	0.176	0.69	0.087	0
SH-FF	SS-GP	0	0	0	0	0	0	0	0.069	0.222	0.843	0
SH-FC	SS-GP	0	0	0	0	0	0	0	0.306	0.548	0.038	0
SS-FC	SS-FF	0	0	0.221	0.332	0.726	0.06	0	–	–	0.003	0.01
SH-GP	SS-FF	0	0	0	0	0	0	0	–	–	0.766	0
SH-FF	SS-FF	0	0	0	0	0	0	0	–	–	0.062	0
SH-FC	SS-FF	0	0	0	0	0	0	0	–	–	0.002	0
SH-GP	SS-FC	0.007	0	0	0	0	0	0	–	–	0.051	0
SH-FF	SS-FC	0.008	0.27	0	0	0	0	0	–	–	0	0

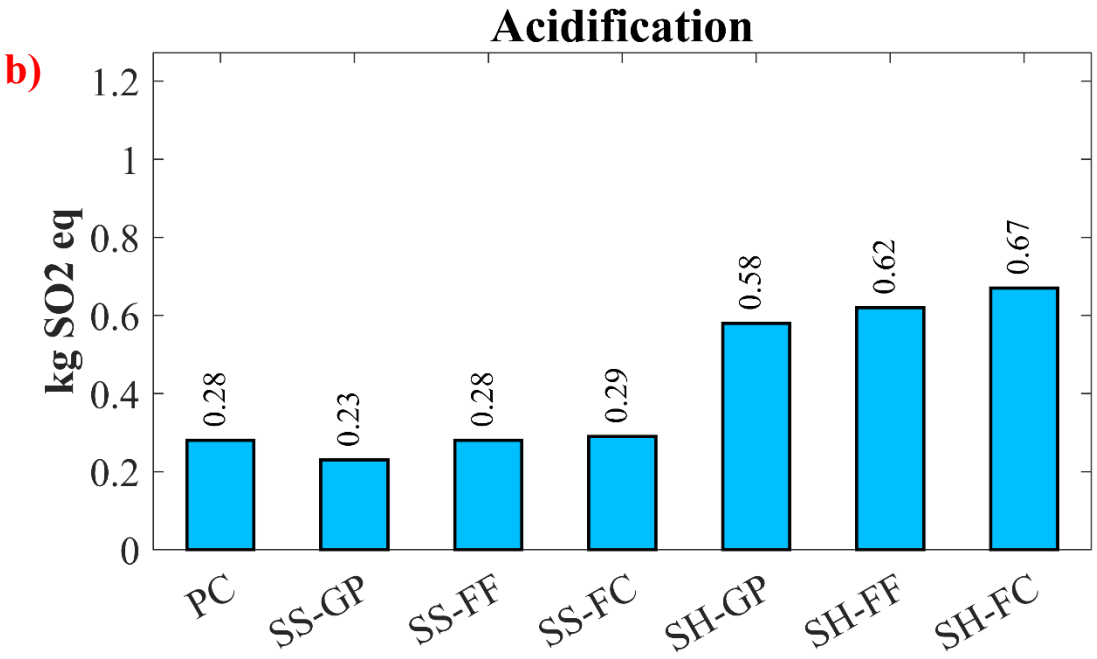
SH-FC	SS-FC	0	0.169	0	0	0	0	0	–	–	0	0
SH-FF	SH-GP	0.173	0	0.003	0.208	0.699	0	0	0.811	0.241	0.077	0
SH-FC	SH-GP	0.001	0	0	0	0.001	0	0	0.678	0.49	0.004	0.002
SH-FC	SH-FF	0	0.306	0.015	0	0.001	0.001	0	0.428	0.923	0.064	0

*with D: curing days, comp: compressive strength, acid comp: compressive strength after exposure to acid, Flex: flexural strength.

3.4.10. LCA Results

Life cycle assessment (LCA) is a tool for quantifying the environmental impacts of products, systems, or activities. Outlined in ISO 14040-14044-08 [150], LCA is a compiled evaluation of the inputs and outputs of environmental impacts of using different materials and binders. It can identify and evaluate the significance of mixtures in the production process of CSAEBs, where environmental impacts are to be detected or reduced. As discussed in section 2.2.3.2, the impact of 1 m^3 of block manufacturing on site was evaluated, and the results were shown in **Figure 13**. In terms of GWP, the lowest and highest values were SH-FF and SS-GP, respectively. On average, mixtures produced with sodium silicate had a GWP of 118.2 CO_2 eq, compared to 103.9 CO2 eq for sodium hydroxide-based mixtures. Similarly, on average, mixtures produced with fly ash class F, class C, and glass powder produced an average CO_2 eq of 98.0, 103.7, and 131.49 CO_2 eq., respectively. It appears that the grinding process of glass powder has been the primary factor contributing to this impact. In terms of acidification and smog formation, however, sodium silicate-containing mixtures had an average of 0.27 and 7.27 CO_2 eq, respectively. This compares to 0.62 and 8.91 CO_2 eq. for sodium hydroxide-containing mixtures. Similarly, glass powder had an acidification and smog formation value of 0.41 and 6.30 CO_2 eq., respectively. The values mentioned were lower than the average values for fly ash class F (with 0.45 and 8.72) and class C (with 0.48 and 9.25). This shows that, on average, despite the grinding requirements of glass powder, it has lower acidification and smog-formation impacts than fly ash class F and class C. In terms of fossil fuel depletion, however, glass powder has performed worse than fly ash class F and class C due to the electricity required for grinding.


a)
Global warming
kg CO2 eq
250
200
150
100
50
0
137.57
139.68
105.18
109.70
123.31
90.91
97.71
PC
SS-GP
SS-FF
SS-FC
SH-GP
SH-FF
SH-FC


b)
Acidification
kg SO2 eq
1.2
1
0.8
0.6
0.4
0.2
0
0.28
0.23
0.28
0.29
0.58
0.62
0.67
PC
SS-GP
SS-FF
SS-FC
SH-GP
SH-FF
SH-FC

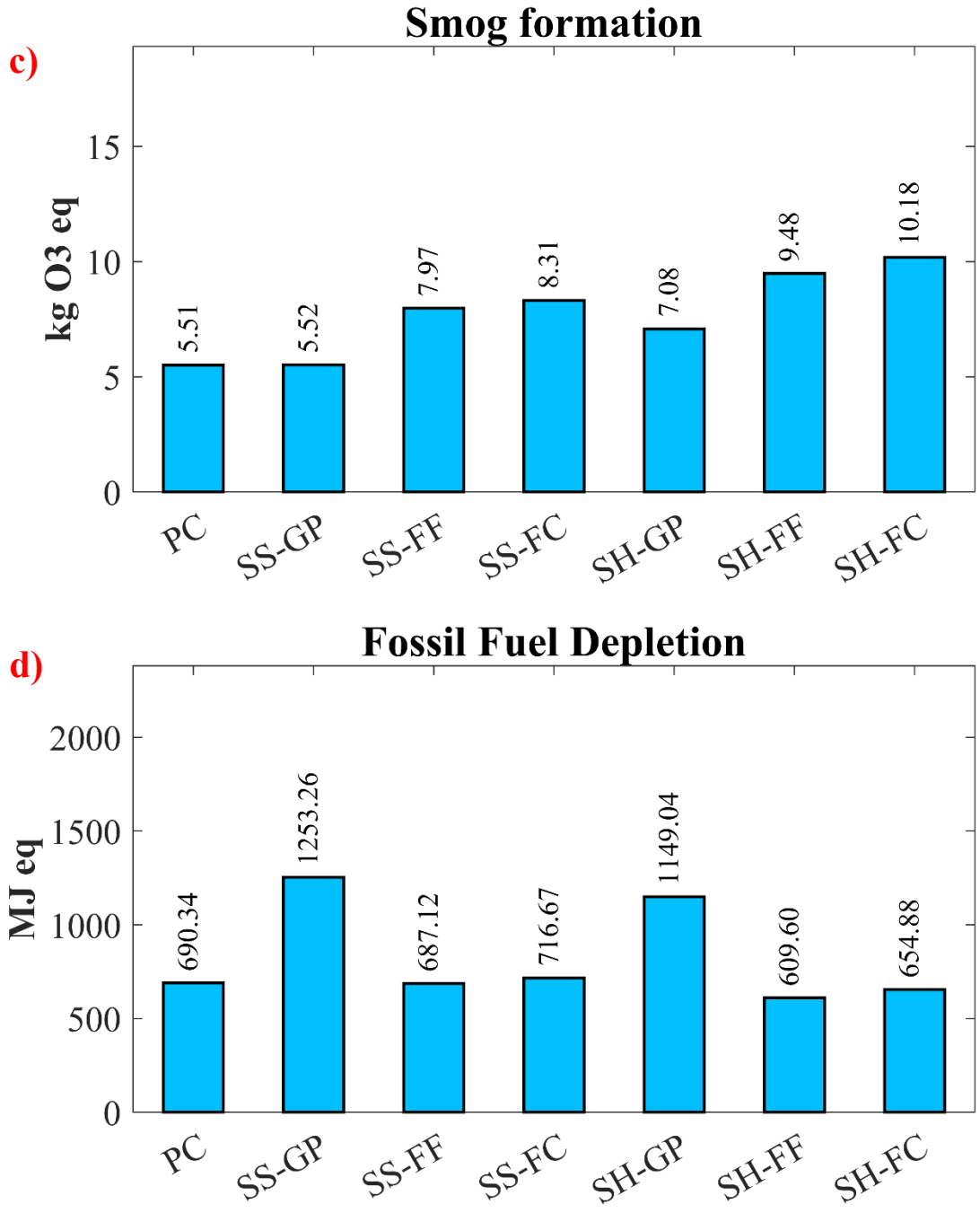


Figure 13. Impact categories of CSAEBs per functional unit of 1 m^3 of earth blocks, with (a) GWP (in kilograms of carbon dioxide equivalent), (b) acidification (in kilograms of sulfur dioxide equivalent), (c) smog formation (in kilograms of ozone equivalent), and (d) fossil fuel depletion (in megajoules (MJ)).

To account for mechanical performance across mixtures and ensure a fair comparison among formulations with different compressive strengths, the life-cycle impacts were normalized by the 28-day compressive strength. In this approach, the environmental indicators for 1 m^3 of blocks were divided by the compressive strength achieved by each mixture on a value of 17.23 MPa, representing the impact required to deliver a unit of functional performance. This adjustment allows mixtures that achieve higher strength with lower material or energy inputs to appear more efficient, while penalizing mixtures that require greater impact to reach equivalent performance. The value of 17.23 MPa is chosen because this value is commonly adopted in the construction industry as the minimum strength required for certain concrete blocks [192], which is slightly higher than ASTM C90-24 [193], at 13.8 MPa to account for any potential deficiency since masonry units can have high variability in their properties [194]. Based on this information, the strength-normalized results are presented in **Figure 14**.

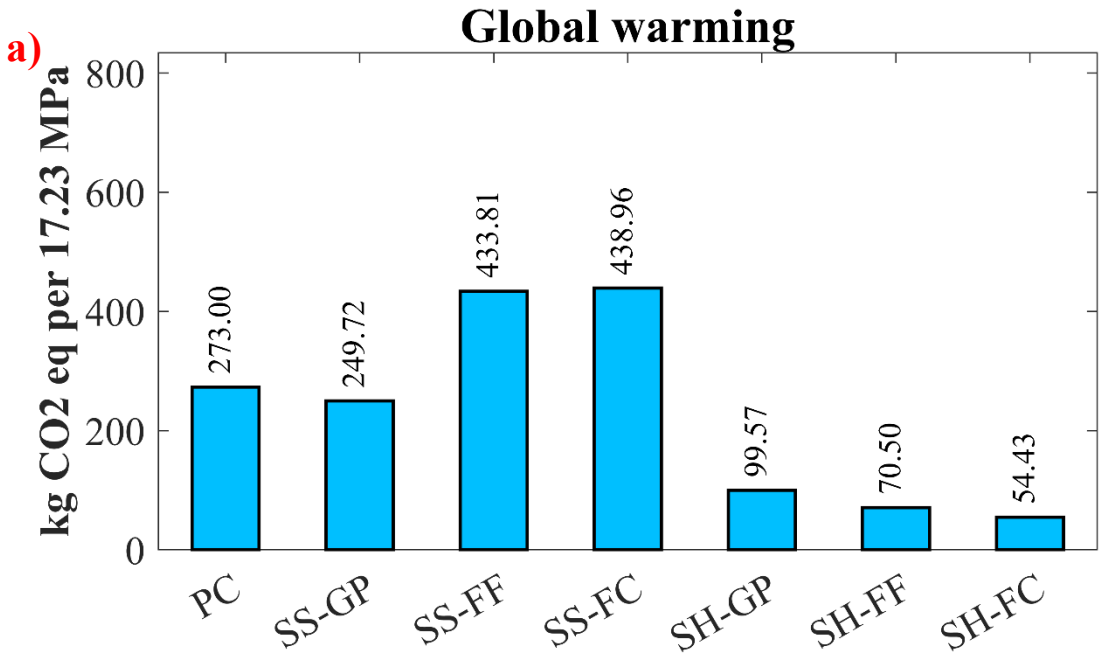
In terms of GWP, the highest strength-adjusted values were observed for the sodium silicate-based mixtures, particularly SS-FF (433.81 kg CO_2 eq) and SS-FC (438.96 kg CO_2 eq), followed closely by SS-GP (249.72 kg CO_2 eq). Among sodium hydroxide-based systems, SH-GP, SH-FF, and SH-FC exhibited substantially lower impacts of 99.57, 70.50, and 54.43 kg CO_2 eq, respectively. When averaged by binder type, the sodium hydroxide-based mixtures demonstrated roughly one-third of the strength-normalized GWP of the sodium silicate-based counterparts, indicating that the improved mechanical efficiency of sodium hydroxide mixtures outweighs the higher chemical impact of the activator itself. Across filler types, Class C and class F fly ash produced the highest normalized GWP, largely reflecting the elevated embodied energy associated with their finer particle size and processing requirements.

For acidification, SS-FF and SS-FC again exhibited the greatest strength-adjusted impacts (1.15 and 1.16 kg SO_2 eq), whereas sodium hydroxide-based mixtures ranged between 0.37 and 0.48 kg SO_2 eq. The SH-FC mixture yielded the lowest acidification potential of all studied systems, suggesting that, once strength is considered, the reduced binder content and high reactivity of the sodium hydroxide-based matrix compensate for the environmental burden of the alkaline activator. Similarly, the smog formation potential followed the same pattern: SS-FF and SS-FC mixtures recorded the highest values (32.86 and 33.25 kg O_3 eq), while SH-GP, SH-FF, and SH-FC remained below 7.5 kg O_3 eq. The overall trend confirms that the strength normalization magnifies differences between binders, emphasizing the superior performance efficiency of sodium hydroxide-based systems in terms of emissions related to photochemical oxidant formation.

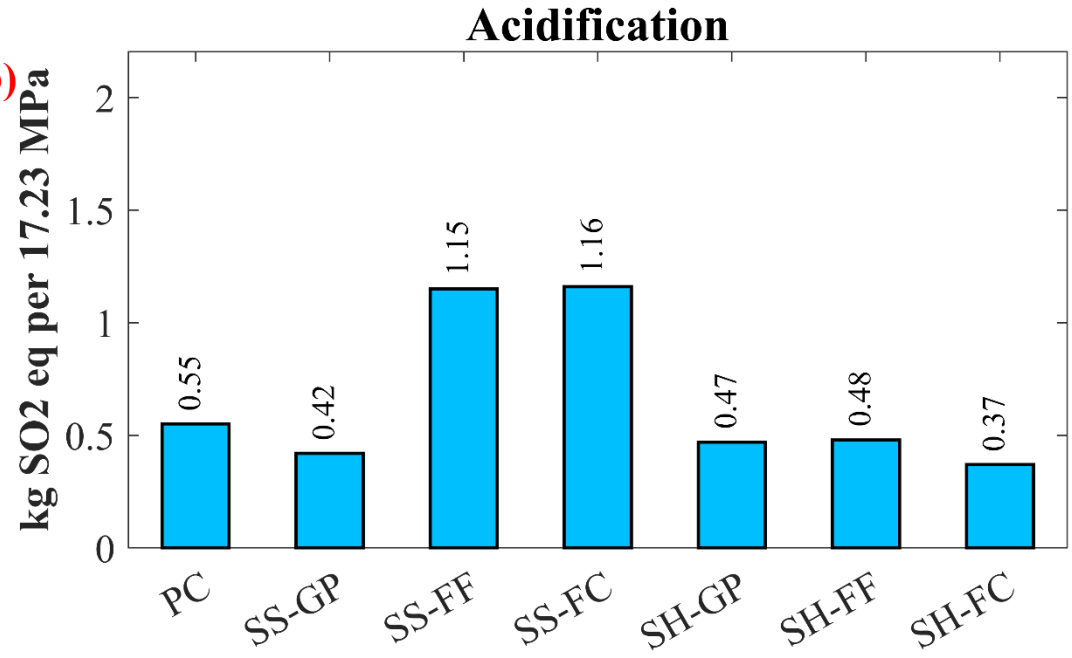
The fossil fuel depletion indicator displayed the same overall ranking. sodium silicate-based mixtures, particularly those containing fly ash class F and class C, showed the highest strength-adjusted energy demand, reaching 2833.84 and 2867.60 MJ eq, respectively. In contrast, sodium hydroxide-based mixtures required substantially lower fossil fuel energy, from 927.81 MJ eq (SH-GP) to only 364.81 MJ eq (SH-FC). The large difference reflects both the lower embodied energy of the sodium hydroxide binder and the higher compressive strength achieved at comparable material mass, which together lead to a more favorable energy-to-performance ratio.

In general, strength normalization alters the interpretation of environmental performance relative to unadjusted LCA results. While the ordinary (mass-based) assessment suggested that

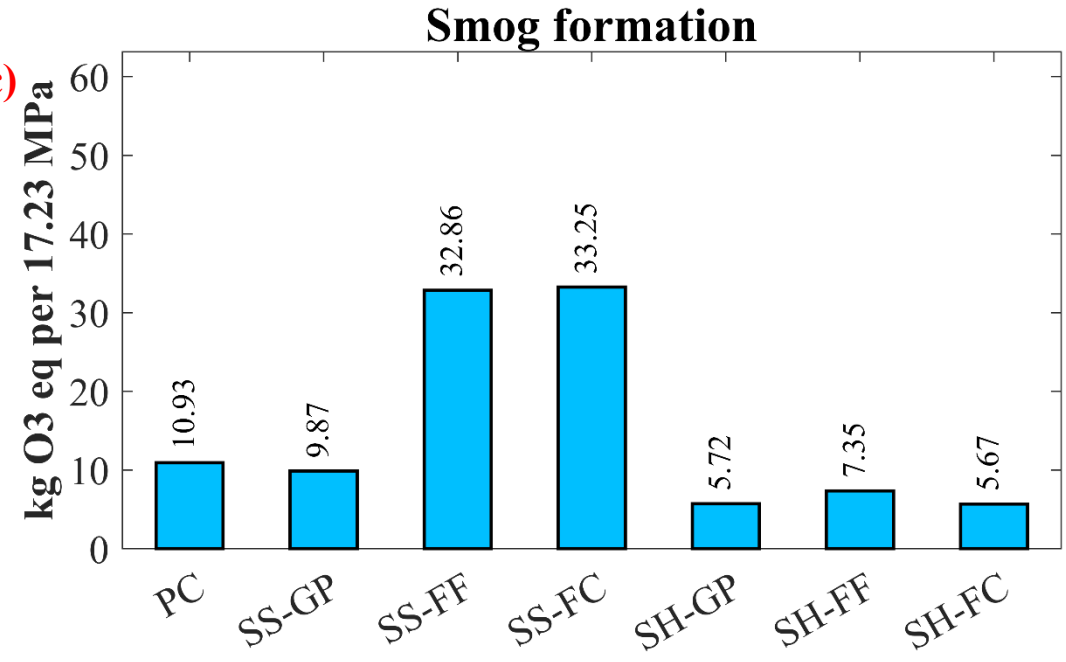
sodium silicate-based mixtures, particularly those with glass powder, performed well in several categories, the strength-factored analysis reveals that sodium hydroxide-based mixtures provide substantially lower impacts per unit of mechanical function. This indicates that, despite their chemical intensity, sodium hydroxide-activated systems are more environmentally efficient when strength development is considered, offering a stronger balance between mechanical performance and environmental sustainability for the production of soil-based alkali-activated blocks.



b)


Acidification
kg SO2 eq per 17.23 MPa
0
0.5
1
1.5
2
0.55
0.42
1.15
1.16
0.47
0.48
0.37
PC
SS-GP
SS-FF
SS-FC
SH-GP
SH-FF
SH-FC

c)


Smog formation
kg O3 eq per 17.23 MPa
0
10
20
30
40
50
60
10.93
9.87
32.86
33.25
5.72
7.35
5.67
PC
SS-GP
SS-FF
SS-FC
SH-GP
SH-FF
SH-FC

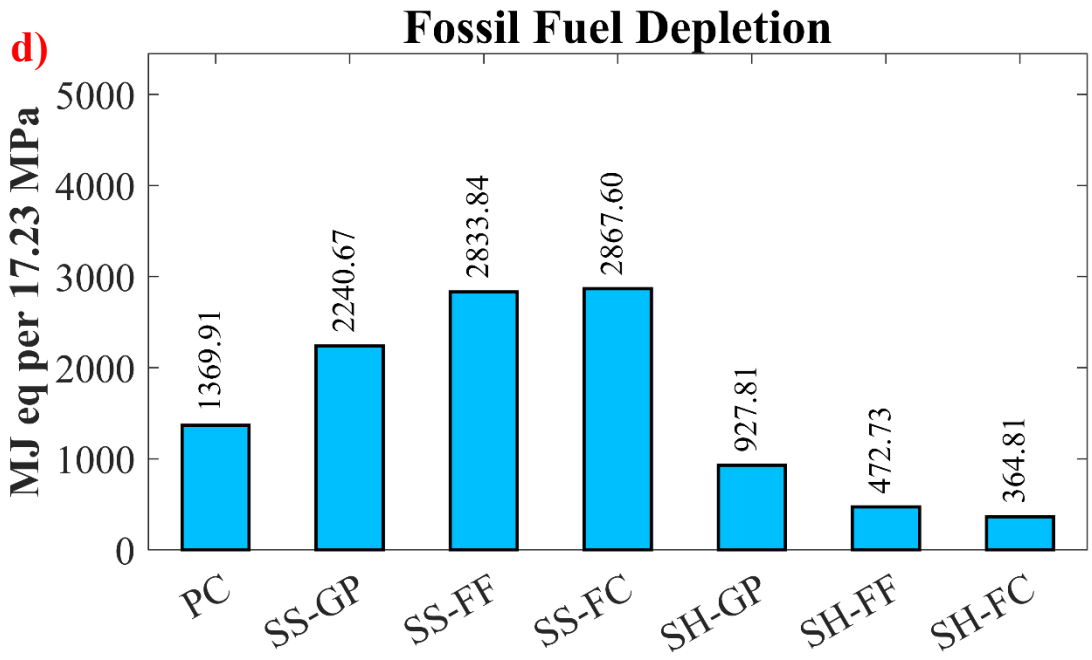
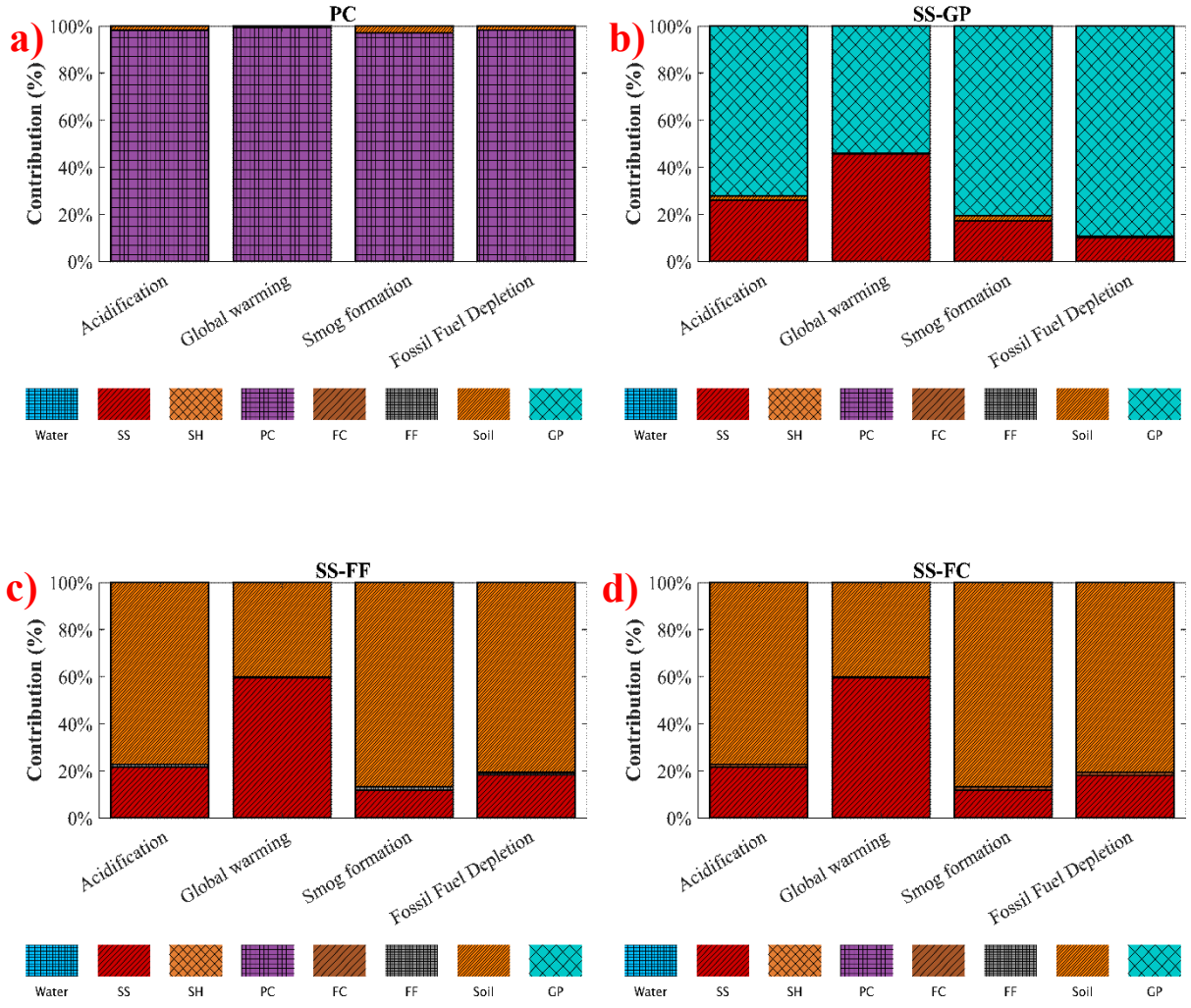


Figure 14. Impact categories of strength-normalized CSAEBs per functional unit of 1 m^3 of earth blocks, with (a) GWP (in kilograms of carbon dioxide equivalent per 17.23 MPa compressive strength), (b) acidification (in kilograms of sulfur dioxide equivalent per 17.23 MPa compressive strength), (c) smog formation (in kilograms of ozone equivalent per 17.23 MPa compressive strength), and (d) fossil fuel depletion (in megajoules per 17.23 MPa compressive strength).

Figure 15 presents the contributions made by each mixture component in each value reported. Per **Figure 15** (a), the largest contributor in the first mixture (CSEB produced using Portland cement) is the cement itself. In other alkali-activated mixtures, although sodium silicate and sodium hydroxide play a key role, their impact is not as dominant. Among the SCMs, such as the mixtures, SS-GP, SS-FF, and SS-SC, glass powder has the highest impact, followed by fly ash of class F, and then class C. This highlights the importance of transportation distance and any potential processing of SCMs, which can dominate the impacts of the mixtures. In the case of glass powder, its processing (or pulverization) has significantly increased its impact. Regarding the

activators, it appears that sodium hydroxide's share of impact is larger than sodium silicate's in mixtures. Given that the transportation of the two materials is similar, this difference must be caused by the production processes employed at the processing plants.



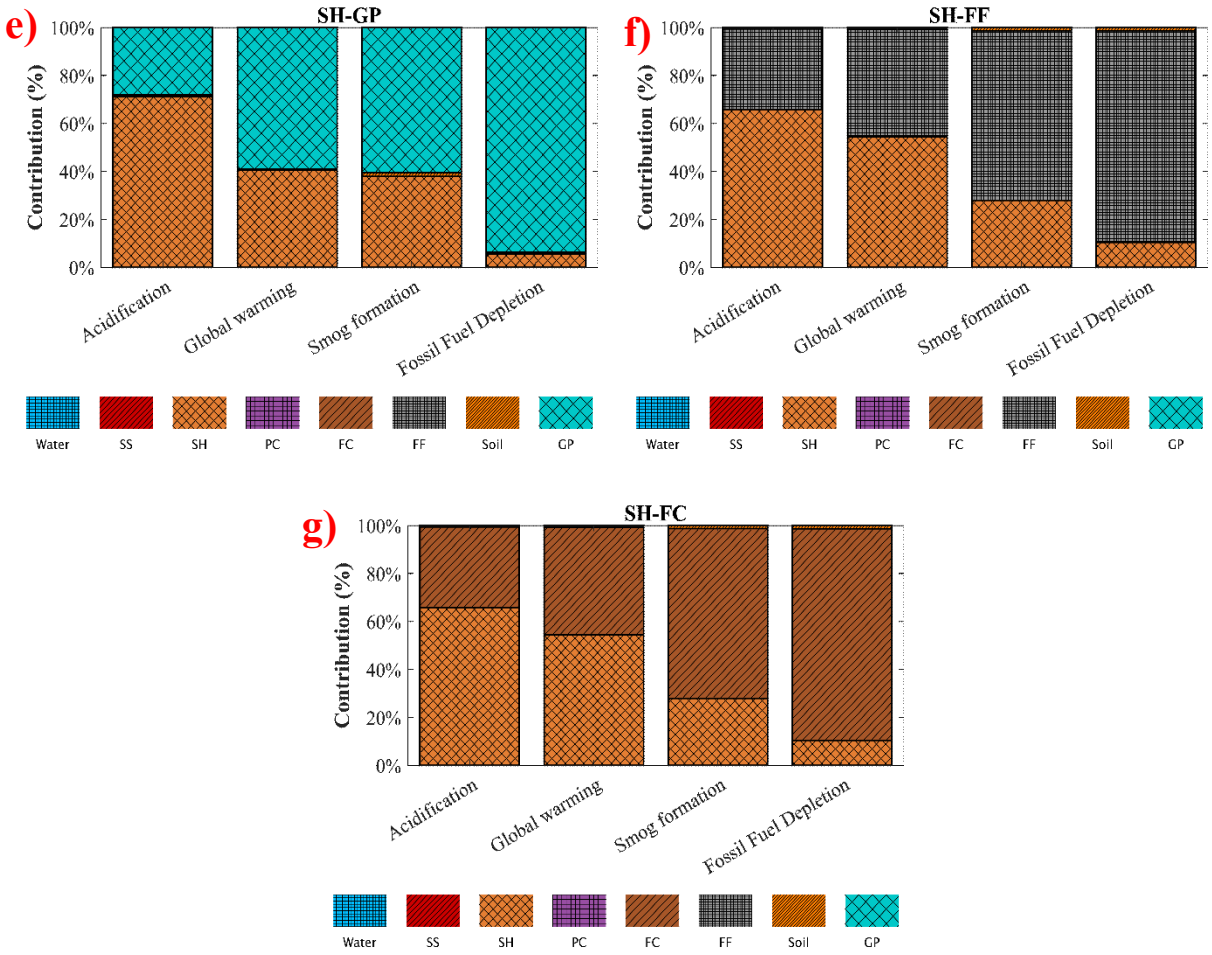


Figure 15. Contribution analysis of individual mixture constituents to different environmental impact categories with (a) PC, (b) SS-GP, (c) SS-FF, (d) SS-FC, (e) SH-GP, (f) SH-FF, (g) SH-FC

3.5. Conclusion

This study presents a comparative evaluation of the impacts of using various precursors (fly ash class F and class C, as well as glass powder) and activators (sodium silicate and sodium hydroxide) on the production of CSAEBs. To ensure that the properties are effectively evaluated, a series of physical, mechanical, durability, microstructural, and sustainability analyses has been conducted. The results of this study are summarized as follows:

- The results of physical and chemical tests on activators show that the level of electrical conductivity, TDS, salinity, and resistivity of the activators used in this study are substantially different. Sodium Silicate, with a pH of 10.80, had an electrical conductivity of 32.2 (mS/cm), a TDS of 22.7 (g/L), salinity measured at 16.1 (ppt), and a resistivity of 31.1 (Ω). Sodium Hydroxide, however, had a pH of 12.37, and an electrical conductivity of 203 (mS/cm), a TDS of 100 (g/L), salinity measured at 98.1 (ppt), and a 5.1 (Ω) resistivity. This significant difference arises from the higher ionic concentration of sodium hydroxide, which directly increases conductivity and TDS values. The stronger alkalinity also contributes to higher salinity and lower resistivity compared to sodium silicate. Together, these characteristics make sodium hydroxide a more reactive activator, capable of promoting faster dissolution of aluminosilicate precursors and more rapid reaction kinetics in mixture formulations.

- The results of hardened density and absorption tests show that the speed of reaction, known as alkali-activation, can result in slightly higher hardened density values and lowered absorption. For instance, when using sodium hydroxide, an average density of 1828.70 ± 59.40 kg/m³ and an average absorption of 13.78 ± 0.95 % are achieved. In turn, samples made from sodium silicate are found to have a density of 1704.20 ± 70.00 kg/m³ and an absorption of 15.90 ± 1.84%, respectively. These differences are statistically significant, with p-values below 0.05 in all SH–SS comparisons, except for PC vs. SH-GP with $p = 0.241$. In addition to reaction time, the specific gravity and morphology of SCMs are also found to be determining factors in density and absorption values. The highest

hardened density and lowest absorption of blocks were found in the fly ash class C-based samples, with 1838.77 ± 86.00 kg/m³ and 13.25 ± 0.41 %, respectively, and these samples also had the highest specific gravity. These values for glass powder samples are 1742.90 ± 94.40 kg/m³ and 16.21 ± 1.37 %, and finally for fly ash class F samples 1713.80 ± 71.40 kg/m³ and 15.07 ± 1.84 %. The mentioned values are believed to be directly related to the specific gravities of raw SCMs, except for glass powder, which has an angular shape and results in higher porosity and absorption. This trend is also supported by statistical analysis; for example, SH-FC was denser than SS-GP ($p = 0.000$) and SH-GP ($p = 0.008$), while SH-GP showed significantly lower absorption than SS-GP ($p = 0.000$) and SS-FF ($p = 0.001$).

- Similarly, the results of mechanical properties (e.g., compressive and flexural strength) show that samples with lower absorption values tend to develop higher strengths. However, another major factor influencing strength is the pH of the activating solution. For instance, samples containing sodium silicate with a pH = 10.8 developed a mean 28-day compressive strength of 6.04 ± 2.40 MPa, while those containing sodium hydroxide with a pH = 12.37 reached a significantly higher average of 24.85 ± 5.65 MPa ($p < 0.001$). Similarly, the average flexural strength of sodium hydroxide-based blocks was 0.41 ± 0.02 MPa, which is much higher than sodium silicate-based blocks (0.12 ± 0.05 MPa, $p = 0.000$).

- The results of wet compressive strength also support the other mechanical performance observations, but are further indicative of the higher sensitivity of alkali-activated materials to water exposure compared to Portland cement-based blocks. sodium hydroxide-based

samples showed an average wet compressive strength of 18.57 ± 6.03 MPa, compared to 7.70 ± 0.41 MPa for PC and 5.01 ± 2.94 MPa for sodium silicate-based mixtures. Despite their higher initial strengths, sodium hydroxide mixtures also had the highest relative strength loss after exposure to water, with a reduction of 67.95%, compared to 39.89% for PC and 36.72% for sodium silicate. It should be noted that the lower performance of the sodium silicate-based mixtures is not unexpected, as sodium silicate was used without sodium hydroxide in this study; combining sodium silicate with sodium hydroxide is a widely established practice in both research and industry, and is known to enhance geopolymerization. Therefore, the behavior of the sodium silicate-only mixtures reflects the limitations of this activator when used in isolation, rather than representing a novel finding.

- The results of the wire brush and acid resistance durability tests showed that there is a direct relationship between the strength and absorption values and the durability performance of the samples. Nonetheless, it was found that alkali-activated samples performed worse than Portland cement-based blocks when saturated, with a saturated weight loss of 20.56% compared to 22.27%. In contrast, under acid exposure, all alkali-activated samples, regardless of their original strength values or compositions, have performed better than Portland cement-based blocks. For example, on average, samples produced with sodium silicate and sodium hydroxide experienced a mass loss of 7.4, and 6.7%, respectively. These values are lower than what Portland cement-based samples experienced (e.g., 8.4%). Similarly, samples produced with glass powder, fly ash class C and class F experienced a relatively similar mass loss of ~7%, which shows that the choice of SCM did not

significantly impact the results.

- The result of microstructural analyses (XRF & SEM) showed that the studied SCMs are a significant factor for microstructural development, though the presence of soil and the type of activator can result in slight differences in composition. The SEM images show rather loosely connected particles, including fly ash particles and angular glass powder particles that seem unreacted when sodium silicate was used as the activator. These features are consistent with the mechanical properties reported earlier. Unlike the sodium silicate-based samples, when samples were made by sodium hydroxide, they were found to have numerous interconnected clusters along with a complex arrangement of fibrous hydrated products, platelets, or globular features, which represented the calcium and sodium silicate hydrate (C-A-S-H and N-A-S-H) gels.

- Statistical analysis of all test categories confirmed that the observed differences between mixtures were largely significant. In strength-related properties from 7-day, 28-day, and 56-day compressive and flexural strength tests, most comparisons yielded p-values below 0.05, indicating that mixture compositions had a statistically significant influence on performance. However, a larger variability was seen in durability-related tests, such as dry and saturated weight loss, as well as acid-induced mass loss, especially for glass powder-containing mixtures. Several comparisons in these categories resulted in non-significant results (with $p > 0.05$). These findings point to potential inconsistencies in the behavior of glass powder under chemical or mechanical degradation. This may be attributed to the angular morphology of glass particles and the difficulty in mixing glass powder particles,

which can lead to variable microstructure and reaction kinetics. Altogether, the statistical results support the conclusion that both activator type and precursor material had a meaningful impact on the mechanical and durability performance of the blocks.

- The results of LCA show that the production of CSAEBs can reduce the overall impacts in different categories. To do so, the use of a locally available activator and SCM is an important consideration. For instance, sodium hydroxide reduces the overall GWP of CSAEBs, as compared to sodium silicate-based blocks, but results in higher acidification, smog formation, and fossil fuel depletion rate. Similarly, the choice of SCM should be based on local availability, post-processing requirements, and performance in the masonry units. Other considerations may also be important, but in terms of ecological impacts, the ones mentioned are shown to play a key role. For example, in this study, glass powder was expected to be ground from 4 mm to 0.1 mm, which has a higher GWP than fly ash class F or class C. However, since waste glass or crushed glass is generally available locally, the impact of transportation is lowered when using glass in the mixtures. As a result, it is found that glass powder can have lower impacts on acidification and smog formation than fly ash class F and class C. In terms of fossil fuel depletion, however, glass powder has performed worse than fly ash class F and class C due to the electricity required for grinding. In this work, results were also normalized for strength of 17.23 MPa, where a significant shift in impacts is seen. For instance, sodium silicate mixtures averaged GWP of 118.2 kg CO_2-eq, compared to 103.9 kg CO_2-eq for sodium hydroxide mixtures. After strength-normalization, sodium silicate systems showed much higher GWP (average of 374.1 kg CO_2-eq), whereas sodium-hydroxide mixtures were lowest (74.83 kg CO_2-eq).

4. Comparative Properties of Soil-Based 3D-Printed Cementitious Materials Produced with Ordinary Portland Cement and Geopolymer Binders

3D printing of cementitious materials is a layer-by-layer construction method that eliminates the need for formwork. However, most mixtures used in 3D printing rely on high contents of Ordinary Portland Cement (e.g., 1.5-2 times of ordinary mixtures), finely sieved aggregates, and multiple chemical admixtures. To make this technique more sustainable, the following research has pursued two directions: (i) developing low-impact alkali-activated binders, and (ii) incorporating locally available natural soils inspired by traditional masonry materials. The present study comparatively evaluates the performance of 3D-printed mixtures in terms of fresh and hardened properties, as well as life cycle analysis (LCA), showing how binder and filler choices affect behavior. Four mixtures were developed using two binder types (Portland cement and geopolymer-based) and two filler types (sand and soil). Statistical analyses have also been conducted across most comparisons to assess the validity of the results. Results show 3D-printed soil-based components achieved compressive strengths ranging from 6.7–15.8 MPa at 28 days, which is comparable to the performance of printed sand-based mixtures (13.86–15.1 MPa at 28 days). Strengths in this range are consistent with those used for masonry units and low-rise construction, making the materials suitable for non-load-bearing or lightly loaded applications, such as infill walls, partitions, printed panels, and small structural modules, particularly in contexts where locally sourced materials are preferred. LCA results showed notable GWP variations, with sodium-hydroxide mixtures averaging 103.9 kg CO_2-eq (mass-based) and 74.8 kg CO_2-eq (strength-normalized), whereas sodium-silicate systems increased from 118.2 to 374.1 kg CO_2-eq after strength adjustment.

4.1. Introduction

The use of 3D printing in construction has grown rapidly in recent years. This technology allows for building cementitious elements layer by layer, without the need for formwork or extensive manual labor [195]. The leading interest in implementing and using 3D printing comes from the potential to reduce labor requirements and often expected material [196] and cost savings [197]. Despite the interests and potential benefits, recent studies have shown that to make 3D printable mixtures stiff enough to hold their shape, they generally need to contain about 1.5-2 times more binder than ordinary concrete mixtures [49], [70]. In addition, 3D printing mixtures are heavily reliant on chemical admixtures such as viscosity-modifying agents, retarders, and plasticizers [49], leading to concerns over its higher environmental impacts than ordinary concrete [198].

As a result, there has been growing interest in making 3D-printed construction more sustainable [73]. Over time, two main approaches have emerged in the literature. The first focuses on replacing cement with industrial byproducts such as coal fly ash or other waste materials, combined with alkaline solutions like sodium hydroxide or sodium silicate to produce alkali-activated binders [199], [200]. This class of materials has historically shown good mechanical performance with comparatively lowered CO_2 emissions to Portland cement-based binders [201], [202]. The second approach moves in a different direction and looks at using locally available materials, especially masonry-inspired, soil-based components [203], as a main ingredient [204], [205], [206], [207]. This strategy reduces the demand for processed materials such as chemical

admixture, and high content of stabilizers (e.g., Portland cement with an estimated embodied carbon of approximately 0.8 kg CO_2 eq per kg used [208]) and cuts down on transportation-related impacts because natural soil can often be sourced locally [209], [210]. It also makes the process of securing materials more practical in areas with limited access to industrial resources.

Although both of these ideas have been explored separately [211], [212], there has been very limited work combining the two routes adopted to produce sustainable 3D-printed cementitious materials. As a result, the main research gap that this study intends to address is the lack of a systematic evaluation of how binder type (Portland cement-based vs. alkali-activated) and filler type (sand vs. soil-based) mixtures interact to influence the fresh, hardened, and environmental impacts of 3D-printed mixtures. Most previous efforts have focused on one sustainability strategy or the other [213], [199] without considering how these approaches compare against each other. This gap limits the ability of stakeholders to make informed decisions when selecting materials, especially in places where industrial byproducts, chemical admixtures, and local soils are available.

For instance, Faleschini et al. [35] produced earth-based 3D-printed mixtures using a large group of materials, such as locally available soil, hydraulic lime binder, unaltered rice husk, shredded rice husk, marble waste dust, municipal solid waste incinerator bottom ash, silica sand, and natural fibers, including jute, coconut, sisal, and goat hair. It was also shown that a soil-based mixture, a mixture containing lime as binder and sisal as long fibers, could achieve a compressive strength of 1.26 MPa, and embodied carbon of about 0.05239 kgCO_2 eq/kg. The study calls for further optimization of mixtures to achieve better performance (e.g., compressive strength and

lowered embodied carbon). The shortcoming of the study compared to the present work is that the specimens were poured into molds and not cored out of printed specimens. Similarly, the mixtures were made of combined sand-soil composites and not individual earth or (crushed) sand-based 3D printing. Ji et al. [33], in turn, sampled four different soils with different granularity (e.g., particle size distribution), clay content (e.g., ranging from 4% to 31% clay), and linear shrinkage, as suitable materials for printing, and developed analytical models of plastic collapse based on each soil type. In the study mentioned, extrudability of materials from the printer's nozzle, yield stress values, and analytical models for buildability (e.g., referring to the successful placement of layer on layer) are provided. As a result, only printability parameters were evaluated and discussed, but not actual mechanical properties of the 3D printed components.

Perrot et al. [74], provided an outline of soil printing by using a biopolymer binder (alginate) with a rapid hardening tendency. The compressive strength of 3D-printed materials was then compared to ordinary earthen materials, such as conventional cob and found to be comparable (e.g., 1.21 ± 0.03 for printed material with alginate and 1.22 ± 0.04 without alginate). Similar to other studies, no major mechanical or microstructural properties of soil-based materials were provided. Many other studies (e.g.,[74], [75], [76]) attempted to use earth (or natural soil) in producing 3D-printed components, but to date, no study has separated the two sustainable methods of producing 3D-printed cementitious materials and evaluated them in one study.

As a result, this study has three main motivations: 1. Evaluating the impacts of using locally extracted soil in 3D printing of cementitious materials in terms of fresh, mechanical, and environmental impacts. 2. Evaluating the properties of geopolymer 3D-printed binder in two filler

systems (soil vs. crushed sand), and 3. Conducting a life cycle analysis (LCA) that can provide comparative environmental impacts of 3D-printed soil-based materials and geopolymer binding systems, compared to ordinary materials (i.e., Portland cement and sand).

As a result of the mentioned research gap, four mixtures were developed in this study to compare the impacts of binders (two mixtures for each binder) as well as that of a low-plasticity silt soil (one mixture per binder), compared to ordinary crushed sand (one mixture per binder). These mixtures were printed using the same 3D printing process, and their performance was evaluated across three main areas: fresh properties, mechanical behavior, and life cycle assessment (LCA).

4.1.1. Novelty and Relevance

This study provides a comparative evaluation of two different strategies for improving the sustainability of 3D-printed cementitious materials: (1) using low-impact alkali-activated binders, and (2) incorporating local natural soils in place of processed sand. While both directions have been explored independently in past research [74], [75], [76], [200], [214], the original contribution of this work lies in combining and directly comparing these two sustainability pathways under identical experimental conditions, including the same mixture design logic, 3D printing setup, and testing protocols. This unified approach allows for an unbiased evaluation of how binder chemistry and filler type together influence printability, strength, and environmental performance.

To do this, four mixtures were developed by the authors: (1) by combining two binding systems (Portland cement-based and geopolymer-based), and (2) with two different fillers (natural soil and crushed sand). This experimental framework represents the first comprehensive comparison of soil- and sand-based 3D-printed mortars with different binder chemistries, isolating the effects of both factors while maintaining consistent printing parameters. Unlike prior work that often relied on molded samples or hybrid soil-sand composites, this study uses fully 3D-printed components and isolates each variable for analysis. The samples were tested for their fresh and mechanical performance, as well as environmental impacts through cradle-to-gate LCA.

Finally, to ensure that the results also reflect the mechanical performance of each mixture, the environmental impacts are further expressed as a strength-normalized impact, with all results normalized to a reference 28-day compressive strength achieved by the C-So and C-Sa mixtures. This approach follows the methodology proposed in [155], [156], in which compressive strength is treated as an indicator of functional performance to facilitate performance-based comparisons among mixtures. The strength-corrected comparisons conducted in this study provide a more realistic perspective on sustainability than simple mass- or volume-based evaluations. As a result, this work contributes to the field by offering a side-by-side analysis of sustainable 3D printing strategies and clarifying the trade-offs between printability, strength, and environmental impact. The findings have direct implications for the selection of binder and filler systems in both urban and remote areas, where material availability and sustainability are critical factors.

4.2. Materials

The materials used in this study include: (1) natural soil and crushed sand, (2) coal fly ash and Portland cement, and (3) alkaline activators for geopolymer binders.

4.2.1. Soil and Crushed Sand

The natural soil and crushed sand used in this study were sourced from Ace Hardware in Davis, California. It was reported by the supplier that, to reduce organic content, the soil was extracted from subsurface layers several meters below ground level. Both the soil and sand were mechanically sieved using a TS-1 Gilson shaker to achieve a maximum particle size of 1.18 mm (No. 16 sieve), per ASTM C136-14 [133]. The coarser materials were discarded. The size of 1.18 had been chosen by the authors based on trials conducted on the mixtures and the printer used to produce components in this study. Following sieving, the materials were oven-dried at 110°C for 24 hours to minimize residual moisture and remove any organic content. The materials were then placed in a sealed dry bucket until used. The temperature was adopted per ASTM C136-14 [133] and ASTM D2216-19 [134]. Additional characterization, including particle size distribution, Atterberg limits, and compaction behavior (Proctor test), is presented in **Table 10**. Based on these results and classification under ASTM D2487-11 [135] and Unified Soil Classification System, the soil was identified as a low-plasticity silt (ML). In this study, sieve analysis was conducted in accordance with ASTM C117/C136 to characterize soil and sand, and the soil was washed per ASTM D6913-17 [136]. The original dry mass of the sample was 1336.30 g, and the wash mass was 521.90 g, resulting in a wash loss of 60.9%.

Table 10. Property characterization of natural soil and crushed sand.

Laboratory tests	Standards	Property	Value

			Soil	Sand
Particle-size analysis	ASTM C117-17 [137] , C136-14 [132], D6913-17 [136]	Cumulative % Retained #4 (4.75mm)	0.0	0.0
		Cumulative % Retained #8 (2.36mm)	0.0	0.0
		Cumulative % Retained #10 (2mm)	0.0	0.0
		Cumulative % Retained #16 (1.18mm)	0.0	0.7
		Cumulative % Retained #30 (0.6mm)	8.2	43.5
		Cumulative % Retained #40 (0.425mm)	14.0	65.5
		Cumulative % Retained #50 (0.3mm)	19.0	80.8
		Cumulative % Retained #100 (0.15mm)	29.4	96.2
		Cumulative % Retained #200 (75µm)	38.1	99.1
		Pan	100.0	100.0
Atterberg limits	ASTM D4318-10 [138]	Liquid limit LL (%)	20.8	–
		Plastic limit PL (%)	13.9	–
		Plasticity index PI (%)	6.8	–
Soil compaction tests	ASTM D698-21 [139]	Optimum moisture content (%)	13.0	–
		Maximum dry density (kg/m^3)	1873.3	2610.8

4.2.2. Fly Ash and Portland Cement

This study used coal fly ash class F supplied by the Salt River Materials Group from Stockton, CA, and ordinary Portland cement type I/II supplied by Nevada Cement Inc. from Reno, NV. X-ray fluorescence (XRF) spectroscopy of the cementitious materials was conducted using the Rigaku model Super mini-200 and then analyzed by the software provided by the manufacturer,

named ZSX. The method of calculating the oxides was recommended by the manufacturer [141], which is a semi-quantitative XRF (also called SQX). The XRF results are outlined in **Table 11.**

Table 12 shows the result of the mill certification provided by Nevada Cement Inc. for the Portland cement. It shows that about 58% of the content consists of C_3S, 18% C_2S, while C_3A and C_4AF have about 7% and 9%, respectively.

Table 11. XRF results for fly ash and natural soil.

Chemical compound	Fly ash (F)	Soil (low plasticity silt)
SiO_2 (%)	59.33	73.79
Al_2O_3 (%)	23.78	7.06
Fe_2O_3 (%)	6.22	15.10
CaO (%)	3.86	0.00
MgO (%)	1.39	1.79
SO_3 (%)	0.18	0.00
Na_2O (%)	0.35	0.56
K_2O (%)	0.00	0.00

Table 12. Result of mill certificate supplied by Nevada Cement Inc.

Phase composition	Content (%)
Tricalcium silicate (C_3S)	58
Dicalcium silicate (C_2S)	18
Tricalcium aluminate (C_3A)	7
Tetracalcium aluminoferrite (C_4AF)	9

4.2.3. Alkaline Activators

This study used sodium hydroxide supplied by Duda Energy Inc., located in Decatur, AL, with a molecular weight of 39.99, a pH of 12.44, and a relative density of 2.13. The sodium hydroxide was supplied in solid flakes. After mixing the flakes with water in the fume hood, the sodium hydroxide-water mixture was left at lab temperature (25±5 ºC) for at least 24 hours to cool down. In order to improve the sustainability of the mixtures, a very low molarity of 6 was chosen to be used. To ensure that the liquids used in this study were fully characterized, a portable PC400S meter kit supplied by APERA instruments (shown in **Figure 16**) was used with two separate probes. Each probe was recalibrated before the testing. Results on the physical and chemical properties of the tap water and sodium hydroxide used in this study are reported in **Table 13.**



Figure 16. The device used to measure the pH, electrical conductivity, total dissolved solids, salinity, and resistivity of the fresh mixtures.

Table 13. Tested properties of tap water and sodium hydroxide solution used in this study.

Material	pH	Electrical conductivity (mS/cm)	Total dissolved solids (g/L)	Salinity (ppt)	Resistivity (ohm)

Tap water	8.66 (±0.03)	380.00 (±0.15)	270.00 (±0.07)	0.19 (±0.01)	2.60 (±0.06)
Sodium hydroxide (M6)	12.44 (±0.04)	216.00 (±0.13)	100.00 (±0.10)	100.00 (±1.09)	4.70 (±0.07)

4.3. 3D Printer and Methods

This section describes the printer used in this study and the methodology followed in sampling and testing standards.

4.3.1. 3D Printer

The 3D printer used for this study was a SCARA Elite (**Figure 17)** purchased from 3D Potter's Inc., located in Palm City, FL. The 3D printer extrudes the construction material through a 50.8 mm diameter nozzle using an auger system. A consistent printing speed of 15 mm/s has been adopted based on the researchers' experience with the printer.



Figure 17. SCARA Elite printer.

4.3.2. Mixture Selection

A total of four mixtures, two based on Portland cement and two based on geopolymer binding systems, were produced. Similarly, two of the four mixtures used crushed sand while the other two used natural soil as their main ingredients or filler. The reason for choosing these four mixtures was to evaluate the two common schools of thought practiced in literature as the sustainable routes for 3D printing of cementitious materials: first, using soil as the main ingredient, which is sourced locally and is expected to require the least amount of processing (therefore sustainable [215]), and second, using an alkali-activated (geopolymer in this case) binding system to produce sustainable 3D-printed materials. This assumption that alkali-activated materials are sustainable, is made because in general past studies (e.g., [216], [217]) have confirmed that alkali-activated materials are more sustainable than conventional Portland cement-based materials. For instance, Bajpai et al., 2020 [218] conducted a cradle to grave LCA with a functional unit of 1 m^3 and showed that the global warming potential (GWP) of conventional cement concrete is approximately 597.54 kg CO_2-eq. In comparison, geopolymer mixtures show substantially lower impacts: 148 kg CO_2-eq for geopolymer without silica fume, 135 kg CO_2-eq for geopolymer with silica fume. As a result, the two approaches to comparing properties and sustainability (in this case cradle to gate LCA) 3D printing mixture of cementitious materials are considered in this study.

Table 14 presents the mixture proportions adopted in this study. The mixture identifiers consist of two parts separated by a hyphen: the first part identifies the binder as cement (C) or geopolymer (G), whereas the second part identifies the major ingredient as natural soil (So) or crushed sand

(Sa). These proportions were established based on preliminary trial mixtures designed to identify combinations that were both printable and comparable in performance. A total of four mixtures were selected, C-Sa, C-So, G-Sa, and G-So, representing two binder types (cementitious and geopolymeric) and two filler types (sand and soil).

Table 14. Mixture proportions used for 3D printing, expressed per thousand grams.

Mixture name	Water	SH	PC	Fly ash F	Sand	Soil
C-Sa	167.4	0.0	163.3	424.5	244.9	0.0
C-So	208.3	0.0	208.3	138.9	0.0	444.4
G-Sa	0.0	216.2	0.0	270.3	0.0	513.5
G-So	167.4	0.0	163.3	424.5	244.9	0.0

SH: sodium hydroxide solution with a molarity of 6; PC: Portland cement type I/II.

4.3.3. Testing Matrix

Table 15 presents the tests conducted in this study and the corresponding standards followed. A minimum of five samples were produced and tested for each mixture and standard with the same equipment and crew members. For compressive strength tests, 50×50×50 mm cubic samples were fabricated by coring them from freshly printed materials. To evaluate the effect of the printing process on mechanical anisotropy, compressive strength was measured in two orientations: (i) parallel to the printing direction, where the load was applied along the direction of layer deposition, and (ii) perpendicular to the printing direction, where the load was applied across the interfaces between layers. All other mechanical tests were conducted based on samples cored from freshly printed parts. The printed filaments had an average layer length of 470 mm, a width of 120 mm, and a layer thickness of 19 mm. The values were determined from the caliper measurements during

printing. These parameters were kept constant across all mixtures to ensure consistent layer formation and interfacial behavior. During fabrication, three layers were printed, and the cubes cored included two interlayers each. After samples were cored, they were left at a lab temperature of 25±5°C and a relative humidity of 50±10 % to minimize variability. Unlike the conventional 24-hour demolding period used in conventional concrete studies, samples were demolded after 48 hours to ensure adequate early strength and prevent damage during removal. All specimens were subsequently stored under the same laboratory temperature and ambient conditions until testing.

Table 15. Tests and corresponding standards used in this study.

Test*	Standard	Curing age (day)
SEM/EDS (ThermoFisher Quattro S ESEM)	–	–
XRF (Rigaku model Super mini-200)	–	–
Sieve analysis	ASTM C117-17 [137] , C136-14 [132], D6913-17 [136], D7928-21 [143]	–
Fresh density and air content	ASTM C138-13 [219]	–
Mini-Slump	ASTM C143-14 [220]	–
pH	ASTM D4262-18 [144]	–
Electrical resistivity	–	–
Salinity	–	–
Penetrometer**	ASTM C403-08 [221]	–
Water absorption	ASTM C20-22 [222]	28
Compressive strength	ASTM C109-21 [223]	7, 14, 28, 56, 91
Anisotropic behavior	ASTM C109-21 [223]	28
Splitting tensile	ASTM C496-17 [224]	28
Interlayer shear strength	ASTM C1425-13 [225]	28
LCA	ISO 14040-14044-08 [150]	–

*In this study, sieve analysis is conducted on soil and sand. Fresh density, air content, pH, resistivity, salinity, and penetrometer tests are conducted on freshly mixed materials or activators used. Finally, water absorption, compressive strength, anisotropic behavior, splitting tensile strength and interlayer shear strength are conducted on hardened samples.

**It is important to note that, according to ASTM C403-08 [221], at least six penetration resistance measurements are typically recommended to determine the setting behavior of cementitious mixtures. In this study, three data points were collected at each interval (instead of six), which provided a representative trend while balancing the practical constraints of limited fly ash availability and testing resources. Although fewer than prescribed in the standard, the results were sufficient to capture the comparative differences among mixtures, which was the primary objective of this test. Future work should include additional data points to construct a more detailed setting profile.

4.4. Statistical Analysis, Quality Assurance, and Quality Control

The results collected from the 3D-printed samples were statistically evaluated for consistency, variability, and significance in terms of differences between groups. For each group, the mean, standard deviation (SD), and coefficient of variation (COV) were calculated using Microsoft Excel version 2024. In addition to basic statistical analyses, in-depth statistical analyses were performed using MATLAB R2024a, including Levene's test, Shapiro-Wilk test, standard two-sample t-test, and Welch's t-test. To ensure the validity of the tests, three main assumptions were considered, including (1) independence of observations, (2) normal distributions, and (3) homogeneity of variances among groups [189], [190]. The first assumption was ensured by the experimental design, which ensured that all samples were cast, printed, and tested independently. To assess the normality of each group, and since the number of samples tested was relatively low (i.e., 5 samples per test), the Shapiro–Wilk test was applied. In cases where both groups would satisfy the normality assumption ($p > 0.05$), Levene's test was used to evaluate the equality of variances.

Depending on the outcome of Levene's test, either a standard two-sample t-test (assuming equal variances) or Welch's t-test (for unequal variances) was used. If the normality assumption was violated in either group, the comparison was performed using the non-parametric Mann–Whitney U test. A significance level of $\alpha = 0.05$ was used consistently as the threshold for rejecting the null hypothesis. All results found to be statistically significant are reported explicitly throughout the manuscript. Also, to ensure a fair comparison, the standard deviations and coefficient of variation (COV) are reported whenever comparisons are made throughout the manuscript.

In terms of quality assurance, standardized tests, such as the ones put forth by the American Society for Testing and Materials (ASTM), were carefully followed throughout this research. Also, all equipment used in the preparation, curing, and testing of 3D-printed materials was recalibrated per the manufacturer's guidelines before testing. In cases where non-standardized procedures were needed or used, reference materials and previous research studies were reviewed, and credible justifications were provided in the methodology sections. Also, temperature and humidity during specimen curing and testing phases were kept similar to lab conditions (i.e., 25±5 °C and a relative humidity of 50±10 % to minimize variability).

In terms of quality control, testing procedures were equally conducted with the same crew and instruments to minimize other sources of variability in the collected data. Generally, for each test, more than five specimens were prepared to ensure that no outlier in the reporting data would exist to impact the results. Specimens that exhibited obvious signs of physical damage or handling errors were the outliers that were excluded from the analysis. Such outliers were then also removed from the final statistical analysis to avoid impacting the results. This approach ensured that the reported

findings accurately reflected the behavior of the 3D-printed mortar specimens under investigation. Also, in each figure, the reported mean is followed by ± the calculated STD. A similar reporting method is used to explain the results.

4.5. Experimental Results

This section reports the results of material characterization through SEM and XRF, as well as the experimental tests corresponding to the characterization of fresh and physical properties, and hardened mechanical properties for all four mixtures considered in this study.

4.5.1. SEM Imaging of Hardened Materials

Figure 18 (a)-(h) show the SEM images of 3D-printed samples at 80× and 3500× magnifications for all mixtures. These two magnifications were selected because they can show both macro and micro features, based on trials conducted by the authors. **Figure 18** (a)-(b), shows C-Sa samples with a relatively compact texture and several spherical voids. At the high magnification (**Figure 18** (b)) the reactant materials appear consumed, and a dense cluster with fewer disconnected particles can be seen. The denser microstructure and reduced unreacted particle content indicate a more complete reaction and improved binder formation.

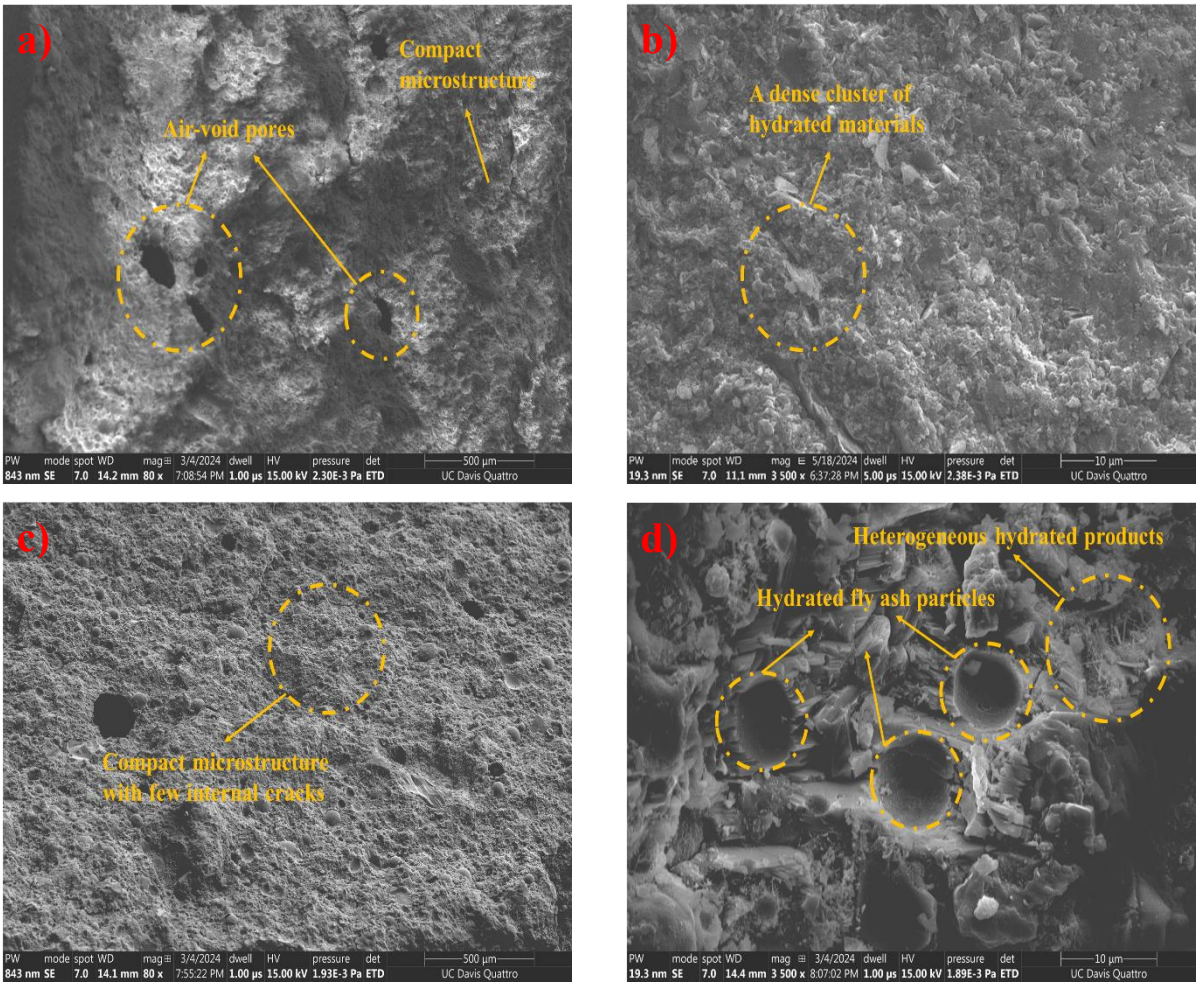
Figure 18 (c)-(d) shows the C-So mixture, which appears more heterogeneous but still very compact with few internal cracks, compared to C-Sa. For example, at low magnification (**Figure 18** (c)) there are almost no internal cracks, and the microstructure appears very compact. At the high magnification (**Figure 18** (d)), a variety of hydrated products can be seen, including reacted

fly ash particles incorporated into the binding matrix. Comparing C-So images to those of C-Sa, the surface shows more irregularity, likely due to the broader particle size distribution of the natural soil. However, the microstructure still shows a high degree of connectivity, which is aligned with the strength results discussed earlier.

Figure 18 (e)-(f) show the G-Sa mixture while **Figure 18** (g)-(h) shows G-So mixture. These images are relatively similar and show a loose and unreacted matrix with a greater number of micro air voids (**Figure 18** (e)) and unreacted particles (**Figure 18** (f)). In addition to the mentioned, in the case of G-So (in **Figure 18** (h)), deep cracks and microstructural voids can be seen across clusters of partially reacted materials (**Figure 18** (g)-(h)). These pores can result from higher water content in the microstructure or even different gel structures, as reported by previous studies [226], [227].

These microstructural observations are consistent with the mechanical results discussed in previous sections, confirming that the geopolymer samples did not develop strengths comparable to the Portland cement–based mixtures. Also, based on previous studies [228], [229], [230], sodium hydroxide helps in dissolving alumina (Al_2O_3) and silica (SiO_2) content, but it lacks additional silicate species necessary for effective polymerization. It can result in slower setting and weaker strength values due to incomplete geopolymer network formation. Ref. [231] reported that the lack of connectivity in geopolymer particles originates from unreacted fly ash particles that allow empty spaces to form interconnected porosity.

Taken together, the SEM results support the mechanical data and help explain the observed differences, whereby the soil-based mixtures (C-So and G-So) generally display a more heterogeneous surface with diverse reacted phases. In turn, sand-based mixtures appear more homogeneous, particularly in the Portland cement-based mixes, which display better hydration products and matrix connectivity.



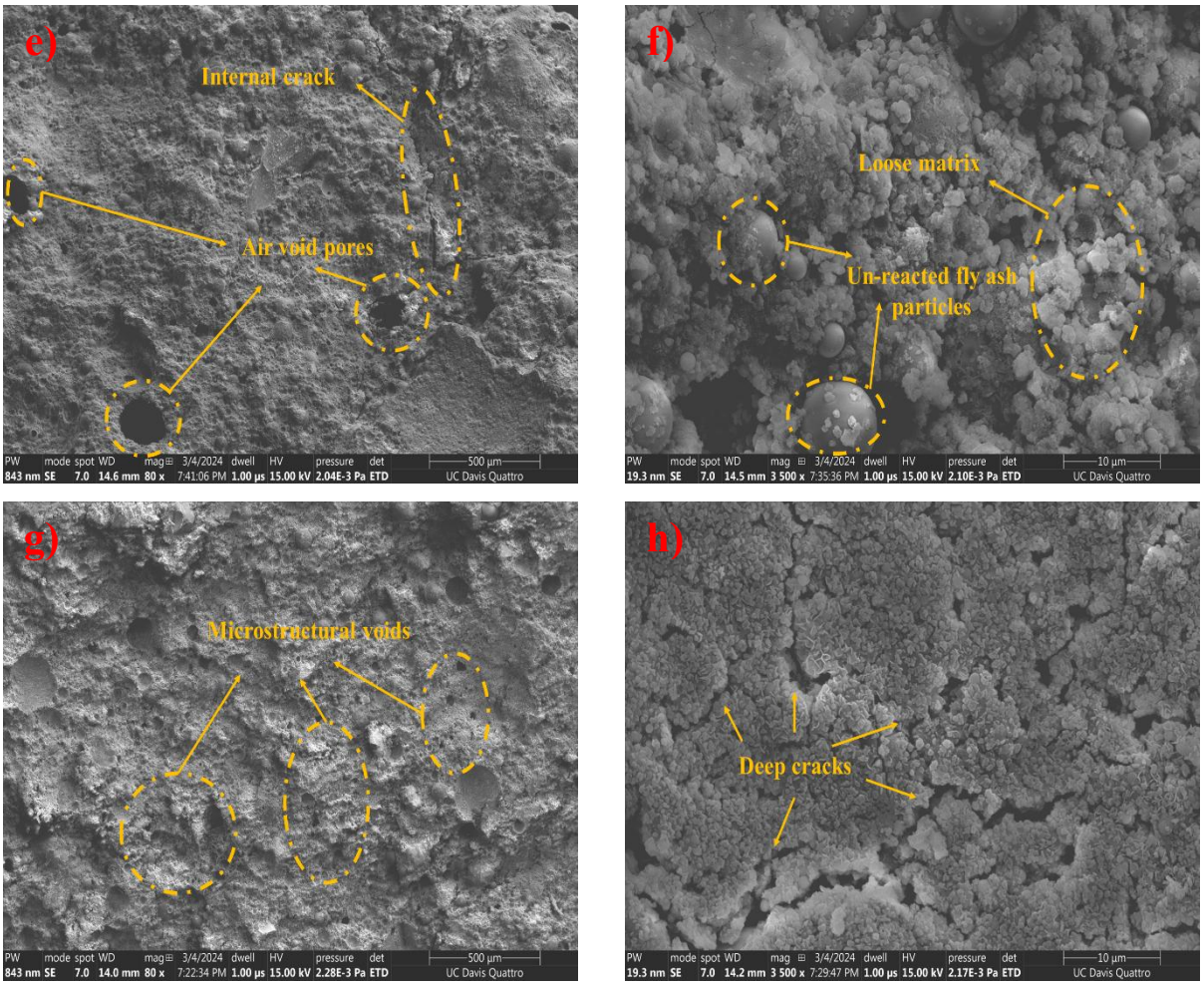


Figure 18. SEM results: (a) C-Sa at 80× magnification, (b) C-Sa at 3500× magnification, (c) C-So at 80× magnification, (d) C-So at 3500× magnification, (e) G-Sa at 80× magnification, (f) G-Sa at 3500× magnification, (g) G-So at 80× magnification, (h) G-So at 3500× magnification.

4.5.2. Oxide Composition of Hardened Materials Using XRF

The results of the XRF analysis conducted on 28-day and ground samples are presented in **Table 16**. C-So and G-So are found to have the highest concentrations of Fe_2O_3 and SiO_2 compared to C-Sa and G-Sa, which is consistent with the oxide content shared in **Table 11**. Likewise, geopolymer-based samples exhibited notably higher amounts of Na_2O and SiO_2. For instance, G-

Sa and G-So recorded Na_2O contents of 4.26% and 7.49%, respectively. In turn, C-Sa and C-So have recorded values of 0.70% and 0.60%, respectively. These differences reflect the contribution of sodium hydroxide as an activator in geopolymer formulations.

It's important to note that a higher Na_2O content in the geopolymer microstructure might indicate long-term durability issues, as suggested in the literature [232]. Moreover, the microstructural differences mentioned, especially the high alkali content in soil-based geopolymer samples, should be further investigated to understand their impact on the long-term durability of 3D-printed components.

Table 16. XRF results from 3D-printed samples after 28-day curing.

Oxides	C-Sa	C-So	G-Sa	G-So
Na_2O (%)	0.70	0.60	4.26	7.49
MgO (%)	1.44	1.13	1.67	1.79
Al_2O_3 (%)	13.45	9.41	18.64	15.55
SiO_2 (%)	35.95	37.57	49.31	52.12
P_2O_5 (%)	0.82	0.44	1.25	0.85
SO_3 (%)	1.59	1.45	0.64	0.48
K_2O (%)	1.11	1.40	0.94	1.85
CaO (%)	34.48	37.06	11.88	8.60
TiO_2 (%)	1.58	0.91	1.63	1.17
Fe_2O_3 (%)	7.92	9.54	8.80	9.34

4.5.3. Fresh Mixture Properties

The fresh properties of the mixtures are shown in **Table 17**. C-Sa showed the highest slump of all groups with 129.0 ± 1.6 mm, followed by G-Sa with 115.0 ± 1.4 mm. The lowest values were recorded for C-So with 110.0 ± 1.9 mm and G-So with 100.0 ± 2.2 mm. These differences were statistically significant both within the cement group (such as C-Sa vs. C-So, $p = 0.0079$) and within the geopolymer group (such as G-Sa vs. G-So, $p = 0.0079$). When grouped by binder type, cement-based mixtures showed higher flowability with 119.5 mm compared to geopolymer-based mixtures with 107.5 mm and $p = 0.0094$, which shows a statistically significant difference. When evaluated based on the filler, sand-based mixtures (C-Sa and G-Sa) developed a higher slump than soil-based ones (C-So and G-So), with $p = 0.0002$, suggesting that particle gradation and angularity differences between sand and natural soil had a measurable impact on fresh workability.

In terms of air content, G-Sa developed the highest value of 6.04 ± 0.11%, followed by G-So with 5.46 ± 0.18%. Cement-based mixtures, such as C-Sa and C-So, recorded lower values of 5.50 ± 0.16% and 4.50 ± 0.23%, respectively. All pairwise comparisons were statistically significant, including C-Sa vs. C-So ($p = 0.0079$), C-Sa vs. G-Sa ($p = 0.0079$), C-So vs. G-Sa ($p = 0.0079$), C-So vs. G-So ($p = 0.0079$), and G-Sa vs. G-So ($p = 0.0079$). The only exception was C-Sa vs. G-So, which showed no statistically significant difference ($p = 0.7857$). In general, geopolymer-based mixtures showed higher air content values than cement-based ones ($p = 0.0079$), which is in line with previous reports of greater porosity in geopolymer systems [165]. The lower air content in C-So may also be explained by the finer particle size of the soil and its higher surface area, which can result in a higher packing density and reduce the air content.

In general, a lower porosity corresponds to a more compact microstructure [233], [234], which supports the lower air content and higher density observed in cement-based mixtures.

Fresh density results are also aligned with the trends in air content. For instance, C-So presented the highest average density (1914.9 ± 0.9 kg/m³), followed by C-Sa (1882.7 ± 1.0 kg/m³), then G-So (1869.4 ± 0.6 kg/m³), and G-Sa (1849.0 ± 1.0 kg/m³). Statistically speaking, all pairwise comparisons were significant, including C-Sa vs. C-So ($p = 0.0079$), C-Sa vs. G-Sa ($p = 0.0079$), C-Sa vs. G-So ($p = 0.0079$), C-So vs. G-Sa ($p = 0.0079$), C-So vs. G-So ($p = 0.0079$), and G-Sa vs. G-So ($p = 0.0079$). Cement-based mixtures showed higher fresh densities than geopolymer-based ones ($p = 0.0000$), while the effect of filler type (sand vs. soil) was also statistically significant ($p = 0.0130$). These results align with the observed air content trends, suggesting that the use of finer soil particles promoted denser packing, especially in the absence of vibration during the 3D printing process.

The measured pH values also varied across binders and fillers. G-Sa samples had the lowest pH of 11.40 ± 0.07, while the other three mixtures (i.e., C-Sa, C-So, and G-So) recorded higher values between 12.36 and 12.68. Statistically significant differences were found across most group comparisons, including C-Sa vs. C-So ($p = 0.0079$), C-Sa vs. G-Sa ($p = 0.0079$), and C-Sa vs. G-So ($p = 0.0079$). The difference between C-So and G-So, however, was not statistically significant ($p = 0.9524$), indicating similar alkalinity between these two soil-based mixtures. Cement-based mixtures had significantly higher pH than geopolymer-based ones ($p = 0.0032$), while the effect of filler was not statistically significant ($p = 1.0000$). This observation is important because previous

studies have shown that a higher pH can generally increase the hydration rate in cementitious materials [235], [236].

In addition, the salinity values clearly reflected the type of binder used. Both cement-based mixtures were found to have low salinity levels, with C-Sa measuring 1.95 ± 0.04 ppt and C-So at 1.86 ± 0.05 ppt. In contrast, geopolymer samples recorded substantially higher values of 21.16 ± 1.73 ppt for G-Sa and 32.87 ± 2.58 ppt for G-So. These differences were all statistically significant. Specifically, C-Sa vs. C-So ($p = 0.0238$), C-Sa vs. G-Sa ($p = 0.0079$), C-Sa vs. G-So ($p = 0.0079$), C-So vs. G-Sa ($p = 0.0079$), and C-So vs. G-So ($p = 0.0079$) each showed clear differences. Additionally, the difference between G-Sa and G-So ($p = 0.0079$) may reflect the greater sodium retention in the soil-based geopolymer mixture compared to its sand-based counterpart. These results highlight the combined influence of binder chemistry and filler type on salinity levels, particularly in systems activated with sodium hydroxide. On average and based on the mentioned, geopolymer-based mixtures had smaller slump and fresh density values, as well as higher air content than their cement-based counterparts, which is consistent with results reported in the literature [106].

Table 17. Measured properties of fresh mixtures.

Mixture ID	Slump (mm)	Air content (%)	Fresh density (kg/m^3)	pH	Salinity (parts per thousand)
C-Sa	129.0 (±1.58)	5.50 (±0.16)	1882.7 (±0.97)	12.68 (±0.03)	1.95 (±0.04)
C-So	110.0 (±1.87)	4.50 (±0.23)	1914.8 (±0.88)	12.36 (±0.05)	1.86 (±0.05)
G-Sa	115.0 (±1.41)	6.04 (±0.11)	1849.0 (±1.00)	11.40 (±0.07)	21.16 (±1.73)
G-So	100.0 (±2.24)	5.46 (±0.18)	1869.4 (±0.55)	12.36 (±0.09)	32.87 (±2.58)

4.5.4. Penetration Resistance and Initial Set Time

The results of the penetrometer test in terms of penetration strength versus time are shown in **Figure 19**. All mixtures have similar penetration strength values (ranging between 0.14 and 0.28 MPa) at 25 minutes (i.e., at the first measuring time). This initial strength is closely linked to the material's buildability and is influenced by factors such as particle size distribution and surface texture. A low resistance value also shows that the mixtures had a low stiffness build-up, which is required for printing. Over time, however, the rate of strength gain varied significantly among the different binder and filler combinations. C-So, for instance, showed the most rapid increase in penetration resistance, reaching 21.65 MPa at 600 minutes, followed by C-Sa at 13.21 MPa. These results suggest that cement-based mixtures, particularly when combined with soil, develop stiffness more quickly during the early-age setting process. This accelerated stiffening can be attributed to the finer particle size distribution and higher water absorption capacity of the soil compared with sand. The finer particles increase the overall surface area available for cement hydration, promoting faster formation of hydration products and a denser early microstructure. Additionally, the soil's higher water absorption reduces the amount of free water in the paste, leading to a higher effective solid fraction and increased interparticle friction. Together, these effects accelerate the transition from a plastic to a rigid state, enhancing early buildability but potentially reducing workable time.

In contrast, geopolymer-based mixtures, especially G-Sa, showed much lower penetration resistance values throughout the test duration. G-Sa reached only 1.27 MPa after 10 hours, while G-So peaked at 3.51 MPa. This difference indicates that geopolymer mixtures build internal structure more slowly than their cement-based counterparts. Previous studies have highlighted the

rheological differences of Portland cement-based vs. geopolymer binders in more detail [237]. This difference is believed to be highly dependent on the activator and aluminosilicate material types used in the geopolymer and Portland cement mixtures [238]. Although the same supplementary cementitious materials are used in this study, their behavior has a heavy impact on the mixture proportioning and potential mixture optimization. Among geopolymer mixtures, the presence of soil in G-So appeared to help slightly increase penetration resistance compared to G-Sa. Nonetheless, the differences remained relatively small throughout the test. In general, these trends confirm that the concentration of binder strongly affects the rate and magnitude of stiffening [106], with Portland cement-based mixtures consistently outperforming geopolymer-based ones in terms of early-age structural build-up. It can also be noted that the printing region, defined here as the starting point of the penetrometer test, corresponding to the material's initial workable state, appears to be far below the ASTM-recommended initial setting strength of 3.44 MPa. According to ASTM C403/C403M, the initial and final setting times are defined as the points at which the penetration resistance reaches 3.44 MPa and 27.6 MPa, respectively. Among the mixtures studied, C-So was the first to achieve the initial setting strength of 3.44 MPa, after approximately 350 minutes from mixing, followed by C-Sa at around 500 minutes. G-So reached that threshold at about 600 minutes, whereas G-Sa did not attain it even after 600 minutes.

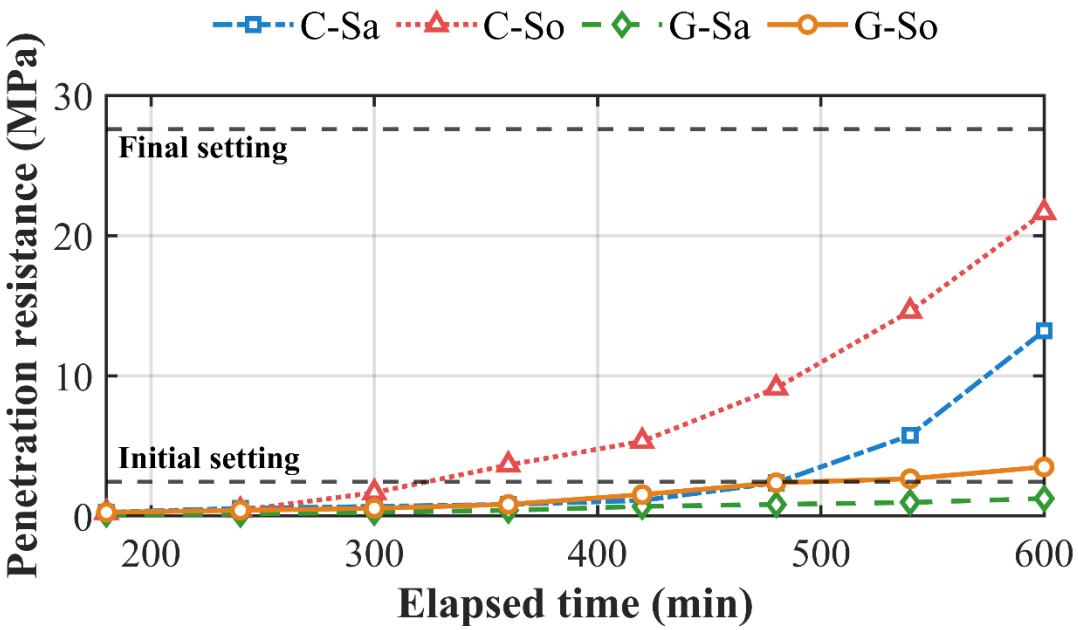


Figure 19. Results of the penetrometer test.

4.5.5. Water Absorption

Based on **Figure 20** C-Sa samples showed an average absorption of 10.20 ± 1.04%, which was significantly higher than that of C-So samples (7.90 ± 0.22%), with p = 0.0079. In turn, G-Sa samples showed an average absorption of 10.28 ± 0.11%, which was significantly lower than that of G-So samples (16.04 ± 0.36%), also with p = 0.0079. In terms of binder type, cement-based samples (C-Sa and C-So) had an average absorption of 9.1 ± 1.40%, which was significantly lower than that of geopolymer-based samples (G-Sa and G-So) at 13.2 ± 3.05%, with p = 0.0027. The higher absorption value of geopolymer samples is consistent with results reported in the literature [239], [226], [227].

In terms of COV, C-Sa samples developed a value of 0.102, which compares to 0.027 for C-So samples. In the same way, G-Sa and G-So developed values of 0.009 and 0.024, respectively.

Based on COVs, C-So and G-So both developed higher COVs. It shows that the results in these groups showed higher variability, probably caused by the increased heterogeneity when soil is used.

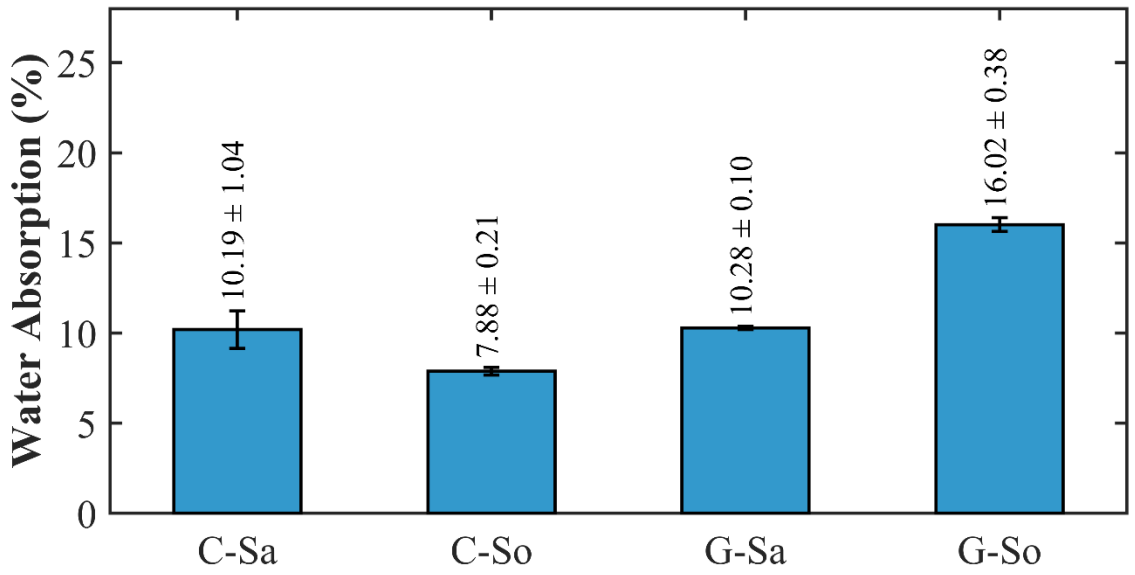


Figure 20. Water absorption test results.

4.5.6. Mechanical Properties of Hardened Mixtures

To evaluate the hardened properties, a set of mechanical properties tests has been conducted. It includes compressive strength over different curing ages to understand the strength development rate of each mixture. Due to the specific manufacturing method (i.e., laminated printing), anisotropic, splitting tensile, and interlayer shear strengths tests are also performed. The tests and the resulting properties are outlined in the following sections.

4.5.6.1. Compressive Strengths

Figure 21 shows the compressive strength test results. During the 7 and 14 days of curing, C-So had the highest strength with 13.57 ± 1.81 MPa at 7 days and 15.15 ± 1.69 MPa at 14 days. C-Sa developed similar strength, with 13.52 ± 1.67 MPa (7 days) and 14.33 ± 1.05 MPa (14 days). On the 7th day mark, both cement-based mixtures (i.e., C-Sa with 13.52 ± 1.67 and C-So with 13.57 ± 1.81) outperformed geopolymer mixtures (i.e., G-Sa with 3.17 ± 0.56 and G-So with 2.60 ± 0.46) with $p = 0.0079$ for all pairwise comparisons, and were statistically significant. However, the difference between C-Sa and C-So showed no statistically significant difference ($p = 0.8413$). During the 14 days, C-Sa and C-So (i.e., C-Sa with 14.33 ± 1.35 and C-So with 15.15 ± 1.69) continued outperforming G-So with $p = 0.0079$, while the difference between C-So and G-Sa (with 12.80 ± 1.93) was not statistically significant ($p = 0.2222$). As for the geopolymer mixtures, G-Sa (with 12.80 ± 1.93) showed higher strength than G-So (with 6.34 ± 0.85), and the difference became statistically significant at 14 days ($p = 0.0079$), even though it was not significant at 7 days ($p = 0.2222$).

At 28 days, C-So remained the top-performing mixture with 15.80 ± 1.27 MPa, followed by C-Sa with 15.12 ± 1.14 MPa. G-Sa continued to improve, reaching 13.86 ± 3.05 MPa, while G-So reached 6.70 ± 0.66 MPa. The difference between G-Sa and G-So was statistically significant ($p = 0.0079$), highlighting the important effect of filler type on strength development in geopolymer mixtures.

At extended curing times of 56 and 91 days, cement-based samples continued to develop higher strength values. For instance, C-So reached 20.32 ± 2.26 MPa at 91 days, while C-Sa followed

closely with 18.06 ± 1.32 MPa. This shows that both cement-based mixtures developed relatively high strengths, and their pairwise statistical analysis showed that their differences are not significant ($p = 0.1508$). Similarly, G-Sa developed a strength of 16.23 ± 1.66 MPa at 91 days, while G-So remained the lowest with 11.50 ± 2.40 MPa. The differences between G-Sa and G-So were again statistically significant on both 56 days ($p = 0.0079$) and 91 days ($p = 0.0159$). Additionally, C-So with 20.32 ± 2.26 MPa outperformed G-Sa with 16.23 ± 1.66 MPa at 91 days with $p = 0.0317$. The higher strength of C-So shows the long-term strength advantage of the soil-cement mixtures, as compared to the geopolymer-sand mixture in this case.

In terms of COV, cement-based mixtures showed the lowest values, especially C-Sa at 14, 28, and 91 days with 0.073, 0.076, and 0.073, respectively. With C-So in the middle, G-Sa and G-So displayed higher variability, especially at 28 and 91 days, with COVs reaching 0.220 and 0.208. These results suggest that geopolymer mixtures, particularly those combined with soil, are more sensitive to localized inhomogeneities and exhibit greater performance variability over time.

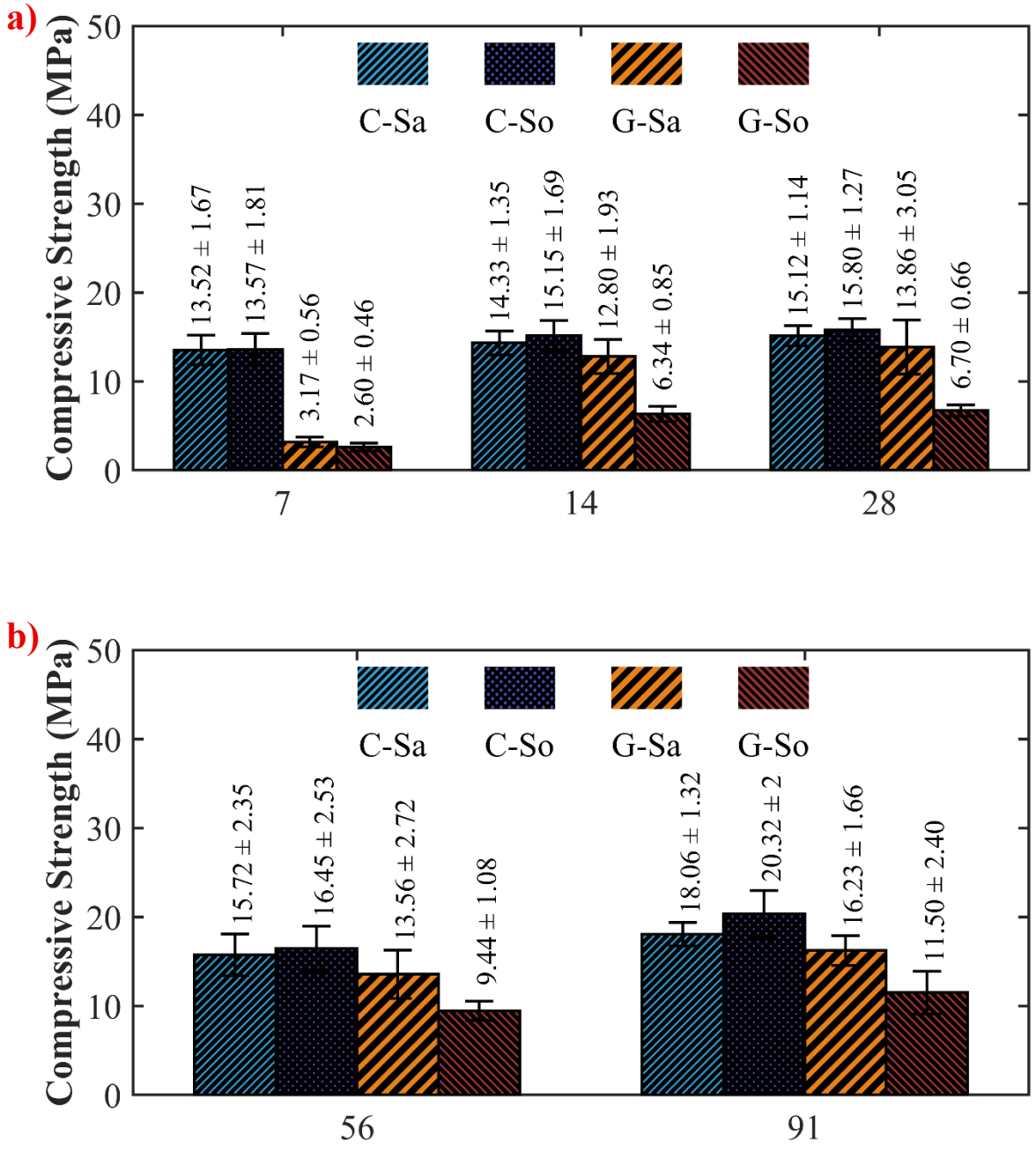


Figure 21. Compressive strength of samples with (a) 7, 14, and 28 day cured samples, and (b) 56 and 91 day cured samples

4.5.6.2. Anisotropic Behavior Effects on Compressive Strength

Figure 22 shows the 28-day compressive strength of cubic samples tested in two different directions: (a) along the printing direction (referred to as printing direction hereinafter) and (b) perpendicular to the printing direction (referred to as perpendicular direction hereinafter). In the printing direction, C-Sa reached an average compressive strength of 15.12 ± 1.14 MPa, which was statistically similar to C-So (15.80 ± 1.27 MPa, $p = 0.4206$). No significant difference was found between C-Sa (15.12 ± 1.14 MPa) and G-Sa (14.30 ± 2.72 MPa, $p = 0.8413$), or between C-So (15.80 ± 1.27 MPa) and G-Sa (14.30 ± 2.72 MPa, and $p = 0.3333$), suggesting that strength remained relatively consistent across these three mixtures regardless of binder or filler type. In turn, G-So recorded a substantially lower average strength of 6.48 ± 0.94 MPa. It is also found that the differences were statistically significant when G-So is compared to C-Sa ($p = 0.0079$), C-So ($p = 0.0079$), and G-Sa ($p = 0.0079$), which indicates that while mixtures with sand provided comparable performance across binders, the use of soil in combination with a geopolymer binder led to a considerably lower strength.

The COVs in the printing direction also show the highest variability for G-So with 0.145 and G-Sa with 0.190. The COVs for cement-based mixtures are found as C-Sa with 0.076 and C-So with 0.081. This suggests that geopolymer samples, especially with soil, showed less consistency in strength values, which can be explained by potential heterogeneity in microstructure.

In the perpendicular direction, C-Sa samples had an average strength of 12.50 ± 1.46 MPa, which was not significantly different from C-So samples with 11.52 ± 1.60 MPa, and $p = 0.2540$. Similarly, no statistical difference was observed between C-Sa (with 12.50 ± 1.46 MPa) and G-Sa

(with 11.46 ± 1.24 MPa, and $p = 0.3095$). This finding suggests that similar performance is recorded between cement-sand and geopolymer-sand mixtures. However, C-Sa (with 12.50 ± 1.46 MPa) significantly outperformed G-So (with 5.94 ± 0.94 MPa, and $p = 0.0079$). C-So samples (with 11.52 ± 1.60 MPa) also showed significantly higher strength than G-So with $p = 0.0079$, presenting the higher strength of soil-cement mixtures. Among the geopolymer mixtures, G-Sa with 11.46 ± 1.24 MPa outperformed G-So with 5.94 ± 0.94 MPa with a $p = 0.0079$, confirming that sand-based mixtures have performed better than their soil-based counterparts in anisotropic performance. In general, it is hypothesized that this anisotropic behavior for the compressive strength derives from the 3D printing process, which lays randomly distributed pores and voids in a directional manner. Previous studies in this area also reported similar strength variations, with printing direction having a stronger compressive strength than perpendicular to printing direction [240], [241], [242].

In terms of COV in the perpendicular direction, the highest variability was seen in G-So with 0.158, followed by C-So with 0.139, while C-Sa and G-Sa had a COV of 0.117 and 0.108, respectively. The COV values show a potentially higher variability of samples produced with soil, which can result from microstructural differences and higher heterogeneity that result in higher variability.

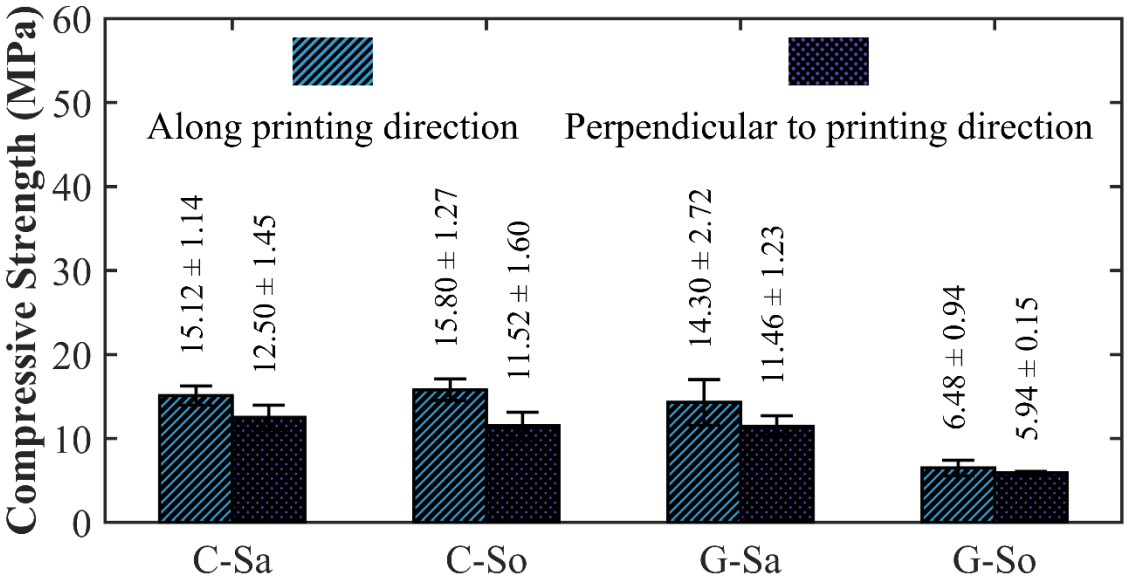


Figure 22. Compressive strength of cubes in two different directions (a) along printing direction, (b) perpendicular to printing direction

4.5.6.3. Splitting Tensile Strength

The results of 28-day cured cylinder samples tested for splitting tensile strength are shown in **Figure 23.** Based on the results, C-Sa samples averaged 3.08 ± 0.24 MPa, which was not significantly different from C-So samples with 2.74 ± 0.25 MPa, and p = 0.0556, indicating the two types of materials have almost similar strength and the difference was not statistically significant. This is similar to the compressive strength values reported earlier. Nonetheless, C-Sa samples developed significantly higher tensile strength than both G-Sa (1.98 ± 0.37 MPa, p = 0.0079) and G-So (0.81 ± 0.17 MPa, p = 0.0079). In turn, C-So samples also showed significantly higher tensile strength than G-Sa (p = 0.0159) and G-So (p = 0.0079). Among the geopolymer-based mixtures, G-Sa outperformed G-So with statistical significance (p = 0.0079).

In terms of COV, they followed a similar pattern as the strengths, with lower variability recorded for C-Sa and C-So with 0.079 and 0.090, respectively, while a higher variability has been recorded in G-So (0.205) and G-Sa (0.186). The difference in variability in the case of cement-based mixtures show better consistency, while the increased variability in geopolymers results may be due to the sensitivity of tensile properties to the higher micro-pores of the geopolymer samples. Previous studies (e.g., [243]) have reported that in general, geopolymer samples develop a more porous microstructure.

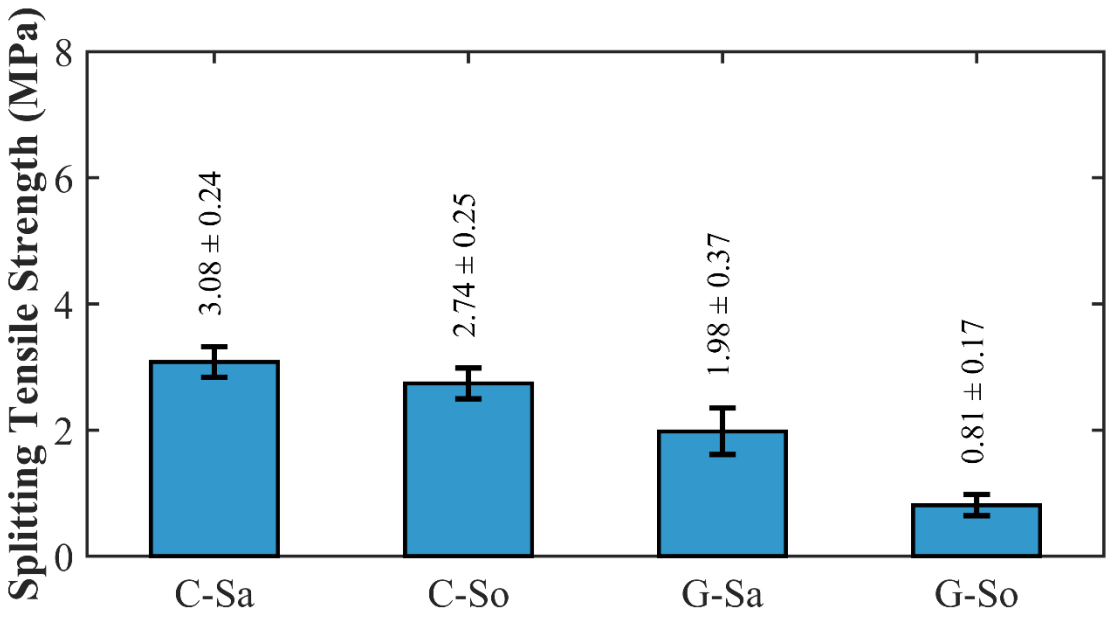


Figure 23. Splitting tensile strength.

4.5.6.4. Interlayer Shear Strength

The shear strength test corresponding to ASTM C1425-19 [225] was conducted to evaluate the interlayer bonding of 3D-printed samples. **Figure 24** (a) shows the testing outline per standard, and **Figure 24** (b) shows the results. Based on the results, C-Sa samples had an average value of 4.33 ± 0.60 MPa. In turn, C-So samples achieved a higher average of 5.90 ± 0.38 MPa, with the difference between the two cement-based mixtures being statistically significant ($p = 0.0079$). Compared to the cement-based mixtures, G-Sa showed a considerably lower value, averaging 0.78 ± 0.04 MPa ($p = 0.0079$). G-So samples followed a similar trend, with an average shear strength of 0.71 ± 0.09 MPa. Although G-Sa and G-So developed similarly low strengths relative to cement-based mixtures, the difference between them was not statistically significant ($p = 0.1984$). The reason for the very low shear strength values of geopolymer samples can be related to the high porosity and absorption of geopolymer binders, as well as the higher brittleness that is reported by previous studies [180].

The interlayer shear results also show considerably higher COV in C-Sa (0.138) and G-So (0.131), in contrast to C-So (0.065) and G-Sa (0.053). This indicates that shear performance in these two groups might have been more influenced or dominated by the differences in interfacial quality, sample printing orientation, or local inhomogeneities across specimens.

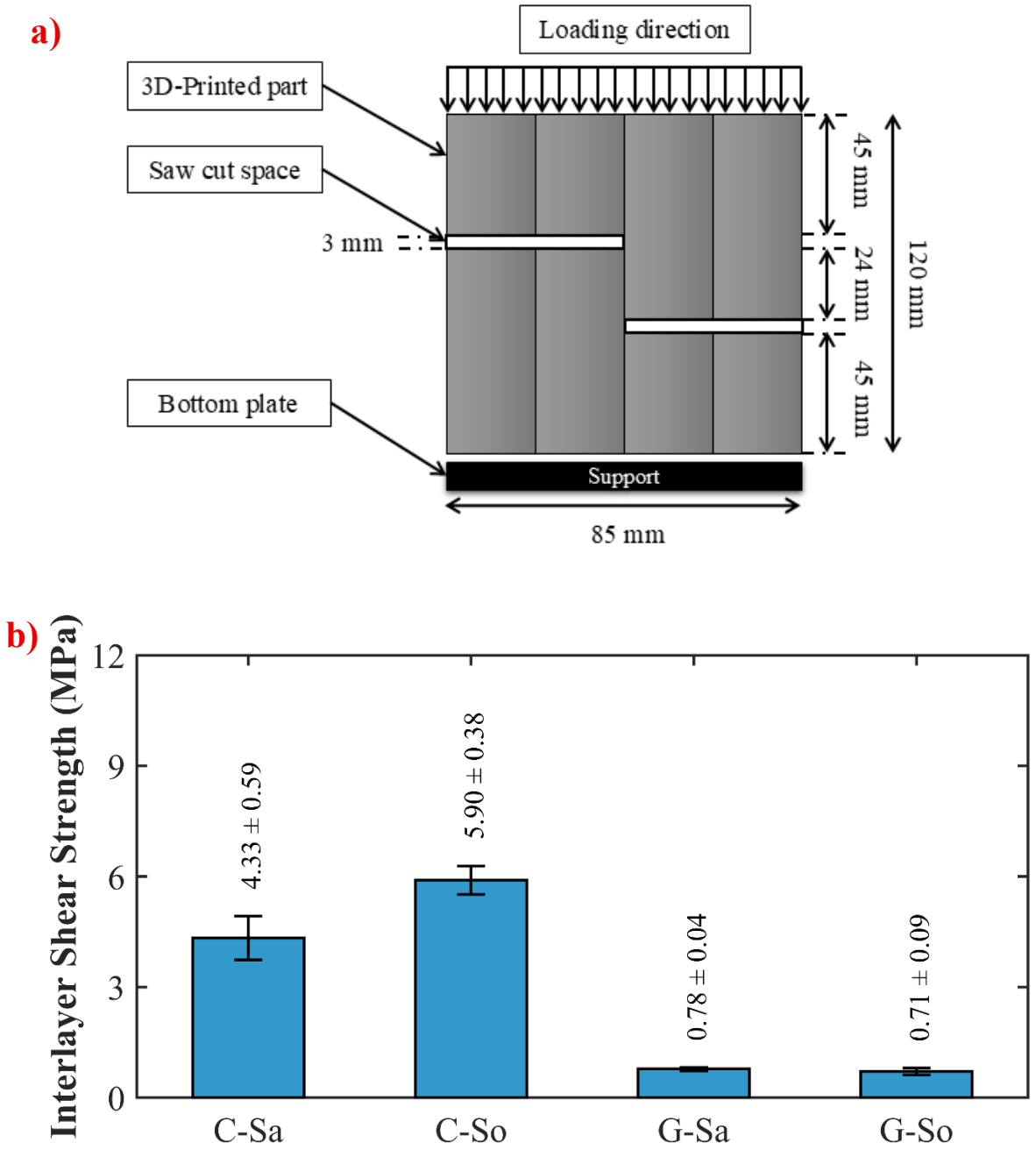


Figure 24. Presenting (a) testing set up per ASTM C1425-19, and (b) results of shear test.

4.5.7. Life Cycle Analysis (LCA)

The life cycle assessment (LCA) methodology is used here to quantify the environmental impacts of the four mixtures considered in this study, following ISO 14040-14044 [150]. The aim of this LCA is not only to compare the four mixtures, but also to identify the phases in the production process with the highest environmental impacts, thus providing suggestions for optimization of the fabrication process.

4.5.7.1. System Definition and Boundaries

A scale-up of lab conditions to an industrial scale has been conducted to evaluate the life cycle environmental impacts of producing 3D-printed soil-based and sand-based structural walls. The functional unit used in this study is the materials needed to build a 1 m (height) × 1 m (length) wall with a width of 0.1 m. This functional unit was selected because it represents a realistic and directly comparable structural element that can be printed under identical boundary conditions, reflecting the primary function of the product to act as a load-bearing wall segment. By fixing the wall geometry, the functional unit ensures that all mixtures are evaluated on an equivalent physical basis, while preserving practical relevance to construction-scale applications. The selected dimensions are consistent with typical experimental or pilot-scale 3D printing setups and can be readily scaled to larger structural systems. Furthermore, this choice aligns with recent developments in additive manufacturing of prefabricated structural components, as several studies have focused on 3D printing discrete wall segments intended for assembly in modular construction [244], [245]. Therefore, adopting a wall section as the functional unit provides both a structurally meaningful and practically applicable basis for comparison among the investigated mixtures.

In addition, since each mixture proportion has a specific 28-day strength, the same wall is analyzed separately for a condition where its thickness is calculated based on its strength. Previous studies have conducted similar calculations to capture a more realistic environmental impact [155], [156] and have referred to it as a strength-normalized functional unit [244] (hereinafter referred to as strength factor). In this case, it is assumed that for the two compositions C-Sa and C-So, the required thickness of the wall is 0.1 m (due to similar compressive strength values of 15.8±1.14 and 15.1±1.27 MPa). For G-Sa and G-So the wall thickness with the strength factor is then calculated by multiplying 0.1 m by the ratio between the (28-day) compressive strength of the composition and the average strength of the compositions C-Sa and C-So, giving a thickness equal to 0.12 m for G-Sa and 0.21 m for G-So.

The wall is assumed to be made onsite, and two sites are considered: (1) the first site has coordinates 38°41'31.5"N 121°30'54.8"W (near Sacramento, CA), and (2) the second site has coordinates 40°01'16.2"N 75°14'11.1"W (near Philadelphia, PA). These two locations were selected to also assess the effects of the transportation of construction materials.

To conduct the LCA, the system boundary for the study was chosen to represent a cradle-to-gate condition, which includes: (a) raw materials supply, and (b) transportation to the site. It is important to note that the separation between product (cradle-to-gate) and construction (cradle to practical completion) stages is not as distinct as in other types of construction technologies. However, since the construction stage remains consistent for all four mixtures considered in this study, and the focus is on the environmental effects of using different materials, the cradle-to-gate

comparison selected for this study is adequate for properly comparing the various investigated materials. **Table 18** provides information about the amounts of materials used per mixture to produce a wall with the factor of strength mentioned for a wall with the size of 1 m (height) × 1 m (length) and the mentioned widths. It also provides the distances from the suppliers to the construction site, which is calculated in the LCA.

Table 18. The quantity needed for the functional unit between two locations.

		Water	Sodium hydroxide	Portland cement	Fly ash F	Sand	Soil
Composition with the strength factor	C-So (kg)	71.5	15.8	0.0	109.2	0.0	207.4
	C-Sa (kg)	28.4	6.3	0.0	110.2	81.1	0.0
	G-Sa (kg)	40.3	0.0	40.3	26.9	0.0	86.0
	G-So (kg)	31.7	0.0	30.9	80.4	46.4	0.0
Composition without the strength factor	C-So (kg)	34.3	7.6	0.0	52.4	0.0	99.5
	C-Sa (kg)	24.4	5.4	0.0	94.8	69.7	0.0
	G-Sa (kg)	40.3	0.0	40.3	26.9	0.0	86.0
	G-So (kg)	31.7	0.0	30.9	80.4	46.4	0.0
Location	Sacramento, CA (km)	0.0	146.0	262.0	1368.0	37.0	0.0
	Philadelphia, PA (km)	0.0	33.0	5.5	145.0	27.0	0.0

4.5.7.2. Life Cycle Inventory (LCI)

The LCI used in this study is based on the database Tool for the Reduction and Assessment of Chemical and other Impacts (TRACI v2.1) [158]. **Table 19** provides the global warming potential (GWP) of all materials used in this study. The following subsections provide more details on the assumptions made in this study and the methods used to calculate soil excavation and transportation of the materials to the construction site.

Table 19. GWP of all materials used in LCA calculations.

Diesel combusted in industrial	Sodium hydroxide (per 1 kg)	Sand production (per 1 kg)	Electricity; at user; consumption	Portland cement (Type I/II), (per 1 kg)	Combination diesel-powered

equipment (per kg diesel used)			mix - 2022 US (per 1 MJ)		truck transport (per 1 kg-km)
3.88E+00	1.04E+00	4.89E-03	1.39E-01	9.19E-01	9.40E-05

4.5.7.3. Soil Excavation

To supply soil for the masonry production, local soil is excavated using a diesel-powered 20-metric ton excavator (model Deere 210G LC) with a fuel consumption of approximately five gallons of diesel per hour (MPG 5), equivalent to 16.2 kg h^{-1} assuming a diesel density of 0.85 kg L^{-1}. Based on consultations with industry professionals, the excavator's production rate is estimated at 25 m^3 h^{-1}. With an assumed bulk density of 1500 kg m^{-3}, this corresponds to 37500 kg of soil excavated per hour. The soil is assumed to be taken from about 1 m below the surface to minimize organic matter content; however, since this depth is typical for foundation preparation, no additional energy is assigned for digging below ground level.

To account for the environmental impacts of soil excavation, a diesel-to-soil productivity ratio was calculated to relate the mass of soil excavated to the amount of diesel combusted. The excavator's productivity corresponds to 2314.8 kg of soil per kg of diesel, derived from the ratio of 37500 kg soil h^{-1} to 16.2 kg diesel h^{-1}. Accordingly, for every kilogram of soil used in the mixtures, the diesel requirement was determined as:

$$\text{Diesel required (kg)} = \frac{\text{Soil mass (kg)}}{2314.8} \qquad \text{Eq. 3}$$

This calculated diesel mass was then multiplied by the corresponding unit impacts of diesel combustion in each environmental category to obtain the total contribution of soil excavation to the life-cycle results.

4.5.7.4. Transportation

For transportation, a heavy-duty truck with a gross vehicle weight rating of approximately 32 metric tons was assumed for transporting secondary materials, covering the distance from the supplier to the construction site. A fuel consumption of five miles per gallon (MPG) was assumed.

The energy required for transportation was subsequently calculated based on the weight of the materials. Since transporting machinery for 3D printing was considered to be similar across different mixtures, the corresponding energy consumption was excluded from the LCA calculations. Similarly, the impact of shipping materials based on the two separate locations mentioned was also calculated. The calculation included the distance multiplied by the LCI value for transporting the amount of material per specified MPG.

4.5.7.5. LCA Calculations

For the LCA calculations, the following four impact categories were selected for the LCA due to their relevance to construction materials: First, GWP (kg CO_2-eq) has been chosen since it captures greenhouse gas emissions related to climate change. TEC (MJ) reflects the total energy required across the life cycle, which is an important parameter given the high energy intensity of

activators used in geopolymer binders. Smog formation (kg SO_2-eq) has also been selected to account for pollutants that contribute to urban air quality degradation. Finally, acidification (kg SO_2-eq) measures emissions that lead to acid rain and ecosystem damage have been chosen.

After establishing the wall size with and without a strength correction factor, based on the hardened density (28-day) of each mixture, the amount of materials needed for each mixture is normalized. Based on that and the unit impact of each material, the amount of each material's impact in each mixture is then calculated. In doing so, the amount of materials needed is multiplied by their corresponding impacts for each mixture proportion. After calculating all the materials for all the mixtures with and without the strength factor, transportation is calculated based on the distances noted in **Table 18**. Finally, all the corresponding impacts of materials production and shipment are summed up and analyzed.

4.5.7.6. LCA Results

The results of the LCA (cradle-to-gate) are presented in **Table 20** and **Table 21** for two different locations of Sacramento, CA, and Philadelphia, PA, with and without the inclusion of a strength correction factor. As explained earlier, a correction factor was applied to account for the differences in mechanical performance by adjusting the wall width according to the 28-day compressive strength of each mixture. In doing so, a more realistic environmental comparison was made between mixtures that would otherwise not meet similar structural requirements.

In terms of GWP, the geopolymer mixtures continued to show the lowest emissions overall, although the relative differences between soil- and sand-based systems changed compared with the previous analysis. When the strength-correction factor was applied (as in **Table 20**), G-Sa recorded the lowest GWP in Sacramento (21.46 kg CO_2-eq), followed by G-So (31.04 kg CO_2-eq). The same trend was observed in Philadelphia, where G-Sa and G-So produced 8.64 kg CO_2-eq and 18.32 kg CO_2-eq, respectively. This finding is generally aligned with previous studies in the literature that mentioned the lower impacts of the geopolymer binding system [246], [247]. In contrast, the cement-based mixtures exhibited higher impacts, ranging from 39.94 kg CO_2-eq for C-Sa to 41.62 kg CO_2-eq for C-So in Sacramento, and from 29.90 kg CO_2-eq to 37.56 kg CO_2-eq in Philadelphia. When the strength factor was not applied (as in **Table 21**), GWP values decreased for all geopolymer mixtures, particularly G-So (14.90 kg CO_2-eq in Sacramento and 8.79 kg CO_2-eq in Philadelphia). This reduction highlights how accounting for mechanical performance can substantially alter perceived environmental benefits. For example, the geopolymer mixtures appear more sustainable on a mass basis but lose some of this advantage when normalized for strength.

For TEC, the geopolymer mixtures again exhibited higher values, particularly when the strength factor was applied. In Sacramento, G-So consumed the highest energy content (828.14 MJ), followed by G-Sa (450.88 MJ). A similar pattern appeared in Philadelphia, where G-So required 659.26 MJ and G-Sa 280.68 MJ. These elevated energy values reflect the energy-intensive production of sodium hydroxide, which dominates the embodied energy of alkali-activated systems [106], [248]. By contrast, cement-based mixtures required substantially less energy, ranging from 159.28 MJ to 292.58 MJ across both locations. When the strength factor was omitted, the same overall pattern persisted, but with lower absolute values. For example, G-So

decreased to 397.51 MJ and G-Sa to 387.76 MJ in Sacramento, while C-Sa and C-So remained nearly unchanged (292.58 MJ and 242.42 MJ, respectively).

Regarding smog formation and acidification, geopolymer mixtures again showed higher sensitivity to the strength correction. In Sacramento, the acidification impact of G-So increased from 0.10 kg SO_2-eq (for non-normalized) to 0.21 kg SO_2-eq (when normalized per strength), while smog emissions rose from 1.61 kg SO_2-eq to 3.35 kg SO_2-eq. Similar trends occurred in Philadelphia, where G-So increased from 0.07 kg SO_2-eq to 0.15 kg SO_2-eq in acidification and from 0.60 kg SO_2-eq to 1.26 kg SO_2-eq in smog formation after strength adjustment. The cement-based mixtures showed smaller differences between the two conditions, remaining within 0.09–0.11 kg SO_2-eq for acidification and 2.11–2.86 kg SO_2-eq for smog in Sacramento. Regional differences also remained evident. For example, Philadelphia consistently produced lower impact values due to shorter transportation distances and smaller transportation-related energy burdens. It's interesting to note that the differences in values between regions highlight the role of location in LCA analyses and their subsequent interpretation. Similar conclusions are also made by [249]. However, when comparing mixtures primarily by the filler type (without strength correction), soil-based mixtures generally performed slightly better environmentally than their sand-based counterparts in most categories. For instance, C-So recorded lower energy use (242.42 MJ) and lower acidification (0.09 kg SO_2-eq) than C-Sa (292.58 MJ and 0.11 kg SO_2-eq, respectively). Similarly, G-So exhibited lower smog formation (1.61 kg SO_2-eq) than G-Sa (2.34 kg SO_2-eq), although it had marginally higher energy use. However, once the strength factor was applied, this pattern changed, with the lower compressive strength of soil-based mixtures requiring greater material quantities to meet equivalent structural performance, thereby increasing their overall

environmental impact. This reversal underscores the importance of incorporating mechanical performance into sustainability evaluations. Simply selecting a material with lower embodied impacts per kilogram does not necessarily yield a more sustainable printing process. Instead, the true environmental performance depends on the combination of material formulation, mechanical efficiency, and printing yield.

In general, the results demonstrate that geopolymer binders can substantially reduce GWP compared with cement-based systems; however, these reductions are accompanied by trade-offs in total energy consumption and smog-related impacts due to the energy-intensive production of alkali activators. Similarly, soil-based fillers help lower impacts in certain categories, such as energy use and acidification, but tend to lose this advantage once results are normalized for strength. These shifts, driven by binder type, transportation distances, and filler selection, emphasize that sustainability in 3D-printed materials cannot be evaluated solely on the basis of low-impact ingredients. Instead, the actual quantity of material required to achieve a given performance level must also be considered, as mixtures with lower embodied emissions may still yield higher overall impacts when strength or buildability limitations are accounted for. Consequently, sustainability assessments should be grounded in performance-based LCA, where mixture optimization considers not only environmental metrics but also mechanical behavior, rheological performance, and region-specific supply chain conditions.

Table 20. Result of LCA per functional unit of 1 m (height) × 1 m (length) wall with a variable width (per strength) on the two different locations with the strength-normalization factor.

	Location 1 (Sacramento, CA)				**Location 2 (Philadelphia, PA)**			
Impacts	**C-Sa**	**C-So**	**G-Sa**	**G-So**	**C-Sa**	**C-So**	**G-Sa**	**G-So**

GWP (kg CO_2 eq per compressive strength of 15 MPa)	39.94	41.62	21.46	31.04	29.90	37.56	8.64	18.32
TEC (MJ per compressive strength of 15 MPa)	292.58	242.42	450.88	828.14	159.28	188.5	280.68	659.26
Smog formation (kg SO_2 eq per compressive strength of 15 MPa)	2.86	2.11	2.73	3.35	1.22	1.45	0.62	1.26
Acidification (kg SO_2 eq per compressive strength of 15 MPa)	0.11	0.09	0.13	0.21	0.06	0.07	0.07	0.15

Table 21. Result of LCA per functional unit of 1 m (height) × 1 m (length) wall with a width of 0.1 m on the two different locations without the strength-normalization factor.

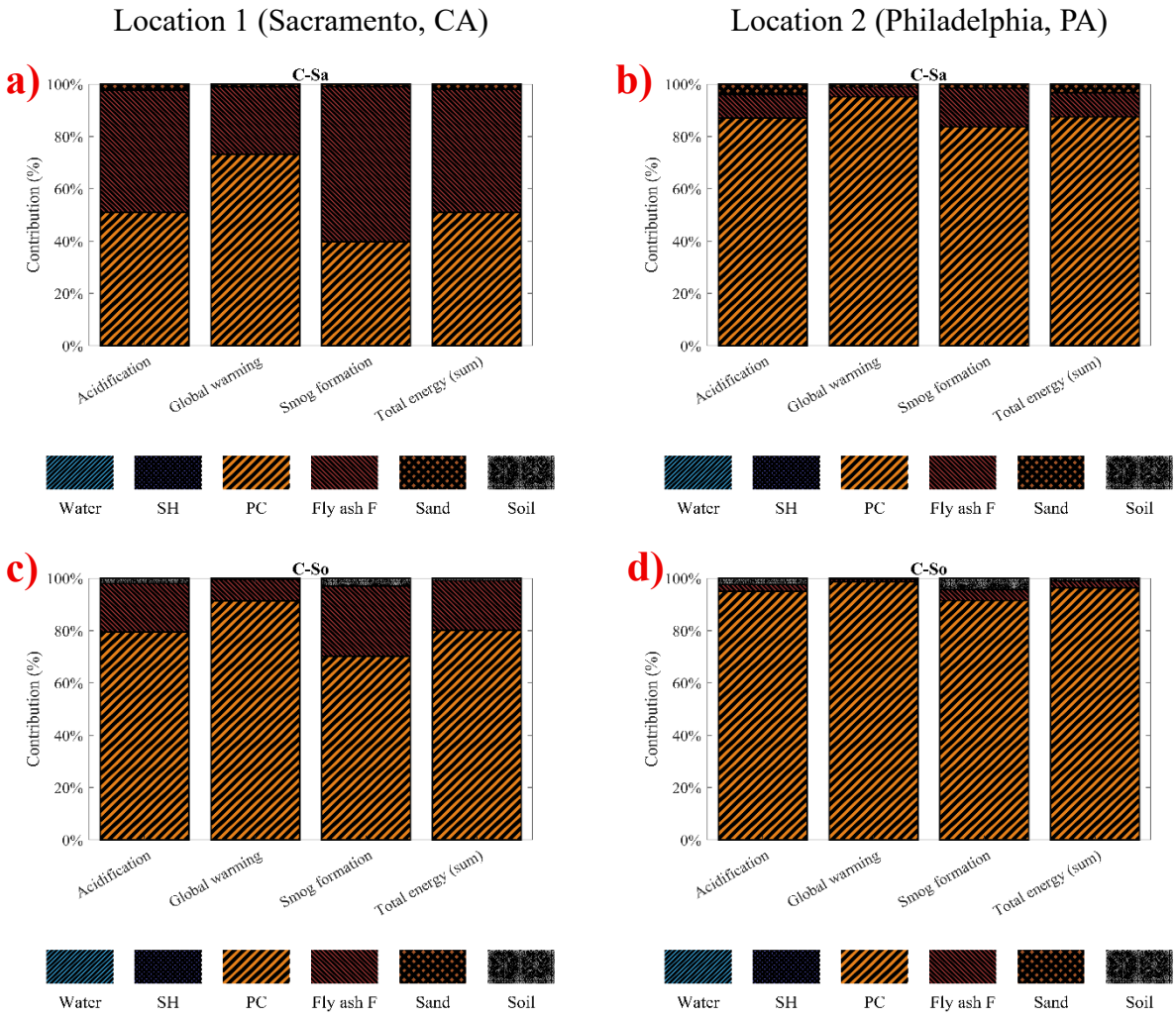
	Location 1 (Sacramento, CA)				**Location 2 (Philadelphia, PA)**			
Impacts	**C-Sa**	**C-So**	**G-Sa**	**G-So**	**C-Sa**	**C-So**	**G-Sa**	**G-So**
GWP (kg CO_2 eq)	39.94	41.62	18.46	14.90	29.90	37.56	7.43	8.79
TEC (MJ)	292.58	242.42	387.76	397.51	159.28	188.50	241.38	316.45
Smog formation (kg SO_2 eq)	2.86	2.11	2.34	1.61	1.22	1.45	0.54	0.60
Acidification (kg SO_2 eq)	0.11	0.09	0.11	0.10	0.06	0.07	0.06	0.07

Figure 25 presents the component-level contributions to environmental impacts for each of the four mixtures across two locations of Sacramento, CA, and Philadelphia, PA. The environmental impacts of the cement-based mixtures (i.e., C-Sa and C-So), are largely governed by their Portland cement content, which remains the dominant contributor across all impact categories. In the case of C-Sa, shown in **Figure 25** (a) and (b), Portland cement and fly ash together account for over 80% of the total environmental impacts in nearly all categories, especially in GWP and total energy use. Other components, such as water and sand, play a minor role in the impacts, with less than 10% in all cases. C-So, on the other hand, shows a similar minor dominance of fly ash but higher impacts of Portland cement, particularly in acidification and smog formation categories. In terms of locations, similar to the C-Sa case, C-So has a higher impact of fly ash particles when the construction site is considered to be in Sacramento, due to a longer distance of fly ash particles to the construction site.

In the geopolymer mixtures, G-Sa (**Figure 25** (e) and (f)) shows a major shift in environmental contributions. With no Portland cement present, the mixture relies heavily on fly ash and sodium hydroxide. The higher fly ash content in G-Sa, compared to G-So, results in an even larger share of impacts from this material, especially in the GWP and total energy categories. The effect of location is also clear, that the fly ash contribution is considerable in Sacramento due to the longer transport distance compared to Philadelphia. The longer distance is also seen to overshadow the overall effect of sodium hydroxide (comparing **Figure 25** (e) to (f)).

Finally, G-So, presented in **Figure 25** (a) and (b) has a similar composition to G-Sa, but with slightly lower fly ash content and slightly higher contribution from soil. In both locations, sodium

hydroxide consistently emerges as the dominant contributor, followed by fly ash and soil. However, due to the longer transportation distance of fly ash to Sacramento, its contribution is noticeably higher there as well, particularly in total energy and GWP warming categories. These results confirm that in alkali-activated systems, sodium hydroxide and fly ash remain the largest environmental contributors, while for Portland cement-based binders, it is the Portland cement and fly ash (due to the long transportation distance).



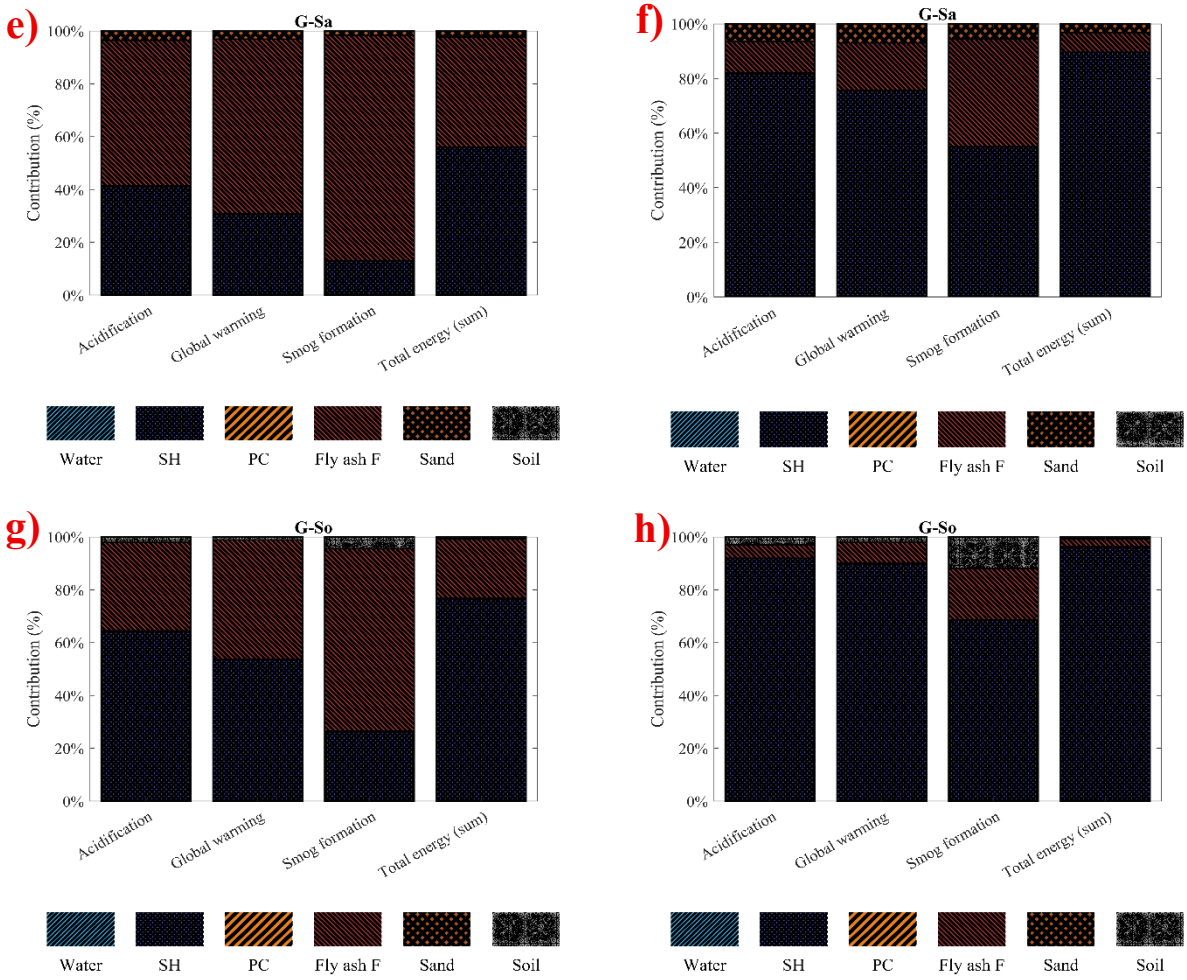


Figure 25. Comparison of the relative contributions from different components to the different environmental impact categories with (a) C-Sa in Sacramento, (b) C-Sa in Philadelphia, (c) C-So in Sacramento, (d) C-So in Philadelphia, (e) G-Sa in Sacramento, (f) G-Sa in Philadelphia, (g) G-So in Sacramento, and (h) G-So in Philadelphia.

4.6. Conclusion

This study evaluates the performance of 3D-printed mixtures in terms of hardened properties and sustainability by combining two strategies: (a) replacing Ordinary Portland Cement with alkali-activated binders, and (b) replacing sieved sand with locally available natural soil (low plasticity silt). In doing so, four different mixtures were developed using two binder types (cement

and geopolymer), and two filler types (sand and soil). All mixtures were then collected from freshly printed parts and cured until tested. A cradle-to-gate LCA has also been conducted to compare the impacts of different mixtures. Based on the results and analysis, the following conclusions can be drawn:

- SEM images of 28-day cured samples, at both low (80×) and high (3500×) magnifications, showed that cement-based mixtures, especially C-Sa, formed denser microstructures with better hydration products and fewer unreacted particles. C-So also showed a compact structure, despite having more irregularity due to the inclusion of natural soil. In contrast, geopolymer-based mixtures, especially G-So, showed more visible cracks, larger micro-voids, and a higher number of unreacted fly ash particles. These differences help explain the lower mechanical strengths and higher porosity seen in geopolymer samples. In addition to the SEM, XRF results confirmed the chemical differences seen in the microstructure. For instance, geopolymer samples were found to have a substantially higher Na_2O content (G-Sa: 4.26%, G-So: 7.49%) compared to the cement-based mixtures (with C-Sa having 0.69%, and C-So having 0.60%). C-So and G-So also showed higher Fe_2O_3 and SiO_2 contents, consistent with the natural mineralogy of the soil used. Geopolymer mixtures, especially in G-So, are found to have a high alkali content that may pose durability risks in the long term.

- Results of slump, air content, fresh density, pH, and salinity revealed statistically significant differences between binders and fillers. Cement-based mixtures showed greater

flowability (e.g., C-Sa: 129.0 ± 1.6 mm vs. C-So: 110.0 ± 1.9 mm, $p = 0.0079$) and higher fresh densities (C-So: 1914.9 ± 0.9 kg/m³) compared to geopolymer-based mixtures (G-Sa: 1849.0 ± 1.0 kg/m³, $p = 0.0079$), with sand-based mixtures consistently producing higher slump than soil-based ones ($p = 0.0002$). Geopolymer mixtures also showed significantly higher air content (G-Sa: 6.04 ± 0.11%, vs. C-So: 4.50 ± 0.23%, $p = 0.0079$) and substantially greater salinity (G-So: 32.87 ± 2.58 ppt vs. C-Sa: 1.95 ± 0.04 ppt, $p = 0.0079$). These trends are likely tied to finer particle grading in soil and the presence of sodium hydroxide in geopolymer systems. The effect of filler on pH was not statistically significant ($p = 1.0000$), but geopolymer mixture overall had slightly lower pH and more porous fresh structures. The data confirm that both binder type and filler type play a measurable role in shaping fresh mixture behavior.

- The result of the penetrometer test shows that all mixtures showed low initial penetration resistance (~0.14 to 0.28 MPa at 25 minutes), confirming a specific region or relationship where the force and time of all mixtures almost match. This region is believed to be the printability region, referring to a specific rheological parameter that must be met for a mixture to be printable. However, strength gain rates varied significantly. C-So hardened the fastest, reaching 21.65 MPa at 600 minutes, followed by C-Sa at 13.21 MPa. Geopolymer mixtures showed much slower development, with G-Sa and G-So reaching only 1.27 MPa and 3.51 MPa, respectively, after 600 minutes from mixing. These differences are linked to the binder type, with Portland cement-based systems developing early buildability more rapidly (e.g., C-So reached 3.44 MPa in ~350 min vs. G-So at ~600 min). The soil's finer particles likely accelerated stiffening in cement-based mixtures.

Similarly, soil-based samples (C-So and G-So) reached 3.44 MPa at 350 and 600 minutes, respectively, while their sand-based counterparts (C-Sa and G-Sa) took longer, at approximately 500 minutes for C-Sa and did not reach within 600 minutes for G-Sa.

- With regards to the water absorption test, when binder types were averaged, cement-based samples (C-Sa and C-So) had a significantly lower average water absorption of $9.1 \pm 1.40\%$ compared to geopolymer-based mixtures (G-Sa and G-So) at $13.2 \pm 3.05\%$ ($p = 0.0027$). Among all mixtures, G-So recorded the highest absorption at $16.04 \pm 0.36\%$, while C-So had the lowest $7.90 \pm 0.22\%$. These trends show and align with previous findings on the porous nature of geopolymer binders. COV analysis also indicated higher variability in soil-based mixtures (e.g., COV = 0.102 for C-Sa, and 0.027 for C-So), suggesting that natural soil contributed to more to a heterogeneous moisture uptake across specimens.

- In terms of mechanical properties, cement-based mixtures demonstrated significantly faster and higher early-age strength development than geopolymer mixtures. For instance, at 7 days, C-So and C-Sa recorded strengths of 13.57 ± 1.81 MPa and 13.52 ± 1.67 MPa, respectively, whereas G-Sa and G-So reached only 3.17 ± 0.56 MPa and 2.60 ± 0.46 MPa. All pairwise comparisons between cement- and geopolymer-based mixtures were statistically significant (with $p = 0.0079$). At 28 and 91 days, G-Sa showed steady improvement, reaching 13.86 ± 3.05 MPa and 16.23 ± 1.66 MPa, respectively, while G-So remained lower at 6.70 ± 0.66 MPa and 11.50 ± 2.40 MPa. Soil-cement (C-So) outperformed all other mixtures at 91 days with 20.32 ± 2.26 MPa, its difference with G-

Sa was statistically significant ($p = 0.0317$), showing the long-term strength advantage of soil-cement mixtures. Accordingly, it is concluded that Portland cement-based systems hydrate more rapidly than their geopolymer counterparts. In terms of anisotropic behavior, C-Sa, C-So, and G-Sa performed similarly in the printing direction (15.12–15.80 MPa), while G-So recorded much lower strength (6.48 ± 0.94 MPa, $p = 0.0079$ vs. all others). Similar trends were observed in the perpendicular direction, with C-Sa (12.50 ± 1.46 MPa), C-So (11.52 ± 1.60 MPa), and G-Sa (11.46 ± 1.24 MPa) performing significantly better than G-So (5.94 ± 0.94 MPa, $p = 0.0079$). These results show that the heterogeneity introduced by soil does not lead to better hydration, at least in the geopolymer binding system used in this study. Similar results are documented for splitting tensile and interlayer shear strength, both of which support the conclusions made about the compressive strength values.

- The results of the cradle-to-gate life cycle assessment (LCA) revealed that environmental performance was governed not only by mixture composition but also by the mechanical strength of the printed components. When a strength-based correction factor was applied to account for equivalent structural performance, the apparent advantages of soil-based mixtures were substantially reduced. For example, although G-So initially showed lower impacts in some categories, its lower compressive strength necessitated greater material use, leading to higher global warming potential (GWP) and total energy consumption (TEC) after normalization. In contrast, sand-based geopolymer mixtures, particularly G-Sa, demonstrated consistently lower GWP values (e.g., 8.64 kg CO_2-eq in Philadelphia and 21.46 kg CO_2-eq in Sacramento with strength correction), making them more favorable

when both mechanical and environmental criteria are considered. The assessment also confirmed that the production of sodium hydroxide remains the dominant contributor to the high energy demand of geopolymer systems. Overall, these findings highlight that mixture selection for sustainable 3D-printed construction should not be based solely on material composition or embodied impacts. Instead, sustainability must be evaluated on a performance-adjusted basis, incorporating mechanical strength, printability, and regional supply-chain conditions to accurately reflect real-world construction scenarios.

5. Effects of Specimen Preparation on Mechanical Properties of 3D-Printed Cementitious Materials

3D printing of cementitious materials is a novel method for producing concrete components using a semi-automated system that avoids formwork. Despite benefits, the mechanical properties of 3D-printed concrete vary widely across studies, often due to a lack of available standards, inconsistent specimen preparation, or testing procedures. In this study, the effect of fabrication methods on mechanical properties are studied. More than 670 cylindrical and cubic specimens were produced using two cement-based mixtures, one with soil-based (C-So) and another sand-based (C-Sa), representing two main fillers used in the literature. Cylindrical and cubic samples were made from freshly 3D-printed parts and mold cast specimen. Samples were cored, cut to size (cubes only), rodded, vibrated (15s and 30s), and tested for water absorption, compressive and splitting tensile strength, modulus of elasticity, and scanning electron microscopy (SEM). Advanced statistical analyses are also performed to determine whether the differences in results originate from material behavior or the production process. Results show significant differences among each fabrication type, with a maximum difference of 29.1% (C-So) and 46.3% (C-Sa) for cubes, and 109% (C-So) and 136% (C-Sa) for cylinders (28-day compressive strength). Similar variabilities were recorded across different tests per fabrication methods, pointing to the nature of 3D printing mixtures, requiring significant buildability (compared to conventional mold-cast mixture designs and samples), resulting in difficulty to properly compact and extract samples. Results strongly suggest freshly coring and cutting-to-size (from cured sections) are the most reliable fabrication methods from 3D-printed specimens with most $p < 0.05$.

5.1. Introduction

Additive manufacturing, also known as 3D printing, originated in the 1980s and 1990s as a method to streamline the fabrication of complex components [250], [251]. Unlike traditional methods, such as mold casting or machining, 3D printing builds objects layer by layer, which removes the need for extensive programming, detailed planning, or post-processing [251], [252]. In the last twenty years, 3D printing has made its way into the construction sector, with initial concepts and systems developed by Khoshnevis et al. during the late 1990s and early 2000s [253], [254], [255], [256]. Today, most 3D printing applications in the construction industry rely on extrusion-based techniques whereby the material is extruded through a nozzle [257]. In cementitious materials, extrusion-based 3D printing offers several benefits. First, it avoids the need for formwork, which can take both time and be costly. Second, it reduces waste by only mixing the materials needed, and finally, it allows for a semi- to fully- automated construction process [195], [258]. Another major benefit of 3D printing is its ability to create non-standard geometries, which has led to many successful early trials, ranging from bridge decks [259], [260] to residential buildings [261]. Some studies have taken this even further, introducing integrated systems for the reinforcement of 3D-printed components [262] and even drone-based 3D printing of cementitious materials [263].

Despite these advances, the unique characteristics of the printing process (i.e., layer-by-layer fabrication) present several challenges. First, a successful printing process requires strict control of rheological and morphological properties [264], [265], such as water-to-binder ratio, aggregate-to-binder, and fly ash-to-binder ratios, as well as fresh-state parameters [258], [266]. Second, once the printed part is hardened, it generally exhibits directional mechanical behavior due to interlayer

porosity and weak bonding between layers [242], [267], [268]. This anisotropic behavior can significantly affect the overall structural performance, yet it remains difficult to fully quantify due to a lack of standardized testing protocols. International Organization for Standardization and American Society for Testing and Materials (ISO/ASTM 52903-20 parts one and two) [269], [270], ISO/ASTM 52901-16 [271], and ISO/ASTM 52939-23 [272] are early attempts to standardize testing for 3D-printed materials, by providing guidance (mostly qualitatively) on specimen preparation and mechanical property evaluation. Specifically, ISO/ASTM 52939-23 [272] was introduced to establish qualification principles for structural and infrastructure components produced by additive manufacturing in construction. The information provided, however, is preliminary concepts regarding 3D printing structures rather than the implementation of major qualitative or quantitative measures. This lack of quantitative measures creates the need for the gradual development of methodologies and testing procedures specific to the 3D printing of cementitious materials. Yet, as highlighted by several researchers [273], [274], [275], the field still lacks a basic consensus on acceptable mechanical performance and testing procedures, print-induced variability, and representative sample selection for quality assessment.

To better understand and compare the mechanical properties of 3D-printed materials, more robust sampling and testing procedures must be developed. This need for a standardized sampling and testing procedure is evident in the many attempts made in this area. Kaliyavaradhan et al. (2022) [273] provided a review of experimental tests reported in the literature, highlighting the need for enhanced standardization of testing protocols for hardened-state properties. The study highlights that most prior work in the literature has focused on fresh property tests due to specific printing requirements and the difficulty in reproducing the mechanical tests. Among those that

have focused on mechanical properties, different sampling methods are used. For example, Kruger et al. (2021) [276], Zhang et al. (2020) [277], and Alanazi et al. (2022) [278] are among the many examples of authors who have saw-cut their specimens from a 3D-printed component. Some others, however, have printed specimens inside molds, such as [86]. The problem with cutting samples (or extracting from larger samples) is the large size variation that can result from human error. Similarly, printing the entire sample can cause precision issues since 3D-printed layers often do not develop high strength and can deform when more layers are printed on top. This can cause significant warping and deformation, leading to a semi-triangular shape, as reported by [279]. The same can be discussed regarding printing specimens inside molds, as it negates the major benefit of 3D printing: removing formwork.

Others, such as Aramburu et al., 2022 [280], Peng et al., 2015 [281], and Casagrande et al., 2020 [282] have printed samples similar to mold-cast sizes and tested them after curing. One argument against such methods is that in such studies, the authors have used a smaller printer with a smaller nozzle that would not likely be used for printing an actual structural component or a house wall.

Van Den Heever et al., 2022 [268] cored samples from a larger print and evaluated their properties for porosity and mechanical properties. Other authors, such as Ma et al. (2024) [283], Salet et al., 2018 [259] that printed larger sections and tested them for their intended purposes to avoid any variabilities caused by the sampling discrepancies. Another technique used is non-destructive tests, such as the one proposed by Wolfs et al. (2018) [284] to use ultrasonic tests and compare it to early age 3D-printed concrete. However, that would still not address the issue at

hand, which is needing a standard benchmark (fabrication method) and quality control (or testing procedure) for the hardened properties of 3D-printed components. Sikora et al. (2022) [285] compared the results of mold-cast specimen with those of 3D printed and cut-to-size samples. The results of 28-day compressive strength showed that printed specimen could reach a strength range of ~70-76 MPa, while mold cast specimen reached ~92 MPa. The authors also mentioned that some of the differences among a sample set could have been caused during the cutting process of specimens, which results in potential micro-cracking and imperfections.

Given the vast methodologies and techniques used in the works of literature, some authors have attempted to establish benchmarks and quality control systems for 3D-printed concrete, with focus, however, on fresh-state evaluation. Buswell et al. 2022 [275], Rehman et al., 2023 [286], Mortada et al. (2022) [287] all proposed different frameworks and methodologies (again mostly qualitative) to address the variabilities and provide a direct comparison for the performance of 3D-printed components.

As a result, a clear gap remains in understanding how specimen preparation and sampling methods influence the hardened mechanical properties of 3D-printed cementitious materials. Since these properties are sensitive to factors, such as anisotropy, compaction, and porosity, quantifying their variability can offer significant insights, especially in future standardization of 3D-printed components. As a result, this study addresses this gap by quantifying, both mechanically and statistically, the effects of manufacturing methods on the mechanical performance of 3D-printed cementitious components, using standardized sample sizes, paired comparisons, and p-values to highlight statistically significant differences.

5.1.1. Novelty and Relevance

This study has three main research questions to respond to. First, it investigates how different specimen preparation methods influence the mechanical properties of 3D-printed cementitious materials. The sampling methods considered include (a) cored, (b) mold-cast rodded (hereinafter rodded), (c) mold-cast vibrated (for 15s and 30s), and (d) cut-to-size, which were selected based on practices reported in the literature as well as the authors' previous experience. Quantifying the variations resulting from the sampling methodologies is a major step toward standardizing the testing protocols for 3D-printed concrete.

Second, the study examines how these sampling-induced variations differ between soil-based and sand-based mixture compositions. These two material systems were selected because current industry efforts are largely split between optimizing sand-based [288] and soil-based [289] printable concretes. Understanding how each would respond to different preparation methods can provide critical insight into their performance and potential for broader applications. Third, this work addresses the main differences between 3D-printed materials and those produced using conventional construction practices. These distinctions are discussed in depth in the final section, with a focus on how the unique processing conditions of 3D printing affect the hardened-state properties.

Additionally, the significance of this study lies in its support for future efforts to establish standardized testing protocols, ultimately guiding the design codes specifically crafted for additive manufacturing in construction.

5.2. Materials

The following subsections discuss the material properties used in this study.

5.2.1. Soil

The natural soil used in this study was sourced from Ace Hardware in Davis, California. It was reported that, to reduce organic content, the soil was extracted from subsurface layers several meters below ground level. The soil was then mechanically sieved using a TS-1 Gilson shaker to achieve a maximum particle size of 1.18 mm (No. 16 sieve), per ASTM C136-14 [132]. The coarser materials were discarded. The size of 1.18 had been chosen by the authors based on trials conducted on the mixtures and the printer used to produce components in this study. Following sieving, the materials were oven-dried at 110°C for 24 hours to minimize residual moisture and remove any organic content. The materials were then placed in a sealed dry bucket until used. The temperature was adopted per ASTM C136-14 [133] and ASTM D2216-19 [134]. Additional characterization, including particle size distribution, Atterberg limits, and compaction behavior (Proctor test), is presented in **Table 22**. Based on these results and classification under ASTM D2487-11 [135] and Unified Soil Classification System, the soil was identified as a low-plasticity silt (ML). In this study, sieve analysis was conducted in accordance with ASTM C117/C136 to characterize soil and sand, and the soil was washed per ASTM D6913-17 [136]. The original dry mass of the sample was 1336.30 g, and the wash mass was 521.90 g, resulting in a wash loss of 60.9%.

Table 22. Physical properties of soil and sand.

Laboratory tests	Standards	Property	Value	
			Soil	Sand
Particle-size analysis	ASTM C117-17 [137] , C136-14 [132], D6913-17 [136]	Cumulative % Retained #4 (4.75mm)	0.0	0.0
		Cumulative % Retained #4 (4.75mm)	0.0	0.0
		Cumulative % Retained #8 (2.36mm)	0.0	0.0
		Cumulative % Retained #10 (2mm)	0.0	0.7
		Cumulative % Retained #16 (1.18mm)	8.2	43.5
		Cumulative % Retained #30 (0.6mm)	14.0	65.5
		Cumulative % Retained #40 (0.425mm)	19.0	80.8
		Cumulative % Retained #50 (0.3mm)	29.4	96.2
		Cumulative % Retained #100 (0.15mm)	38.1	99.1
		Cumulative % Retained #200 (75µm)	100.0	100.0
		Pan	20.8	–
Atterberg limits	ASTM D4318-10 [138]	Liquid limit LL (%)	13.9	–
		Plastic limit PL (%)	6.8	–
Soil compaction tests	ASTM D698-21 [139]	Plasticity index PI (%)	13.0	–
		Optimum moisture content (%)	1873.3	2610.8

5.2.2. Fly ash and Portland Cement

The coal fly ash class F used in this study was supplied by Paragon-Aggregate Products Corp. in Glendale, Arizona. The Portland cement used in this study was acquired from the Nevada Cement group, located in Reno, Nevada. The result of the mill certificate is presented in **Table 23**.

To ensure that the composition of fly ash and soil is recorded, X-ray fluorescence (XRF) analysis of the cementitious materials was conducted using a Rigaku model Super mini-200, and then analyzed using the manufacturer's provided software, ZSX. The method of calculating the oxides was recommended by the manufacturer [141], which is a semi-quantitative XRF (also called SQX). The XRF results are presented in **Table 24**.

Table 23. The result of mill certificate provided by Nevada Cement, Inc.

Phase composition	Percent content (%)
Tricalcium silicate (C_3S)	58
Dicalcium silicate (C_2S)	18
Tricalcium aluminate (C_3A)	7
Tetracalcium aluminoferrite (C_4AF)	9

Table 24. Compositions of supplementary cementitious materials and soil filler used in this study, according to XRF analyses

Chemical compounds	Fly ash (F)	Soil (low plasticity silt)
SiO_2 (%)	58.9	60.5
Al_2O_3 (%)	17.4	12.0
Fe_2O_3 (%)	8.2	6.1
CaO (%)	7.0	3.2
MgO (%)	1.2	2.0
SO_3 (%)	0.8	0.5
Na_2O (%)	1.0	0.8
K_2O (%)	3.5	1.5
LOI (%)	1.5	8.1

5.2.3. Mixing Water

The mixing water was sourced locally from Davis, California, with a pH of 8.66, a salinity of 0.19 ppt, and a total dissolved solids (TDS) concentration of 270 mg/L.

5.3. 3D Printer

A Scara Elite 3D printer from 3D Potter's Inc., located in Palm City, FL, was used in this study. The 3D printer had a nozzle with a circular diameter of 50.8 mm and operated based on an auger system with a constant printing speed of 15 mm/s. **Figure 26** shows the printer and a soil-cement composite made during the study.



Figure 26. (a) Scara Elite Printer in operation and (b) a printed sample.

5.4. Mixtures and Methods

The following subsections discuss the mixture proportions selected for this study and the tests conducted.

5.4.1. Mixture Proportions

In this study, two mixtures, one soil-based (C-So) and one sand-based (C-Sa), were produced to evaluate the influence of filler type on the printability, strength, and sustainability of 3D-printed cementitious mortars. While both mixtures incorporate ordinary Portland cement as a binder, the C-Sa mixture also includes a larger mass of fly ash to achieve a comparable water demand and workability to that of the soil-based system. This adjustment was necessary because sand, being more angular and less cohesive than soil, required additional fines to improve print stability and reduce segregation during extrusion. Thus, fly ash was incorporated not as a variable of study but as a binder-balancing component to maintain equivalent printability between the two filler systems.

The design intent, therefore, was not to directly compare identical binder chemistries but to ensure comparable rheological performance between mixtures so that the effects of filler type (soil versus sand) could be isolated as much as possible. **Table 25** summarizes the mixture proportions adopted in this study. The names of each mixture consist of three letters. Letter “C” refers to the use of Portland cement, followed by an acronym indicating the primary filler, with “So” referring to soil and “Sa” to sand. Accordingly, C-So refers to the cement-soil mixture, while C-Sa represents its cement-sand counterpart.

Table 25. Mixture proportions used for 3D printing expressed per standardized 1000 grams

Mixture name	Water	PC*	Fly ash F	Sand	Soil
C-So	208.3	208.3	138.9	0.0	444.4
C-Sa	167.4	163.3	424.5	244.9	0.0

*PC: ordinary Portland cement type I/II.

5.4.2. Specimen Preparation and Testing Matrix

In this study, multiple batches of material, each weighing approximately 6-7 kg, were mixed sequentially and loaded into the printer's funnel. This process was repeated until a sufficient number of layers were extruded to produce specimens. From each printed element, cylindrical (100 × 200 mm) and cubic (50 × 50 × 50 mm) specimens were produced. Cylindrical samples were cored directly from freshly printed mortar using lubricated plexiglass tubes, which were cut to size and inserted into the extruded layers. All cored specimens were extracted from the same printed geometry of a straight wall measuring approximately 610 mm in length and 51 mm in thickness. Print quality was visually inspected before each coring operation to ensure consistency.

Mold-cast cubes (rodded and vibrated) were prepared in accordance with ASTM C109-16 [148], while mold-cast cylinders were prepared per ASTM C31-19 [290], using rodding (25 strokes per layer). Vibrated specimens were subjected to mechanical vibration on a standard shake table for two durations of 15 seconds or 30 seconds. All specimens, regardless of preparation method, were left in molds for 48 hours before demolding. This curing duration was chosen based on the authors' prior experience to prevent damage to 3D-printed specimens. Error! Reference source not found.**Figure 27** shows the fresh-state coring process used to obtain cylindrical and cubic specimens directly from the printed elements. In this process, a bottomless cylindrical or cubic mold was gently pressed into the freshly printed filament to extract material of the desired

geometry without disturbing its layered structure. It is important to note that the term coring used here follows the notation commonly used in literature (e.g., [291], [292], [293] for the process described above.

Cut-to-size specimens were extracted from a 3D-printed wall with a dimension of 610 (L) × 120 (H) × 300 mm (D) after 28 days of curing. The cutting was performed with a dry saw-cutter with a cutter blade width of 3.5 mm, with no water or other lubricants was used in the cutting process to maintain a fair comparison with other methods.

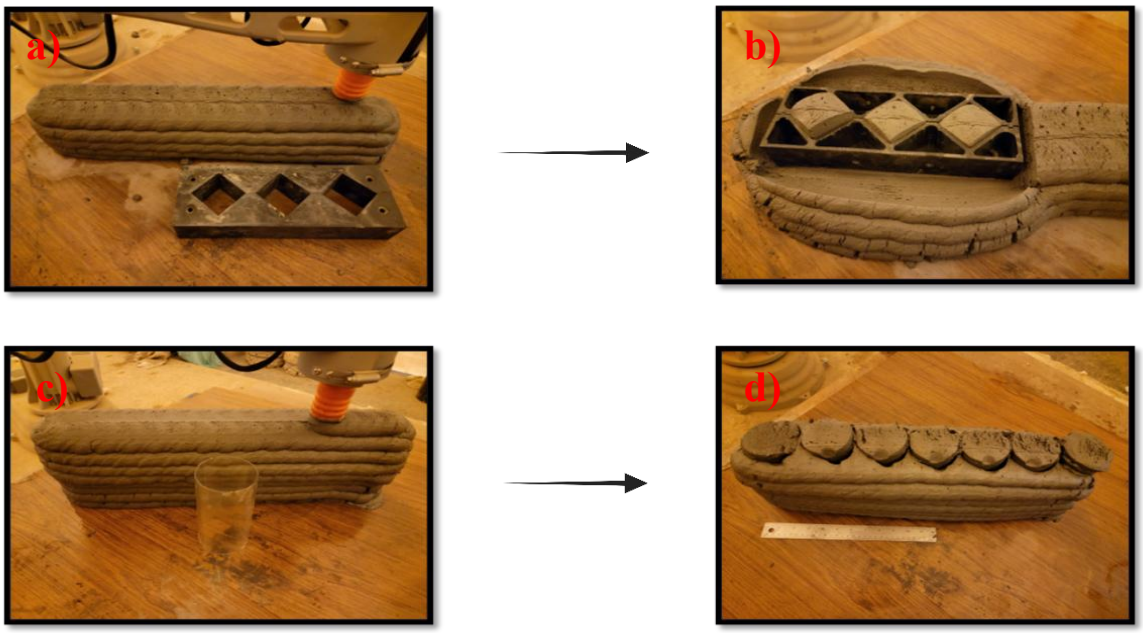


Figure 27. The coring procedure used to extract samples from freshly printed elements with (a) and (b) coring of cubic specimens, while (c) and (d) coring of cylindrical specimens.

Table 26 Table 26. Tests conducted and the standards that followedsummarizes the testing matrix used in this study, including the standard followed and the specimen curing age tested. The approximate number of samples produced is also noted in the table. Since the study was focused

on evaluating the effects of specimen preparation based on the mechanical and physical properties, it included compressive strength (ASTM C109-16 [148] for cubes and ASTM C39-05 [294] for cylinders), water absorption (ASTM C20-10 [145]), modulus of elasticity (ASTM C469-14 [295]), and splitting tensile strength (ASTM C496-08 [296]).

Cubic specimens with a size of 50×50×50 mm were used for absorption testing and as part of the compressive strength tests. Cylindrical specimens 76.2×152.4 mm were used for the other part of compressive strength, modulus of elasticity, and splitting tensile strength. For compressive strength testing, both cubes and cylinders were prepared and tested in accordance with the relevant ASTM standards (C109 and C39, respectively), using standard capping procedures and alignment practices to ensure uniform load application and prevent end restraint effects.

Sample preparation methods included coring from freshly printed elements, mold-casting by rodding, and vibration for both 15 and 30 seconds. Cut-to-size preparation was also included for cubes only due to the difficulty of cutting cylinders from a hardened specimen. Compressive strength was evaluated at six curing ages of 3, 7, 14, 28, 56, and 91 days, while all other properties were tested at a standard 28 days after printing.

To ensure statistical reliability, a minimum of five samples were cured and tested for each condition or testing duration mentioned. Throughout the research, the same equipment and trained personnel were used in all stages of material fabrication to testing, in order to reduce variability. During the curing stage, all samples were kept in their molds for the first 48 hours to prevent damage during demolding and to allow adequate strength development. After demolding,

specimens were stored in the laboratory under the same ambient conditions (≈25 ± 5 °C and 40 ± 10% relative humidity) until the designated testing ages (7, 14, 28, 56, and 91 days). This ensured consistent curing throughout the testing period while replicating realistic environmental exposure for 3D-printed and cast specimens.

Table 26. Tests conducted and the standards that followed.

Information	Absorption	Compressive strength	Modulus of elasticity	Splitting tensile strength
Standard	ASTM C20-10 [145]	ASTM C109-16 [148] and ASTM C39-05 [294]	ASTM C469-14 [295]	ASTM C496-08 [296]
Shape	Cube	Cube and cylinder	Cylinder	Cylinder
Preparation	Cored, rodded, vibrated 15s, vibrated 30s, and cut-to-size	Cored, rodded, vibrated 15s, vibrated 30s, (and cut-to-size for cubes only)	Cored, rodded, vibrated 15s, vibrated 30s	Cored, rodded, vibrated 15s, vibrated 30s
Time (days)	28	3, 7, 14, 28, 56, 91	28	28
Number of samples tested	50	540	40	40

5.4.3. Statistical Analysis, Quality Assurance, and Quality Control

In the present study, a two-level statistical analysis is conducted to (a) verify the results and (b) ensure valid comparisons are made. For each mechanical property and curing age, a minimum of five data points were acquired from the tests, and their standard deviation (STD) and coefficient

of variation were calculated. These values are reported throughout the study to ensure statistical reliability.

In addition to basic statistical analyses, two advanced analyses were also conducted on all data, including: (a) a two-way ANOVA, and (b) a pairwise comparison analysis. The two-way ANOVA test was used to assess the main effects of the two mixture types (i.e., C-So and C-Sa) and the five sampling methods (i.e., cored, rodded, vibrated 15s, vibrated 30s, and cut-to-size) used in this study. Additionally, their interaction effect on the measured tests (e.g., compressive strength, absorption, among others) was also assessed. The analyses were performed independently at each curing age. When the assumption of equal variances was not met (as verified by Levene's test), Welch's ANOVA was used as a more robust alternative. This high-level analysis helped determine whether either factor or their combination had a statistically significant influence on each measured property. This approach is fully discussed in section 6. However, while ANOVA identifies the presence of significant differences across groups, it does not specify which groups differ from one another.

To resolve this, a second level of analysis (b) involving pairwise comparisons was conducted and is reported throughout the results section each time a comparison is made among the mixtures. For each curing age and mixture, all possible pairwise combinations of preparation methods were compared using a stepwise protocol. Specifically, six pairwise comparisons were made per mixture per age: (a) cored vs. rodded, (b) cored vs. vibrated (15s), (c) cored vs. vibrated (30s), (d) rodded vs. vibrated (15s), (e) rodded vs. vibrated (30s), and (f) vibrated (15s) vs. vibrated (30s). For cube specimens only, a seventh comparison of cut-to-size vs. other fabrication methods was included

where applicable. These comparisons were performed separately for cube and cylinder specimens to isolate geometry-dependent effects.

Each pairwise test began with an assessment of normality using the Shapiro-Wilk test. If both groups were normally distributed, Levene's test was used to determine whether the assumption of equal variances was valid. Based on the outcomes, either a standard independent sample t-test (equal variances) or Welch's t-test (unequal variances) was then applied. If normality was not satisfied in either group, the non-parametric Mann-Whitney U test was used. All the statistical tests conducted in this work had a significance level of $\alpha = 0.05$. Additionally, the results are reported as the mean ± standard deviation, with their respective p-values. This statistical framework ensured that both high-level trends and specific group differences were analyzed and discussed at length. All statistical analyses were performed using MATLAB 2024a (developed by MathWorks Inc.).

In terms of quality assurance, all testing experiments closely followed the procedures set forth by the American Society for Testing and Materials (ASTM), as discussed in Section 4.3. Additionally, to ensure testing accuracy, the equipment used during mixing, curing, and mechanical testing was calibrated before testing.

To ensure high-quality control and reproducibility, all specimens were prepared and tested by the same trained personnel throughout the research. All materials used in this study were also from the same source and the same batch to avoid any potential inconsistencies in the results. Any specimen showing physical damage or any other indication of defects was excluded from analysis.

Outliers that deviated more than 10% (if any) were also excluded to ensure test repeatability. In all instances of reporting testing results throughout the study, results are presented as mean values accompanied by the standard deviation (mean ± STD).

5.5. Experimental Results

The experimental results of this study, including compressive strength, absorption, modulus of elasticity, and splitting tensile strength, are presented in the following sub-sections.

5.5.1. Absorption

Figure 28 shows the water absorption results. For C-So, cored samples results show an average absorption of 10.0±0.5% with a COV of 5.3%, which was significantly lower than that of the rodded samples (14.5±0.3%, COV = 2.2%, with a $p < 0.001$). The higher absorption of rodded specimens suggests that rodding has been less effective in compacting the samples, probably due to the high buildability of the 3D printing mixtures.

Compared to rodded samples, vibrated samples performed significantly better, with average absorption values of 7.9±0.2% and COV = 2.7% for 15s vibrated samples (with $p < 0.001$ when compared to rodded samples) and 8.7±0.2% and COV = 2.7% for 30s vibration (with $p < 0.001$ when compared to rodded samples). The small difference between the two durations (15s and 30s, with $p = 0.0043$ when compared) suggests that extended vibration did not improve absorption, possibly due to particle segregation resulting from over-vibrating. As discussed by previous studies, over-vibrating of samples can cause significant segregation of particles [297], [298],

whereby the denser and heavier coarse aggregates settle toward the bottom, while the lighter cementitious paste and finer particles rise toward the surface. Finally, cut-to-size samples had a moderate average absorption value of 9.9 ± 0.6% and a COV = 6.1%. These values are comparable to the vibrated samples but are statistically higher than the 15s vibration case (with a $p = 0.0079$).

For C-Sa mixtures, a similar trend was seen. Cored samples recorded an absorption of 11.2±1.1% (with COV = 10.2%), which is significantly lower than rodded samples (with 14.6±0.2%, COV = 1.5%, and a $p < 0.01$). In turn, vibrated samples again performed well, with absorption values of 10.2±1.0% for 15s, with a COV = 10.2% and 10.1±0.1% for 30s, with a COV = 1.4%. Both 15s and 30s vibrated samples had significantly lower absorption values than rodded samples ($p = 0.0005$ and $p < 0.001$, respectively). However, there was no statistical difference between the two vibration durations ($p = 1.000$), which suggests that a short vibration period is sufficient to achieve a good compaction. Cut-to-size samples showed similar performance to vibrated specimens, with a mean of 10.4±0.6% and a COV of 5.4%, and no significant difference compared to the 30s vibration samples ($p = 0.4762$).

These results highlight the critical role of the fabrication method in water absorption. In both C-So and C-Sa mixtures, rodded samples consistently performed worst, while vibrated and cut-to-size specimens produced more compacted, less absorbent outcomes.

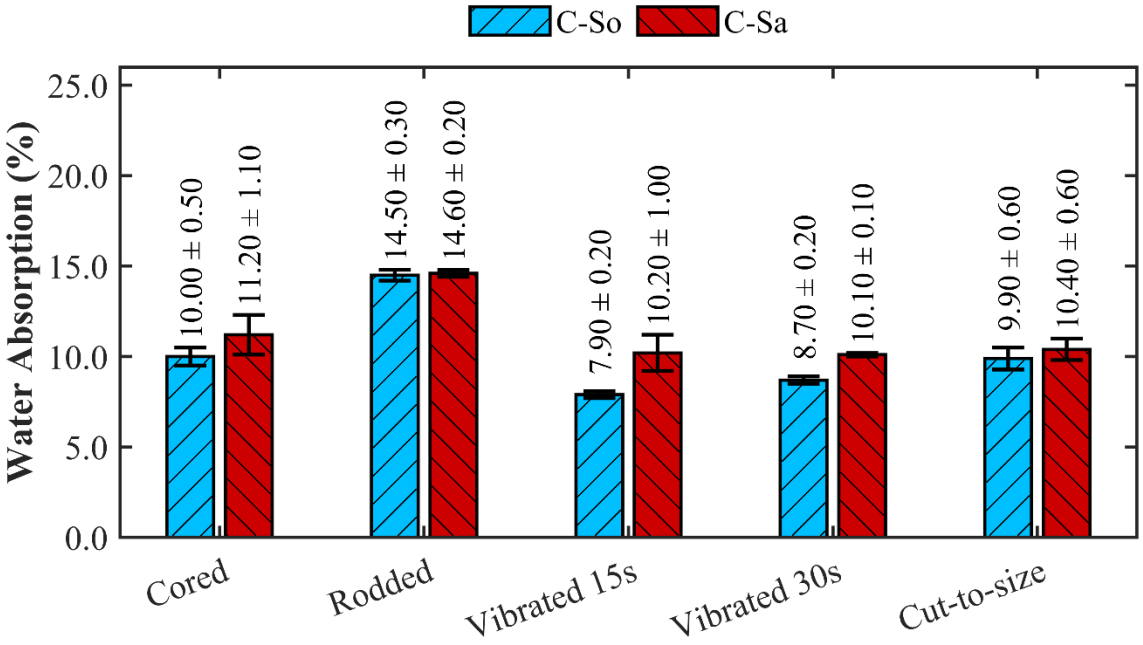


Figure 28. Absorption results of different samples

5.5.2. Compressive Strength

The compressive strength results of cored, rodded, and vibrated samples are provided in the following subsections. Cut-to-size cubes have also been tested and are included in the results, since it is a common method used in literature as a means to evaluate the compressive strength of 3D-printed cementitious materials [299], [300], [301].

5.5.2.1. Cubic Samples

A complete summary of all compressive strengths of cubic samples is provided later in **Table 27**. This placement allows the experimental methods and observations to be explained first, before presenting the compiled results for clarity.**Table 27**

Among C-So samples, vibrated specimens consistently achieved higher compressive strengths than those from other methods at all curing ages. After 3 days, 15s vibrated samples reached 11.5 ± 1.5 MPa (COV = 12.9%) and 30s vibrated samples reached 11.1 ± 0.7 MPa (COV = 6.1%), and their difference was significant with a p-value of 0.0019. Cored samples reached 7.7 ± 0.5 MPa with COV = 6.6% and rodded samples reached 11.8 ± 1.3 MPa with COV = 11.4%, with a significant statistical difference (p-value of 0.0284). Statistical analysis also confirmed that the difference between 30s vibrated and cored samples was significant ($p = 0.0090$), while 15s vibrated samples were not statistically different from rodded (with $p = 0.0847$) or cored samples (with $p = 0.1459$).

At 7 days, 15s and 30s, C-So vibrated samples further improved to an average of 17.0 ± 1.6 MPa (COV = 9.5%) and 15.9 ± 0.8 MPa (COV = 5.2%), respectively. Both were significantly stronger than cored samples, with an average of 13.6 ± 1.8 MPa and rodded with 13.5 ± 1.0 MPa. All had $p < 0.002$, showing statistically significant results. As for the vibrated samples (15s and 30s), their difference was not statistically significant ($p = 0.2268$). Again, it means that the added vibration time did not yield a significant increase in strength at this age. By 14 days, 15s vibrated samples (C-So) exhibited the highest strength at 19.5 ± 0.5 MPa (with COV = 2.6%), outperforming the rodded (with 14.4 ± 1.1 MPa) and cored (with 15.2 ± 1.7 MPa) samples significantly (with $p = 0.0007$ and $p = 0.0142$, respectively). The difference between 15s (19.53 ± 0.51) and 30s vibrated samples (18.5 ± 1.1 MPa) continued to remain statistically insignificant ($p = 0.1643$).

At 28 days, a similar trend was observed for C-So samples, with 15s- and 30s-vibrated samples reaching 20.4 ± 3.3 MPa and 19.1 ± 1.9 MPa, respectively. These were both significantly higher than cored (15.8 ± 1.3 MPa) and rodded (15.1 ± 1.1 MPa) samples, with p-values < 0.006 in all cases. However, the difference between 15s and 30s vibrated samples remained statistically insignificant ($p = 0.135$), even though the 15s vibration showed a higher mean strength. It is also found that the maximum difference of 29.1% from C-So (15.80 ± 1.27 MPa from cored, and 20.40 ± 3.27 MPa from vibrated), and 46.3% from C-Sa (15.10 ± 1.14 MPa from cored, and 22.10 ± 3.87 MPa from vibrated) are achieved among different fabrication methods.

At 91 days, while vibrated samples still had the highest average strength of 22.8 ± 1.0 MPa (for 15s) and 21.3 ± 1.7 MPa (for 30s), the relative differences narrowed. The comparison between 30s vibrated and rodded (19.1 ± 1.7 MPa) was not significant ($p = 0.0757$), and neither was the comparison with cut-to-size samples (21.3 ± 1.7 MPa, $p = 1.000$). Nonetheless, vibrated samples remained significantly stronger than cored samples (20.3 ± 2.3 MPa, $p = 0.0161$). However, the 30s vibrated samples had the lowest variability, with a COV of 7.8% at 91 days, which was the most consistent among all other samples.

C-Sa samples exhibited similar trends, but with generally higher early-age strengths. After 3 days, 15s and 30s vibrated samples reached 14.5 ± 1.6 MPa (COV = 11.2%) and 13.2 ± 2.0 MPa (COV = 15.3%), respectively with no statistical significance ($p = 0.3283$), while both significantly outperformed cored (12.7 ± 1.2 MPa with 15s vs. cored $p = 0.012$ and 30s vs. cored $p = 0.1459$) and rodded (11.8 ± 1.3 MPa with 15s vs. rodded $p = 0.0009$ and 30s vs. rodded $p = 0.0639$) samples.

At 7 days, C-Sa vibrated samples reached an average compressive strength of 18.4 ± 1.1 MPa for 15s with a COV = 6.0% and then 17.3 ± 1.1 MPa for 30s with a COV of 6.2%. Both of which were significantly stronger than the cored samples (13.5 ± 1.1 MPa) and rodded samples (13.1 ± 3.2 MPa), with all p-values below 0.032. The difference between the two vibrated samples was also statistically significant, with a p = 0.0030. This finding is interesting because, so far, all statistical comparisons between the two vibrating samples have been insignificant, indicating that segregation does not have a linear impact on the results. However, since sand particles are larger and more prone to segregation, longer vibration duration had a clear effect on strength.

At 14 days, 15s vibrated samples continued to outperform other fabrication methods, by reaching an average of 20.9 ± 0.8 MPa and a COV = 3.9%, compared to 17.7 ± 0.6 MPa and a COV = 3.4% for 30s. Rodded and cored samples were measured at 15.8 ± 2.8 MPa and 14.3 ± 1.1 MPa, respectively. These differences were statistically significant, with p = 0.0001 for cored vs. 15s, p = 0.0009 for rodded vs. 30s, and p = 0.0003 for 15s vs. 30s, confirming that vibration improved strength and consistency.

At 28 days, the strength of vibrated samples reached a value of 22.1 ± 3.9 MPa for 15s and 17.9 ± 1.4 MPa for 30s, both statistically higher than cored (15.1 ± 1.1 MPa) and rodded (20.7 ± 2.9 MPa) samples, with all relevant p-values less than 0.016. While the 15s group showed higher average strength, the difference between the two vibrated samples was again not statistically significant (p = 0.3721).

At 91 days, the difference between vibrated samples narrowed further, with the 15s group averaging 23.4 ± 5.1 MPa and the 30s group at 20.3 ± 2.3 MPa. These values remained statistically different from cored samples with an average of 18.1 ± 1.3 MPa, and a $p = 0.0015$, but the difference between the two vibrated samples was not significant with a $p = 0.5945$. The 30s vibrated sample again showed the lowest COV at this age, with COV = 11.4%, showing stable performance over time despite having lower early-age strength than the 15s group.

Table 27. Compressive strength of cubic samples produced with different manufacturing methods.

Sample age (days)	Information	Cored		Rodded		Cut-to-size		Vibrated 15s		Vibrated 30s	
-	-	C-So	C-Sa	C-So	C-Sa	C-So	C-Sa	C-So	C-Sa	C-So	C-Sa
3	Average	7.70 ± 0.51	12.70 ± 1.18	11.80 ± 1.34	12.90 ± 0.77	10.10 ± 2.15	11.10 ± 3.01	11.50 ± 1.48	14.50 ± 1.62	11.10 ± 0.67	13.20 ± 2.03
	COV	6.6	9.3	11.4	6.0	21.3	27.0	12.9	11.2	6.1	15.3
7	Average	13.60 ± 1.81	13.50 ± 1.05	14.00 ± 1.01	17.20 ± 1.51	13.80 ± 2.08	13.10 ± 3.22	17.00 ± 1.61	18.40 ± 1.10	15.90 ± 0.84	17.30 ± 1.08
	COV	13.3	7.3	7.2	8.8	15.1	24.5	9.5	6	5.2	6.2
14	Average	15.20 ± 1.69	14.30 ± 1.14	14.40 ± 1.10	18.70 ± 1.50	14.40 ± 2.06	15.80 ± 2.80	19.50 ± 0.51	20.90 ± 0.82	18.50 ± 1.11	17.70 ± 0.60
	COV	11.1	7.6	7.6	8.0	14.3	17.7	2.6	3.9	6.0	3.4
28	Average	15.80 ± 1.27	15.10 ± 1.14	16.70 ± 1.70	20.70 ± 3.48	18.30 ± 2.89	20.70 ± 2.92	20.40 ± 3.27	22.10 ± 3.87	19.10 ± 1.89	17.90 ± 1.38
	COV	8.1	7.6	10.2	16.9	15.8	14.1	16.0	17.5	9.9	7.7
56	Average	16.50 ± 2.53	15.70 ± 2.35	16.90 ± 1.26	18.90 ± 2.32	19.10 ± 1.52	21.50 ± 1.55	21.90 ± 1.65	22.90 ± 0.77	21.40 ± 1.56	20.80 ± 0.60
	COV	15.4	14.9	7.4	12.3	7.9	7.2	7.6	3.4	7.3	2.9
91	Average	20.30 ± 2.26	18.10 ± 1.32	19.10 ± 1.70	19.90 ± 1.24	19.70 ± 0.37	21.70 ± 1.57	22.80 ± 0.97	23.40 ± 5.05	21.30 ± 1.67	20.30 ± 2.30
	COV	11.1	7.3	8.9	6.3	1.9	7.2	4.2	21.6	7.8	11.4

5.5.2.2. Cylindrical Samples

A complete summary of all compressive strengths of cylindrical samples is provided later in **Table 28**. This placement allows the experimental methods and observations to be explained first, before presenting the compiled results for clarity. **Table 28**

At 3 days, vibrated samples outperformed all other fabrication methods. C-So vibrated samples reached an average of 16.0 ± 1.5 MPa and a COV = 9.6% (for 15s vibrated) and 15.9 ± 0.8 MPa and a COV = 5.3% (for 30s vibrated), which are significantly higher than the cored (8.7 ± 0.3 MPa, COV = 3.5%) and rodded (8.4 ± 0.3 MPa, COV = 3.6%) counterparts. Statistical comparisons confirmed that 15s and 30s vibrated samples were significantly stronger than cored samples ($p < 0.0003$ for both mixtures), while the difference between the two vibrated groups was again not significant ($p = 0.4739$). Similar trends were observed in C-Sa with a 3-day strength of 18.0 ± 0.8 MPa, and COV = 4.4% (for 15s vibrated samples) and 17.3 ± 1.7 MPa, with COV = 9.6% (for 30s vibrated samples). These values can be compared to cored samples with an average of 9.9 ± 1.2 MPa, and a COV = 12.1%, and rodded samples with an average of 9.7 ± 0.7 MPa, and a COV = 7.5%. Again, all the pairwise statistical differences between vibrated and non-vibrated samples were statistically significant with a $p < 0.01$.

By 7 days, C-So vibrated samples continued to gain higher strength, with an average of 16.3 ± 0.8 MPa (for 15s vibrated samples) and 16.0 ± 0.5 MPa (for 30s vibrated samples). The mentioned values are significantly higher than those of cored (13.7 ± 0.3 MPa) and rodded

(11.3 ± 1.0 MPa) specimens, with $p < 0.002$ for all comparisons. The same was true for C-Sa, where 20.9 ± 0.8 MPa (for 15s vibrated samples) and 18.0 ± 1.8 MPa (for 30s vibrated samples) again exceeded cored and rodded samples (with 14.5 ± 1.7 MPa and 10.6 ± 1.2 MPa, respectively), with statistically significant differences ($p < 0.001$).

At 14 days, the 15s vibrated samples reached peak values of 19.1 ± 1.2 MPa (C-So) and 22.9 ± 0.8 MPa (C-Sa), with low COVs of 6.5% and 3.4%, respectively. In both mixtures, 15s vibrated samples were significantly stronger than cored (with C-So having 15.1 ± 0.3 MPa, and C-Sa reaching 17.1 ± 1.7 MPa) and rodded samples (with C-So 13.0 ± 1.0 MPa, and C-Sa with 13.8 ± 1.0 MPa). All the p-values were < 0.005 across all pairwise tests.

At 28 days, a sharp increase in strength was noted, especially for C-Sa vibrated samples. An average of 35.5 ± 7.6 MPa (for 15s vibrated samples) and 32.8 ± 2.1 MPa (30s vibrated samples) was recorded. These values were significantly greater than cored (17.3 ± 1.5 MPa) and rodded samples (15.0 ± 0.8 MPa), with p-values well below 0.001. Despite the high mean, the 15s vibrated samples at this age also showed the highest variability with a COV of 21.5%. The maximum difference between fabrication methods among the 28-day strength results is found to be 109% from C-So (14.2 ± 1.10 MPa from rodded, and 29.8 ± 1.93 MPa from vibrated (15s) samples), and 136% for C-Sa (15.0 ± 0.83 MPa from rodded, and 35.5 ± 7.61 MPa from vibrated (15s) samples). The mentioned are higher than cubic samples which reflects more difficulty to properly compact and extract cylindrical samples than cubes, due to the high stiffness of 3D printed specimen.

At 56 days, vibrated samples continued to outperform others. For instance, C-So 15s vibrated samples achieved 31.5 ± 3.1 MPa, followed by 28.2 ± 4.6 MPa when vibrated for 30s, both of which were significantly higher than cored (27.1 ± 2.0 MPa) and rodded samples (18.1 ± 1.7 MPa; with all $p < 0.001$). In C-Sa samples, a strength of 39.1 ± 1.6 MPa (for 15s) and 38.3 ± 1.9 MPa (for 30s) was achieved. They again far surpassed cored (29.4 ± 1.5 MPa) and rodded (20.6 ± 2.1 MPa) samples, with p-values < 0.0005.

At 91 days, vibrated samples reached their peak long-term performance at 38.8 ± 1.5 MPa (for C-So, 15s) and 35.0 ± 0.6 MPa (30s), compared to 28.2 ± 1.2 MPa (cored) and 31.1 ± 1.8 MPa (rodded). The statistical analysis confirmed significant differences between the vibrated and cored or rodded methods ($p < 0.01$), while the difference between 15s and 30s vibrated samples remained nonsignificant ($p = 0.4739$). The lowest variability was observed in 30s-vibrated samples (COV = 1.6%), supporting their reliability for long-term strength development. For C-Sa, similar trends of achieving a higher strength than other fabricating methods were observed (with 41.8 ± 1.0 MPa for 15s and 40.9 ± 4.2 MPa for 30s), both significantly higher than cored (31.6 ± 2.0 MPa) and rodded (30.3 ± 2.6 MPa) samples ($p < 0.002$ for all comparisons).

In general, vibrated samples, especially those exposed to 30s vibration, showed very high long-term compressive strength with lower variability. Although 15s vibration provided marginally higher strength in several cases, its higher variability (with COV up to 21.5%) may reduce confidence in the results. This is especially the case since no statistically significant difference was found among 15s and 30s samples across different curing ages for cylinder samples. Further, while the cored samples were not the strongest, they showed relatively stable results across all ages.

Table 28. Compressive strength of cylindrical samples produced with different manufacturing methods.

Curing days	Information	Cored		Rodded		Vibrated 15s		Vibrated 30s	
-	-	C-So	C-Sa	C-So	C-Sa	C-So	C-Sa	C-So	C-Sa
3	Average	8.7 ± 0.31	9.9 ± 1.2	8.4 ± 0.30	9.7 ± 0.72	16.0 ± 1.53	18.0 ± 0.79	15.9 ± 0.84	17.3 ± 1.67
	COV	3.54	12.15	3.59	7.46	9.56	4.37	5.25	9.60
7	Average	13.7 ± 0.29	14.5 ± 1.70	11.3 ± 0.97	10.6 ± 1.16	16.3 ± 0.77	20.9 ± 0.82	16.0 ± 0.48	18.0 ± 1.76
	COV	2.10	11.73	8.57	10.93	4.73	3.91	2.99	9.75
14	Average	15.1 ± 0.30	17.1 ± 1.73	13.0 ± 0.96	13.8 ± 1.05	19.1 ± 1.24	22.9 ± 0.77	18.5 ± 1.11	20.8 ± 0.60
	COV	1.98	10.15	7.38	7.62	6.49	3.37	6.00	2.87
28	Average	16.4 ± 0.72	17.3 ± 1.48	14.2 ± 1.10	15.0 ± 0.83	29.8 ± 1.93	35.5 ± 7.61	26.1 ± 2.61	32.8 ± 2.11
	COV	4.40	8.55	7.72	5.55	6.48	21.47	9.98	6.43
56	Average	27.1 ± 1.97	29.4 ± 1.50	18.1 ± 1.74	20.6 ± 2.11	31.5 ± 3.06	39.1 ± 1.60	28.2 ± 4.59	38.3 ± 1.93
	COV	7.26	5.10	9.58	10.25	9.70	4.08	16.25	5.04
91	Average	28.2 ± 1.17	31.6 ± 2.02	31.1 ± 1.79	30.3 ± 2.56	38.8 ± 1.45	41.8 ± 1.05	35.0 ± 0.55	40.9 ± 4.22
	COV	4.16	6.40	5.74	8.46	3.74	2.53	1.56	10.31

5.5.2.3. Cylinder-Cube Relationship

Another point regarding the results is the relationship between the strength of the cylinder and cube samples. **Table 29** summarizes the cylinder-to-cube strength ratio, expressed as coefficient k, for different mixtures and curing ages. In conventional concrete, k values typically fall in the range of 0.78-0.83 [302] when comparing 150 mm cubes to 150 × 300 mm cylinders, indicating that cubes generally provide higher strengths. The results in this study, however, reveal a more complex behavior that depends on both mixture type and fabrication method.

At early ages (3 and 7 days), k values varied widely across mixtures and preparation methods. For cored specimens, k values ranged from 0.78 to 1.13, with soil-based mixtures tending toward unity (e.g., 1.13 at 3 days, 1.01 at 7 days), while sand-based mixtures showed more scatter (0.62-1.07). Rodded specimens consistently exhibited k values below unity at early ages (0.62-0.90), indicating that cylinders were weaker than their cube counterparts, consistent with conventional expectations. By contrast, vibrated samples, particularly those vibrated for 15 and 30 seconds, showed unusually high k values at 3 days (1.43-1.59), suggesting that cylinders in these cases outperformed cubes. This may be linked to enhanced compaction efficiency in taller specimens under vibration, whereas the smaller cubes were more sensitive to segregation effects. In other words, vibrated cubes have likely experienced a significant segregation, leading to lower compressive strength results.

As curing continued, the ratios evolved. By 14 and 28 days, cored specimens stabilized near unity (0.99-1.19), reflecting comparable strengths between cylinders and cubes. Rodded specimens remained below unity (0.73-0.90), reaffirming the expected results and limited

effectiveness of rodding for consolidating soil- and sand-based printable mixtures. Vibrated samples again demonstrated higher k values, with some exceeding 1.6 at 28 days, suggesting that vibration favored the cylindrical geometry over the cubic one, probably because of particle segregation.

At later ages (56 and 91 days), k values increased across all preparation methods. Cored samples reached values as high as 1.87 for sand-based mixtures at 56 days, while vibrated mixtures produced ratios approaching 2.0 at 91 days. Such unusually high ratios contrast with conventional concrete behavior and are likely due to the unique characteristics of fine soil- and sand-based binders that are 3D-printed. Several mechanisms may contribute: (a) ongoing reactivity and densification in the larger volume of cylinders, which benefits more from extended curing; (b) differences in compaction efficiency, where vibration or coring improves cylinder uniformity relative to cubes; and (c) size effects, as the smaller 50-mm cubes tend to over-represent heterogeneity and localized flaws compared to the taller 76.2×152.4 mm cylinders. It is also possible that (d) the stacking of layers (self-weight) has helped cylindrical samples in 3D-printed samples.

In general, the results indicate that the cylinder-cube strength relationship in soil- and sand-based mixtures cannot be described by a single fixed coefficient, as is commonly assumed for Portland cement concrete. Instead, the ratio depends strongly on fabrication (sampling) method, mixture type, and curing age. Rodded samples followed the conventional trend of cylinders being weaker than cubes ($k < 1.0$), while vibrated and cored samples often produced the opposite trend ($k \geq 1.0$). These findings suggest that using cube results to estimate cylinder strengths or vice versa

without accounting for fabrication and curing effects may lead to misleading conclusions. For soil- and sand-based printable materials, it is therefore recommended to directly test the intended specimen geometry, especially when the results are used for structural performance evaluations.

However, the unusually high k values observed at later ages (up to 1.9-2.0) deviate significantly from conventional concrete behavior and likely arise from a combination of specimen geometry, material heterogeneity, and curing effects. First, the smaller 50 mm cubes are more susceptible to edge effects and localized flaws, whereas the taller cylinders experience more uniform stress distribution during testing. Second, vibration and fine-grained soil matrices may have induced particle segregation in the cubes, reducing their apparent density and strength. Third, the larger volume of the cylinders likely retained moisture more effectively, promoting continued reaction and strength development over time, especially since the two mixtures had a high fly ash content and the fact that the curing method used in the study was ambient temperature with a relative humidity of 40 ± 10%. In this case, the cylinder samples can withhold higher moisture content while small cubes Fourth, layer-by-layer deposition during 3D printing can lead to preferential vertical compaction under self-weight, thereby enhancing strength in the printing (axial) direction. Finally, as mentioned in section 4.2, since the sample testing strictly followed standard procedures (e.g., having used standard molds, testing procedures, and even capping), the results are most likely a collection of the mentioned factors, which are governed by both fabrication and material-specific phenomena rather than standard geometric scaling. However, it is hypothesized that the increasing k ratios with age might have been heavily impacted by the reactivity rate of fly ash particles, which tends to progress slowly under ambient curing conditions. As the pozzolanic reactions continue, the strength gain in the larger cylindrical specimens (where

moisture retention and internal curing are more favorable) can outpace that of the smaller cubes, leading to a gradual widening of the cylinder-to-cube strength ratio over time.

Table 29. The result of the strength coefficient (k), calculated based on the compressive strength between cylinder/cube samples, on different curing days.

Curing days	Cored		Rodded		Vibrated 15s		Vibrated 30s	
-	C-So	C-Sa	C-So	C-Sa	C-So	C-Sa	C-So	C-Sa
3	1.13	0.78	0.72	0.75	1.59	1.43	1.57	1.57
7	1.01	1.07	0.81	0.62	1.18	1.22	1.23	1.13
14	0.99	1.19	0.90	0.74	1.33	1.17	1.17	1.12
28	1.04	1.14	0.85	0.73	1.63	1.26	1.74	1.72
56	1.65	1.87	1.07	1.09	1.65	1.32	1.79	1.79
91	1.39	1.75	1.63	1.52	1.97	1.61	1.83	1.92

5.5.3. Modulus of Elasticity and Poisson's Ratio

5.5.4. Splitting Tensile Strength

The result of the splitting tensile test is presented in **Figure 29**. Among the C-So specimens, vibrated 15s samples showed the highest average strength at 2.76 ± 0.15 MPa (with COV = 5.43%), followed closely by cored samples with 2.74 ± 0.25 MPa (with COV =8.97%). However, their difference was not statistically significant ($p = 0.8813$). The vibrated 30s and rodded samples developed slightly lower strengths of 2.60 ± 0.05 MPa (with COV = 2.06%) and 2.63 ± 0.12 MPa (with COV = 4.39%), respectively. Their statistical difference, however, was not significant ($p = 0.6124$).

In contrast, C-Sa specimens showed higher overall splitting tensile strength. Vibrated for 15s samples reached 3.41 ± 0.06 MPa (with COV = 1.73%), which represents the highest among all tested groups. This was significantly greater than the strength of rodded (2.84 ± 0.35 MPa, with COV = 12.2%, and p = 0.0196) and vibrated 30s (2.78 ± 0.19 MPa, with COV = 6.6%, and p = 0.0079) samples. The difference between vibrated for 15s and cored samples (3.08 ± 0.24 MPa, with COV = 7.8%) was also statistically significant (with a p = 0.0342). These findings highlight that the 15s vibration condition yielded the most reliable and highest-performing samples, as evidenced by its very low COV (1.73%).

In general, while C-Sa mixtures had higher average splitting tensile strength than C-So, they also showed slightly higher average variability (COV = 7.1%, as compared to 5.2%). This trend is consistent with prior sections and may be attributed to differences in particle morphology and packing density.

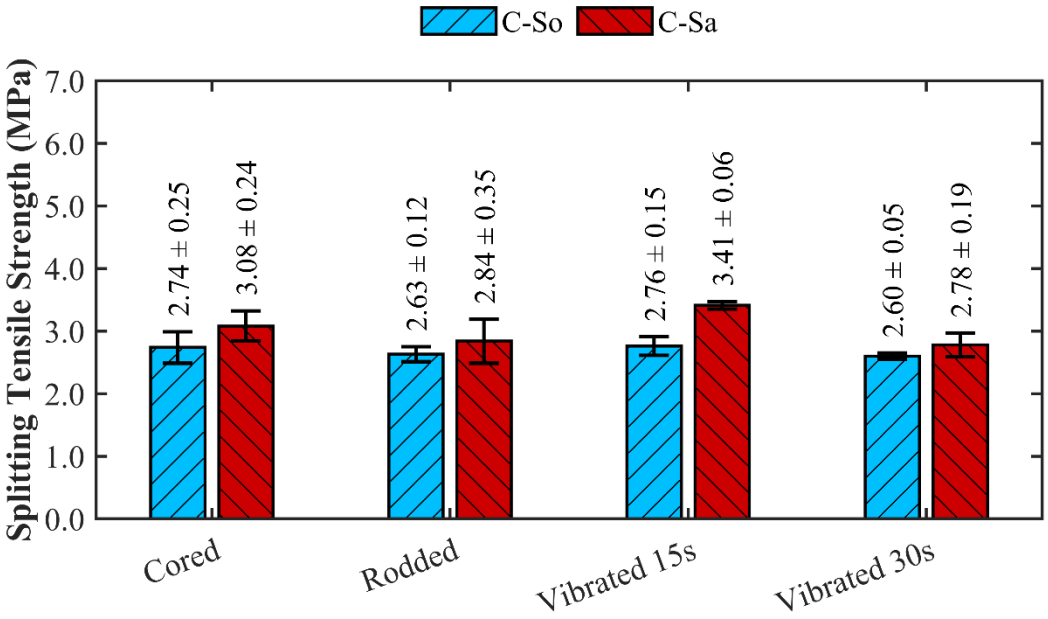


Figure 29. Splitting tensile strength of cylindrical samples produced with different manufacturing techniques.

5.6. Statistical Analysis of Test Results

To better understand the effects of mixture type (e.g., soil versus sand) and preparation method (e.g., cored, rodded, vibrated, and cut-to-size) on test results, a full set of statistical analyses has been conducted. In doing so, a two-way ANOVA was utilized to evaluate the interaction and the main effects of these factors, while Levene's test was applied to verify the assumption of homogeneity of variances. In cases where Levene's test could not verify the assumption of variance homogeneity, the Welch's ANOVA test [191] was used to identify statistically significant differences.

In general, for the ANOVA test, three assumptions must be satisfied: (1) independence of observations, (2) normality of residuals, and (3) homogeneity of variances [189], [190]. The first assumption is inherently satisfied through controlled experimental procedures. The second is deemed acceptable as ANOVA is known to be robust against minor deviations from normality [190]. The third was explicitly verified using Levene's test [188], in which a p-value greater than 0.05 indicates equal variances across groups.

Table 31 provides the results of the analyses. In the table, a p-value of < 0.05 for the classic and Welch's ANOVA models indicates that the model significantly explains the variance in the dependent variable. However, a p-value of > 0.05 indicates that the predictors do not collectively explain the variability in the dependent variable to a statistically significant extent. Also, in

Levene's test, a p-value > 0.05 indicates that the variance assumption is valid for ANOVA. If violated, ANOVA results may be unreliable, in which case Welch's ANOVA is tested.

Based on the table, the mixture type significantly influences the early-age compressive strength of cubes, as indicated by p-values < 0.05 for cubes 3-day cured (p = 0.000) and 7-day cured (p = 0.002). However, this trend reverses, with no significant effect observed at 14-day (p = 0.147), 56-day (p = 0.688), or 91-day (p = 0.989). These findings suggest that the effect of mixture type on compressive strength is time-dependent, especially in cube samples. For cylindrical samples, however, the mixture type remains significant throughout different curing ages. This difference could have been caused by the larger sample size of cylinders that have lower sensitivity to different variables (e.g., mixing and printing).

In terms of preparation methods, a significant effect on compressive strength across all samples (p < 0.05) is recorded. This shows the dominant role of preparation methods in the resulting strength values. The interaction effect between mixture and method, however, is significant for cube samples tested at 7-day (with p = 0.016), 14-day (with p = 0.002), and 56-day (with p = 0.030) compressive strength, as well as absorption (with p = 0.002). The same goes for cylindrical samples tested for compressive strength at 7-day (with p = 0.000), 28-day (with p = 0.001), and 91-day (with p = 0.004), as well as splitting tensile (with p = 0.045) and modulus of elasticity (with p = 0.002). The significance of interaction indicates that the combined influence of these factors varies with curing age.

From the table, Levene's test indicates that variance homogeneity is generally satisfied ($p > 0.05$), except for the absorption results of cubic samples ($p = 0.000$) and the 3-day cured compressive strength of cylindrical samples. Both have been found to be significant in Welch's ANOVA based on the p-values for the mixture, but not for the method. It shows that hydration and overall absorption are more closely related to the component mixture (e.g., soil vs. crushed sand) than to the sampling methodology. Also, hydration and absorption are heterogeneous in nature and cannot be simply quantified by basic tests, often requiring advanced testing, such as computerized tomography (CT scanning).

Table 31. Result of two-way ANOVA for cubic samples.

Sheet Name	Mixture Effect p-value (ANOVA)	Method Effect p-value (ANOVA)	Interaction p-value (ANOVA)	Levene p-value	Welch Mixture p-value	Welch Method p-value
Cube 3-day comp.	0.000	0.000	0.082	0.446	0.000	0.000
Cube 7-day comp.	0.002	0.000	0.016	0.114	0.000	0.000
Cube 14-day comp.	0.147	0.000	0.002	0.095	0.000	0.000
Cube 28-day comp.	0.002	0.000	0.206	0.200	0.000	0.000
Cube 56-day comp.	0.688	0.000	0.030	0.193	0.000	0.000
Cube 91-day comp.	0.989	0.006	0.331	0.072	0.000	0.000
Cube absorption	0.000	0.000	0.002	0.000	0.009	0.086
Cylinder 3-day comp.	0.000	0.000	0.822	0.006	0.000	0.007
Cylinder 7-day comp.	0.000	0.000	0.000	0.106	0.000	0.000

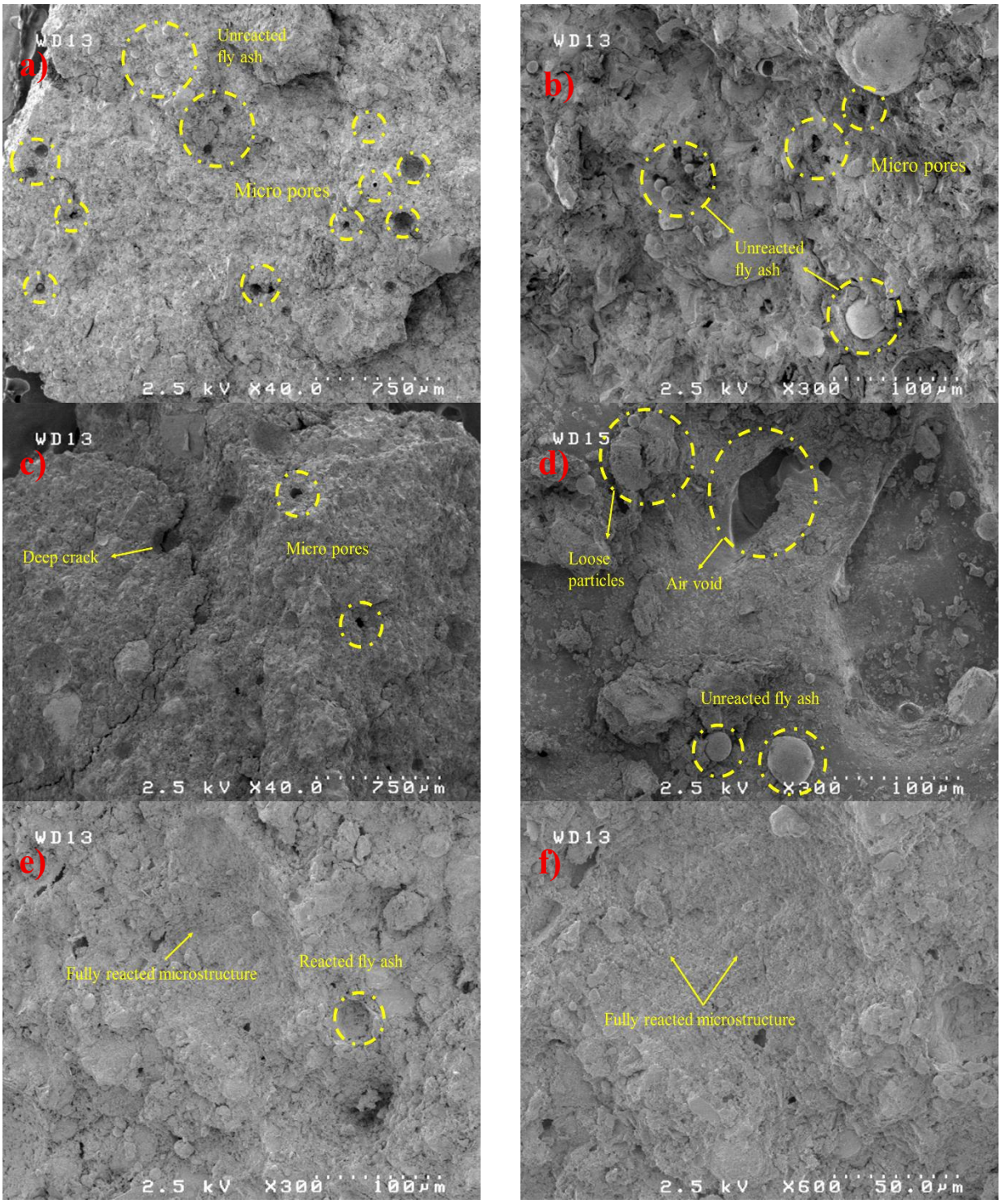
Cylinder 14-day comp.	0.000	0.000	0.258	0.072	0.000	0.000
Cylinder 28-day comp.	0.000	0.000	0.001	0.137	0.000	0.000
Cylinder 56-day comp.	0.000	0.000	0.239	0.162	0.000	0.000
Cylinder 91-day comp.	0.000	0.000	0.004	0.057	0.000	0.000
Cylinder splitting tensile	0.000	0.000	0.045	0.037	0.994	0.980
Cylinder modulus of elasticity	0.000	0.010	0.002	0.324	0.000	0.000

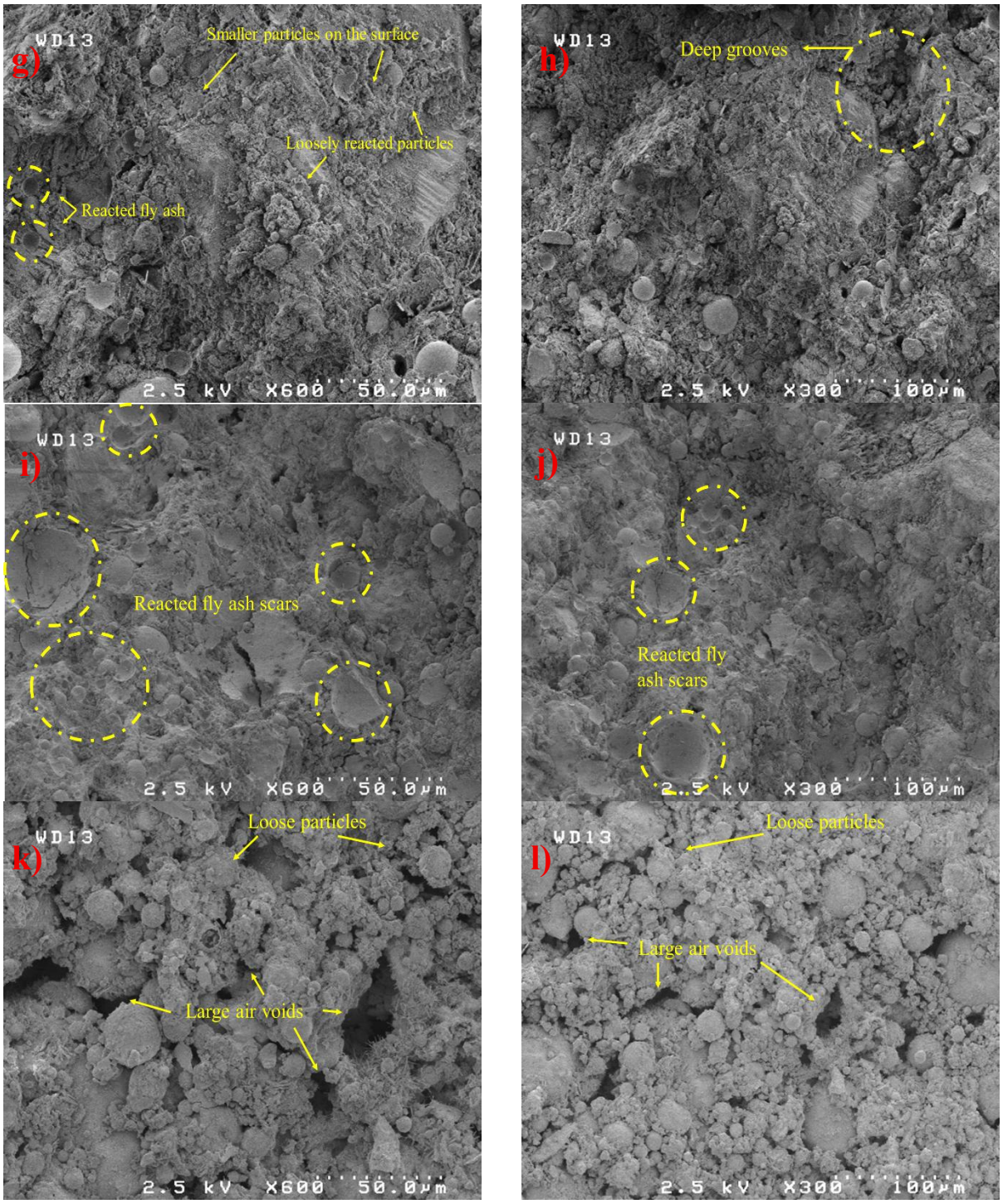
5.7. SEM Imaging of Hardened Materials

Figure 30 (a)-(p) shows the SEM images of different samples after 28 days of curing. For C-So specimens (a)-(h), better particle size distribution and compaction can be seen. Cored C-So ((a)-(b)) samples are slightly porous with some noticeable voids in their microstructure and unreacted fly ash particles. As discussed in Section 5.2, cored samples exhibited limited compaction, consistent with the microstructural findings. Rodded C-So samples ((c)-(d)) also showed weak microstructural integration. Large cracks, air voids, and grooves were visible, and the cementitious matrix appeared loosely bonded, with a large number of incompletely reacted fly ash particles. The large number of air voids in rodded samples indicates that rodding was insufficient to remove major air voids and ensure uniform compaction, consistent with the lower strength and modulus values reported earlier.

In contrast, vibrated C-So samples exhibited more compact, consolidated textures. The 15s vibrated samples ((e)-(f)) showed a good particle distribution with a dense matrix and lower numbers of unreacted fly ash particles. The 30s vibrated samples showed a similar matrix but with slightly more loosely packed particles. There is also an increased number of disconnected or partially hydrated particles, possibly due to over-vibration leading to microstructural segregation.

For C-Sa mixtures that were vibrated for 15s ((m)-(n)), SEM images showed a relatively dense matrix, with sand particles embedded in a continuous binder phase. However, poor particle size distribution was occasionally observed due to the coarser nature of the sand particles. After 30s of vibration ((m)-(n)), images show higher porosity and a more scattered distribution of unreacted fly ash particles. In turn, cored C-Sa ((i)-(j)) samples showed better matrix continuity and lower porosity compared to their vibrated (30s) counterparts. This may be attributed to the printer's auger mixing materials in the printer's funnel during deposition, which could have enhanced the particle dispersion and reactivity. Finally, the C-Sa rodded ((k)-(l)) samples showed the least favorable microstructure with numerous voids, loosely packed regions, and a high concentration of unreacted fly ash particles were present. These findings correlate well with the low compressive strength and modulus values reported in earlier sections.


WD13
a)
Unreacted fly ash
Micro pores
2.5 kV X40.0 750µm
WD13
b)
Micro pores
Unreacted fly ash
2.5 kV X300 100µm
WD13
c)
Deep crack
Micro pores
2.5 kV X40.0 750µm
WD15
d)
Loose particles
Air void
Unreacted fly ash
2.5 kV X300 100µm
WD13
e)
Fully reacted microstructure
Reacted fly ash
2.5 kV X300 100µm
WD13
f)
Fully reacted microstructure
2.5 kV X600 50.0µm


g)
WD13
Smaller particles on the surface
Loosely reacted particles
Reacted fly ash
2.5 kV X600 50.0µm
h)
WD13
Deep grooves
2.5 kV X300 100µm
i)
WD13
Reacted fly ash scars
2.5 kV X600 50.0µm
j)
WD13
Reacted fly ash scars
2.5 kV X300 100µm
k)
WD13
Loose particles
Large air voids
2.5 kV X600 50.0µm
l)
WD13
Loose particles
Large air voids
2.5 kV X300 100µm

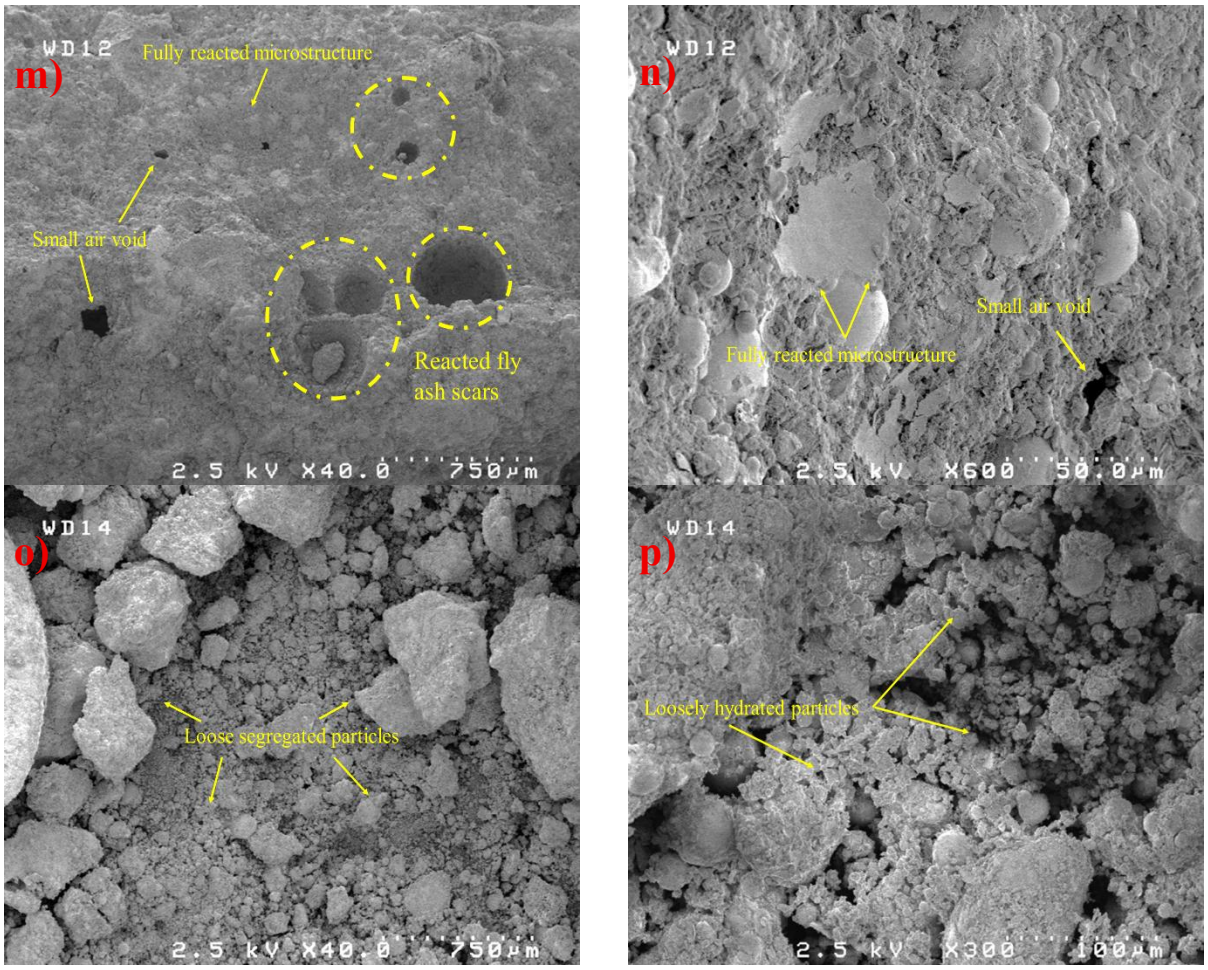


Figure 30. SEM images of samples produced with different manufacturing techniques including: (a)-(b): C-So cored, (c)-(d): C-So rodded, (e)-(f): C-So vibrated 15s, , (g)-(h): C-So vibrated 30s, (i)-(j): C-Sa cored, (k)-(l): C-Sa rodded, (m)-(n): C-Sa vibrated 15s, (o)-(p): C-Sa vibrated 30s.

Table 32 shows the result of the EDS analysis conducted on different samples. Based on elemental composition data, it is evident that sand-based (C-Sa) samples exhibit more consistent chemical profiles, as reflected in their lower standard deviations and coefficients of variation (COVs) across all measured elements. This consistency is probably due to the relatively homogeneous nature of manufactured sand, which exhibits uniform mineralogy and particle surface properties. However, soil-based (C-So) samples show considerably higher variability,

especially in calcium and silicon contents (COV = 18% for both). This higher variability suggests that soil particles are irregular and have a variable composition and surface chemistry. The sodium content in C-So also shows high variability (COV = 78%), probably due to the difficulty in achieving a fully dispersed mixing. Among all preparation methods, rodded C-So samples showed the greatest elemental variability, particularly in calcium (25.6% in cored vs. 16.4% in rodded). The high variability in elemental composition can indicate heterogeneity in hydration and particle distribution. These findings align with the porosity and mechanical performance observed in sections 5.2 and 5.5. Based on the mentioned, the EDS analysis confirms that both material type and preparation method influence not only mechanical behavior but also the chemical uniformity of the 3D-printed and rodded specimens.

Table 32. Result of the EDS analysis.

Mixture	Element	Cored (%)	Rodded (%)	Vib 15s (%)	Vib 30s (%)	Avg ± STD (%)	COV (%)
C-So	Na	1.00	0.50	0.00	0.60	0.52 ± 0.36	78
	Al	4.10	3.90	4.90	5.30	4.55 ± 0.57	14
	Si	14.30	12.50	18.80	17.00	15.65 ± 2.42	18
	Ca	25.60	16.40	23.30	22.90	22.05 ± 3.42	18
	Fe	4.00	3.40	5.20	4.40	4.25 ± 0.65	18
C-Sa	Na	0.90	0.80	0.80	0.60	0.78 ± 0.11	13
	Al	6.20	6.00	6.00	5.90	6.02 ± 0.11	2
	Si	14.80	13.80	13.80	13.80	14.05 ± 0.43	3
	Ca	20.90	21.40	21.40	21.30	21.25 ± 0.21	3
	Fe	2.80	3.70	3.70	2.20	3.10 ± 0.64	23

5.8. Conclusion and Future Study Recommendations

Unlike conventional concrete, 3D-printed mixtures are proportioned differently to develop specific rheological characteristics that enable continuous extrusion and layer buildability, rather than just workability and compaction. However, similar assumptions to those used for mold-cast concrete are often applied when testing 3D-printed materials, even though they do not accurately reflect the behavior of printed systems. Ordinary concrete mix design principles and performance assumptions cannot be directly applied to 3D-printed materials because of: (a) different rheological requirements for printing, (b) the printing process that embeds porosity in a specific orientation throughout the printing process, and (c) difficulty in sampling and a lack of specific standards for 3D-printed cementitious materials. As a result, this study evaluated the impact of different sampling methods used in the literature (rodded, vibrated, and cut-to-size) and introduced a new method (fresh coring). Two sets of materials have been used to represent the ordinary (crushed sand-based) and localized (natural soil-based) mixtures, as reported in the literature. Samples were tested for fresh, mechanical, and microstructural properties. Based on the results, the following conclusions are drawn:

- In terms of absorption, it is found that vibrated samples (for 15s and then 30s) perform best and have a low average absorption value of ~9% and 9.4%, respectively. These values should be compared with 10.1% for cut-to-size samples, 10.3% for cored samples, and 14.5% for rodded samples. Statistical analysis confirms that both 15s and 30s vibrated C-So samples had significantly lower absorption values than rodded samples ($p = 0.0043$ and $p = 0.0022$, respectively). One of the major takeaways from the absorption test is the effect of elongated vibration. Results showed a marginally increased absorption in the 30s group, probably due to segregation. Additionally, the data suggest that 3D printing mixtures may

not be effectively compacted solely by rodding. However, coring and cut-to-size samples are found to yield absorption values closest to those in actual printed conditions.

- In terms of compressive strength, both cubic and cylindrical soil-based samples showed lower variability than their crushed sand-based counterparts. For example, the average coefficient of variation for soil-based cubes was 9.7%, lower than the 10.7% observed in C-Sa samples. The reason for this behavior is likely due to the more uniform particle distribution of the soil used in this study. Regarding the impact of fabrication methods, 15s vibrated samples consistently achieved the highest strength, reaching up to 22.83 ± 0.97 MPa in cubic samples at 91 days. However, when samples were vibrated for 30s, the early-age strengths were reduced due to possible particle segregation. The difference was statistically significant ($p = 0.0019$). Next, rodded samples consistently showed lower strengths than vibrated samples in all curing times. Statistical analysis also showed significant differences at multiple curing times for the lower strengths of rodded samples compared to those of vibrated samples. This trend was more pronounced in cylindrical samples due to the mixtures' higher buildability. It points to the fact that the effectiveness of rodding for compaction of 3D printing mixtures is limited. Interestingly, smaller cubic samples had narrower error margins, challenging the conventional assumption that smaller samples should yield greater uncertainty. Samples with higher compressive strength also tended to show lower variability, probably due to improved internal homogeneity and reduced porosity. Additionally, the large differences across mixture types and preparation methods seen at early ages tended to diminish over time. However, vibrated samples consistently retained their strength advantage over other

preparation methods, even at later ages. Taken together, these results indicate that cored samples may offer the most realistic representation of the mechanical properties of actual 3D-printed components.

- The cylinder-cube strength relationship in soil- and sand-based mixtures deviated from the conventional concrete benchmark ($k \approx 0.8$). Rodded specimens generally showed $k < 1.0$, consistent with cylinders being weaker than cubes, whereas cored and vibrated specimens often produced $k \geq 1.0$, with values approaching 2.0 at later ages. This indicates that fabrication method, curing age, and mixture type strongly influence the cylinder-cube relationship, and that direct testing of the intended specimen geometry is necessary rather than applying fixed conversion factors from conventional concrete.

- In terms of modulus of elasticity, C-Sa generally had a higher stiffness than C-So, with modulus of elasticity values ranging from 13.4 ± 2.1 GPa (for C-Sa cored - lowest) to 16.2 ± 0.8 GPa (for C-Sa vibrated 15s - highest), compared to 9.9 ± 1.1 GPa (for C-So vibrated 30s - lowest) to 12.0 ± 0.5 GPa (for C-So rodded-highest). Statistical comparisons confirmed that these differences were significant in multiple cases, including between cored samples ($p = 0.0378$) and vibrated samples ($p = 0.015$). Among preparation methods, vibration for 15 seconds produced the highest modulus in C-Sa while also having the lowest variability (COV = 4.9%). Rodded samples showed the highest variability in Poisson's ratio, with a standard deviation of 0.17 and a COV of 17.3% in C-Sa. This suggests that while rodding can result in stiff specimens, it also introduces structural inconsistencies that likely do not match those of a 3D-printed specimen. Cored samples,

however, showed moderate stiffness but higher variability, which is probably due to the anisotropic nature of printed layers. In general, these findings suggest that both fabrication methods and filler types have a significant impact on the results, and that cored samples fall between rodded and vibrated samples.

- Statistical analyses conducted in this research showed that the mixture type (whether C-So or C-Sa) can significantly influence the early-age compressive strengths. For cubes, p-values < 0.05 are found for 3-day ($p = 0.000$) and 7-day ($p = 0.002$). Regardless, as the curing age increases, the effect of the mixture also becomes less impactful. Compressive strength results cured for 14-day ($p = 0.147$), 56-day ($p = 0.688$), and 91-day ($p = 0.989$) all show P values above the 0.05 threshold (meaning that they are statistically insignificant). These findings suggest that the effect of mixture type on compressive strength is rather time-dependent, especially in cube samples. For cylindrical samples, the mixture type remains significant throughout different curing ages. This difference could have been caused by the larger sample size of cylinders that have lower sensitivity to different variables (e.g., mixing and printing). In terms of preparation methods, a significant effect on compressive strength across all samples ($p < 0.05$) is recorded. In particular, Levene's test indicates that variance homogeneity is generally satisfied ($p > 0.05$), except for absorption results of cubic samples ($p = 0.000$) and 3-day cured compressive strength of cylindrical samples. Both of these have been found significant in Welch's ANOVA based on the p-values for the mixtures, but not the methods. This shows that hydration and overall absorption are more closely related to the component mixture (e.g., soil vs. crushed sand) than to the sampling methodology.

The following provides a few examples of issues encountered or quantified by this study and can be used for future studies:

- **Strength development expectations and demolding:** It is a common practice in concrete testing methodologies to demold samples after 24 hours. However, 3D printing mixtures have a different rheology and strength development rate. In general, a higher initial and a lower final setting strength are required. This difference from ordinary concrete mixes originates from the self-supporting need and nature of 3D printing. This requires a change in sample demolding time from 24 hours to perhaps a different timeframe. Similarly, often, the 28-day strength is considered when cementitious materials reach their major strength values. However, for 3D printing mixtures, depending on the cementitious material used (e.g., in this study, fly ash content), this can be the 56-day strength. Also, 3-day and 56-day strength values are important due to the strength and printing requirements. Future studies can develop a comprehensive matrix of designing and testing various differences in this area, depending on the binder content and other materials used. As practiced in this study, 48-hour demolding may be a better approach for 3D-printed specimens to achieve sufficient strength and avoid damage during the demolding of the samples.

- **Common expectations:** The conventional empirical relationships used for ordinary concrete and mortars, such as those linking porosity to strength or density, do not accurately describe the behavior of 3D-printed materials. This is because the microstructure of 3D-printed elements is governed by a non-uniform pore distribution that

develops along the printed layers, rather than following the relatively homogeneous and predictable patterns found in well-compacted concrete. As a result, a promising direction for future studies is to explore the influence of rheological and printing parameters on pore structure and mechanical performance, leading to new constitutive relationships and standards tailored specifically for 3D printing practices.

- **Iso- and Aniso-tropic behavior:** Unlike ordinary concrete, 3D printing appears to have a higher strength in the printing direction and a lower strength perpendicular to the printing direction. The ratio of the two is dependent on the randomness of the pore distribution and the type, content, and angularity of the mixed materials. Additionally, printing parameters and the particle size distribution of the mixed materials can play a major role, not only on anisotropy but also in the variability of the results. Based on these factors, future studies can focus on the feasibility of producing functionally graded materials (FGMs), in which the density or printing direction is intentionally varied in a given direction to achieve specific mechanical or durability performance. Such an approach could bridge the development of functional materials and performance-based design strategies in 3D-printed construction.

- **Large difference in rodding versus vibrating and printing:** Although it is expected that the reporting strength of 3D-printed mixtures should be comparable to industry practices, the results of this study showed otherwise: the fabrication method is a major factor in properties. On this basis, the type of sampling and curing to reduce the variability originating from the sampling and curing methods should be further studied. For instance,

future studies can focus on specific curing regimes applicable to 3D-printed components, which should be tested at larger scales to resemble actual structures.

6. Mechanical Properties and Printability Window of Low-Cement, Low-Fly-Ash, Soil-Based 3D-Printed Mixtures

This study maps the rheological printability window for soil-based (low-plasticity silt) mixtures with low cement and fly ash contents, without chemical admixtures. It offers technical insights into the key parameters that ensure successful printing, regardless of the printer's size or specific features. To achieve this, over 100 combinations of Portland cement (5-30%), fly ash (Class F; 0-30%), and water-to-solid ratios (w/s; 0.1-0.4) are investigated to determine a range of printable mixtures and their corresponding properties. Printable mixtures are then assessed for rheology (yield stress, dynamic viscosity), mechanical performance (directional compressive strength), and cradle-to-gate life-cycle impacts. Results show: (1) low-binder, admixture-free formulations can be 3D-printed while achieving acceptable fresh and hardened properties; (2) dynamic viscosity, shear stress, and yield stress provide quantitative bounds for printability, with printable mixtures spanning approximately 4.7×10^{3} to 1.48×10^{4} Pa·s (dynamic viscosity), 1.36×10^{2} to 7.66×10^{2} N/m^2 (yield stress) and 8.46×10^{-1} to 4.28 N/m^2 (shear stress); (3) strength-normalized life cycle analysis (LCA) showed large differences among mixtures, with global warming potential (GWP) impacts ranging from 389-2017 kg CO_2 eq, total energy consumption (TEC) from 2021-10306 MJ, smog from 16.5-88.2 kg O_3 eq, and acidification from 0.8-4.3 kg SO_2 eq per functional wall; and (4) anisotropy in strength arises from both interlayer bonding and particle segregation during extrusion, motivating direction-aware design and testing for soil-based 3D-printed elements.

6.1. Introduction

3D printing of cementitious materials is a relatively new method for rapidly prototyping structural components. Developed initially by Khoshnevis et al. [253], [254] in the early 2000s [303], this method is based on a layer-by-layer construction of cementitious components. It can also be semi-autonomous and cost-competitive, as it avoids the use of formwork [196], [197], [304]. Although the value of 3D printing to the construction industry is considerable, there are currently major challenges in producing a successful 3D-printed component. For instance, previous studies have shown that a 3D printing mixture should have almost twice the binder content as conventional concrete to achieve rapid strength [49]. Rapid strength gain and buildability are essential to depositing subsequent layers without significant layer deformation. A review of previous studies' mixture proportions shows that at least until the year 2022 most mixture proportions relied heavily on chemical additives, such as viscosity-modifying agents, plasticizers, accelerators, shrinkage-reducing agents, and air-entraining agents, among others [49]. As a result, several previous studies have used various forms of supplementary cementitious materials (SCM) [49], clay [305], in addition to chemical additives to achieve printable mixtures [306], [307]. Many studies still struggle to achieve printable mixture rheology, as evident in previous studies [88], [308], [309], [310], [311]. For instance, Nerella and Mechtcherine (2019) [312] mentioned that for the mixture to be pumped properly, concrete needs to be flowable and have relatively low plastic viscosity and moderate yield stress. At the same time, to enable the layer-by-layer printing of concrete immediately after extrusion, it must cease being flowable and exhibit much higher yield stress and plastic viscosity. The authors also mention that a mixture capable of achieving the above, must be thixotropic, quick-setting, quickly hydrated, densely packed, and possess steerable rheological properties, such as static yield stress and plastic viscosity through internal or external triggers. As a result, and to support a pumpable mixture, coal fly ash

is widely used in the 3D printing of cementitious materials due to its spherical particle shape and the significant rheological benefits it provides. According to the literature, inclusion of fly ash results in a reduction of yield stress, plastic viscosity, and bleeding, while also enhancing thixotropy, and water retention [313], [314], [315], [316]. Given the benefits mentioned, fly ash is commonly included in 3D printing mixtures, as demonstrated by many studies [49].

However, in developing 3D-printed cementitious materials, researchers face two pressing challenges: improving environmental sustainability and identifying substitutes for coal fly ash, whose global availability has sharply declined in recent years [317]. As a result, SCMs, such as calcined clays [318], natural pozzolans (e.g., volcanic ash) [319], biomass ash [320], and various other byproducts (e.g., blast furnace slag) [321], [322], [323] are being used. These alternatives are often locally available, and they can offer comparable or even better performance under certain conditions (e.g., durability) [324], [325], [326]. For instance, [317] showed that the inclusion of 25-50% (per volume) glass powder instead of coal fly ash can enhance abrasion resistance up to 45% in a mortar mixture. However, since 3D printing is highly dependent on fresh rheological properties, these new materials should be used with careful consideration of 3D printing's rheological requirements, which vary based on the printer's nozzle size, extrusion method, and the size of particles in relation to the nozzle size. For instance, previous studies have reported that angular particles, and the ones that have a maximum size of roughly 1/5 of the nozzle diameter, can result in clogging and other printing issues [88], [327].

In this context, soil-based cementitious mixtures have been proposed in some studies due to the positive impact of clay particles on printability [328], [329]. Locally sourced soil can offer

many benefits and has been used for about eight thousand years in masonry construction [330]. Similarly, soil-based 3D printing is adopted from masonry construction [48], [331]. For over thousands of years [330], masonry units (e.g., adobe, cob, Compressed Earth Blocks (CEBs), and rammed earth) have been produced primarily from local soil (or earth). This old technology has recently re-emerged as a potential solution for reducing the content of processed materials (e.g., Portland cement with an estimated embodied carbon of approximately 0.8 kg CO_2 eq per kg used [208]) in the mixtures [332]. Using local soil can help increase buildability due to better compaction, increase yield stress, and it can also reduce the need for binder content when it is well-compacted and cohesive [333], [334], [335]. Another reason for using local soil is its aesthetic and cultural significance to many areas of the world. For instance, earthen construction has shaped building architecture for thousands of years, with examples ranging from adobe buildings in the American Southwest [9] to rammed earth temples in Asia [10] and cob settlements across Europe [11].

Despite the historical success of earthen construction, integrating soil into modern 3D printing practices introduces new challenges in formulation and standardization. While local soils offer some advantages, their use in 3D printing is not yet widely adopted due to concerns regarding rheology, early strength, and consistency in layer deposition. Prior work has primarily focused on enhancing printability through high binder contents or intensive use of chemical admixtures [49]. However, these approaches often contradict the underlying goals of sustainability and cost-efficiency that motivate the adoption of 3D printing in the first place.

Lyu et al. (2023) [336] demonstrated that natural soil can be utilized as a binder to partially replace cement in printing soil-based mortar. In the study, authors partially replaced natural sand content with soil, along with other ingredients, to help grow vegetation in soil-sand-based 3D-printed concrete. Kumar et al. (2025) [337] used low-clay soil as fine aggregates in 3D printing concrete. In the study, it was reported that the inclusion of soil led to a reduction of up to 15% in the flow value required for printing and increased open time by 13-60% compared to the control mixture. Both extrudability and buildability have also been reported to improve significantly. Soda et al. (2024) [338] used excavated soil to produce soil-cement mortar. The study reports that the plastic viscosity was reduced by 40-50% and the buildability significantly increased, as compared to a natural sand-based reference mixture, where buildability was measured as critical height to failure during printing. Other authors [207], [339], [340], [341] have advocated using soil- or clay-based materials for 3D printing, and have also pointed to the similar enhanced rheological properties of mixtures containing earth. For instance, Kumar et al. (2025) [337] used a locally sourced soil with 4% clay content to replace 30-50% natural sand by weight. Results showed that the inclusion of soil led to a reduction of up to 15% in the flow value required for printing and increased open time by 13–60% compared to the control mix. The authors also reported that both extrudability and buildability improved, as a result of including local soil and managed to print crack-free sections of more than 30 layers. Soda et al. (2024) [342] used a local soil with clay content of 42.5% to replace natural sand up to 25-50%. The authors also reported that non-expansive clay in the soil led to a steeper reduction in apparent viscosity, increased flow retention by 12–15 %, and lowered the plastic viscosity up to 50–60% for soil-based mixes. However, to date, no study has established the printable boundaries of soil-based 3D printing mixtures, nor have they evaluated those mixtures for their environmental impacts. This topic is fundamental

because: (a) 3D printing heavily relies on mixture rheology; (b) soil-based systems have unique particle size distribution, water requirements and minerology that is not as consistent as processed sand; (c) understanding rheological boundary for printing is essential in structural integrity and dimensional accuracy; (d) established rheological boundaries can help quantifying environmental impacts of soil-based systems; and (e) the absence of established rheological boundaries limits the scalability and adoption of soil-based mixtures due to uncertainty in hardened state properties of the printed components.

To address this gap, the current study investigates the feasibility of 3D printing low plasticity silt-based mixtures with minimal use of cement and fly ash. Rather than relying on a single optimized formulation, this research adopts a systematic approach of varying the content of ordinary Portland cement (5%, 10%, 20%, and 30%), fly ash (0%, 5%, 10%, 20%, and 30%), and w/s ratios (0.1 to 0.4). By testing more than 100 combinations using a single soil type (low-plasticity silt), the objective is to establish a bounded region of printability free of any chemical admixtures and independent of the printer's nozzle size. In doing so, the nozzle size was not treated as a parameter within the experimental region, and all mixtures were evaluated using the same 50.8 mm (diameter) extrusion nozzle to avoid coupling mixture performance with printer geometry. As a result, the proposed printability boundaries reflect intrinsic rheological thresholds of the mixtures rather than printer-specific effects. Such boundaries would define the underlying rheological thresholds at which a soil-based mixture becomes printable. Based on past research [343], [344], [345], dynamic viscosity, shear stress, and yield stress are selected to represent printability.

In addition to assessing fresh-state behavior, the hardened properties of successful mixtures are examined to ensure structural performance. Furthermore, a cradle-to-gate LCA is conducted to evaluate the environmental implications of each composition. The results demonstrate that sustainable performance is not solely dependent on substituting cement with byproducts, but also on optimizing the mixture as a whole to balance printability, mechanical performance, and environmental impacts. By defining both the upper and lower rheological limits for printability, this study provides a foundational reference for future development of soil-based 3D printing mixtures, particularly those aimed at reducing binder content without compromising print quality or performance.

6.1.1. Novelty and Relevance

This study addresses three research questions: First, it aims to establish printable rheological boundaries for 3D-printed soil-based mixtures with low cement and low fly ash proportions. The boundaries provided include the basic but fundamental parameters, such as dynamic viscosity to indicate a material's resistance to flow (or shape retention), shear stress to indicate nozzle clogging potential, and yield point to indicate the initiation of flow, which are considered. The mentioned parameters can help in identifying the printable region of mixture proportioning and provide a baseline for future studies. This is also the originality of the work to establish a printability window specific to soil-based, low-binder 3D-printed mortars because it is an area largely unexplored in existing research. Second, this study aims to demonstrate the feasibility of printing with low cement (5-30%) and fly ash content (0-30%), utilizing no chemical admixtures. This is done to highlight the importance of mixture granularity and particle size distribution, which can be addressed by using natural, unprocessed soil. The third research aim of this study is to connect the

properties studied with a cradle-to-gate LCA to show the comparative strength of environmental impact for each mixture. This can help future studies to design mixtures with a better understanding of their environmental impacts.

This study is relevant because it quantifies a printability window for soil-based (low-plasticity silt), 3D-printed mortars, linking rheology to extrudability (flow through the nozzle) and buildability (shape retention/stacking). These criteria enable the optimization of mixtures using locally available soils and lay the groundwork for automated, data-driven mixture design.

6.2. Materials and Equipment

The following subsections discuss the material properties used in this study.

6.2.1. Soil

The natural soil used in this study was sourced from Ace Hardware in Davis, California. It was reported by the supplier that, to reduce organic content, the soil was extracted from subsurface layers several meters below ground level. The soil was then mechanically sieved using a TS-1 Gilson shaker to achieve a maximum particle size of 1.18 mm (No. 16 sieve), per ASTM C136-14 [132]. The coarser materials were discarded. The size of 1.18 had been chosen by the authors based on trials conducted on the mixtures and the printer used to produce components in this study. Following sieving, the materials were oven-dried at 110°C for 24 hours to minimize residual moisture and remove any organic content. The materials were then placed in a sealed dry bucket until used. The temperature was adopted per ASTM C136-14 [133] and ASTM D2216-19 [134].

Additional characterization, including particle size distribution, Atterberg limits, and compaction behavior (Proctor test), is presented in **Table 33**. Based on these results and classification under ASTM D2487-11 [135] and Unified Soil Classification System, the soil was identified as a low-plasticity silt (ML). In this study, sieve analysis was conducted in accordance with ASTM C117/C136 to characterize soil, and the soil was washed per ASTM D6913-17 [136]. The original dry mass of the sample was 1336.30 g, and the wash mass was 521.90 g, resulting in a wash loss of 60.9%. These standards were used in place of the ASTM D7928 [143] hydrometer method, which requires specialized equipment; therefore, the reported gradation reflects sieve-plus-washing characterization rather than full sedimentation-based classification.

Table 33. Physical properties of soil.

Laboratory tests	Standards	Property	Value
Particle-size analysis	ASTM C117-17 [137] , C136-14 [132], D6913-17 [136]	Cumulative % Retained #4 (4.75mm)	0.0
		Cumulative % Retained #8 (2.36mm)	0.0
		Cumulative % Retained #10 (2mm)	0.0
		Cumulative % Retained #16 (1.18mm)	0.0
		Cumulative % Retained #30 (0.6mm)	8.2
		Cumulative % Retained #40 (0.425mm)	14.0
		Cumulative % Retained #50 (0.3mm)	19.0
		Cumulative % Retained #100 (0.15mm)	29.4
		Cumulative % Retained #200 (75µm)	38.1

		Pan	100.0
Atterberg limits	ASTM D4318-10 [138]	Liquid limit LL (%)	20.8
		Plastic limit PL (%)	13.9
		Plasticity index PI (%)	6.8
Soil compaction tests	ASTM D698-21 [139]	Optimum moisture content (%)	13.0
		Maximum dry density (kg/m3)	1,873.3

6.2.2. Fly ash and Portland Cement

The coal fly ash class F used in this study was supplied by Paragon-Aggregate Products Corp. in Glendale, Arizona. The Portland cement used in this study was obtained from the Nevada Cement group in Reno, Nevada. The result of the mill certificate is presented in **Table 34**. To ensure that the composition of all SCMs is recorded, X-ray fluorescence (XRF) analysis of the cementitious materials was conducted using a Rigaku Super Mini-200 and analyzed using the manufacturer's provided software, ZSX. The method of calculating the oxides was recommended by the manufacturer [141], which is a semi-quantitative XRF (also called SQX). The XRF results are presented in **Table 35**.

Table 34. The result of mill certificate provided by Nevada Cement Inc.

Phase composition	Percent content (%)
Tricalcium silicate (C_3S)	58
Dicalcium silicate (C_2S)	18
Tricalcium aluminate (C_3A)	7
Tetracalcium aluminoferrite (C_4AF)	9

Table 35. The XRF result of cementitious materials used in this study

Chemical compounds	Fly ash (F)	Soil (low plasticity silt)
SiO_2 (%)	58.9	60.5
Al_2O_3 (%)	17.4	12.0
Fe_2O_3 (%)	8.2	6.1
CaO (%)	7.0	3.2
MgO (%)	1.2	2.0
SO_3 (%)	0.8	0.5
Na_2O (%)	1.0	0.8
K_2O (%)	3.5	1.5
LOI (%)	1.5	8.1

6.2.3. Mixing Water

The mixing water was sourced locally from Davis, California, with a pH of 8.66, a salinity of 0.19 ppt, and a total dissolved solids (TDS) concentration of 270 mg/L.

6.2.4. 3D Printer

A Scara Elite 3D printer from 3D Potter's Inc., located in Palm City, FL, was used in this study. The 3D printer had a nozzle with a circular diameter of 50.8 mm and operated based on an auger system with a constant printing speed of 15 mm/s. **Figure 31** shows the printer and a soil-cement composite made during the study.

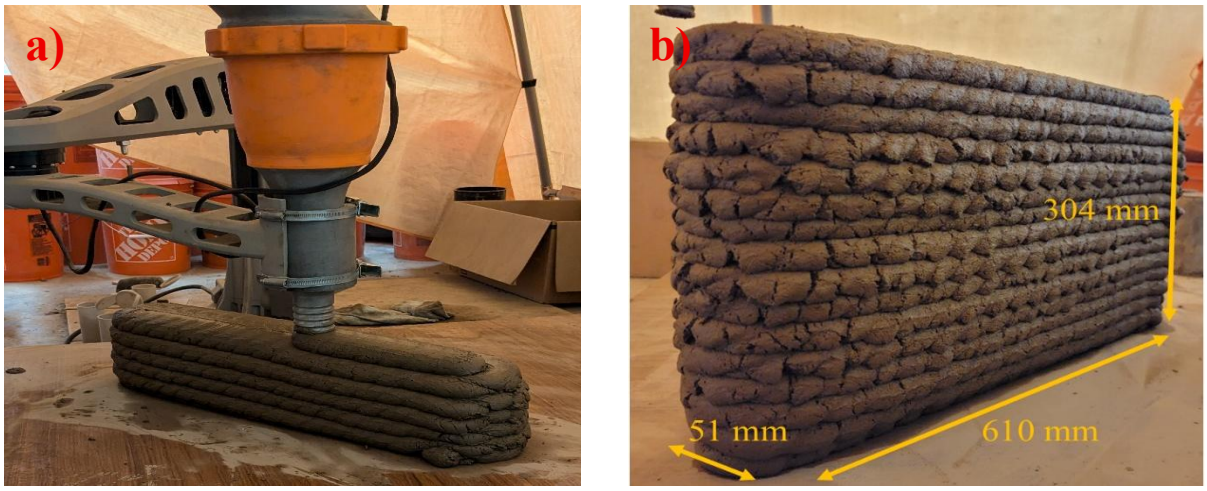


Figure 31. Showing (a) Scara Elite Printer and (b) a printed sample.

6.2.5. Viscometer

In this study, rheological properties of the fresh 3D-printed mixtures were characterized using a rotational viscometer (Anton Paar, Model 300H [346]). The instrument has a viscosity measurement range of 24 to 3.2×10^8 mPa·s. A vane spindle (V-73) was employed throughout testing, with spindle and yield measuring constants of 53.5 and 10, respectively. The vane spindle is 51 mm long, with a radius of 6.33 mm.

During testing, the viscometer records the applied torque (M) and the rotational speed (N). These raw measurements are converted, using the manufacturer's software (APConnect v3.1.1), to shear stress (τ) and shear rate (γ) using spindle-specific geometry. For a vane of radius R and height H, shear stress is calculated as:

$$\tau = \frac{M}{2\pi R^2 H} \qquad \text{Eq. 4}$$

This formula directly relates the measured torque to the average shear stress acting on the sample. The corresponding shear rate is obtained from the rotational speed using a manufacturer-supplied geometry-dependent conversion factor. To characterize the flow behavior, stepped shear rates within the instrument's operating range are then applied, and the resulting shear stress–shear rate data are plotted as flow curves. These data are then fitted to the Bingham plastic model:

$$\tau = \tau_0 + \mu_p \gamma \qquad \text{Eq. 5}$$

where τ_0 is the yield stress and μ_p is the plastic (dynamic) viscosity. These two rheological parameters are obtained from a linear regression analysis of the flow curve data generated by the software.

During the testing, the viscometer was placed on its adjustable stand, checked, and leveled. The V-73 vane spindle was then tilted slightly, inserted into the center of the specimen surface, and carefully attached to the instrument, ensuring no side pressure on the shaft to avoid misalignment. The spindle was immersed until the immersion mark on the shaft just touched the sample surface, after which the container was centered relative to the spindle. At that point, the program was started that would initiate the rotation of the spindle, automatically, such that the torque reading fell within 10–100% of the instrument's scale, with preference toward mid-scale values to improve accuracy. The viscometer was allowed to rotate until a stable torque reading was obtained, and the corresponding torque and viscosity values were then automatically recorded.

During the entire testing process, measurements were taken at a constant laboratory temperature of 25±5°C to ensure consistency in the results.

6.3. Mixtures, Methods, and LCA

The following subsections discuss the mixture proportioning selected for this study, the tests conducted, and the methodology employed.

6.3.1. Mixture Proportions

In this study, a total of 100 mixture proportions have been produced and tested for printability, which included ratios of 30%, 20%, 10%, and 5% for Portland cement and 30%, 20%, 10%, and 5% for fly ash. With the mentioned mixture proportions, water-to-solid ratios of 0.4, 0.3, 0.2, 0.15, and 0.1 have also been produced. These ranges were selected to capture both low and moderate binder proportions and to identify the minimum cement and fly ash contents capable of achieving printable consistency. A mixture was classified as "printable" if it could be continuously extruded through the 50.8 mm diameter nozzle without tearing or clogging, and if the deposited filament retained its shape without excessive deformation or collapse. These criteria reflect the two core requirements of 3D printing: extrudability, which refers to continuous extrusion, and buildability, which refers to shape retention after extrusion. The list of all mixtures is included in **Table 36**. Among the 100 mixtures, 13 were found to be printable and are included in **Table 37**. The water content calculations included adding sufficient additional water to reach the optimum moisture content for the soil (i.e., 13.06%), found through the proctor compaction test as specified by ASTM D698-21 [139]. The mixture names or labels have been created based on the percent fly ash content

(designated as F), the percent cement (designated as P), and the water-to-solid ratio (designated as W). For instance, 0F5P0.2W refers to a soil-cement composite with 0% fly ash and 5% Portland cement and a water-to-solid ratio of 0.2.

Table 36. The total of 100 mixtures tested in this study for printability (normalized per 1000 g mass).

Number	Mixture Name	Water (g)	Fly ash F (g)	Portland cement (g)	Soil (g)
1	0F5P0.4W	335.4	0.0	31.7	632.9
2	0F5P0.3W	290.5	0.0	33.8	675.7
3	0F5P0.2W	239.1	0.0	36.2	724.6
4	0F5P0.15W	210.5	0.0	37.6	751.9
5	0F5P0.1W	179.7	0.0	39.1	781.3
6	0F10P0.4W	325.2	0.0	61.4	613.5
7	0F10P0.3W	281.1	0.0	65.4	653.6
8	0F10P0.2W	230.8	0.0	69.9	699.3
9	0F10P0.15W	202.9	0.0	72.5	724.6
10	0F10P0.1W	172.9	0.0	75.2	751.9
11	0F20P0.4W	306.4	0.0	115.6	578.0
12	0F20P0.3W	263.8	0.0	122.7	613.5
13	0F20P0.2W	215.7	0.0	130.7	653.6
14	0F20P0.15W	189.2	0.0	135.1	675.7
15	0F20P0.1W	160.8	0.0	139.9	699.3
16	0F30P0.4W	289.6	0.0	163.9	546.5
17	0F30P0.3W	248.6	0.0	173.4	578.0
18	0F30P0.2W	202.5	0.0	184.1	613.5
19	0F30P0.15W	177.2	0.0	189.9	632.9
20	0F30P0.1W	150.3	0.0	196.1	653.6

21	5F5P0.4W	325.2	30.7	30.7	613.5
22	5F5P0.3W	281.1	32.7	32.7	653.6
23	5F5P0.2W	230.8	35.0	35.0	699.3
24	5F5P0.15W	202.9	36.2	36.2	724.6
25	5F5P0.1W	172.9	37.6	37.6	751.9
26	5F10P0.4W	315.5	29.8	59.5	595.2
27	5F10P0.3W	272.2	31.7	63.3	632.9
28	5F10P0.2W	223.0	33.8	67.6	675.7
29	5F10P0.15W	195.8	35.0	69.9	699.3
30	5F10P0.1W	166.7	36.2	72.5	724.6
31	5F20P0.4W	297.8	28.1	112.4	561.8
32	5F20P0.3W	256.0	29.8	119.1	595.2
33	5F20P0.2W	208.9	31.7	126.6	632.9
34	5F20P0.15W	183.0	32.7	130.7	653.6
35	5F20P0.1W	155.4	33.8	135.1	675.7
36	5F30P0.4W	281.9	26.6	159.6	531.9
37	5F30P0.3W	241.6	28.1	168.5	561.8
38	5F30P0.2W	196.4	29.8	178.6	595.2
39	5F30P0.15W	171.8	30.7	184.1	613.5
40	5F30P0.1W	145.6	31.7	189.9	632.9
41	10F5P0.4W	315.5	59.5	29.8	595.2
42	10F5P0.3W	272.2	63.3	31.7	632.9
43	10F5P0.2W	223.0	67.6	33.8	675.7
44	10F5P0.15W	195.8	69.9	35.0	699.3
45	10F5P0.1W	166.7	72.5	36.2	724.6
46	10F10P0.4W	306.4	57.8	57.8	578.0
47	10F10P0.3W	263.8	61.4	61.4	613.5
48	10F10P0.2W	215.7	65.4	65.4	653.6
49	10F10P0.15W	189.2	67.6	67.6	675.7

50	10F10P0.1W	160.8	69.9	69.9	699.3
51	10F20P0.4W	289.6	54.6	109.3	546.5
52	10F20P0.3W	248.6	57.8	115.6	578.0
53	10F20P0.2W	202.5	61.4	122.7	613.5
54	10F20P0.15W	177.2	63.3	126.6	632.9
55	10F20P0.1W	150.3	65.4	130.7	653.6
56	10F30P0.4W	274.6	51.8	155.4	518.1
57	10F30P0.3W	235.0	54.6	163.9	546.5
58	10F30P0.2W	190.8	57.8	173.4	578.0
59	10F30P0.15W	166.7	59.5	178.6	595.2
60	10F30P0.1W	141.1	61.4	184.1	613.5
61	20F5P0.4W	297.8	112.4	28.1	561.8
62	20F5P0.3W	256.0	119.1	29.8	595.2
63	20F5P0.2W	208.9	126.6	31.7	632.9
64	20F5P0.15W	183.0	130.7	32.7	653.6
65	20F5P0.1W	155.4	135.1	33.8	675.7
66	20F10P0.4W	289.6	109.3	54.6	546.5
67	20F10P0.3W	248.6	115.6	57.8	578.0
68	20F10P0.2W	202.5	122.7	61.4	613.5
69	20F10P0.15W	177.2	126.6	63.3	632.9
70	20F10P0.1W	150.3	130.7	65.4	653.6
71	20F20P0.4W	274.6	103.6	103.6	518.1
72	20F20P0.3W	235.0	109.3	109.3	546.5
73	20F20P0.2W	190.8	115.6	115.6	578.0
74	20F20P0.15W	166.7	119.1	119.1	595.2
75	20F20P0.1W	141.1	122.7	122.7	613.5
76	20F30P0.4W	261.1	98.5	147.8	492.6
77	20F30P0.3W	222.8	103.6	155.4	518.1
78	20F30P0.2W	180.3	109.3	163.9	546.5

79	20F30P0.15W	157.3	112.4	168.5	561.8
80	20F30P0.1W	133.0	115.6	173.4	578.0
81	30F5P0.4W	281.9	159.6	26.6	531.9
82	30F5P0.3W	241.6	168.5	28.1	561.8
83	30F5P0.2W	196.4	178.6	29.8	595.2
84	30F5P0.15W	171.8	184.1	30.7	613.5
85	30F5P0.1W	145.6	189.9	31.7	632.9
86	30F10P0.4W	274.6	155.4	51.8	518.1
87	30F10P0.3W	235.0	163.9	54.6	546.5
88	30F10P0.2W	190.8	173.4	57.8	578.0
89	30F10P0.15W	166.7	178.6	59.5	595.2
90	30F10P0.1W	141.1	184.1	61.4	613.5
91	30F20P0.4W	261.1	147.8	98.5	492.6
92	30F20P0.3W	222.8	155.4	103.6	518.1
93	30F20P0.2W	180.3	163.9	109.3	546.5
94	30F20P0.15W	157.3	168.5	112.4	561.8
95	30F20P0.1W	133.0	173.4	115.6	578.0
96	30F30P0.4W	248.8	140.9	140.9	469.5
97	30F30P0.3W	211.8	147.8	147.8	492.6
98	30F30P0.2W	171.0	155.4	155.4	518.1
99	30F30P0.15W	148.9	159.6	159.6	531.9
100	30F30P0.1W	125.7	163.9	163.9	546.5

Table 37. Mixture proportions found to be printable (normalized per 1000 g mass).

Mixture Name	Water (g)	Fly ash F (g)	Portland cement (g)	Soil (g)
0F10P0.2W	230.8	0.0	69.9	699.3
0F20P0.2W	215.7	0.0	130.7	653.6

5F5P0.2W	230.8	35.0	35.0	699.3
10F5P0.2W	223.0	67.6	33.8	675.7
10F10P0.2W	215.7	65.4	65.4	653.6
5F10P0.2W	223.0	33.8	67.6	675.7
5F30P0.3W	241.6	28.1	168.5	561.8
10F30P0.3W	235.0	54.6	163.9	546.4
20F20P0.3W	235.0	109.3	109.3	546.4
20F30P0.3W	222.8	103.6	155.4	518.1
30F5P0.3W	241.6	168.5	28.1	561.8
30F10P0.3W	235.0	163.9	54.6	546.4
30F20P0.3W	222.8	155.4	103.6	518.1

6.3.2. Testing matrix

Table 38 shows the tests performed in this study and the standards followed. For each test, at least 5 samples were produced and tested only for mixtures classified as printable. The non-printable mixtures were evaluated only in the fresh state (extrudability and shape retention) and were not cast or printed for mechanical testing. The reason that at least five samples have been tested is to ensure a standard deviation is derived from the tested samples. For the duration of the tests, the same equipment and crew members were used to ensure consistency in procedures and minimize variability in the results. For the compressive strength tests, 50×50×50 mm cubic samples have been made and cored from freshly printed mortars. The coring process is performed

using a bottomless cylindrical or cubic mold, which is gently pressed into the freshly printed filament to extract material of the desired geometry without disturbing the layered structure of the freshly printed component. It is important to note that the term coring used here follows the notation commonly used in literature (e.g., [291], [292], [293] for the process described above. For this purpose, the printed shape is also shown in **Figure 31** (b) with the specified dimensions.

All other tests have been conducted using cored samples from freshly printed parts, except for fresh property tests, such as pH, flow table, and viscosity tests, which were conducted within 2-3 minutes after mixing. Also, all samples were cured under lab conditions at 25±5°C and 50±10 % relative humidity to minimize variability. During the curing stage, all samples were kept in the mold for an initial duration of 48 hours to ensure that they would not be damaged upon demolding and have sufficient strength. After demolding, specimens were stored in the laboratory under the same ambient conditions (~25±5°C and 50±10%) until the designated testing ages

Table 38. Tests and the standards that followed in this study.

Test*	Standard	Curing age (day)
Sieve analysis	ASTM C117-17 [137] , C136-14 [132], D6913-17 [136]	-
Atterberg limits	ASTM D4318-10 [138]	-
Proctor compaction	ASTM D698-21 [139]	-
Fresh density	ASTM C138-13 [347]	-
Mini-slump	ASTM C143-14 [348]	-
pH	ASTM D4262-18 [144]	-
Flow table	ASTM C230-10 [349]	-
Viscosity properties	ASTM D2196-20 [350]	-
Anisotropic behavior	ASTM C109-16 [148]	28

Compressive strength	ASTM C109-16 [148]	7, 14, 28
Life cycle analysis	ISO 14040 [351, p. 14040]	-

*Sieve analysis conducted on soil and sand; Atterberg limits and proctor compaction conducted on soil samples; fresh density, mini-slump, pH, flow table, and viscosity tests were conducted on freshly mixed materials; Anisotropic behavior, and compressive strength were conducted on hardened samples;

6.3.3. Statistical Analysis, Quality Assurance, and Quality Control

All experimental results were statistically analyzed to assess consistency, variability, and significance across different mixtures. For each group, the mean, standard deviation (STD), and coefficient of variation (COV) were computed using Microsoft Excel 2024. To perform a detailed pairwise comparison, MATLAB R2024a, developed by MathWorks Inc., was used. In the analysis, first, the Shapiro-Wilk test was used to evaluate the normality of each group. If both groups were found to follow a normal distribution, Levene's test was applied to determine variance homogeneity. Based on the outcomes, either a standard two-sample t-test (for equal variances) or a Welch's t-test (for unequal variances) was used. In cases where normality was not satisfied in either group, a non-parametric Mann-Whitney U test was conducted. All tests were performed using a significance level of $\alpha = 0.05$. Results are consistently reported throughout the manuscript as mean ± standard deviation, alongside their corresponding p-values, regardless of statistical significance. Similarly, for a fair comparison between different mixtures, the standard deviations and coefficient of variations (COV) are also reported throughout the manuscript whenever a comparison is made.

For quality assurance, this study strictly followed the standardized tests and procedures established by the American Society for Testing and Materials (ASTM). All equipment used for

preparing, curing, and testing was recalibrated according to the manufacturer's specifications before use. In cases of non-standardized procedures, reference materials and previous research studies were reviewed and cited, and credible justifications were provided in the methodology sections. Additionally, the temperature and humidity during the specimen curing and testing phases were maintained at similar levels across all mixtures.

In terms of quality control, all tests were conducted by the same crew members and with the same instruments to minimize other sources of variability during data collection. Generally, for each test, at least 5 specimens were prepared to ensure that no outliers in the reporting data would affect the results. Specimens that exhibited signs of physical damage or had been subject to handling errors were identified as outliers and excluded from the analysis. Such outliers were then also removed from the final statistical analysis to prevent them from impacting the results. This approach ensured that the reported findings accurately reflected the behavior of the 3D-printed specimens under investigation. Also, in each figure, the reported mean is followed by ± calculated STD. A similar reporting method is used to explain the results.

6.3.4. Life cycle analysis (LCA)

In this section, the methodology of doing LCA is explained.

6.3.4.1. System definition and boundaries

To conduct the LCA, the system boundary for the study was chosen to represent a cradle-to-gate condition, which includes: (a) raw material extraction and processing, and (b) transportation of processed materials to the mixing/production site. It is essential to note that, since the

construction stage remains consistent across all mixtures considered in this study and the focus is on the environmental effects of different mixtures, the construction phases are not examined.

To evaluate the life cycle environmental impacts of producing 3D-printed structural walls using soil-based mixtures, a scale-up from laboratory conditions to industrial-scale production was performed. The functional unit adopted in this study is the quantity of materials required to print a 1 m (height) × 1 m (length) wall with a thickness of 0.1 m. This functional unit was selected because it represents a realistic and directly comparable structural element that can be printed under identical boundary conditions, reflecting the primary function of the product to act as a load-bearing wall segment. By fixing the wall geometry, the functional unit ensures that all mixtures are evaluated on an equivalent physical basis, while preserving practical relevance to construction-scale applications. The selected dimensions are consistent with typical experimental or pilot-scale 3D printing setups and can be readily scaled to larger structural systems. Furthermore, this choice aligns with recent developments in additive manufacturing of prefabricated structural components, as several studies have focused on 3D printing discrete wall segments intended for assembly in modular construction [244], [245]. Therefore, adopting a wall section as the functional unit provides both a structurally meaningful and practically applicable basis for comparison among the investigated mixtures.

Given that each mixture achieves a distinct 28-day compressive strength, the thickness of the wall is proportionally adjusted based on the ratio of each mixture's strength and that of 17.24 MPa (2500 psi), which has been taken as the recommended minimum structural concrete strength [352, p. 318]. Previous studies have conducted similar calculations to capture a more realistic

environmental impact [155], [156] and have referred to it as a strength-normalized functional unit [244] (hereinafter referred to as strength factor). However, recognizing that several authors (e.g., [157]) have cautioned against defining the functional unit solely on material properties (and since this may not fully represent the material's intended function in a specific end-use or structural context), both the declared-unit results (per wall volume) and the strength-normalized results are presented and discussed in parallel to provide a comprehensive assessment. To apply the strength correction factor, the average 28-day strength of each mixture is divided by the minimum recommended strength of 17.24 MPa (as mentioned above), and the inverse of this ratio is multiplied by the original wall thickness of 0.1 m. The results are noted under the column wall thickness of **Table 39**. The wall is assumed to be made onsite, at the coordinates 38°41'31.5"N 121°30'54.8"W (near Sacramento, CA). **Table 39** provides more information on the amounts of materials used per mixture to produce a wall.

Table 39. Materials quantity needed for the functional unit of each mixture.

Mixture	Equivalent wall thickness (m)*	Density of mixtures (kg/m³)	Material needed for full unit (kg)	Water (kg)	Fly ash F (kg)	Portland cement (kg)	Soil (kg)
0F10P0.2W	6.1	1911.1	11601.4	2677.6	0.0	813.3	8110.5
0F20P0.2W	1.6	1918.0	3066.2	674.6	0.0	408.7	1982.9
5F5P0.2W	13.1	1891.2	24726.0	5489.2	830.8	830.8	17572.8
5F10P0.2W	6.3	1887.0	11800.3	2578.4	390.6	781.2	8050.2
5F30P0.3W	2.2	1918.9	4137.0	1052.5	122.5	732.3	2229.9
10F5P0.2W	13.8	1871.0	25733.5	5622.8	1703.6	851.8	17555.4
10F10P0.2W	17.4	1965.6	34297.9	7075.6	2143.6	2143.6	22935.0
10F30P0.3W	1.7	1934.0	3294.8	833.6	193.7	580.9	1686.6

20F20P0.3W	2.6	1895.8	5011.7	1275.0	593.4	593.4	2550.0
20F30P0.3W	1.5	1883.4	2908.4	718.9	334.2	501.4	1353.8
30F5P0.3W	11.0	1836.7	20294.2	5162.8	3592.1	598.7	10940.6
30F10P0.3W	5.9	1843.1	10951.9	2770.8	1930.8	644.0	5606.3
30F20P0.3W	2.8	1855.5	5196.7	1284.6	895.9	597.1	2419.0

*Applied only when considering the strength normalization factor; otherwise, the original thickness of 0.1 m is considered.

6.3.4.2. Life Cycle Inventory (LCI)

The LCI used in this study is based on the database Tool for the Reduction and Assessment of Chemical and other Impacts (TRACI v2.1) [158], which provides midpoint-level impact categories relevant to U.S.-based assessments. **Table 40** provides the GWP of all materials used in this study. This framework was selected to ensure consistency with established methods and comparability with previous research. The following subsections provide more details on the assumptions made in this study and the methods used to calculate soil excavation and transportation of the materials to the construction site.

Table 40. GWP of all materials used in LCA calculations.

Diesel combusted in industrial equipment (per kg diesel used)	Sodium hydroxide (per 1 kg)	Sand production (per 1 kg)	Electricity; at user; consumption mix - 2022 US (per 1 MJ)	Portland cement (Type I/II), (per 1 kg)	Combination diesel powered truck transport (per 1 kg-km)
3.88E+00	1.04E+00	4.89E-03	1.39E-01	9.19E-01	9.40E-05

6.3.4.3. Soil Excavation

Local soil is excavated using a diesel-powered 20-metric ton excavator (model Deere 210G LC) with a fuel consumption of approximately five gallons of diesel per hour (MPG), equivalent to 16.2 kg h^{-1} assuming a diesel density of 0.85 kg L^{-1}. Based on consultations with industry professionals, the excavator's production rate is estimated at 25 m^3 h^{-1}. With an assumed bulk density of 1500 kg m^{-3}, this corresponds to 37500 kg of soil excavated per hour. The soil is assumed to be taken from about 1 m below the surface to minimize organic matter content; however, since this depth is typical for foundation preparation, no additional energy is assigned for digging below ground level.

To account for the environmental impacts of soil excavation, a diesel-to-soil productivity ratio was calculated to relate the mass of soil excavated to the amount of diesel combusted. The excavator's productivity corresponds to 2314.8 kg of soil per kg of diesel, derived from the ratio of 37500 kg soil h^{-1} to 16.2 kg diesel h^{-1}. Accordingly, for every kilogram of soil used in the mixtures, the diesel requirement was determined as:

$$\text{Diesel required (kg)} = \frac{\text{Soil mass (kg)}}{2314.8} \qquad \text{Eq. 6}$$

This calculated diesel mass was then multiplied by the corresponding unit impacts of diesel combustion in each environmental category to obtain the total contribution of soil excavation to the life-cycle results.

6.3.4.4. Transportation

For transportation, a heavy-duty truck with a gross vehicle weight rating of approximately 32 metric tons was assumed for transporting secondary materials, covering the distance from the supplier to the construction site. A fuel consumption of five miles per gallon (MPG) was assumed.

The energy required for transportation was subsequently calculated based on the weight of the materials. Since transporting machinery for 3D printing was considered to be similar across different mixtures, the corresponding energy consumption was excluded from the LCA calculations. The calculation included multiplying the distance by the LCI value for transporting the specified amount of material per MPG, as discussed in the subsequent section.

6.3.4.5. LCA Calculations

For the LCA calculations, the following four impact categories were selected due to their relevance to construction materials. First, GWP (per unit of kg CO_2 eq) was chosen since it captures greenhouse gas emissions related to climate change. Next, TEC (in MJ per unit) was selected, as it reflects the total energy required for each mixture. TEC is a crucial parameter, given the high energy intensity of binders. In addition, smog formation (kg SO_2 eq) has been selected to account for pollutants that degrade urban air quality. Finally, acidification (kg SO_2 eq), which measures emissions that cause acid rain and ecosystem damage, has been selected.

After establishing the wall size based on the strength factor and the hardened density (28-day) of each mixture, the amount of materials needed for each mixture is normalized. Based on that and the unit impact of each material, the amount of each material's impact in each mixture is then calculated. In doing so, the amount of materials needed is multiplied by their corresponding impacts for each mixture proportion. After calculating the impact of all materials for all the mixtures with and without the strength factor, transportation is calculated based on the distances noted in **Table 41**. Finally, all the corresponding impacts of materials production and shipment are summed up and analyzed.

Table 41. Kilometer distances from suppliers to the construction site considered in this study.

	Water (kg)	**Fly ash F (kg)**	**Portland cement (kg)**	**Soil (kg)**
Distance (km)	0	33	5.5	0

6.4. Experimental Results

The experimental results of this study are presented in the following sub-sections.

6.4.1. Flow Table, Fresh Density, and pH

The results of the fresh property tests, including the flow table, fresh density, and pH, are outlined in **Table 42**. Flow table results ranged from a low spread value of 151±20.6 mm (COV = 13.61%) for 5F30P0.3W to a larger value of 202±10.1 mm (COV = 5.01%) for 30F5P0.3W. The high flow spread in 30F5P0.3W is believed to be caused by high fly ash (30%) and high water-to-solid ratio (hereinafter referred to as 0.3W). When the flow spread results of 0.2W and 0.3W are

averaged, the spread values are found to be 175.3 mm and 186.0 mm, respectively, with a statistically significant difference ($p = 0.034$). In turn, when the results are grouped by the fly ash content of 0% as opposed to 30% (the lowest and highest contents), the results are found to be 174.5 mm and 191.3 mm, respectively. However, these differences were not statistically significant ($p = 0.068$), which may be due to variations in mixing or printing among different samples. Furthermore, when comparing the mixtures produced with 10% and 30% cement content, the results show an average of 183.6 mm versus 175.7 mm, respectively, with no statistically significant difference ($p = 0.676$). These results show that there is considerable variability in the addition of cement and fly ash particles, but not in water content, probably because of their impact on mixing.

In terms of fresh density, the results ranged from 1836.7±11.9 kg/m³, belonging to 30F5P0.3W (with COV = 0.65%), to 1965.6±21.9 kg/m³ (COV = 1.11%) from 10F10P0.2W, with a statistically significant difference ($p < 0.001$). On average, the 0.2W mixtures had a higher average density at 1907.3 kg/m³ than the 0.3W mixtures with 1881.1 kg/m³ ($p = 0.006$). A lower density shows an increased water and air content when a higher w/s ratio is used. Similarly, the 0% fly ash mixtures had a higher average density of 1914.6 kg/m³ when compared to their 30% fly ash-containing counterparts with an average of 1845.1 kg/m³ ($p < 0.001$). Interestingly, 30% Portland cement mixtures averaged 1912.1 kg/m³, which is slightly higher than the 1866.3 kg/m³ observed in 5% Portland cement mixtures, though the difference was not significant ($p = 0.435$). The higher fresh density of 30% Portland cement mixtures indicates that an increased cement content can marginally improve the solid mass per unit volume, although the effect is less pronounced compared to an increase in water or fly ash content.

In terms of pH, all mixtures maintained a highly alkaline environment, with pH values ranging from 11.2±0.07 (COV = 0.63%) in 30F5P0.3W to 12.3±0.07 (COV = 0.57%) in 0F10P0.2W (with $p = 0.000$) and 0F20P0.2W (with COV = 0.57% and $p = 0.000$), respectively. From these results, it can be stated that the high fly ash content reduced hydroxide ion availability through partial dilution of cement and enhanced pozzolanic consumption. The average pH value of mixtures containing a 0.2W ratio was 12.05, while those with a 0.3W ratio averaged 11.76 ($p < 0.001$). The higher pH of the 0.2W w/s ratio suggests that increasing water content can dilute the ionic concentration and alkalinity in the pore solution. Similarly, 0% fly ash containing mixtures averaged 12.3, while their 30% fly ash containing counterparts showed a significantly lower average of 11.67 ($p < 0.001$). This finding confirms that higher fly ash content reduced the alkalinity of the mixtures. Finally, 5% Portland cement mixtures had an average pH of 11.73, while 30% Portland cement mixtures had a higher pH of 11.83; however, the difference was not significant ($p = 0.070$).

Table 42. Chemical and fresh properties of mixtures used in this study.

Mixture name	Flow diameter (mm)	COV (%)	Fresh density (kg/m3)	COV (%)	pH	COV (%)
0F10P0.2W	184 (±24.7)	13.41	1911.1 (±19.4)	1.02	12.3 (±0.07)	0.57
0F20P0.2W	165 (±22.8)	13.80	1918.0 (±21.8)	1.14	12.3 (±0.07)	0.57
5F5P0.2W	184 (±18.0)	9.80	1891.2 (±18.7)	0.99	12.1 (±0.10)	0.83
5F10P0.2W	154 (±24.7)	16.02	1887.0 (±22.5)	1.19	11.8 (±0.07)	0.60

5F30P0.3W	151 (±20.6)	13.61	1918.9 (±20.6)	1.07	11.7 (±0.07)	0.60
10F5P0.2W	165 (±16.8)	10.16	1871.0 (±23.6)	1.26	11.9 (±0.07)	0.59
10F10P0.2W	200 (±20.6)	10.28	1965.6 (±21.9)	1.11	11.9 (±0.07)	0.59
10F30P0.3W	191 (±20.6)	10.76	1934.0 (±25.0)	1.29	11.9 (±0.07)	0.59
20F20P0.3W	201 (±10.4)	5.19	1895.8 (±10.9)	0.58	11.8 (±0.10)	0.85
20F30P0.3W	185 (±11.1)	5.98	1883.4 (±11.3)	0.60	11.9 (±0.07)	0.59
30F5P0.3W	202 (±10.1)	5.01	1836.7 (±11.9)	0.65	11.2 (±0.07)	0.63
30F10P0.3W	187 (±11.7)	6.26	1843.1 (±9.4)	0.51	11.9 (±0.07)	0.59
30F20P0.3W	185 (±9.5)	5.13	1855.5 (±10.8)	0.58	11.9 (±0.07)	0.59

6.4.2. Printability Limits

Table 43 shows the result of the printability test on the 13 printable mixtures. These parameters include (a) dynamic viscosity, (b) shear stress, (c) yield stress, and (d) apparent strain values. **Table 44** presents additional analyses of the results, including averages, maximum, and minimum values for each viscosity category. Based on the tables, the dynamic viscosity values ranged from 4.7×10^3 Pa·s ± 1.47×10^3 (COV = 31.3%, 10F30P0.3W) to 1.48×10^4 Pa·s ± 1.22×10^3 (COV = 8.22%, 10F5P0.2W), and this difference between the two mixtures was statistically significant ($p < 0.001$). The variation in viscosity of different mixtures likely results from differences in packing density, initial setting, and interparticle friction. When mixtures are compared based on their w/s ratios, the addition of water is found to reduce the viscosity values, probably due to better particle lubrication. For instance, mixtures with 0.2W had an average dynamic viscosity of 1.28×10^4 Pa·s

$\pm 2.28 \times 10^3$ (COV = 15.4%), while 0.3W mixtures had an average of 8.65×10^3 Pa·s $\pm 2.90 \times 10^3$ (COV = 61.7%), with the difference being statistically significant ($p < 0.001$). As expected, the increase in water content lowered viscosity and promoted easier flow.

In terms of the influence of fly ash, mixtures with 0% fly ash had an average dynamic viscosity of 1.36×10^4 Pa·s $\pm 2.0 \times 10^2$ (COV = 1.6%), compared to 8.80×10^3 Pa·s $\pm 3.14 \times 10^3$ (COV = 36.4%) for those with 30% fly ash, with the reduction being statistically significant ($p < 0.001$). The reduced values in mixtures with high fly ash content indicate a potentially better dispersion and reduced internal friction. The spherical morphology of fly ash particles, combined with the lower water demand of fly ash particles compared to soil or cement, can explain this behavior. On the other hand, mixtures with 5% Portland cement had a viscosity of 1.12×10^4 Pa·s $\pm 3.24 \times 10^3$ (COV = 23.8%), while those with 30% Portland cement exhibited a lower mean value of 8.94×10^3 Pa·s $\pm 3.78 \times 10^3$ (COV = 42.9%), and this difference between cement levels was significant ($p = 0.035$). The lowered dynamic viscosity shows that higher cement contents may promote better homogenization and reduce the system's resistance to flow under steady shear.

Shear stress values followed similarly consistent trends. The values ranged from a minimum of 0.85 N/m^2 $\pm 7.02 \times 10^{-2}$ (COV = 8.31%, 10F30P0.3W) to a maximum of 4.28 N/m^2 $\pm 1.29 \times 10^3$ (COV = 30.1%, 10F10P0.2W), and this difference was statistically significant ($p < 0.001$). Similarly, 0.2W mixtures averaged 3.60 N/m^2 $\pm$ 1.15 (COV = 26.9%), while 0.3W mixtures averaged 1.64 N/m^2 $\pm$ 0.71 (COV = 83.8%), with the reduction being highly significant ($p < 0.001$). These values suggest that mixtures with lower water content develop lower stress levels under shear, probably due to lowered interparticle friction. Mixtures with 0% fly ash had an average

shear stress of 3.81 N/m^2 ± 0.56 (COV = 15.6%), while those with 30% fly ash averaged 1.45 N/m^2 ± 0.48 (COV = 29.2%), with this reduction being statistically significant ($p < 0.001$). This finding again points to a consistent reduction in resistance with increased fly ash content. Interestingly, 5% cement mixtures had a mean shear stress of 2.32 N/m^2 ± 1.61 (COV = 42.2%), compared to 1.95 N/m^2 ± 1.01 (COV = 69.7%) for 30% cement mixtures, and this difference was also significant ($p < 0.001$).

In terms of yield stress, 10F30P0.3W had the lowest value with 1.36×10^2 N/m^2 ± 1.47 (COV = 1.08%, while 10F10P0.2W developed the highest with 7.66×10^2 N/m^2 ± 2.30×10^1 (COV = 3.0%, and their difference was statistically significant ($p < 0.001$). In terms of water content, mixtures with 0.2W showed a higher average yield stress of 6.40×10^2 N/m^2 ± 2.25×10^2 (COV = 29.4%), compared to 2.61×10^2 N/m^2 ± 1.28×10^2 (COV = 94.3%) for those with 0.3W, with their difference being significant ($p < 0.001$). The higher yield stress in 0.2W mixtures confirms that lower water content increases internal resistance to flow and increases the rigidity of mixtures at the start of deformation. It is also clear that the inclusion of coal fly ash had a significant impact. For instance, mixtures with 0% fly ash had a considerably higher average yield stress of 6.73×10^2 N/m^2 ± 1.22×10^2 (COV = 19.1%), compared to those with 30% fly ash with an average of 2.20×10^2 N/m^2 ± 7.24×10^1 (COV = 27.7%), and this reduction was also statistically significant ($p < 0.001$). The variations mentioned suggest that increased fly ash content reduces interparticle cohesion within the soil-cement matrix. Conversely, variations in cement content led to relatively smaller changes. For instance, mixtures with 5% cement showed a mean yield stress of 3.89×10^2 N/m^2 ± 3.22×10^2 (COV = 47.9%), while mixtures with 30% cement content yielded a slightly lower average of 3.24×10^2 N/m^2 ± 1.82×10^2 (COV = 82.7%), and this difference was also

significant ($p = 0.002$). These findings further confirm that higher cement content may provide only marginal improvements in early structural strength.

Apparent strain values ranged from 9.0×10^{-3} rad ± 9.68×10^{-4} (COV = 10.7%, 10F10P0.2W) to 2.95×10^{-1} rad ± 3.08×10^{-2} (COV = 10.4%, 5F5P0.2W), and this difference was statistically significant ($p < 0.001$). Mixtures with 30% and 5% cement showed averages of 0.235 rad ± 4.6×10^{-2} (COV = 20.9%) and 0.185 rad ± 0.15 (COV = 15.2%), respectively, with the difference being statistically significant ($p < 0.001$). This similarity points to a saturation threshold that exists in cement's controlling contribution to the deformation of the mixture. In other words, after a threshold is reached, its impact is likely to be amplified through a more complex behavior that influences other rheological properties, such as viscosity, particle packing, or thixotropy. Unlike the effect of cement, changes in fly ash content showed more noticeable effects. For example, mixtures with 0% fly ash developed an average apparent strain of 9.96×10^{-2} rad ± 1.06×10^{-1} (COV = 118%). Those with 30% fly ash, however, developed an average of 0.22 rad ± 6.73×10^{-2} (COV = 29.1%), with this increase being significant ($p < 0.001$). Water content also influenced deformation. For instance, mixtures with 0.2W developed an average strain of 8.95×10^{-2} rad ± 1.19×10^{-1} (COV = 40.3%), while 0.3W mixtures showed a higher value of 0.231 rad ± 4.86×10^{-2} (COV = 53.9%), and this difference was significant ($p < 0.001$). These observations highlight that although dynamic viscosity and yield stress govern flow initiation and resistance, apparent strain offers critical insight into post-yield deformation and shape retention, both of which are vital for ensuring geometric stability in 3D-printed layers.

Based on the rheological results of the thirteen mixtures and the interpretation provided, a printable window can be identified. In that regard, the mixtures that were successfully extruded without collapse or excessive deformation had a dynamic viscosity range of approximately 4.7×10^3 to 1.48×10^4 Pa·s, with the extremes being statistically significant ($p < 0.001$). This range provides sufficient resistance to flow while maintaining pumpability. Yield stress values between 1.36×10^2 and 7.66×10^2 N/m^2 were observed, and this range was also statistically significant ($p < 0.001$), providing enough cohesion to retain structural shape without causing excessive blockage or requiring excessive extrusion pressure. Similar to other parameters, apparent strain values remained below 0.295 rad across all mixtures, with the difference between the lowest (9.0×10^{-3} rad) and the highest value being significant ($p < 0.001$). Mixtures exceeding this strain threshold are more susceptible to slumping or lateral deformation after printing. On the other hand, very high yield stress values (e.g., $>7.0 \times 10^2$ N/m^2) or dynamic viscosities approaching 1.48×10^4 Pa·s can be associated with poor flow or increased risk of nozzle clogging. These findings provide a set of rheological limits for a printable soil-based mortar mixture.

Table 43. The viscosity limits of printable mixtures, with ± standard deviation and COV in parentheses.

Sample Name	Dyn. Visc. (Pa·s)	Shear Stress (N/m²)	Yield stress (N/m²)	Strain (rad)
0F10P0.2W	1.370E+04 ± 8.680E+02 (6.33E+00%)	3.410E+00 ± 8.000E-01 (2.35E+01%)	5.860E+02 ± 1.680E+00 (2.86E-01%)	1.740E-01 ± 3.100E-02 (1.78E+01%)
0F20P0.2W	1.340E+04 ± 1.760E+03 (1.31E+01%)	4.200E+00 ± 1.320E+00 (3.13E+01%)	7.590E+02 ± 2.300E+01 (3.03E+00%)	2.490E-02 ± 1.470E-03 (5.92E+00%)
5F5P0.2W	8.470E+03 ± 2.320E+03 (2.74E+01%)	1.350E+00 ± 1.950E-01 (1.44E+01%)	2.030E+02 ± 1.180E+00 (5.81E-01%)	2.950E-01 ± 3.080E-02 (1.04E+01%)
5F10P0.2W	1.230E+04 ± 9.890E+02 (8.03E+00%)	4.170E+00 ± 1.400E+00 (3.35E+01%)	7.620E+02 ± 2.220E+01 (2.92E+00%)	2.110E-02 ± 2.080E-03 (9.88E+00%)
5F30P0.3W	1.020E+04 ± 1.460E+03 (1.43E+01%)	2.820E+00 ± 7.700E-01 (2.73E+01%)	4.980E+02 ± 1.850E+00 (3.71E-01%)	2.410E-01 ± 3.240E-02 (1.35E+01%)
10F5P0.2W	1.480E+04 ± 1.220E+03 (8.22E+00%)	4.180E+00 ± 1.370E+00 (3.28E+01%)	7.610E+02 ± 2.340E+01 (3.07E+00%)	1.210E-02 ± 9.980E-04 (8.23E+00%)
10F10P0.2W	1.420E+04 ± 1.490E+03 (1.05E+01%)	4.280E+00 ± 1.290E+00 (3.01E+01%)	7.660E+02 ± 2.300E+01 (3.00E+00%)	9.020E-03 ± 9.680E-04 (1.07E+01%)
10F30P0.3W	4.700E+03 ± 1.470E+03 (3.13E+01%)	8.460E-01 ± 7.020E-02 (8.31E+00%)	1.360E+02 ± 1.470E+00 (1.08E+00%)	2.790E-01 ± 3.040E-02 (1.09E+01%)
20F20P0.3W	7.300E+03 ± 2.240E+03 (3.07E+01%)	1.270E+00 ± 2.990E-01 (2.35E+01%)	1.950E+02 ± 7.730E-01 (3.97E-01%)	2.520E-01 ± 3.180E-02 (1.26E+01%)

20F30P0.3W	1.190E+04 ± 1.270E+03 (1.06E+01%)	2.170E+00 ± 3.550E-01 (1.64E+01%)	3.390E+02 ± 2.710E+00 (8.00E-01%)	1.870E-01 ± 2.910E-02 (1.55E+01%)
30F5P0.3W	1.040E+04 ± 2.070E+03 (2.00E+01%)	1.440E+00 ± 3.500E-01 (2.43E+01%)	2.020E+02 ± 7.960E-01 (3.95E-01%)	2.470E-01 ± 3.240E-02 (1.31E+01%)
30F10P0.3W	5.180E+03 ± 1.640E+03 (3.17E+01%)	9.730E-01 ± 1.040E-01 (1.07E+01%)	1.580E+02 ± 3.370E-01 (2.13E-01%)	2.690E-01 ± 3.190E-02 (1.19E+01%)
30F20P0.3W	1.080E+04 ± 1.720E+03 (1.58E+01%)	1.930E+00 ± 3.360E-01 (1.74E+01%)	3.000E+02 ± 5.600E+00 (1.87E+00%)	1.430E-01 ± 2.460E-02 (1.72E+01%)

Table 44. The upper and lower limits of printable mixtures, ± standard deviation and COV in parentheses.

Mix name	Dyn. Visc. (Pa.s)	Shear Stress (N/m²)	Yield stress (N/m²)	Apparent strain (Rad)
Upper range	1.480E+04 ± 1.220E+03 (8.22E+00%)	4.280E+00 ± 1.290E+00 (3.01E+01%)	7.660E+02 ± 2.300E+01 (3.00E+00%)	2.950E-01 ± 3.080E-02 (1.04E+01%)
Lower range	4.700E+03 ± 1.470E+03 (3.13E+01%)	8.460E-01 ± 7.020E-02 (8.31E+00%)	1.360E+02 ± 1.470E+00 (1.08E+00%)	9.020E-03 ± 9.680E-04 (1.07E+01%)
Average 0.2W	1.28E+04 ± 2.28E+03 (1.54E+01%)	3.60E+00 ± 1.15E+00 (2.69E+01%)	6.40E+02 ± 2.25E+02 (2.94E+01%)	8.95E-02 ± 1.19E-01 (4.03E+01%)
Average 0.3W	8.65E+03 ± 2.90E+03 (6.17E+01%)	1.64E+00 ± 7.09E-01 (8.38E+01%)	2.61E+02 ± 1.28E+02 (9.43E+01%)	2.31E-01 ± 4.86E-02 (5.39E+02%)

Average 0% fly ash	1.36E+04 ± 2.00E+02 (1.56E+00%)	3.81E+00 ± 5.60E-01 (1.56E+01%)	6.73E+02 ± 1.22E+02 (1.91E+01%)	9.96E-02 ± 1.06E-01 (1.18E+02%)
Average 30% fly ash	8.80E+03 ± 3.14E+03 (3.64E+01%)	1.45E+00 ± 4.77E-01 (2.92E+01%)	2.20E+02 ± 7.24E+01 (2.77E+01%)	2.20E-01 ± 6.73E-02 (2.91E+01%)
Average 5% Portland cement	1.12E+04 ± 3.24E+03 (2.38E+01%)	2.32E+00 ± 1.61E+00 (4.22E+01%)	3.89E+02 ± 3.22E+02 (4.79E+01%)	1.85E-01 ± 1.51E-01 (1.52E+02%)
Average 30% Portland cement	8.94E+03 ± 3.78E+03 (4.29E+01%)	1.95E+00 ± 1.01E+00 (6.97E+01%)	3.24E+02 ± 1.82E+02 (8.27E+01%)	2.35E-01 ± 4.60E-02 (2.09E+01%)

6.4.3. Mechanical Properties

In this section, the compressive strength and anisotropic behavior of 3D-printed materials are presented and discussed.

6.4.3.1. Compressive Strength

Figure 32 shows the compressive strength results of all mixtures tested for 7, 14, and 28 days. At 7 days, the highest compressive strength was recorded for mixture 10F30P0.3W at 8.3 ± 0.7 MPa (COV = 8.4%), followed by 20F30P0.3W with 6.4 ± 0.12 MPa (COV = 1.9%, p = 0.000 vs 10F30P0.3W), and 0F20P0.2W with 6.1 ± 0.75 MPa (COV = 12.3%, p = 0.001 vs 10F30P0.3W). The lowest strength was obtained for mixture 10F5P0.2W at 0.8 ± 0.05 MPa (COV = 6.3%), which was lower than the mixture with 0% fly ash and 10% cement (0F10P0.2W) at 1.8 ± 0.36 MPa (COV = 20.0%, p = 0.003). The lower strength of 10F5P0.2W shows insufficient early-age hydration, probably due to the higher overall soil and fly ash content in the mixtures.

On the 14th day, the strengths improved considerably among all mixtures. 20F30P0.3W achieved the highest average strength at 9.5 ± 0.37 MPa (with a COV = 3.9%), followed closely by 0F20P0.2W at 8.9 ± 0.69 MPa (with a COV = 7.8%), with their difference not being significant (p = 0.137). Here again, the addition of fly ash has retarded the mixture's strength gain, as 0F20P0.2W showed higher values than 5F30P0.3W (p = 0.001) and 10F5P0.2W (p < 0.001). Mixture 5F30P0.3W also showed lower performance with 6.6 ± 0.85 MPa (and a COV = 12.9%), probably due to higher water content (0.3W) and the presence of 5% fly ash. The lowest strength at this age remained with 10F10P0.2W (with 0.9 ± 0.02 MPa, and a COV = 2.3%) and then 10F5P0.2W (with 1.0 ± 0.07 MPa, COV = 7.2%, and p= 0.021), both of which were significantly

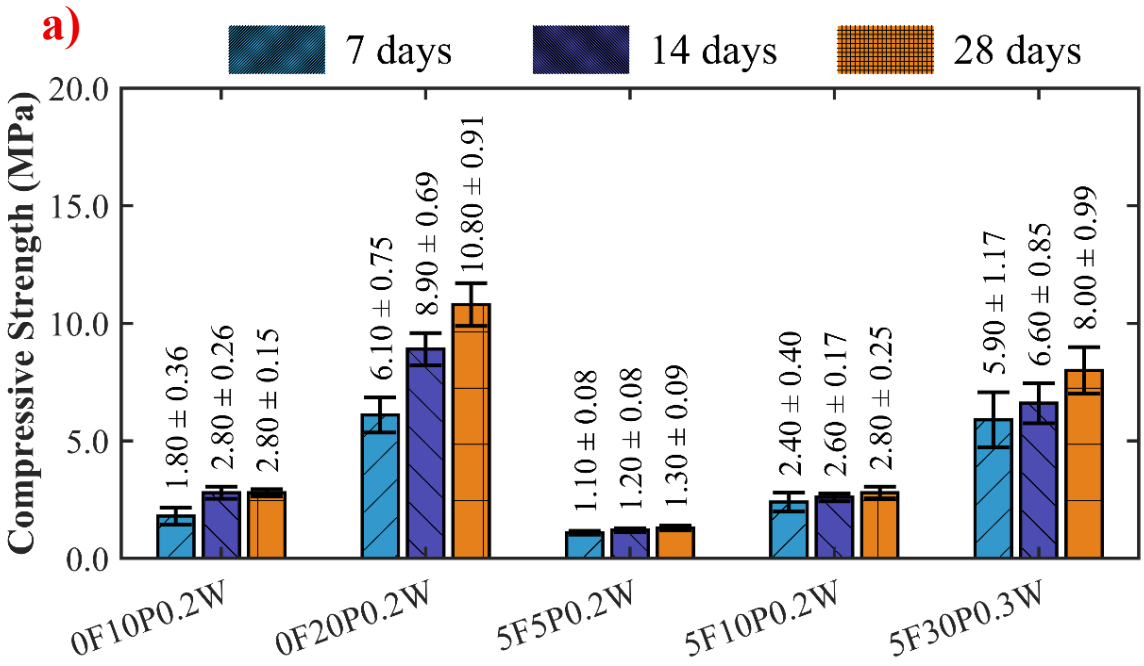
lower than 0F10P0.2W ($p < 0.001$). These results highlight that, for a given w/s ratio, the addition of fly ash and low-cement blends (e.g., 10F5P0.2W) shows very limited hydration at early stages. Previous studies (e.g., [353], [354]) reported similar performance and attributed it to a lack of calcium availability for pozzolanic reactions. It can also originate from the heterogeneity of soil particles, whose chemical composition and surface texture can significantly alter the bindability with the interfacial transition zone (ITZ) of different particles.

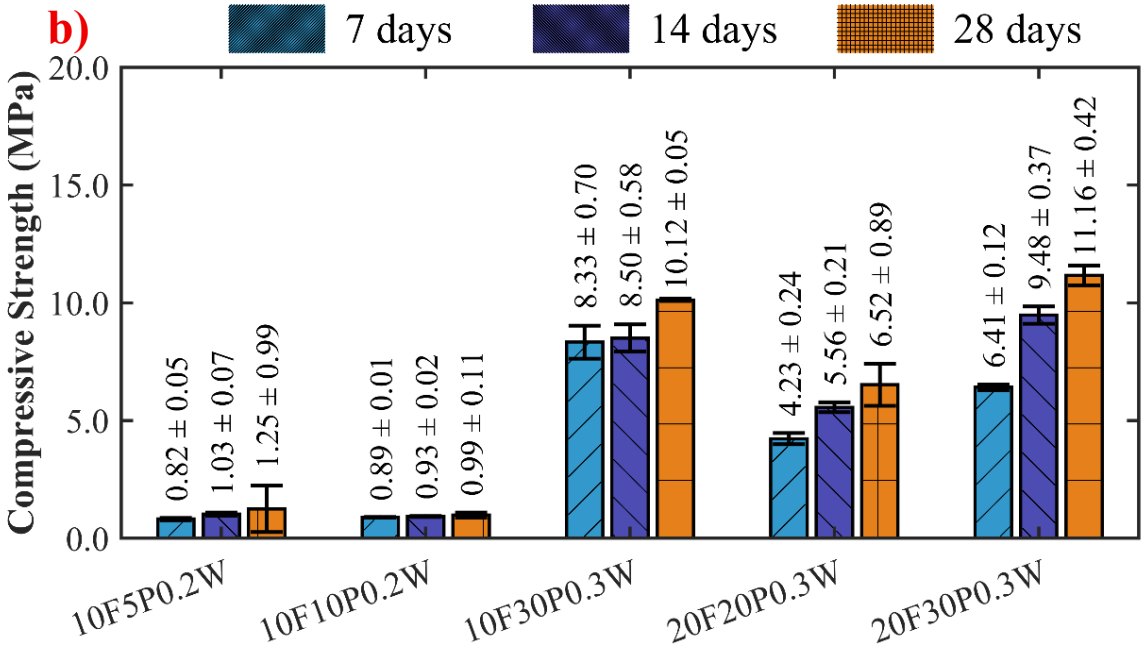
At 28 days, the highest strength was recorded for 20F30P0.3W at 11.2 ± 0.42 MPa (with a COV = 3.8%), which was comparable to 0F20P0.2W (at 10.8 ± 0.91 MPa, COV = 8.4%, $p = 0.431$, not significant) and 10F30P0.3W at 10.1 ± 0.89 MPa (with COV = 8.8%, $p = 0.013$), where no significant differences were observed between the latter two ($p = 0.277$). In contrast, mixtures with low binder content, such as 10F10P0.2W (1.0 ± 0.05 MPa) and 10F5P0.2W (1.3 ± 0.11 MPa, $p = 0.001$), remained weaker than all other mixtures ($p < 0.001$), which is aligned with previous studies (e.g., [355]) noted that fly ash alone cannot compensate for low cement content in at least early strength development.

In general, a few noteworthy trends are evident in the results. First, mixtures with a 0.3 w/s ratio exhibited higher long-term strengths compared to their counterparts with a 0.2 w/s ratio. The average 28-day strength of 0.3W mixtures was 6.6 MPa, compared to 3.3 MPa for 0.2W mixtures, and this difference was statistically significant ($p < 0.001$). This may be due to internal curing by the soil particles, which absorb moisture during the initial stages of curing. Second, fly ash content generally reduced the strength values. For instance, at 28 days, mixtures with 30% fly ash achieved an average strength of 3.5 MPa, whereas mixtures with 0% fly ash averaged 6.8 MPa; however,

this difference was not statistically significant ($p = 0.071$). At 7 days, the reduction was more evident, with mixtures containing 30% fly ash averaging 2.43 MPa, compared to 3.95 MPa for 0% fly ash mixtures, with $p=0.055$.

Lastly, as expected, cement dosage remained a primary determinant of strength. Mixtures with 30% cement achieved an average compressive strength of 9.8 MPa at 28 days, outperforming 5% cement mixtures by 1.4 MPa, and this difference was statistically significant ($p < 0.001$). However, there are notable exceptions. For instance, the 0F20P0.2W mixture, which contained no fly ash and only 20% cement, reached a 28-day strength of 10.8 MPa ± 0.91 MPa and COV = 8.5%. This strength is particularly higher than that of the mixture with 30% cement and 5% fly ash (5F30P0.3W), with 8.0 ± 1.0 and CO = 12.4%, $p = 0.001$. Such results highlight some important aspects of 3D-printed mixtures: (a) flow properties can significantly impact the optimum results that are achieved, and (b) printing defects and non-linearities can impact the results substantially.


a)
7 days
14 days
28 days
Compressive Strength (MPa)
20.0
15.0
10.0
5.0
0.0
1.80 ± 0.36
2.80 ± 0.26
2.80 ± 0.15
6.10 ± 0.75
8.90 ± 0.69
10.80 ± 0.91
1.10 ± 0.08
1.20 ± 0.08
1.30 ± 0.09
2.40 ± 0.40
2.60 ± 0.17
2.80 ± 0.25
5.90 ± 1.17
6.60 ± 0.85
8.00 ± 0.99
0F10P0.2W
0F20P0.2W
5F5P0.2W
5F10P0.2W
5F30P0.3W


b)
7 days
14 days
28 days
Compressive Strength (MPa)
20.0
15.0
10.0
5.0
0.0
0.82 ± 0.05
1.03 ± 0.07
1.25 ± 0.99
0.89 ± 0.01
0.93 ± 0.02
0.99 ± 0.11
8.33 ± 0.70
8.50 ± 0.58
10.12 ± 0.05
4.23 ± 0.24
5.56 ± 0.21
6.52 ± 0.89
6.41 ± 0.12
9.48 ± 0.37
11.16 ± 0.42
10F5P0.2W
10F10P0.2W
10F30P0.3W
20F20P0.3W
20F30P0.3W

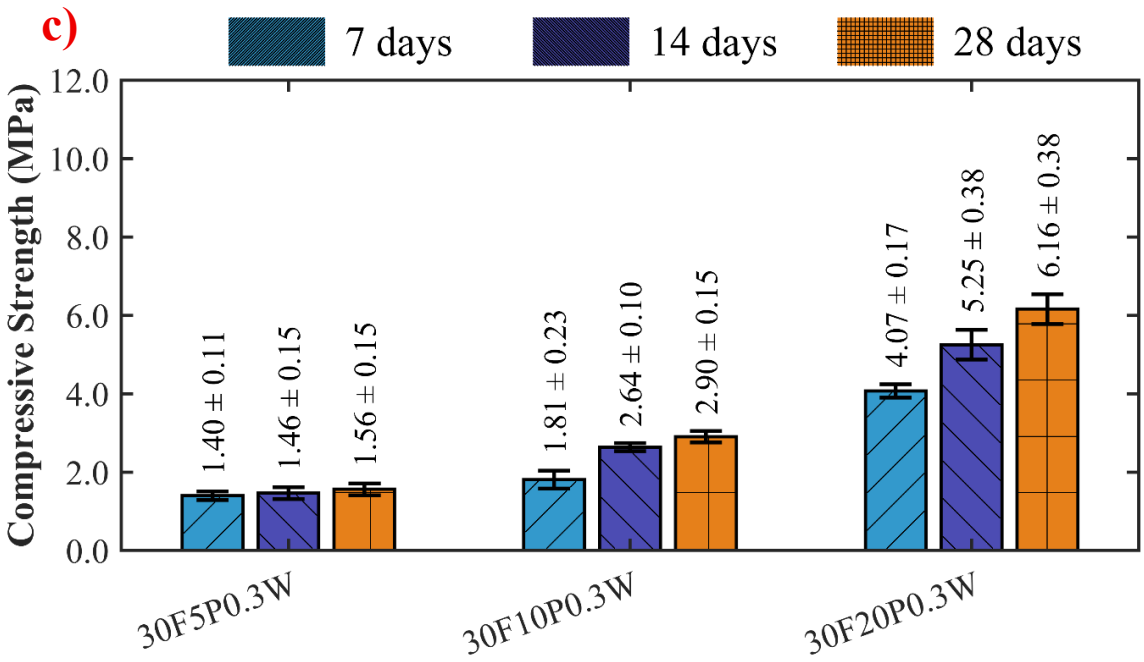


Figure 32. Compressive strength, including the 7, 14, and 28-day cured samples with (a) including 0F10P0.2W, 0F20P0.2W, 5F5P0.2W, 5F10P0.2W, and 5F30P0.3W, (b)10F5P0.2W, 10F10P0.2W, 10F30P0.3W, 20F20P0.3W, and 20F30P0.3W, and (c) 30F5P0.3W, 30F10P0.3W, 30F20P0.3W.

6.4.3.2. Anisotropic Behavior

Figure 33 shows the directions in which the samples were tested, including (a) printing direction, and (b) perpendicular to the printing direction. Given the presence of this interlayer, its influence on load transfer and failure behavior becomes an important consideration. In 3D-printed materials, the interface between layers is often the weakest plane, and its orientation relative to the applied load can significantly affect stiffness, cracking patterns, and peak strength. Owing to the small size of the 50-mm cubes, each specimen consisted of only two printed layers, producing one interlayer positioned approximately at mid-depth. **Figure 34** shows the 28-day cured compressive strength of cubic samples tested in the two mentioned directions. Based on the figure, the highest

compressive strength is achieved in the perpendicular to printing direction is mixture 20F30P0.3W with an average of 5.8 ± 0.22 MPa and a COV = 3.7%. This is followed by 20F20P0.3W with 4.4 ± 0.16 MPa (and a COV = 3.6% and p = 0.000). These mixtures had a high fly ash and cement content, along with a 0.3 w/s ratio. In contrast, the lowest compressive strengths were recorded in mixtures 10F5P0.2W and 10F10P0.2W, both with 0.8 ± 0.08 MPa (and a COV = 9.5% and 8.9%, respectively). However, the pairwise statistical comparison of these two mixtures was not significant (p = 0.823). These mixtures had a lower total binder content and a reduced w/s ratio of 0.2, which might have increased their variability due to the difficulty in mixing. Similarly, when mixtures are averaged by w/s ratio, 0.3 w/s mixtures outperformed the 0.2 w/s mixtures in terms of compressive strength in both printing direction and perpendicular to printing direction. For instance, the average strength for 0.3 w/s in the printing direction was 6.6 MPa, which can be compared to 3.3 MPa for 0.2W mixtures, with p = 0.000. In terms of perpendicular to printing direction, these values change to 3.6 MPa for 0.3 w/s mixtures and 1.6 MPa for 0.2 w/s mixtures, which were again statistically significant with p = 0.000. This is similar to the previous section in that a higher w/s ratio in the mixtures has increased the long-term strength values.

In terms of fly ash, mixtures with 30% fly ash recorded perpendicular to printing direction average strength of 2.4 MPa, as compared to 2.9 MPa for mixtures with 0% fly ash (with p = 0.233). These numbers compare to the printing direction of 3.5 MPa and 6.8 MPa for 30% and 0% fly ash mixtures, respectively, with a p-value of 0.071. This is an interesting result that shows the fly ash particles have performed differently in different directions, and is clearly confirmed by statistical tests. This phenomenon might have originated from the segregation of particles during printing, where the fly ash particles are concentrated at the top or bottom of the layers, leading to

directional variability in interfacial bonding. Given the finer particle size and spherical morphology of fly ash, it is possible that during extrusion, the fly ash particles migrated preferentially along the layer interfaces or toward the outer zones of the filament. This could enhance flowability and packing in one direction while disrupting the uniformity of interlayer bonding in the perpendicular direction. As a result, mixtures with higher fly ash content may exhibit improved performance along the printing path due to better cohesion and reduced voids, while simultaneously suffering from weaker interlayer adhesion across printed layers

Another trend observed across all mixtures is that samples tested in the printing direction developed significantly higher strength than those tested perpendicular to the printing direction. These results are also consistent with the failure modes shown in **Figure 34** (d) and (e), where the direction of the layers has been defined by the failure modes. It also highlights the significance of printing parameters in directional strength development, probably caused by the difference in the pore characteristics of interlayer regions, as discussed by previous studies [356], [357], [358].

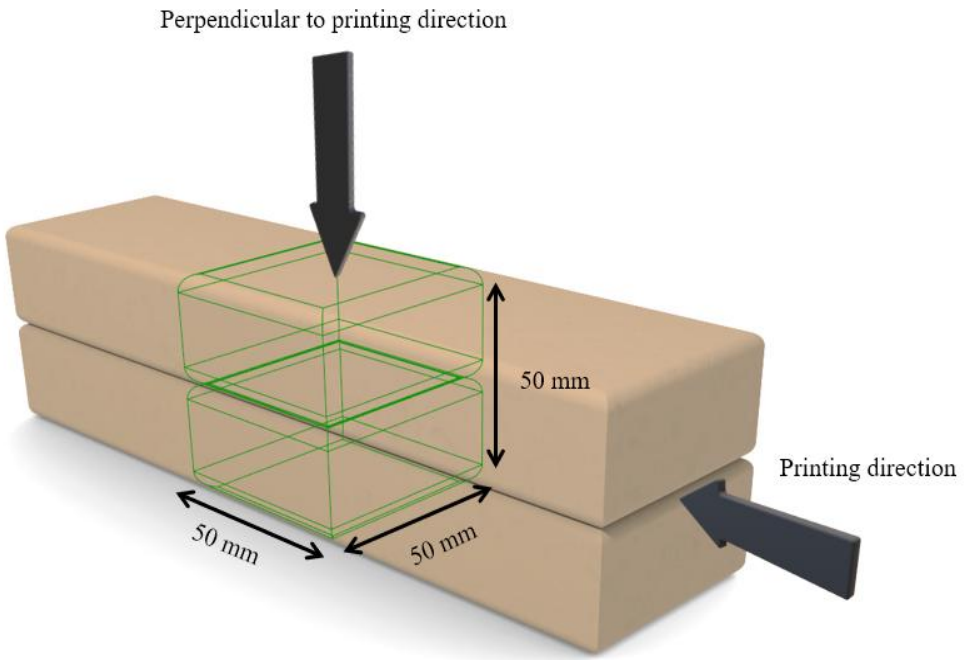
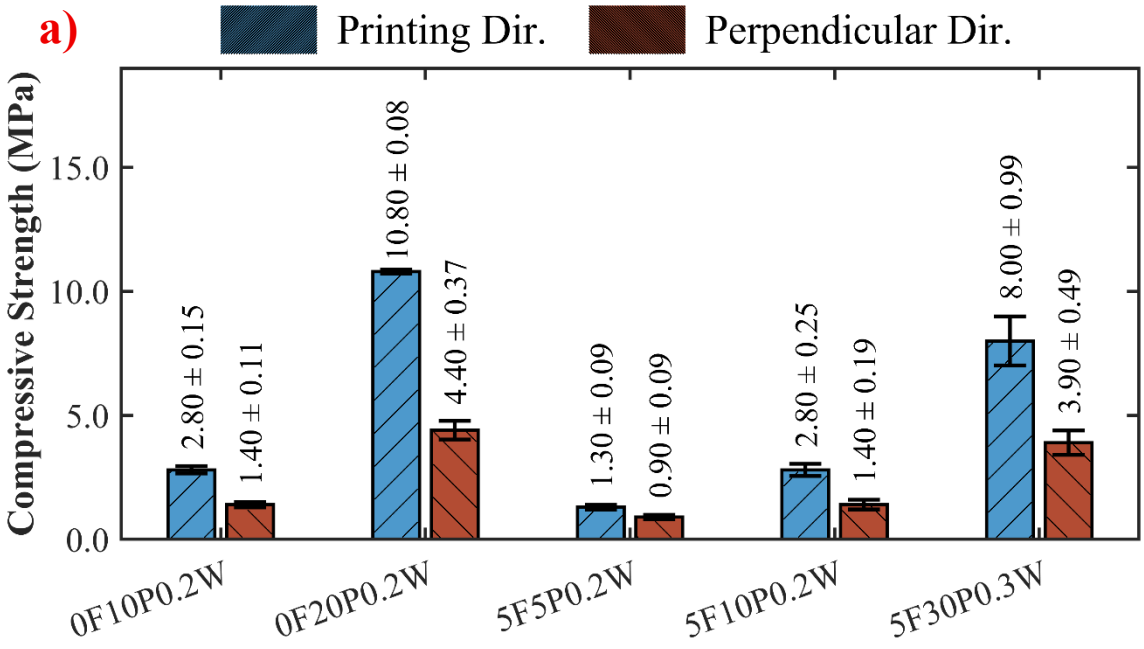
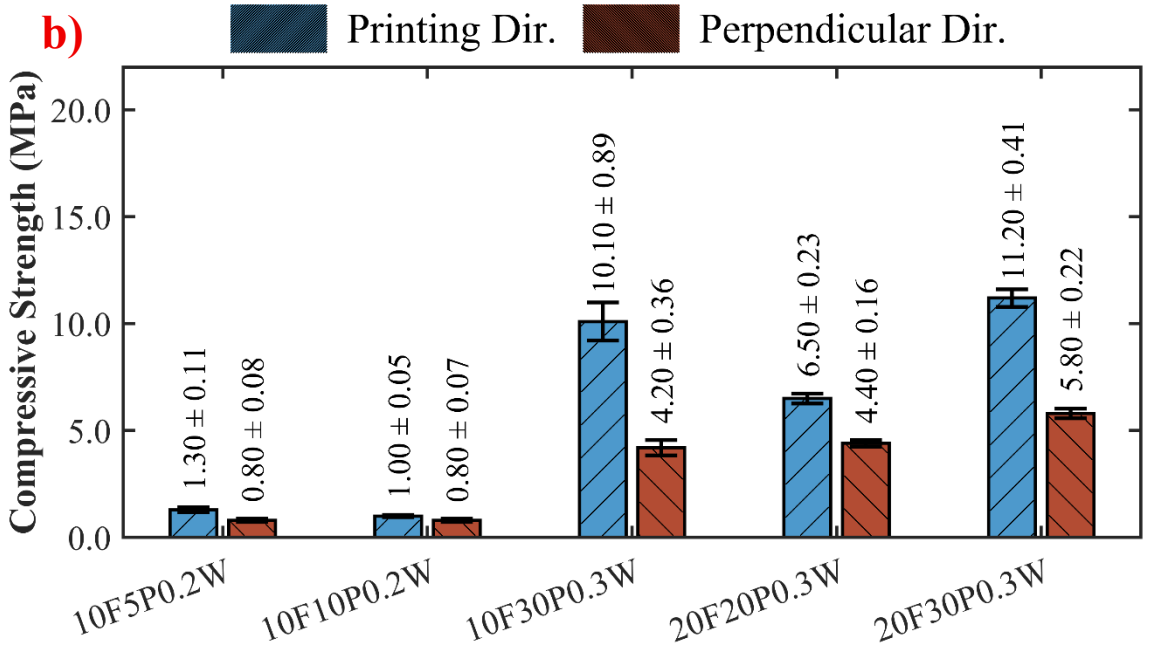
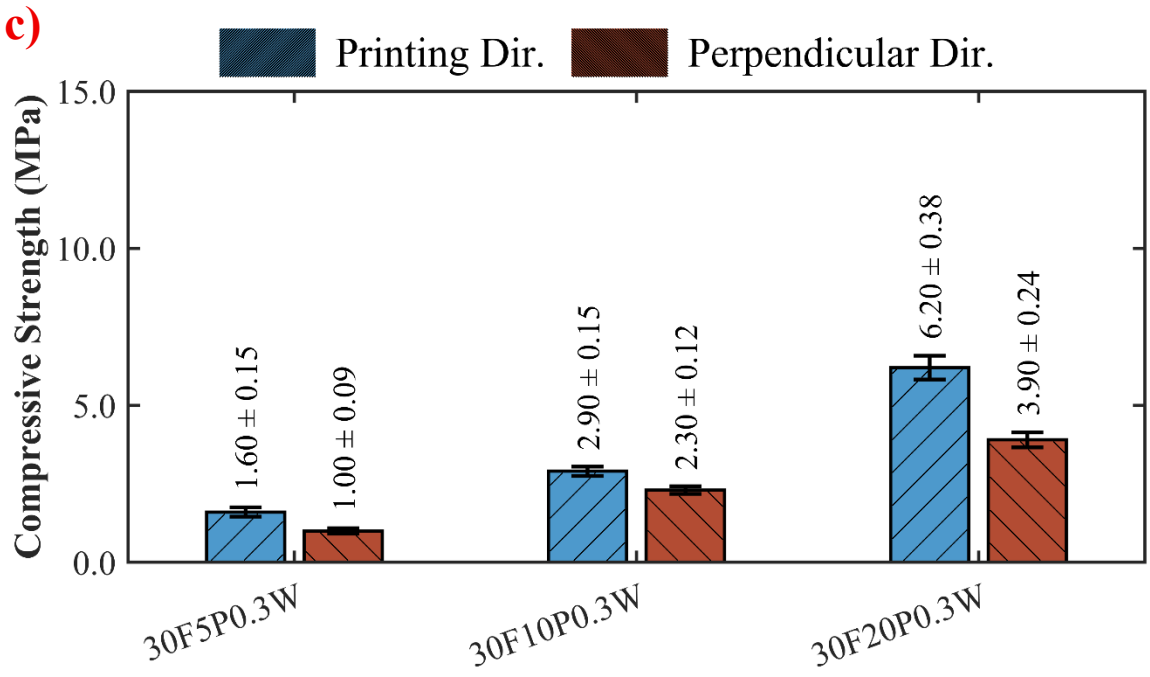


Figure 33. Clarifying the directions for testing samples.




b)
Printing Dir.
Perpendicular Dir.
Compressive Strength (MPa)
20.0
15.0
10.0
5.0
0.0
1.30 ± 0.11
0.80 ± 0.08
1.00 ± 0.05
0.80 ± 0.07
10.10 ± 0.89
4.20 ± 0.36
6.50 ± 0.23
4.40 ± 0.16
11.20 ± 0.41
5.80 ± 0.22
10F5P0.2W
10F10P0.2W
10F30P0.3W
20F20P0.3W
20F30P0.3W


c)
Printing Dir.
Perpendicular Dir.
Compressive Strength (MPa)
15.0
10.0
5.0
0.0
1.60 ± 0.15
1.00 ± 0.09
2.90 ± 0.15
2.30 ± 0.12
6.20 ± 0.38
3.90 ± 0.24
30F5P0.3W
30F10P0.3W
30F20P0.3W

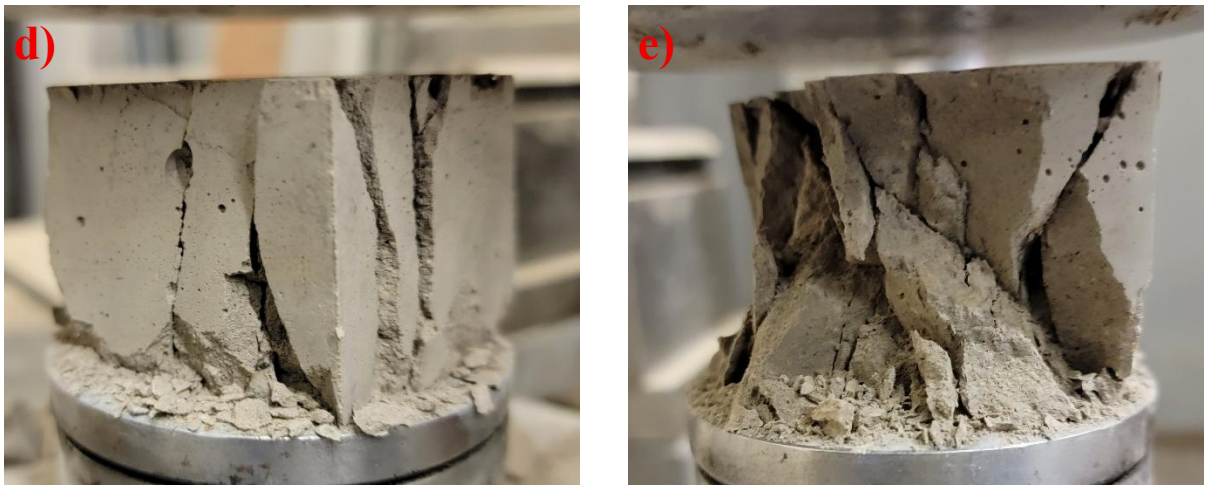


Figure 34. Compressive strength of cubes in two different directions, including the 28-day cured samples with (a) including 0F10P0.2W, 0F20P0.2W, 5F5P0.2W, 5F10P0.2W, and 5F30P0.3W, (b)10F5P0.2W, 10F10P0.2W, 10F30P0.3W, 20F20P0.3W, and 20F30P0.3W, (c) 30F5P0.3W, 30F10P0.3W, 30F20P0.3W, (d) failure mode in printing direction, and (e) failure mode in perpendicular to printing direction.

6.4.4. LCA Results

Table 45 presents the results of LCA with the strength factor, scaling the wall's thickness to an equivalent 28-day compressive strength of 17.24 MPa (or 2500 psi). This approach ensures that the comparisons reflect not only the material input but also the mechanical performance of each mixture in practice [155], [156]. All values reported in the table are after being adjusted using a strength correction factor. In terms of GWP, mixture 0F20P0.2W showed the lowest emissions, with a corrected value of 389.1 kg CO_2 eq. Followed by that, 20F30P0.3W, with 464.5 kg CO_2 eq, and then 10F30P0.3W with 537.7 kg CO_2 eq. In contrast, mixture 10F10P0.2W showed the highest GWP at 2017.0 kg CO_2 eq. This significant variation across mixtures highlights the importance of balancing binder content with mechanical performance. High-binder mixtures with poor strength-

to-material ratios can dramatically increase environmental burdens when the structural performance is considered.

Similar trends were observed for TEC. Mixtures 0F20P0.2W consumed the least energy at 2020.9 MJ, followed by 20F30P0.3W and then 10F30P0.3W with 2306.5 MJ and 2666.9 MJ, respectively. Mixture 10F10P0.2W recorded the highest energy demand at 10305.6 MJ, similar to GWP. These results reinforce that energy impacts are not only dependent on the quantities of cement or fly ash, but also on how efficiently the mixture performs structurally.

With respect to smog formation, the most favorable results were again observed in 0F20P0.2W, with 16.5 kg SO_2 eq, and then for 30F5P0.3W, with 17.6 kg SO_2 eq. Mixture 10F10P0.2W showed the highest impact in this category as well, with 88.2 kg SO_2 eq. The same trend can be observed for acidification, especially in 0F20P0.2W and 20F30P0.3W, which performed best with 0.8 and 0.9 kg SO_2 eq, respectively, while 10F10P0.2W again had the largest impact at 4.3 kg SO_2 eq.

In general, these results suggest that mixtures with moderate binder content and optimized w/s ratios can meet structural demands while minimizing environmental impact. In contrast, mixtures that use relatively high binder content without reasonable strength development (e.g., 10F10P0.2W) have led to substantially higher impacts across all categories.

Table 45. Result of LCA per functional unit of 1 m (height) × 1 m (length) wall with a variable width (per strength) with the strength-normalization factor.

Mixture name	GWP (kg CO_2 eq / 17.24 MPa compressive strength)	TEC (MJ / 17.24 MPa compressive strength)	Smog formation (kg SO_2 eq / 17.24 MPa compressive strength)	Acidification (kg SO_2 eq / 17.24 MPa compressive strength)
0F10P0.2W	761.7	3862.2	32.6	1.6
0F20P0.2W	389.1	2020.9	16.5	0.8
5F5P0.2W	920.8	5856.2	60.9	2.5
5F10P0.2W	801.2	4633.2	42.9	1.9
5F30P0.3W	710.6	3797.9	31.2	1.5
10F5P0.2W	846.5	4708.5	46.2	2.0
10F10P0.2W	2017.0	10305.6	88.2	4.3
10F30P0.3W	537.7	2666.9	20.4	1.1
20F20P0.3W	551.9	2761.1	21.7	1.1
20F30P0.3W	464.5	2306.5	21.7	0.9
30F5P0.3W	580.5	3114.9	17.6	1.3
30F10P0.3W	607.8	3119.5	26.2	1.3
30F20P0.3W	556.0	2787.2	21.8	1.1

The cradle-to-gate life cycle impacts of all 13 mixtures without the strength normalization are presented in **Table 46**. When evaluated on a constant-volume basis (**Table 45**), the environmental burdens of all mixtures remained relatively low since the wall geometry and material volume were fixed at 0.1 m thickness, independent of strength. Under this unnormalized condition, the impacts primarily reflect differences in mixture composition, namely, the proportions of Portland cement, fly ash, and w/s ratios, rather than structural performance. In terms of GWP, mixture 30F5P0.3W exhibited the lowest emissions (5.25 kg CO_2 eq), followed closely by 5F5P0.2W (7.04 kg CO_2 eq) and 10F5P0.2W (7.48 kg CO_2 eq). These mixtures contain reduced cement content and a relatively high proportion of supplementary materials, such as fly ash, which substantially decrease the

clinker-related CO_2 footprint. Conversely, mixtures with higher binder contents (e.g., high Portland cement), resulted in higher impacts. For example, 0F20P0.2W (24.34 kg CO_2 eq) and 5F30P0.3W (32.96 kg CO_2 eq) recorded among the highest emissions, largely attributable to the increased embodied energy of Portland cement and the higher mass of binder per cubic meter.

Similar patterns were observed across the other environmental categories. TEC followed the same ranking, with 30F5P0.3W again achieving the lowest energy demand (28.19 MJ), while mixtures with greater cement usage showed higher values, reaching up to 176.16 MJ for 5F30P0.3W. Smog formation and acidification potential displayed proportional increases with binder content, since these impacts are strongly associated with the upstream energy intensity and emissions from cement production.

In general, the unnormalized analysis emphasizes the dominant influence of binder content and activator chemistry on environmental performance per unit volume. Mixtures rich in fly ash or with reduced Portland cement concentration demonstrate the most favorable environmental outcomes. However, this assessment does not account for mechanical performance differences, meaning that mixtures appearing environmentally advantageous here may not necessarily achieve sufficient strength for structural applications. As a result, the fixed-volume evaluation represents a material-efficiency snapshot rather than a true functional comparison, serving as a baseline before integrating strength-based normalization in the subsequent analysis.

As a result, the comparison between **Table 45** and **Table 46** highlights the importance of integrating mechanical performance into environmental assessments. When impacts are expressed

per fixed wall volume and hardened densities, mixtures with low binder content appear highly sustainable. However, when the same mixtures are scaled to provide equivalent structural strength, their apparent environmental advantage diminishes or disappears entirely. In contrast, mixtures that develop higher compressive strength per unit of binder retain their low-impact ranking under both evaluation methods, confirming their superior strength-to-impact efficiency.

For 3D-printed construction, where structural integrity is critical, the strength-normalized results provide a more realistic representation of sustainability. They demonstrate that binder optimization should aim not only to minimize material emissions but also to ensure sufficient load-bearing capacity, as under-performing mixtures will ultimately require more material and energy to achieve equivalent performance. Accordingly, 0F20P0.2W and 20F30P0.3W emerge as the most balanced and sustainable formulations across both functional-unit definitions. The fact that 0F20P0.2W is an outperforming mixture is even more interesting, which shows that it is possible to 3D print soil-based cementitious components without even relying on fly ash at all.

Table 46. Results of LCA on all mixtures without the strength-normalization per functional unit of 1 m (height) × 1 m (length) wall with a width of 0.1 m.

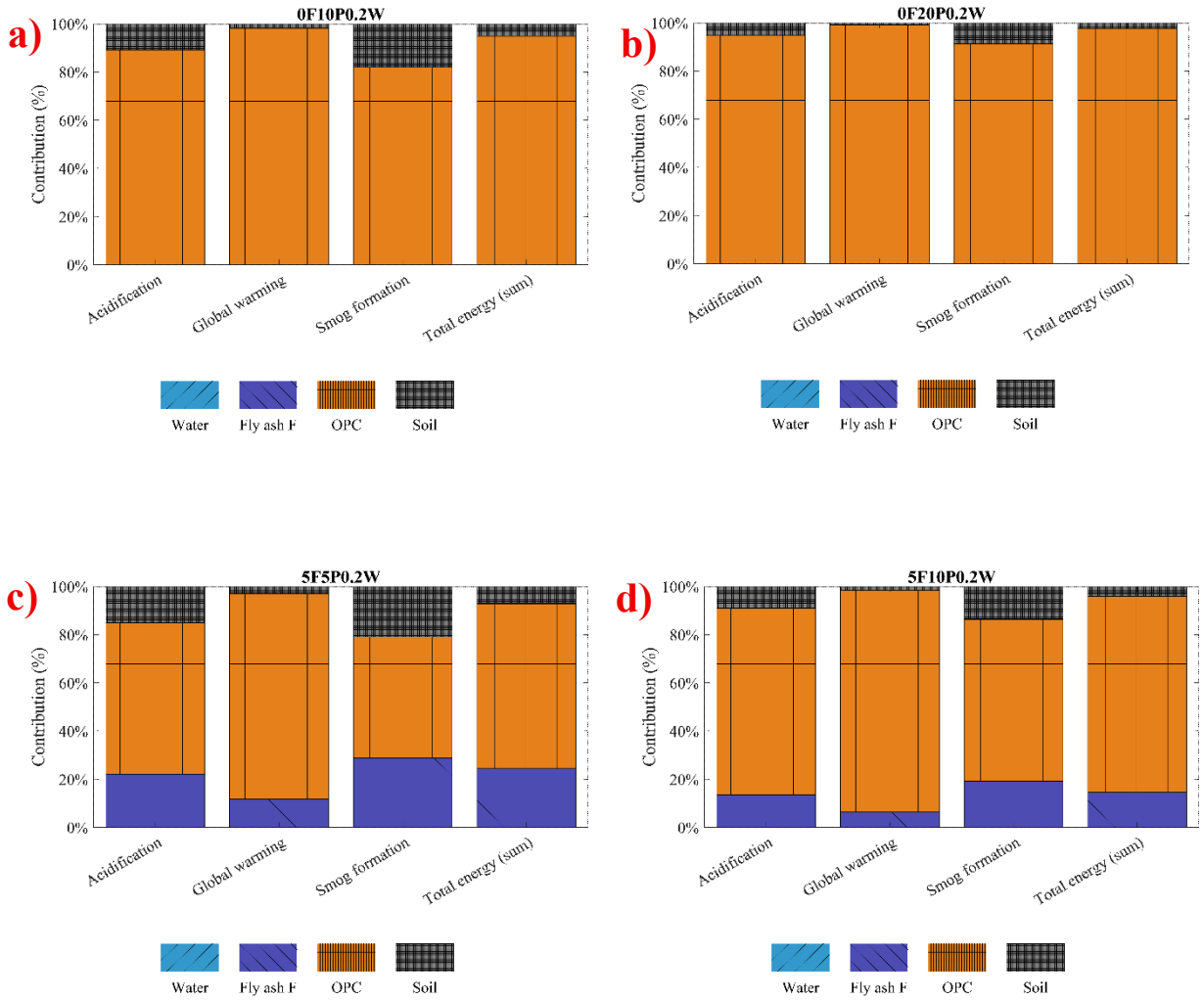
Mixture name	GWP (kg CO_2 eq)	TEC (MJ)	Smog formation (kg SO_2 eq)	Acidification (kg SO_2 eq)
0F10P0.2W	12.55	63.62	0.54	0.03
0F20P0.2W	24.34	126.41	1.03	0.05
5F5P0.2W	7.04	44.79	0.47	0.02
5F10P0.2W	12.81	74.09	0.69	0.03
5F30P0.3W	32.96	176.16	1.45	0.07
10F5P0.2W	7.48	51.78	0.55	0.02

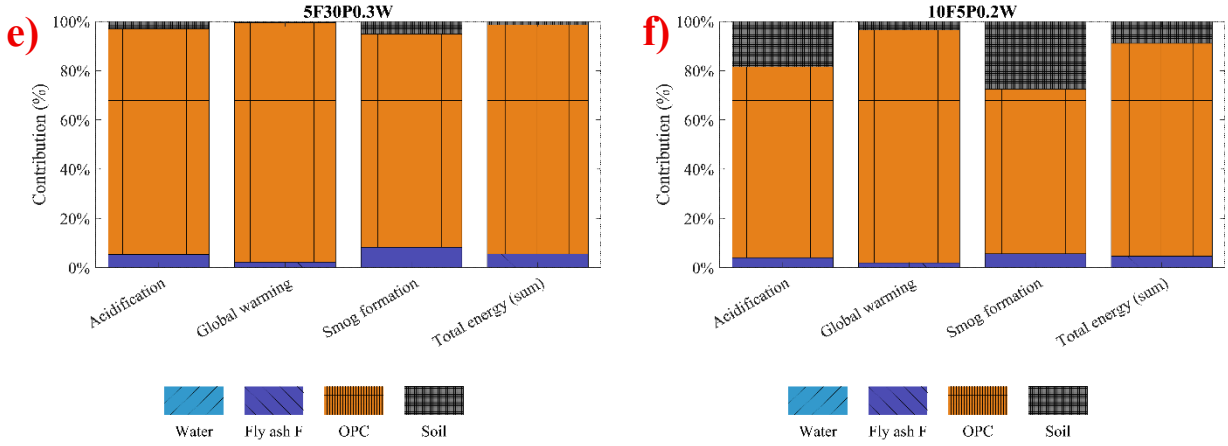
10F10P0.2W	11.56	59.06	0.51	0.02
10F30P0.3W	31.56	156.54	1.20	0.06
20F20P0.3W	20.88	104.44	0.82	0.04
20F30P0.3W	30.08	149.36	0.82	0.06
30F5P0.3W	5.25	28.19	1.14	0.01
30F10P0.3W	10.23	52.50	0.44	0.02
30F20P0.3W	19.85	99.52	0.78	0.04

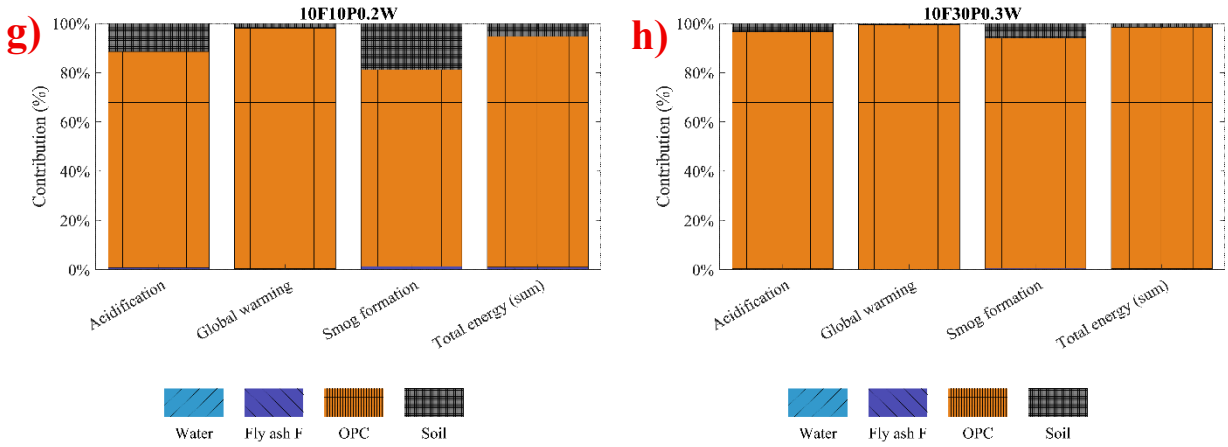
Figure 35 presents the component-level contributions of each material and each mixture to the four environmental impact categories for all 3D-printed mixtures. In general, Portland cement remains the main contributor (often over 90%) in all mixtures and impact categories. This trend confirms that the environmental impacts of these earth-based systems are strongly tied to cement content in the mixtures.

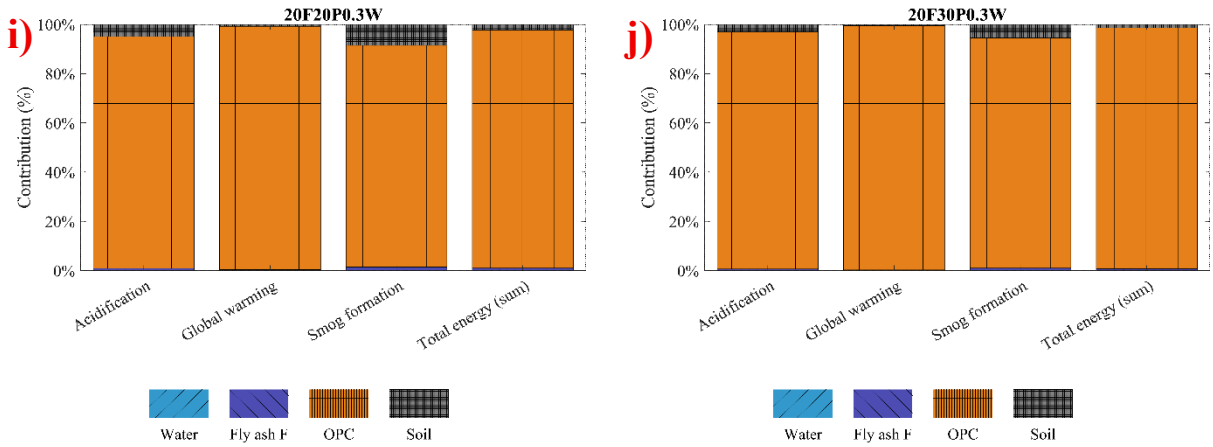
Another interesting finding is the effect of using fly ash. Based on the figures, fly ash becomes a more prominent contributor in mixtures with higher replacement levels and higher w/s ratios. For example, in mixtures, such as 30F10P0.3W and 30F20P0.3W, fly ash contributes significantly to smog formation and total energy use. This is largely attributed to its transportation-related emissions, which remain substantial, even though fly ash is considered a byproduct material in this study. The transportation burden of fly ash is particularly apparent in GWP and total energy results, where its contribution grows in direct proportion to its dosage. Following the impacts of cement and fly ash, the soil's impact is the third most intense, but considerably less than those of the other two. Nevertheless, its role becomes slightly more pronounced in lower-binder-content systems such as 0F20P0.2W and 10F5P0.2W, where the reduced cement or fly ash content elevates the proportional impact of soil.

In general, these findings highlight that Portland cement content remains the principal driver of environmental impacts in soil-based 3D-printed mortars. Cement is followed by fly ash in cases where its content is substantial. Soil plays a passive yet stabilizing role, while water has a negligible influence.




e)
5F30P0.3W
f)
10F5P0.2W
Contribution (%)
100%
80%
60%
40%
20%
0%
Acidification
Global warming
Smog formation
Total energy (sum)
Water
Fly ash F
OPC
Soil


g)
10F10P0.2W
h)
10F30P0.3W
Contribution (%)
100%
80%
60%
40%
20%
0%
Acidification
Global warming
Smog formation
Total energy (sum)
Water
Fly ash F
OPC
Soil


i)
20F20P0.3W
j)
20F30P0.3W
Contribution (%)
100%
80%
60%
40%
20%
0%
Acidification
Global warming
Smog formation
Total energy (sum)
Water
Fly ash F
OPC
Soil

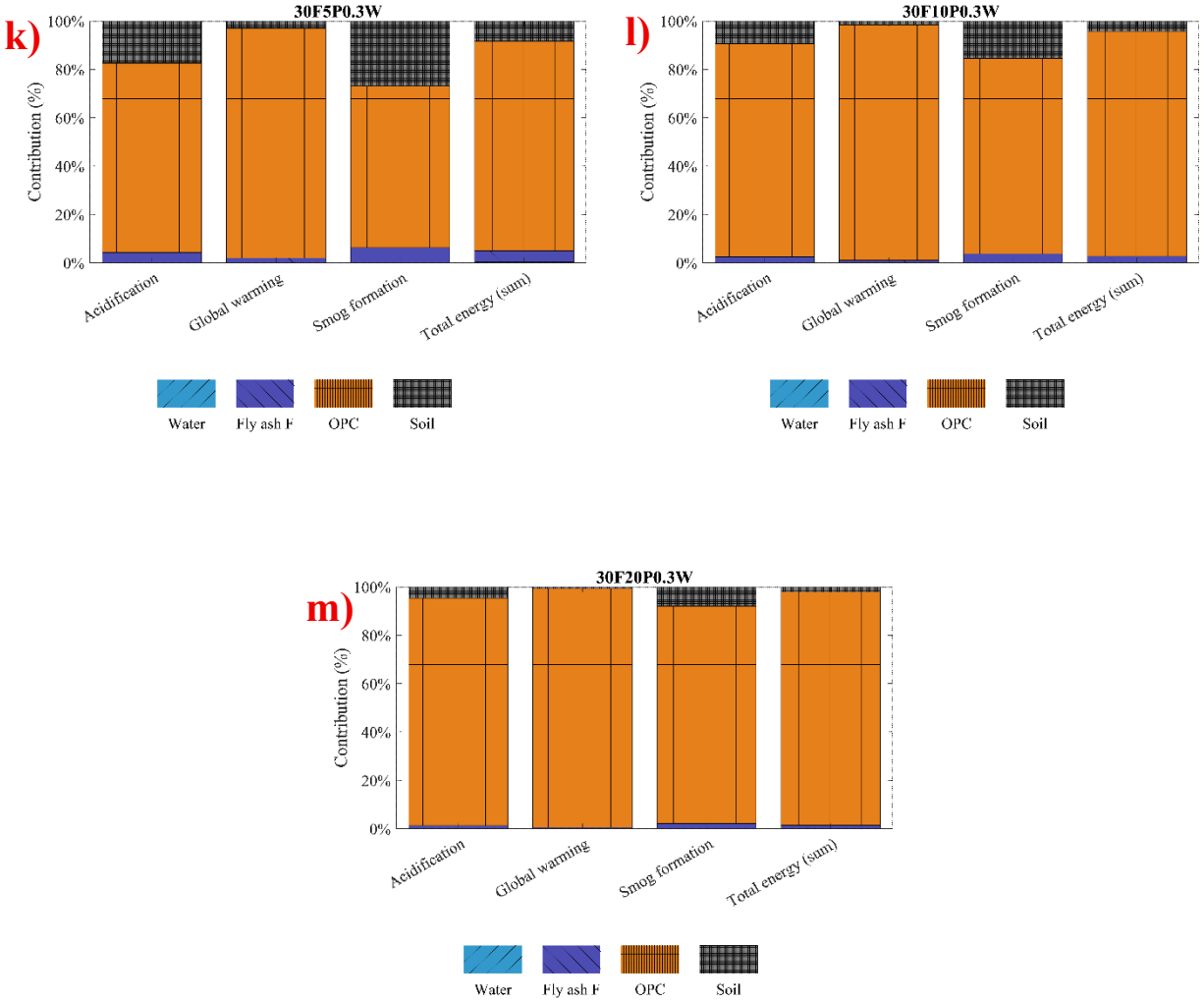


Figure 35. Comparison of the relative contributions from different components to the different environmental impact categories of: (a) 0F10P0.2W, (b) 0F20P0.2W, (c) 5F5P0.2W, (d) 5F10P0.2W, (e) 5F30P0.3W, (f) 10F5P0.2W, (g) 10F10P0.2W, (h) 10F30P0.3W, (i) 20F20P0.3W, (j) 20F30P0.3W, (k) 30F5P0.3W, (l) 30F10P0.3W, and (m) 30F20P0.3W.

6.5. Conclusion

This study evaluated the printability of approximately 100 soil-based cementitious mixtures and identified 13 that were successfully printable across varying proportions of Portland cement (5-30%), fly ash (Class F; 0-30%), and water-to-solid ratios (w/s; 0.1-0.4). All mixtures were produced without chemical admixtures, allowing the effects of raw material proportions to be isolated. The printable mixtures were then examined through a comprehensive set of fresh-state and hardened-state tests. In particular, their rheological properties were characterized in depth to establish practical printability thresholds for yield stress, dynamic viscosity, and shear stress. These thresholds provide a reference that can guide the development of sustainable, soil-based 3D-printed mixtures without reliance on admixtures or printer-specific tuning (e.g., nozzle-dependent adjustments). The results demonstrate that mixture proportioning plays a decisive role in both the fresh behavior and mechanical performance of 3D-printed materials. Based on the results presented and discussed, the following conclusions are made:

- In terms of fresh properties, mixtures with a 0.3 w/s ratio generally showed an improved flowability, with flow table spread reaching 186.0 mm, as compared to mixtures with 0.2W with 175.3 mm. Similarly, the inclusion of fly ash has increased the average spread diameter (from 174.5 mm to 191.3 mm, $p = 0.034$), while an increase in fly ash content from 0% to 30% has increased the flow from 174.5 mm to 191.3 mm, with $p = 0.068$, respectively. Unlike fly ash inclusion, when the cement content increased from 10% to 30%, it reduced the flow values from 183.6 mm to 175.67 mm, with $p = 0.676$. The average density values were also reduced when the w/s ratio or fly ash content was increased within the mixtures. pH values remained consistently alkaline with minor variations across different mixtures.

- In terms of printability limits, (a) dynamic viscosity (to show materials' resistance to flow or shape retention), (b) shear stress (to show nozzle clogging potential), and (c) yield point (to show flow initiation), were established to provide a printable range for sustainable, soil-based mixtures. Results outlined that an upper and lower range of: (a) 1.480E+04 ± 1.220E+03 (with COV=8.22E+00%) Pa.s to 4.700E+03 ± 1.470E+03 (with COV=3.13E+01%) Pa.s for dynamic viscosity, (b) 4.280E+00 ± 1.290E+00 N/m² (COV=3.01E+01%) to 8.460E-01 ± 7.020E-02 N/m² (COV=8.31E+00%) for shear stress, and (c) 7.660E+02 ± 2.300E+01 (COV=3.00E+00%) N/m^2 to 1.360E+02 ± 1.470E+00 (COV=1.08E+00%) N/m^2 for yield stress is required. In general, an increase in the w/s ratio tends to reduce dynamic viscosity, shear, and yield (due to reduced particle friction). Similarly, an increase in fly ash content tends to reduce these parameters (due to its spherical shape and lower interparticle friction). It is important to note that the rheological boundaries identified in this study were not dependent on the nozzle diameter of the 3D printer, indicating that they represent material-level thresholds rather than printer-specific settings.

- Compressive strength results showed that, in general, higher binder content leads to higher strength values; for instance, mixture 20F30P0.3W achieved the highest 28-day strength at 11.2 ± 0.42 MPa (with COV = 3.8%). It was followed by 0F20P0.2W at 10.8 ± 0.91 MPa (with p=0.431). There were, however, a few exceptions, such as cases where a high cement and high fly ash content was included in the mixtures (e.g., 20F20P0.3W, as opposed to 0F20P0.2W, with p = 0.000). Such results highlight some important aspects of 3D-printed

mixtures: (a) flow properties can significantly impact the optimum results that are achieved, and (b) printing defects and non-linearities can impact the mechanical results substantially. In contrast, mixtures with low cement and high fly ash, such as 10F10P0.2W and 10F5P0.2W ($p = 0.001$), failed to exceed 1.3 MPa after 28 days, likely due to insufficient hydration. Notably, a higher w/s led to a higher strength value (e.g., 6.63 MPa for 0.3W mixtures, as opposed to 3.32 MPa for 0.2 w/s, $p = 0.000$). Fly ash content also reduced early and long-term (28-day) strength; for example, on average, 30% fly ash mixtures averaged 3.5 MPa, while 0% fly ash mixtures reached 6.8 MPa, with $p=0.071$.

- Anisotropic strength behavior was also evident across all samples and mixture proportions. In this study, each cube contained two printed layers, resulting in a single interlayer located near mid-height. In all mixtures, the strength along the printing direction was consistently higher than that in the perpendicular direction, averaging 5.1 MPa, while the perpendicular direction averaged only 2.7 MPa. Results highlighted the defining impact of interlayers on strength and failure mode, as well as the importance of improved material dispersion to reduce anisotropic behavior. This was particularly evident in mixtures with 0.3W, where stronger values were achieved in both directions compared to their 0.2W counterparts. Additionally, the directional difference was linked to interlayer bonding quality and possible segregation of fly ash particles during extrusion. This was especially evident in fly ash–rich mixtures, where the difference between printing and perpendicular strengths widened, likely due to the segregation of fly ash particles during printing deposition.

- Life-cycle assessment of 3D-printed mixtures showed that both the composition and mechanical performance govern sustainability. On a fixed-volume basis, mixtures with lower cement content and moderate fly-ash replacement showed the lowest embodied impacts, confirming the dominant influence of cement on total emissions. When results were normalized to a target compressive strength of 17.24 MPa, low-strength mixtures lost their apparent environmental advantage, while 0F20P0.2W and 20F30P0.3W remained the most efficient, demonstrating superior strength-to-impact ratios. In terms of material contributions, cement accounted for 85–90% of all impacts, with soil playing a minor role. These findings show that sustainable 3D-printed earthen materials require not only reduced binder content but also an optimized mixture design, enabling structurally sound components even without fly ash.

7. Conclusions and Recommendations for Future Work

This chapter summarizes the key findings discussed in chapters three through six. Recommendations for future work in the area of 3D printing of cementitious materials are also outlined.

7.1. Conclusions

In chapter 3, Compressed and Stabilized Alkali-activated Earth Blocks (CSAEBs) are developed using different precursors and alkaline activators. CSAEBs are developed as an alternative to ordinary Portland cement stabilized compressed earth blocks (CSEBs). Glass powder, coal fly ash class F, and class C are used as precursors, while sodium silicate and sodium hydroxide are used as the main activators. Seven mixtures are developed, including one with Portland cement and three with each activator. The mixtures are then tested for physical, mechanical, durability, and environmental performance (through Life Cycle Analysis (LCA)). Results show that (a) sodium hydroxide with a molarity of 3.0 with a pH of 12.37 can surpass premixed 40:60 (sodium silicate to water) with a pH of 10.8 by a rate of approximately four times higher compressive strength values, and (b) LCA results show sodium silicate mixtures averaged GWP of 118.2 kg CO_2-eq, compared to 103.9 kg CO_2-eq for sodium hydroxide mixtures. After strength-normalization (for a compressive strength of 17.23 MPa), sodium silicate systems showed much higher GWP (average of 374.1 kg CO_2-eq), whereas sodium-hydroxide mixtures were lowest (74.83 kg CO_2-eq). This shift highlights the engineering significance of performance-based metrics: mixtures that seem environmentally promising per kilogram may be poor choices when

evaluated per unit strength. Performance-normalized impacts, therefore, enable more reliable, structurally relevant material selection.

In chapter 4, the properties of ordinary and geopolymer soil-based 3D-printed components are compared to those of ordinary and geopolymer mortars. To do this, four extrusion-based 3D-printed mixtures, using PC- and geopolymer-based binder systems, and two filler types (processed sand and natural low-plasticity silt), were designed and compared. Fresh, mechanical, and microstructural properties were then assessed alongside a cradle-to-gate LCA. The results show that (a) soil-based mixtures can perform similarly to ordinary mixtures in terms of mechanical properties (e.g., compressive strength at 28 day of 6.7-15.8 MPa for soil-based and 13.86-15.1 MPa for sand-based), yet result in a mixture with a higher degree of heterogeneity, (b) soil-based samples are prone to stronger anisotropic behavior (e.g., with strength in printing direction being 6.48 ± 0.94 MPa, and 5.94 ± 0.94 MPa in perpendicular to printing direction with $p<0.05$), (c) LCA results showed notable GWP reductions, with sodium-hydroxide mixtures averaging 103.9 kg CO_2-eq (mass-based) and 74.8 kg CO_2-eq (strength-normalized, compressive strength of 15 MPa), whereas sodium-silicate systems increased from 118.2 to 374.1 kg CO_2-eq after strength adjustment, and (d) strengths developed using soil-based materials, are consistent with those used for masonry units and low-rise construction, making the materials suitable for non-load-bearing or lightly loaded applications, such as infill walls, partitions, printed panels, and small structural modules, particularly in contexts where locally sourced materials are preferred.

In chapter 5, the influence of different specimen fabrication methods, including coring, cutting, and mold casting with either rodding or vibration, is evaluated. A total of 670 specimens are

prepared using each fabrication method across both soil- and sand-based mixtures and tested for their mechanical, physical, and mechanical properties. The results indicate statistically significant differences in the tested properties, depending on the preparation method. 3D printing mixtures are found to be more prone to particle segregation and settlement due to the heavy use of finer materials. The fabrication method strongly influenced the compressive strength values, with differences of 29-46% for cubes and 109-136% for cylinders cured for 28 days. Soil-based mixtures showed lower variability than sand-based ones, while vibration produced the highest strengths (up to 22.8 MPa). However, segregation reduced early-age performance at longer vibration times. Overall, coring and cutting-to-size yielded the most reliable mechanical results. The study also highlights common issues and expectations in printing and sampling procedures and highlights the differences between 3D-printed mixtures and ordinary mortars, ranging from demolding time to the effects of preparation on final properties.

In chapter 6, the rheological boundaries for the printability of low-cement and low-fly ash, soil-based 3D printing mixtures are determined. To do this, over 100 mixture combinations are studied, including a variety of cement and fly ash content, as well as water-to-solid ratios. Based on the mixtures' ability to continuously flow from the nozzle and build on one another, 13 mixtures are deemed printable and are then tested for yield stress, dynamic viscosity, and shear stress. In the study, (a) printable limits are established as 4.7×10^{3} to 1.48×10^{4} Pa·s for dynamic viscosity, 1.36×10^{2} to 7.66×10^{2} N/m^2 for yield stress, and 8.46×10^{-1} to 4.28 N/m^2 for shear stress. All mixtures are produced without the use of chemical admixtures, and these thresholds are correlated with mechanical performance and life-cycle impacts, (b) strength-normalized LCA showed large differences among mixtures, correlated to the developed compressive strengths values, with GWP

impacts ranging from 389-2017 kg CO_2 eq, total energy consumption (TEC) from 2021-10306 MJ, smog from 16.5-88.2 kg O_3 eq, and acidification from 0.8-4.3 kg SO_2 eq per functional wall, and (c) anisotropic behavior of low-cement and low-fly ash mixture is found to be significantly influenced by rheology and its impacts (such as interlayer defects and particle segregation), on the hardened state properties.

7.2. Limitations and Constraints of the Research

Despite the breadth of the investigations conducted in this dissertation, several limitations and constraints should be acknowledged to guide the interpretation of the results and inform future work.

First, the experimental program relied heavily on the materials, equipment, and analytical tools available at the time of testing. This includes the testing equipment that was calibrated a few years prior to the testing program. Also, the natural soil used in multiple phases of this research was not available for retesting with a hydrometer, and its characterization was performed using different methods commonly used for construction sand materials. This means that the soil's clay-sized and silt-sized fractions were not captured with the same fidelity as a full ASTM D422–type analysis. Because soil particles vary widely in mineralogy, shape, and grading, the soil used here represents only one possible material type. Different soils may exhibit very different rheological, mechanical, and environmental behavior, and therefore, the findings of this dissertation should not be generalized to all soils or testing equipment without further validation. As a result, discrepancies in particle-size distributions were unavoidable, reflecting both methodological differences and the inherent heterogeneity of natural soils. Similarly, mixture preparation and compaction were

constrained by the lack of specialized 3D-printing testing standards. All samples were produced according to ASTM procedures; however, these tests were originally developed for conventional mortars and concrete rather than for highly thixotropic, buildable, soil-rich mixtures. Consequently, to keep the COV consistent, all extrusion was done in one single day per chapter. Different crew members or timing in extrusion were found to cause significant variation in the results during the trial phases of the work. Also, sampling methods (coring, cutting, rodding, and vibration) introduced unavoidable biases that reflect practical field conditions but limit direct comparison with traditional concrete data.

Second, the rheology-based printability framework was developed using mixtures prepared without chemical admixtures and cured under ambient conditions (~50% relative humidity). While this allows broader applicability in low-resource settings, it limits the generalization of rheological thresholds to systems that use superplasticizers, accelerators, retarders, or controlled-curing environments. The printability limits were also derived from mixtures aimed to be extruded through a single nozzle geometry and equipment, meaning that nozzle-size effects, pumping pressures, layer dimensions, and subsequently layers' interface impacts were not fully explored.

Third, the mechanical and microstructural properties were evaluated using relatively small specimens (50-mm cubes and 76.2×152.4-mm cylinders), which, especially in soil-based and fly-ash-rich systems, can be highly sensitive to moisture gradients, segregation tendencies, and local heterogeneities. This contributed to the unusually high cylinder-to-cube strength ratios observed at later ages (up to ~2.0), a behavior likely influenced by geometric effects, internal curing

differences, and layer-induced compaction gradients. These findings are accurate for the tested geometries but should not be assumed universal for all printed components.

Finally, the LCA results are bounded by cradle-to-gate assumptions, US-based supply-chain distances, and the adopted strength-normalization methods. Upstream processes for secondary materials such as fly ash were modeled based on current databases, whereas glass grinding energy was explicitly calculated from Rittinger's law (from 4 mm to 0.1 mm only). These assumptions, while transparent and reasonable, introduce uncertainties when considering global deployment scenarios or alternative manufacturing pathways. This is particularly important as the environmental burden of activators can vary significantly depending on their source. As the results showed, sodium hydroxide and sodium silicate carry substantial embodied energy, underscoring the need to explore sustainable or naturally derived alkaline activators. Such low-carbon alternatives have the potential to reduce environmental impacts while maintaining, or even improving, mechanical performance.

As a result, while the results provide a robust foundation for the development of soil-based, alkali-activated, and low-binder 3D-printed materials, these limitations underscore that soil behavior is highly site-specific and can vary significantly. Activator impacts also vary widely, and standardized testing methods for 3D-printed geomaterials remain underdeveloped. Broader material sources, improved soil characterization protocols, alternative activators, and expanded LCA boundaries will be essential for future advancements in this field.

7.3. Future Research Work

Based on the findings of this dissertation, the following directions are proposed for future research:

- Extend the development and testing of CSAEBs to provide optimum mixture ratios per grain size and clay content, as well as the mixture's overall pH levels. The two are particularly important in optimum compaction and strength development, especially since soil particles vary widely in shape, size, and mineralogy, which makes achieving uniform packing and bonding more challenging.

- Investigate designing direction-specific fabrication of 3D-printed components based on the level of anisotropic behavior and loading conditions, and develop standardized factors for converting strength values depending on the direction and sampling method of 3D-printed components.

- Investigate long-term thermal and durability performance of soil-based and alkali-activated mixtures under real environmental exposures. This may include thermal conductivity, diffusivity, and specific heat for thermal performance and freeze-thaw, wet-dry, and chemical attack cycles for durability performance.

- Explore automated mixture proportioning and in-line rheology control systems to adapt soil-based 3D-printing mixtures in real time during production. In doing so, a controlling algorithm or automated dispensing system can be developed to measure the binder, water, aggregate, and admixture qualities during the 3D printing process.

References

[1] M. Nodehi, N. Kumar, S. Mitra, and M. Barbato, “An experimental study on using glass powder in replacement of coal fly ash in compressed and stabilized geopolymer earth blocks (CSGEB),” presented at the Earth USA, Santa Fe, NM, 2024.

[2] International Energy Agency (IEA), “Global Status Report for Buildings and Construction 2019.” Accessed: Sept. 17, 2023. [Online]. Available: https://www.iea.org/reports/global-status-report-for-buildings-and-construction-2019

[3] V. J. L. Gan, J. C. P. Cheng, I. M. C. Lo, and C. M. Chan, “Developing a CO2-e accounting method for quantification and analysis of embodied carbon in high-rise buildings,” *Journal of Cleaner Production*, vol. 141, pp. 825–836, Jan. 2017, doi: 10.1016/j.jclepro.2016.09.126.

[4] A. Pelé-Peltier, R. Charef, and J.-C. Morel, “Factors affecting the use of earth material in mainstream construction: a critical review,” *Building Research & Information*, vol. 51, no. 2, pp. 119–137, Feb. 2023, doi: 10.1080/09613218.2022.2070719.

[5] H. Schroeder, *Sustainable Building with Earth*. Cham: Springer International Publishing, 2016. doi: 10.1007/978-3-319-19491-2.

[6] T. R. Naik, “Sustainability of Concrete Construction,” *Practice Periodical on Structural Design and Construction*, vol. 13, no. 2, pp. 98–103, May 2008, doi: 10.1061/(ASCE)1084-0680(2008)13:2(98).

[7] Healthy Materials Lab, “Material Collection Earth.” Accessed: Nov. 16, 2025. [Online]. Available: https://healthymaterialslab.org/material-collections/earth

[8] S. Halliday, *Sustainable Construction*, 0 ed. Second edition. | New York, NY : Routledge, 2018.: Routledge, 2018. doi: 10.1201/9781315514819.

[9] R. H. Jackson, “The Use of Adobe in the Mormon Cultural Region,” *Journal of Cultural Geography*, vol. 1, no. 1, pp. 82–95, Sept. 1980, doi: 10.1080/08873638009478654.

[10] E. Fodde, “Traditional Earthen Building Techniques in Central Asia,” *International Journal of Architectural Heritage*, vol. 3, no. 2, pp. 145–168, Mar. 2009, doi: 10.1080/15583050802279081.

[11] N. Berend, Ed., *The Expansion of Central Europe in the Middle Ages*, 1st ed. Routledge, 2017. doi: 10.4324/9781315239781.

[12] R. Codispoti, D. V. Oliveira, R. S. Olivito, P. B. Lourenço, and R. Fangueiro, “Mechanical performance of natural fiber-reinforced composites for the strengthening of masonry,” *Composites Part B: Engineering*, vol. 77, pp. 74–83, Aug. 2015, doi: 10.1016/j.compositesb.2015.03.021.

[13] J. Liu, Y. Cao, Y. Xue, D. Li, L. Feng, and Y. F. Chen, “Automatic unit layout of masonry structure using memetic algorithm and building information modeling,” *Automation in Construction*, vol. 130, p. 103858, Oct. 2021, doi: 10.1016/j.autcon.2021.103858.

[14] C. Turco, A. C. Paula Junior, E. R. Teixeira, and R. Mateus, “Optimisation of Compressed Earth Blocks (CEBs) using natural origin materials: A systematic literature review,” *Construction and Building Materials*, vol. 309, p. 125140, Nov. 2021, doi: 10.1016/j.conbuildmat.2021.125140.

[15] P. De Berardinis, M. Rotilio, C. Marchionni, and A. Friedman, “Improving the energy-efficiency of historic masonry buildings. A case study: A minor centre in the Abruzzo region, Italy,” *Energy and Buildings*, vol. 80, pp. 415–423, Sept. 2014, doi: 10.1016/j.enbuild.2014.05.047.

[16] ASTM C62, “Standard Specification for Building Brick (Solid Masonry Units Made From Clay or,” vol. i, pp. 100–103, 2013, doi: 10.1520/C0062-13A.2.
[17] ASTM C216, “Standard Specification for Facing Brick (Solid Masonry Units Made from Clay or,” vol. i, pp. 1–14, 2016, doi: 10.1520/C0216-16.2.
[18] ASTM C652, “Standard Specification for Hollow Brick (Hollow Masonry Units Made From Clay or,” vol. i, pp. 1–6, 2015, doi: 10.1520/C0652-15.1.
[19] ASTM C55, “Standard Specification for Concrete Building Brick,” vol. i, pp. 16–18, 2016, doi: 10.1520/C0055-16.2.
[20] J. E. Amonette, *Reinforced Masonry Engineering Handbook: Clay and Concrete Masonry*. CRC Press, 1998.
[21] G. K. M. Subramanian, M. Balasubramanian, and A. A. Jeya Kumar, “A Review on the Mechanical Properties of Natural Fiber Reinforced Compressed Earth Blocks,” *Journal of Natural Fibers*, vol. 19, no. 14, pp. 7687–7701, Oct. 2022, doi: 10.1080/15440478.2021.1958405.
[22] J. T. Kolawole, O. B. Olalusi, and A. J. Orimogunje, “Adhesive bond potential of compressed stabilised earth brick,” *Structures*, vol. 23, pp. 812–820, Feb. 2020, doi: 10.1016/j.istruc.2019.12.024.
[23] X. Zhang and R. Zheng, “Reducing building embodied emissions in the design phase: A comparative study on structural alternatives,” *Journal of Cleaner Production*, vol. 243, p. 118656, Jan. 2020, doi: 10.1016/j.jclepro.2019.118656.
[24] ACI Committee 122, “ACI 122R Guide to thermal properties of concrete and masonry systems,” 2002.
[25] R. Fioretti and P. Principi, “Thermal Performance of Hollow Clay Brick with Low Emissivity Treatment in Surface Enclosures,” *Coatings*, vol. 4, no. 4, pp. 715–731, Oct. 2014, doi: 10.3390/coatings4040715.
[26] Y. Chihab, R. Bouferra, M. Garoum, M. Essaleh, and N. Laaroussi, “Thermal inertia and energy efficiency enhancements of hollow clay bricks integrated with phase change materials,” *Journal of Building Engineering*, vol. 53, p. 104569, Aug. 2022, doi: 10.1016/j.jobe.2022.104569.
[27] W. Khaliq and M. F. Bashir, “High temperature mechanical and material properties of burnt masonry bricks,” *Mater Struct*, vol. 49, no. 12, pp. 5195–5208, Dec. 2016, doi: 10.1617/s11527-016-0854-0.
[28] C. Turco, M. O. Teixeira, E. Teixeira, and R. Mateus, “Mechanical properties and durability of compressed earth blocks incorporating natural materials,” *Journal of Building Engineering*, vol. 111, p. 113386, Oct. 2025, doi: 10.1016/j.jobe.2025.113386.
[29] C. T. S. Beckett, P. A. Jaquin, and J.-C. Morel, “Weathering the storm: A framework to assess the resistance of earthen structures to water damage,” *Construction and Building Materials*, vol. 242, p. 118098, May 2020, doi: 10.1016/j.conbuildmat.2020.118098.
[30] R. Eires, A. Camões, and S. Jalali, “Ancient Materials and Techniques to Improve the Earthen Building Durability,” *KEM*, vol. 634, pp. 357–366, Dec. 2014, doi: 10.4028/www.scientific.net/KEM.634.357.
[31] A. Azil *et al.*, “Earth construction: Field variabilities and laboratory reproducibility,” *Construction and Building Materials*, vol. 314, p. 125591, Jan. 2022, doi: 10.1016/j.conbuildmat.2021.125591.
[32] M. Barnaure, S. Bonnet, and P. Poullain, “Earth buildings with local materials: Assessing the variability of properties measured using non-destructive methods,” *Construction and*

Building Materials, vol. 281, p. 122613, Apr. 2021, doi: 10.1016/j.conbuildmat.2021.122613.
[33] Y. Ji, P. Poullain, and N. Leklou, "The selection and design of earthen materials for 3D printing," *Construction and Building Materials*, vol. 404, p. 133114, Nov. 2023, doi: 10.1016/j.conbuildmat.2023.133114.
[34] A. Perrot, D. Rangeard, and E. Courteille, "3D printing of earth-based materials: Processing aspects," *Construction and Building Materials*, vol. 172, pp. 670–676, May 2018, doi: 10.1016/j.conbuildmat.2018.04.017.
[35] F. Faleschini, D. Trento, M. Masoomi, C. Pellegrino, and M. A. Zanini, "Sustainable mixes for 3D printing of earth-based constructions," *Construction and Building Materials*, vol. 398, p. 132496, Sept. 2023, doi: 10.1016/j.conbuildmat.2023.132496.
[36] L. Ding, W. Jiang, Y. Zhou, C. Zhou, and S. Liu, "BIM-based task-level planning for robotic brick assembly through image-based 3D modeling," *Advanced Engineering Informatics*, vol. 43, p. 100993, Jan. 2020, doi: 10.1016/j.aei.2019.100993.
[37] M. Gomaa, S. Schade, D. W. Bao, and Y. M. Xie, "Automation in rammed earth construction for industry 4.0: Precedent work, current progress and future prospect," *Journal of Cleaner Production*, vol. 398, p. 136569, Apr. 2023, doi: 10.1016/j.jclepro.2023.136569.
[38] S. Goessens, C. Mueller, and P. Latteur, "Feasibility study for drone-based masonry construction of real-scale structures," *Automation in Construction*, vol. 94, pp. 458–480, Oct. 2018, doi: 10.1016/j.autcon.2018.06.015.
[39] S. Parascho, I. X. Han, S. Walker, A. Beghini, E. P. G. Bruun, and S. Adriaenssens, "Robotic vault: a cooperative robotic assembly method for brick vault construction," *Constr Robot*, vol. 4, no. 3–4, pp. 117–126, Dec. 2020, doi: 10.1007/s41693-020-00041-w.
[40] B. L., L. K. P. Liu, and A. A., "Climbing Service Robots for Improving Safety in Building Maintenance Industry," in *Bioinspiration and Robotics Walking and Climbing Robots*, M. K., Ed., I-Tech Education and Publishing, 2007. doi: 10.5772/5498.
[41] X. Yang, H. Li, Y. Yu, X. Luo, T. Huang, and X. Yang, "Automatic Pixel-Level Crack Detection and Measurement Using Fully Convolutional Network," *Computer-Aided Civil and Infrastructure Engineering*, vol. 33, no. 12, pp. 1090–1109, 2018, doi: 10.1111/mice.12412.
[42] C. Biscarini, I. Catapano, N. Cavalagli, G. Ludeno, F. A. Pepe, and F. Ubertini, "UAV photogrammetry, infrared thermography and GPR for enhancing structural and material degradation evaluation of the Roman masonry bridge of Ponte Lucano in Italy," *NDT & E International*, vol. 115, p. 102287, Oct. 2020, doi: 10.1016/j.ndteint.2020.102287.
[43] S. Brell-Cokcan and T. J. Adams, *Construction & robotics, Research Driven Project : construction robotics, international M. Sc. programme, Vol. 4: Research Paper / WS 2022*. RWTH Aachen University, 2024, p. pages 109 Seiten : Illustrationen. doi: 10.18154/RWTH-2023-08854.
[44] B. Sun, C. Mao, T. Wang, and Z. Li, "Cost Assessment Framework for Construction Robots: Comparative Study of Robotic and Traditional Construction," *J. Manage. Eng.*, vol. 40, no. 5, p. 05024009, Sept. 2024, doi: 10.1061/JMENEA.MEENG-6122.
[45] N. Melenbrink, J. Werfel, and A. Menges, "On-site autonomous construction robots: Towards unsupervised building," *Automation in Construction*, vol. 119, p. 103312, Nov. 2020, doi: 10.1016/j.autcon.2020.103312.

[46] K. Keyrouz, Y. Chen, and F. Hamzeh, “Integrating Modular Construction, Interlocking Blocks, and Robotic Technology with Lean Principles to Improve Masonry Construction Efficiency,” *Buildings*, vol. 15, no. 12, p. 2133, June 2025, doi: 10.3390/buildings15122133.
[47] S. Parascho, I. X. Han, A. Beghini, and M. Miki, “LightVault: A Design and Robotic Fabrication Method for Complex Masonry Structures”.
[48] P. Carneau, R. Mesnil, N. Roussel, and O. Baverel, “Additive manufacturing of cantilever - From masonry to concrete 3D printing,” *Automation in Construction*, vol. 116, p. 103184, Aug. 2020, doi: 10.1016/j.autcon.2020.103184.
[49] M. Nodehi, T. Ozbakkaloglu, and A. Gholampour, “Effect of supplementary cementitious materials on properties of 3D printed conventional and alkali-activated concrete: A review,” *Automation in Construction*, vol. 138, p. 104215, June 2022, doi: 10.1016/j.autcon.2022.104215.
[50] M. Batikha, R. Jotangia, M. Y. Baaj, and I. Mousleh, “3D concrete printing for sustainable and economical construction: A comparative study,” *Automation in Construction*, vol. 134, p. 104087, Feb. 2022, doi: 10.1016/j.autcon.2021.104087.
[51] R. Robayo-Salazar, R. Mejía De Gutiérrez, M. A. Villaquirán-Caicedo, and S. Delvasto Arjona, “3D printing with cementitious materials: Challenges and opportunities for the construction sector,” *Automation in Construction*, vol. 146, p. 104693, Feb. 2023, doi: 10.1016/j.autcon.2022.104693.
[52] L. H. Lárusson, G. Fischer, and J. Jönsson, “Prefabricated floor panels composed of fiber reinforced concrete and a steel substructure,” *Engineering Structures*, vol. 46, pp. 104–115, Jan. 2013, doi: 10.1016/j.engstruct.2012.06.035.
[53] T. Munmulla *et al.*, “Analyses of Structural Robustness of Prefabricated Modular Buildings: A Case Study on Mid-Rise Building Configurations,” *Buildings*, vol. 12, no. 8, p. 1289, Aug. 2022, doi: 10.3390/buildings12081289.
[54] J. Glass, “Wall panel renaissance: tilt-up concrete construction,” *Proceedings of the Institution of Civil Engineers - Structures and Buildings*, vol. 140, no. 3, pp. 277–289, Aug. 2000, doi: 10.1680/stbu.2000.140.3.277.
[55] S. Malazdrewicz, K. A. Ostrowski, and Ł. Sadowski, “Large Panel System Technology in the Second Half of the Twentieth Century—Literature Review, Recycling Possibilities and Research Gaps,” *Buildings*, vol. 12, no. 11, p. 1822, Oct. 2022, doi: 10.3390/buildings12111822.
[56] S. Nam, J. Yoon, K. Kim, and B. Choi, “Optimization of Prefabricated Components in Housing Modular Construction,” *Sustainability*, vol. 12, no. 24, p. 10269, Dec. 2020, doi: 10.3390/su122410269.
[57] S. Kim, “Prefabricated and Modularized Residential Construction: A Review of Present Status, Opportunities, and Future Challenges,” *Buildings*, vol. 15, no. 16, p. 2889, Aug. 2025, doi: 10.3390/buildings15162889.
[58] O. Iuorio, *From Mass Prefab to Mass Customization: Modern Methods of Constructions from Experimentation to Manufacturing*. in SpringerBriefs in Applied Sciences and Technology. Cham: Springer Nature Switzerland, 2025. doi: 10.1007/978-3-031-73327-7.
[59] E. Hamed, “Modeling, Analysis, and Behavior of Load-Carrying Precast Concrete Sandwich Panels,” *J. Struct. Eng.*, vol. 142, no. 7, p. 04016036, July 2016, doi: 10.1061/(ASCE)ST.1943-541X.0001490.

[60] M. Popescu, L. Reiter, A. Liew, T. Van Mele, R. J. Flatt, and P. Block, “Building in Concrete with an Ultra-lightweight Knitted Stay-in-place Formwork: Prototype of a Concrete Shell Bridge,” *Structures*, vol. 14, pp. 322–332, June 2018, doi: 10.1016/j.istruc.2018.03.001.
[61] S. El-Tawil, K. A. Harries, P. J. Fortney, B. M. Shahrooz, and Y. Kurama, “Seismic Design of Hybrid Coupled Wall Systems: State of the Art,” *J. Struct. Eng.*, vol. 136, no. 7, pp. 755–769, July 2010, doi: 10.1061/(ASCE)ST.1943-541X.0000186.
[62] A. Kantaros, P. Zacharia, C. Drosos, M. Papoutsidakis, E. Pallis, and T. Ganetsos, “Smart Infrastructure and Additive Manufacturing: Synergies, Advantages, and Limitations,” *Applied Sciences*, vol. 15, no. 7, p. 3719, Mar. 2025, doi: 10.3390/app15073719.
[63] F. P. Bos *et al.*, “The realities of additively manufactured concrete structures in practice,” *Cement and Concrete Research*, vol. 156, p. 106746, June 2022, doi: 10.1016/j.cemconres.2022.106746.
[64] M. Kovářík, P. Svoboda, and H. H. Achten, “Limits and Potential of 3D Printing Technologies for Construction of Concrete Shells,” *SSP*, vol. 292, pp. 249–256, June 2019, doi: 10.4028/www.scientific.net/SSP.292.249.
[65] P. Carneau, R. Mesnil, N. Roussel, and O. Baverel, “Additive manufacturing of cantilever - From masonry to concrete 3D printing,” *Automation in Construction*, vol. 116, p. 103184, Aug. 2020, doi: 10.1016/j.autcon.2020.103184.
[66] S. Kawashima, K. Wang, R. D. Ferron, J. H. Kim, N. Tregger, and S. Shah, “A review of the effect of nanoclays on the fresh and hardened properties of cement-based materials,” *Cement and Concrete Research*, vol. 147, p. 106502, Sept. 2021, doi: 10.1016/j.cemconres.2021.106502.
[67] N. A. Tregger, M. E. Pakula, and S. P. Shah, “Influence of clays on the rheology of cement pastes,” *Cement and Concrete Research*, vol. 40, no. 3, pp. 384–391, Mar. 2010, doi: 10.1016/j.cemconres.2009.11.001.
[68] S. S. L. Chan, R. M. Pennings, L. Edwards, and G. V. Franks, “3D printing of clay for decorative architectural applications: Effect of solids volume fraction on rheology and printability,” *Additive Manufacturing*, vol. 35, p. 101335, Oct. 2020, doi: 10.1016/j.addma.2020.101335.
[69] J. Alonso Madrid, G. Sotorrío Ortega, J. Gorostiza Carabaño, N. O. E. Olsson, and J. A. Tenorio Ríos, “3D Claying: 3D Printing and Recycling Clay,” *Crystals*, vol. 13, no. 3, p. 375, Feb. 2023, doi: 10.3390/cryst13030375.
[70] A. U. Rehman and J.-H. Kim, “3D Concrete Printing: A Systematic Review of Rheology, Mix Designs, Mechanical, Microstructural, and Durability Characteristics,” *Materials*, vol. 14, no. 14, p. 3800, July 2021, doi: 10.3390/ma14143800.
[71] M. Uwasu, K. Hara, and H. Yabar, “World cement production and environmental implications,” *Environmental Development*, vol. 10, pp. 36–47, Apr. 2014, doi: 10.1016/j.envdev.2014.02.005.
[72] C. Chen, G. Habert, Y. Bouzidi, and A. Jullien, “Environmental impact of cement production: detail of the different processes and cement plant variability evaluation,” *Journal of Cleaner Production*, vol. 18, no. 5, pp. 478–485, Mar. 2010, doi: 10.1016/j.jclepro.2009.12.014.
[73] Y. Han, Z. Yang, T. Ding, and J. Xiao, “Environmental and economic assessment on 3D printed buildings with recycled concrete,” *Journal of Cleaner Production*, vol. 278, p. 123884, 2021, doi: 10.1016/j.jclepro.2020.123884.

[74] A. Perrot, D. Rangeard, and E. Courteille, “3D printing of earth-based materials: Processing aspects,” *Construction and Building Materials*, vol. 172, pp. 670–676, May 2018, doi: 10.1016/j.conbuildmat.2018.04.017.
[75] G. Cesaretti, E. Dini, X. De Kestelier, V. Colla, and L. Pambaguian, “Building components for an outpost on the Lunar soil by means of a novel 3D printing technology,” *Acta Astronautica*, vol. 93, pp. 430–450, Jan. 2014, doi: 10.1016/j.actaastro.2013.07.034.
[76] J. Daher, J. Kleib, M. Benzerzour, N.-E. Abriak, and G. Aouad, “The Development of Soil-Based 3D-Printable Mixtures: A Mix-Design Methodology and a Case Study,” *Buildings*, vol. 13, no. 7, p. 1618, June 2023, doi: 10.3390/buildings13071618.
[77] CBSNEWS, “3D printing could shake up construction industry and bring tech to the moon.” Accessed: Sept. 05, 2024. [Online]. Available: https://www.cbsnews.com/news/3d-printing-on-earth-and-moon-60-minutes/
[78] J. Zhang, J. Wang, S. Dong, X. Yu, and B. Han, “A review of the current progress and application of 3D printed concrete,” *Composites Part A: Applied Science and Manufacturing*, vol. 125, p. 105533, Oct. 2019, doi: 10.1016/j.compositesa.2019.105533.
[79] G. De Schutter, K. Lesage, V. Mechtcherine, V. N. Nerella, G. Habert, and I. Agusti-Juan, “Vision of 3D printing with concrete — Technical, economic and environmental potentials,” *Cement and Concrete Research*, vol. 112, pp. 25–36, Oct. 2018, doi: 10.1016/j.cemconres.2018.06.001.
[80] J. G. Sanjayan, B. Nematollahi, M. Xia, and T. Marchment, “Effect of surface moisture on inter-layer strength of 3D printed concrete,” *Construction and Building Materials*, vol. 172, pp. 468–475, 2018, doi: 10.1016/j.conbuildmat.2018.03.232.
[81] B. Zhu, J. Pan, B. Nematollahi, Z. Zhou, Y. Zhang, and J. Sanjayan, “Development of 3D printable engineered cementitious composites with ultra-high tensile ductility for digital construction,” *Materials & Design*, vol. 181, p. 108088, Nov. 2019, doi: 10.1016/j.matdes.2019.108088.
[82] A. V. Rahul, M. Santhanam, H. Meena, and Z. Ghani, “Mechanical characterization of 3D printable concrete,” *Construction and Building Materials*, vol. 227, p. 116710, Dec. 2019, doi: 10.1016/j.conbuildmat.2019.116710.
[83] T. Ding, J. Xiao, S. Zou, and Y. Wang, “Hardened properties of layered 3D printed concrete with recycled sand,” *Cement and Concrete Composites*, vol. 113, no. June, p. 103724, 2020, doi: 10.1016/j.cemconcomp.2020.103724.
[84] A. Aramburu, I. Calderon-Uriszar-Aldaca, and I. Puente, “3D printing effect on the compressive strength of concrete structures,” *Construction and Building Materials*, vol. 354, p. 129108, Nov. 2022, doi: 10.1016/j.conbuildmat.2022.129108.
[85] X. Guo, J. Yang, and G. Xiong, “Influence of supplementary cementitious materials on rheological properties of 3D printed fly ash based geopolymer,” *Cement and Concrete Composites*, vol. 114, no. September, p. 103820, 2020, doi: 10.1016/j.cemconcomp.2020.103820.
[86] S.-J. Woo, J.-M. Yang, H. Lee, and H.-K. Kwon, “Comparison of Properties of 3D-Printed Mortar in Air vs. Underwater,” *Materials*, vol. 14, no. 19, p. 5888, Oct. 2021, doi: 10.3390/ma14195888.
[87] *Additive manufacturing for construction Qualification principles Structural and infrastructure elements (ISO-ASTM 52939)*, 2023. [Online]. Available: https://www.iso.org/standard/81177.html

[88] M. Nodehi, L. Omer, B. Asiabanpour, and T. Ozbakkaloglu, “A novel lightweight mechanism for 3D printing of cementitious materials,” *Prog Addit Manuf*, vol. 9, no. 2, pp. 169–183, Apr. 2024, doi: 10.1007/s40964-023-00441-8.
[89] B. Hasanzadeh, “Testing and modeling of the thixotropic behavior of cementitous materials.,” University of Louisville, 2017. doi: 10.18297/etd/2868.
[90] W. Schmidt and J. Link, “Rheological Properties,” in *Measuring Rheological Properties of Cement-based Materials*, vol. 39, M. Sonebi and D. Feys, Eds., in RILEM State-of-the-Art Reports, vol. 39. , Cham: Springer Nature Switzerland, 2024, pp. 7–31. doi: 10.1007/978-3-031-36743-4_2.
[91] M. Nodehi, B. Asiabanpour, L. Omer, and T. Ozbakkaloglu, “Material Characterization of Diversity Aggregated Cementitious Materials Produced with a Modular Lightweight Additive Manufacturing Extrusion System,” in *2021 International Solid Freeform Fabrication Symposium*, University of Texas at Austin, 2021. doi: http://dx.doi.org/10.26153/tsw/17667.
[92] M. T. Mollah, R. Comminal, M. P. Serdeczny, B. Šeta, and J. Spangenberg, “Computational analysis of yield stress buildup and stability of deposited layers in material extrusion additive manufacturing,” *Additive Manufacturing*, vol. 71, p. 103605, June 2023, doi: 10.1016/j.addma.2023.103605.
[93] M. T. Mollah, R. Comminal, M. P. Serdeczny, D. B. Pedersen, and J. Spangenberg, “Numerical Predictions of Bottom Layer Stability in Material Extrusion Additive Manufacturing,” *JOM*, vol. 74, no. 3, pp. 1096–1101, Mar. 2022, doi: 10.1007/s11837-021-05035-9.
[94] S. Ma and S. Kawashima, “Role of shear stress at rest on the viscoelastic response of fresh cement pastes,” *Journal of Rheology*, vol. 64, no. 2, pp. 433–444, Mar. 2020, doi: 10.1122/1.5129676.
[95] A. Sharma, S. Gupta, M. Noman Husain, and S. Chaudhary, “Factors affecting the rheology of cement-based composites: A review,” *J Am Ceram Soc.*, vol. 108, no. 6, p. e20429, June 2025, doi: 10.1111/jace.20429.
[96] A. W. Saak, H. M. Jennings, and S. P. Shah, “The influence of wall slip on yield stress and viscoelastic measurements of cement paste,” *Cement and Concrete Research*, vol. 31, no. 2, pp. 205–212, Feb. 2001, doi: 10.1016/S0008-8846(00)00440-3.
[97] J. Zhang, X. Ren, and Z. Ahmad, *Building Seismic Monitoring and Detection Technology: Proceedings of the 2nd International Conference on Structural Seismic Resistance, Monitoring and Detection (SSRMD 2023), Xiamen, China, 6-8 January 2023*, 1st ed. London: CRC Press, 2023. doi: 10.1201/9781003409564.
[98] Q.-B. Bui *et al.*, “Seismic Assessment of Earthen Structures,” in *Testing and Characterisation of Earth-based Building Materials and Elements*, vol. 35, A. Fabbri, J.-C. Morel, J.-E. Aubert, Q.-B. Bui, D. Gallipoli, and B. V. V. Reddy, Eds., in RILEM State-of-the-Art Reports, vol. 35. , Cham: Springer International Publishing, 2022, pp. 181–210. doi: 10.1007/978-3-030-83297-1_5.
[99] L. Librelotto, P. Ferroli, K. Fahfouhi, F. Craveiro, and H. Bártolo, “The Potential of Earth as a Construction Material: Review and Perspectives,” in *Proceedings of the 3rd International Conference on Water Energy Food and Sustainability (ICoWEFS 2023)*, J. R. D. C. S. Galvão, P. Brito, F. D. S. Neves, H. D. A. Almeida, S. D. J. M. Mourato, and C. Nobre, Eds., in Springer Proceedings in Earth and Environmental Sciences. , Cham: Springer Nature Switzerland, 2024, pp. 623–633. doi: 10.1007/978-3-031-48532-9_58.

[100] F. Pacheco-Torgal and S. Jalali, “Earth construction: Lessons from the past for future eco-efficient construction,” *Construction and Building Materials*, vol. 29, pp. 512–519, Apr. 2012, doi: 10.1016/j.conbuildmat.2011.10.054.
[101] J. Bredenoord and Y. Kulshreshtha, “Compressed Stabilized Earthen Blocks and Their Use in Low-Cost Social Housing,” *Sustainability*, vol. 15, no. 6, p. 5295, Mar. 2023, doi: 10.3390/su15065295.
[102] H. Schroeder, *Sustainable Building with Earth*. Cham: Springer International Publishing, 2016. doi: 10.1007/978-3-319-19491-2.
[103] D. B. Dittenber and H. V. S. GangaRao, “Critical review of recent publications on use of natural composites in infrastructure,” *Composites Part A: Applied Science and Manufacturing*, vol. 43, no. 8, pp. 1419–1429, Aug. 2012, doi: 10.1016/j.compositesa.2011.11.019.
[104] A. Gupta, “Building a Green Home Using Local Resources and Sustainable Technology in Jammu Region – A Case Study,” *Energy Procedia*, vol. 115, pp. 59–69, June 2017, doi: 10.1016/j.egypro.2017.05.007.
[105] P. Patel and A. Patel, “Use of sustainable green materials in construction of green buildings for sustainable development,” *IOP Conf. Ser.: Earth Environ. Sci.*, vol. 785, no. 1, p. 012009, June 2021, doi: 10.1088/1755-1315/785/1/012009.
[106] M. Nodehi, “A Comparative Review of Polymer, Bacterial-based, and Alkali-Activated (also Geopolymer) Binders: Production, Mechanical, Durability, and Environmental impacts (life cycle assessment (LCA)),” *Construction and Building Materials*, 2024, doi: https://doi.org/10.1016/j.conbuildmat.2024.135816.
[107] A. A. Kutty, G. M. Abdella, M. Kucukvar, N. C. Onat, and M. Bulu, “A system thinking approach for harmonizing smart and sustainable city initiatives with United Nations sustainable development goals,” *Sustainable Development*, vol. 28, no. 5, pp. 1347–1365, Sept. 2020, doi: 10.1002/sd.2088.
[108] China Dialogue, “Construction material emissions to peak by 2030, not 2025.” Accessed: Feb. 29, 2024. [Online]. Available: https://chinadialogue.net/en/digest/construction-material-emissions-to-peak-by-2030-not-2025/
[109] G. Habert, J. B. D’Espinose De Lacaillerie, and N. Roussel, “An environmental evaluation of geopolymer based concrete production: Reviewing current research trends,” *Journal of Cleaner Production*, vol. 19, no. 11, pp. 1229–1238, 2011, doi: 10.1016/j.jclepro.2011.03.012.
[110] M. Nodehi and V. M. Taghvaee, “Alkali-Activated Materials and Geopolymer: a Review of Common Precursors and Activators Addressing Circular Economy,” *Circular Economy and Sustainability*, 2021, doi: 10.1007/s43615-021-00029-w.
[111] F. Pacheco-Torgal, Z. Abdollahnejad, A. F. Camões, M. Jamshidi, and Y. Ding, “Durability of alkali-activated binders: A clear advantage over Portland cement or an unproven issue?,” *Construction and Building Materials*, vol. 30, pp. 400–405, 2012, doi: 10.1016/j.conbuildmat.2011.12.017.
[112] M. Lahoti, K. H. Tan, and E.-H. Yang, “A critical review of geopolymer properties for structural fire-resistance applications,” *Construction and Building Materials*, vol. 221, pp. 514–526, Oct. 2019, doi: 10.1016/j.conbuildmat.2019.06.076.
[113] J. R. González-López, C. A. Juárez-Alvarado, B. Ayub-Francis, and J. M. Mendoza-Rangel, “Compaction effect on the compressive strength and durability of stabilized earth

blocks," *Construction and Building Materials*, vol. 163, pp. 179–188, Feb. 2018, doi: 10.1016/j.conbuildmat.2017.12.074.
[114] M.-I. Lavie Arsène, C. Frédéric, and F. Nathalie, "Improvement of lifetime of compressed earth blocks by adding limestone, sandstone and porphyry aggregates," *Journal of Building Engineering*, vol. 29, p. 101155, May 2020, doi: 10.1016/j.jobe.2019.101155.
[115] E. Hall, B. Pulatsu, E. Erdogmus, and B. Skourup, "Compression, Tension, and Fracture Energy Properties of Compressed Cement-Stabilized Earth Blocks," *J. Archit. Eng.*, vol. 28, no. 1, p. 06021005, Mar. 2022, doi: 10.1061/(ASCE)AE.1943-5568.0000524.
[116] N. Schwarz, H. Cam, and N. Neithalath, "Influence of a fine glass powder on the durability characteristics of concrete and its comparison to fly ash," *Cement and Concrete Composites*, vol. 30, no. 6, pp. 486–496, July 2008, doi: 10.1016/j.cemconcomp.2008.02.001.
[117] C. D. Westbroek, J. Bitting, M. Craglia, J. M. C. Azevedo, and J. M. Cullen, "Global material flow analysis of glass: From raw materials to end of life," *J of Industrial Ecology*, vol. 25, no. 2, pp. 333–343, Apr. 2021, doi: 10.1111/jiec.13112.
[118] W. Ferdous *et al.*, "Recycling of landfill wastes (tyres, plastics and glass) in construction – A review on global waste generation, performance, application and future opportunities," *Resources, Conservation and Recycling*, vol. 173, p. 105745, Oct. 2021, doi: 10.1016/j.resconrec.2021.105745.
[119] M. Nodehi and V. Mohamad Taghvaee, "Sustainable concrete for circular economy: a review on use of waste glass," *Glass Structures & Engineering*, vol. 7, no. 1, pp. 3–22, Apr. 2022, doi: 10.1007/s40940-021-00155-9.
[120] S. Dadsetan, H. Siad, M. Lachemi, and M. Sahmaran, "Extensive evaluation on the effect of glass powder on the rheology, strength, and microstructure of metakaolin-based geopolymer binders," *Construction and Building Materials*, vol. 268, p. 121168, Jan. 2021, doi: 10.1016/j.conbuildmat.2020.121168.
[121] W. Dong, W. Li, and Z. Tao, "A comprehensive review on performance of cementitious and geopolymeric concretes with recycled waste glass as powder, sand or cullet," *Resources, Conservation and Recycling*, vol. 172, no. April, p. 105664, 2021, doi: 10.1016/j.resconrec.2021.105664.
[122] A. Raj *et al.*, "Building a Sustainable Future from Theory to Practice: A Comprehensive PRISMA-Guided Assessment of Compressed Stabilized Earth Blocks (CSEB) for Construction Applications," *Sustainability*, vol. 15, no. 12, p. 9374, June 2023, doi: 10.3390/su15129374.
[123] N. Kumar and M. Barbato, "EFFECTS OF HIGH TEMPERATURES ON MECHANICAL STRENGTH OF COMPRESSED AND STABILIZED EARTH BLOCKS," 2022.
[124] E. Idriss *et al.*, "Engineering and structural properties of compressed earth blocks (CEB) stabilized with a calcined clay-based alkali-activated binder," *Innov. Infrastruct. Solut.*, vol. 7, no. 2, p. 157, Apr. 2022, doi: 10.1007/s41062-022-00760-9.
[125] M. B. Diop, M. W. Grutzeck, and L. Molez, "Comparing the performances of bricks made with natural clay and clay activated by calcination and addition of sodium silicate," *Applied Clay Science*, vol. 54, no. 2, pp. 172–178, Nov. 2011, doi: 10.1016/j.clay.2011.08.005.
[126] J. Yu, H.-L. Wu, D. K. Mishra, G. Li, and C. K. Leung, "Compressive strength and environmental impact of sustainable blended cement with high-dosage Limestone and

Calcined Clay (LC2)," *Journal of Cleaner Production*, vol. 278, p. 123616, Jan. 2021, doi: 10.1016/j.jclepro.2020.123616.
[127] J. Ongpeng *et al.*, "Alkali-activated binder as stabilizer in compressed earth blocks," *IOP Conf. Ser.: Mater. Sci. Eng.*, vol. 849, no. 1, p. 012042, May 2020, doi: 10.1088/1757-899X/849/1/012042.
[128] B. Sangeethavani, M. Muthukannan, R. Deepak, and A. Arun Pradeep, "A performance assessment on Compressed Stabilized Earth Block (CSEB) using geo – polymeric binders," *IOP Conf. Ser.: Mater. Sci. Eng.*, vol. 983, no. 1, p. 012001, Nov. 2020, doi: 10.1088/1757-899X/983/1/012001.
[129] O G Aluko and T F Awolusi, "A Study On The Short Term Compressive Strength Of Compressed Stabilised Earth Block With Waste Glass Powder As Part Replacement For Cement," 2019, *Unpublished*. doi: 10.13140/RG.2.2.21117.82400.
[130] J. Rivera, J. Coelho, R. Silva, T. Miranda, F. Castro, and N. Cristelo, "Compressed earth blocks stabilized with glass waste and fly ash activated with a recycled alkaline cleaning solution," *Journal of Cleaner Production*, vol. 284, p. 124783, Feb. 2021, doi: 10.1016/j.jclepro.2020.124783.
[131] S. Larbi, A. Khaldi, W. Maherzi, and N.-E. Abriak, "Formulation of Compressed Earth Blocks Stabilized by Glass Waste Activated with NaOH Solution," *Sustainability*, vol. 14, no. 1, p. 102, Dec. 2021, doi: 10.3390/su14010102.
[132] A. International, "ASTM C136-14, Standard Test Method for Sieve Analysis of Fine and Coarse Aggregates," *ASTM International, West Conshohocken, PA*, vol. i, no. 200, pp. 1–5, 2014, doi: 10.1520/C0136-14.
[133] A. International, "ASTM C136-01, Standard Test Method for Sieve Analysis of Fine and Coarse Aggregates," *ASTM International, West Conshohocken, PA*, vol. i, no. 200, pp. 1–5, 2001, doi: 10.1520/C0136-01.
[134] D18 Committee, *Test Methods for Laboratory Determination of Water (Moisture) Content of Soil and Rock by Mass - ASTM D2216*. doi: 10.1520/D2216-19.
[135] *Standard Practice for Classification of Soils for Engineering Purposes (Unified Soil Classification System)*, D2487-11, 2011.
[136] D18 Committee, *Test Methods for Particle-Size Distribution (Gradation) of Soils Using Sieve Analysis - ASTM D6913*. doi: 10.1520/D6913_D6913M-17R25.
[137] C09 Committee, *ASTM C117-17 Test Method for Materials Finer than 75-m (No. 200) Sieve in Mineral Aggregates by Washing*. doi: 10.1520/C0117-17.
[138] ASTM International., *ASTM D4318-17e1 Standard test methods for liquid limit, plastic limit, and plasticity index of soils*. West Conshohocken, PA: ASTM International, 2017. doi: https://doi.org/10.1520/D4318-17E01.
[139] ASTM D698-21, *Standard Test Methods for Laboratory Compaction Characteristics of Soil Using Standard Effort (12,400 ft-lbf/ft3 (600 kN-m/m3))*. [Online]. Available: https://www.astm.org/d0698-12r21.html
[140] Vitrominerals inc., "Technical data sheet: ACAS-300 Type GS Glass Pozzolans." Accessed: Nov. 17, 2025. [Online]. Available: https://vitrominerals.com/wp-content/uploads/2021/05/ACAS-300-Type-GS-Glass-Pozzolans-TDS-210513.pdf
[141] Rigaku, "Semiquant Analysis by the SQX Scatter FP Method." Accessed: May 06, 2025. [Online]. Available: https://rigaku.com/products/xrf-spectrometers/wdxrf/application-notes/xrf1036-semiquant-analysis-sqx-scatter-fp

[142] J. W. Phair and J. S. J. Van Deventer, “Effect of silicate activator pH on the leaching and material characteristics of waste-based inorganic polymers,” *Minerals Engineering*, vol. 14, no. 3, pp. 289–304, Mar. 2001, doi: 10.1016/S0892-6875(01)00002-4.
[143] D18 Committee, *Test Method for Particle-Size Distribution (Gradation) of Fine-Grained Soils Using the Sedimentation (Hydrometer) Analysis - ASTM D7928-21*. doi: 10.1520/D7928-21E01.
[144] ASTM D4262, *Test Method for pH of Chemically Cleaned or Etched Concrete Surfaces*. doi: 10.1520/D4262-05R18.
[145] American Society for Testing and Materials, *ASTM C20 - 00(2010) “Standard Test Methods for Apparent Porosity, Water Absorption, Apparent Specific Gravity, and Bulk Density of Burned Refractory Brick and Shapes by Boiling Water,”* 2010. doi: 10.1520/C0020-00R15.
[146] ASTM, “ASTM C642 :Standard Test Method for Density, Absorption, and Voids in Hardened Concrete, ASTM International, United States,” *Annual Book of ASTM Standards*, no. March, pp. 1–3, 2013, doi: 10.1520/C0642-13.5.
[147] C09 Committee, “Test Method for Flexural Strength of Concrete (Using Simple Beam With Center-Point Loading) C293,” ASTM International. doi: 10.1520/C0293_C0293M-16.
[148] A. C109/109M-16a, “Standard test method for compressive strength of hydraulic cement mortars (Using 2-in. or cube specimens),” *Annual Book of ASTM Standards*, vol. i, pp. 1–10, 2016, doi: 10.1520/C0109.
[149] ASTM C944, “Standard Test Method for Abrasion Resistance of Concrete or Mortar Surfaces by the Rotating-Cutter Method,” *ASTM (American Society for Testing and Materials)*, 2012, doi: 10.1520/mnl10913m.
[150] ISO14040, “Environmental Management - Life Cycle Assessment - Principles and Framework. International Standard ISO 14040.,” *International Organization for Standardization (ISO)*, 1997, [Online]. Available: http://www.iso.org/iso/catalogue_detail.htm?csnumber=37456
[151] Y. Q. Sun, Y. Liu, and S. P. Cui, “Comparative Life Cycle Assessment of Autoclaved Concrete Blocks and Fired Blocks in China,” *MSF*, vol. 913, pp. 1018–1026, Feb. 2018, doi: 10.4028/www.scientific.net/MSF.913.1018.
[152] N. Youssef, A. Z. Rabenantoandro, Z. Dakhli, F. Hage Chehade, and Z. Lafhaj, “Environmental evaluation of geopolymer bricks,” *MATEC Web Conf.*, vol. 281, p. 03005, 2019, doi: 10.1051/matecconf/201928103005.
[153] E. K. Anastasiou, A. Liapis, and M. Papachristoforou, “Life Cycle Assessment of Concrete Products for Special Applications Containing EAF Slag,” *Procedia Environmental Sciences*, vol. 38, pp. 469–476, 2017, doi: 10.1016/j.proenv.2017.03.138.
[154] A. Tripathy and P. Kumar Acharya, “Ecological impact assessment of sustainable concrete paver blocks based on endpoint damage categories,” *Materials Today: Proceedings*, p. S2214785323029127, May 2023, doi: 10.1016/j.matpr.2023.05.281.
[155] B. L. Damineli, F. M. Kemeid, P. S. Aguiar, and V. M. John, “Measuring the eco-efficiency of cement use,” *Cement and Concrete Composites*, vol. 32, no. 8, pp. 555–562, Sept. 2010, doi: 10.1016/j.cemconcomp.2010.07.009.
[156] J. G. Backes, R. Hinkle-Johnson, and M. Traverso, “The influence of the Functional Unit on the comparability of life cycle assessments in the construction sector: A Systematic

Literature Review and attempt at unification for Reinforced Concrete," *Case Studies in Construction Materials*, vol. 18, p. e01966, July 2023, doi: 10.1016/j.cscm.2023.e01966.
[157] A. Furberg, R. Arvidsson, and S. Molander, "A practice-based framework for defining functional units in comparative life cycle assessments of materials," *J of Industrial Ecology*, vol. 26, no. 3, pp. 718–730, June 2022, doi: 10.1111/jiec.13218.
[158] EPA.GOV, "Tool for Reduction and Assessment of Chemicals and Other Environmental Impacts (TRACI)." Accessed: Oct. 07, 2024. [Online]. Available: https://www.epa.gov/chemical-research/tool-reduction-and-assessment-chemicals-and-other-environmental-impacts-traci
[159] Warren L. McCabe, Julian C. Smith, Peter Harriott, *Unit Operations of Chemical Engineering*. in McGraw-Hill Chemical Engineering. McGraw-Hill, 2004.
[160] J.F. Richardson, J. H. Harker, and J. R. Backhurst, *CHEMICAL ENGINEERING: Particle Technology and Separation Processes*, vol. 2, 2 vols. Butterworth-Heinemann, 2002. [Online]. Available: https://linkinghub.elsevier.com/retrieve/pii/C20090257333
[161] *Chemical Engineering Design*. Elsevier, 2022. doi: 10.1016/C2019-0-02025-0.
[162] A. M. Matos and J. Sousa-Coutinho, "Durability of mortar using waste glass powder as cement replacement," *Construction and Building Materials*, vol. 36, pp. 205–215, Nov. 2012, doi: 10.1016/j.conbuildmat.2012.04.027.
[163] S. Gokulakannan, P. Mukesh, M. Anitha, Sp. Arul Sri, G. Dinesh Kumar, and V. Vijayakumar, "Experimentation on the impact of partial replacement of cement with glass powder in mortar mixture," *Materials Today: Proceedings*, vol. 68, pp. 1628–1634, 2022, doi: 10.1016/j.matpr.2022.07.441.
[164] M. Bameri, M. Mohammadhasani, A. Khaloo, A. Ashour, and M. NikKhah, "Influence of Waste Glass Powder as a Supplementary Cementitious Material (SCM) on the Mechanical Properties, Expansion, Environmental Impact, and Microstructure of Cementitious Mortar," *Engineering Reports*, vol. 7, no. 6, p. e70238, June 2025, doi: 10.1002/eng2.70238.
[165] M. Nodehi, J. Ren, X. Shi, S. Debbarma, and T. Ozbakkaloglu, "Experimental evaluation of alkali-activated and portland cement-based mortars prepared using waste glass powder in replacement of fly ash," *Construction and Building Materials*, vol. 394, p. 132124, Aug. 2023, doi: 10.1016/j.conbuildmat.2023.132124.
[166] T. Mohammed, F. Aguayo, M. Nodehi, and T. Ozbakkaloglu, "Engineering properties of structural lightweight concrete containing expanded shale and clay with high volume class F and class C fly ash," *Structural Concrete*, Sept. 2022, doi: 10.1002/suco.202200562.
[167] "Long-Term Performance of High-Volume Fly Ash Concrete Pavements," *MJ*, vol. 100, no. 2, 2003, doi: 10.14359/12555.
[168] Mehrab Nodehi, "Mechanical properties and cracking potential of alkali-activated materials containing waste glass powder," Texas State University, 2022. Accessed: Jan. 07, 2024. [Online]. Available: https://hdl.handle.net/10877/16830
[169] S. Wang, Q. Xue, Y. Zhu, G. Li, Z. Wu, and K. Zhao, "Experimental study on material ratio and strength performance of geopolymer-improved soil," *Construction and Building Materials*, vol. 267, p. 120469, Jan. 2021, doi: 10.1016/j.conbuildmat.2020.120469.
[170] H. Wu *et al.*, "Effects of binder component and curing regime on compressive strength, capillary water absorption, shrinkage and pore structure of geopolymer mortars," *Construction and Building Materials*, vol. 442, p. 137707, Sept. 2024, doi: 10.1016/j.conbuildmat.2024.137707.

[171] A. E. Danks, S. R. Hall, and Z. Schnepp, “The evolution of ‘sol–gel’ chemistry as a technique for materials synthesis,” *Mater. Horiz.*, vol. 3, no. 2, pp. 91–112, 2016, doi: 10.1039/C5MH00260E.
[172] M. Nodehi, J. Ren, X. Shi, S. Debbarma, and T. Ozbakkaloglu, “Experimental evaluation of alkali-activated and portland cement-based mortars prepared using waste glass powder in replacement of fly ash,” *Construction and Building Materials*, vol. 394, p. 132124, Aug. 2023, doi: 10.1016/j.conbuildmat.2023.132124.
[173] A. Kazemian, A. Gholizadeh Vayghan, and F. Rajabipour, “Quantitative assessment of parameters that affect strength development in alkali activated fly ash binders,” *Construction and Building Materials*, vol. 93, pp. 869–876, Sept. 2015, doi: 10.1016/j.conbuildmat.2015.05.078.
[174] H. Chen, P. Feng, S. Ye, and W. Sun, “The coupling effect of calcium concentration and pH on early hydration of cement,” *Construction and Building Materials*, vol. 185, pp. 391–401, Oct. 2018, doi: 10.1016/j.conbuildmat.2018.07.067.
[175] L. Rossi *et al.*, “Future perspectives for alkali-activated materials: from existing standards to structural applications,” *RILEM Tech Lett*, vol. 7, pp. 159–177, Jan. 2023, doi: 10.21809/rilemtechlett.2022.160.
[176] X. Yu, H. Xiao, Z. Li, J. Qian, S. Luo, and H. Su, “Experimental Study on Microstructure of Unsaturated Expansive Soil Improved by MICP Method,” *Applied Sciences*, vol. 12, no. 1, p. 342, Dec. 2021, doi: 10.3390/app12010342.
[177] P. Kasinikota and D. D. Tripura, “Evaluation of compressed stabilized earth block properties using crushed brick waste,” *Construction and Building Materials*, vol. 280, p. 122520, Apr. 2021, doi: 10.1016/j.conbuildmat.2021.122520.
[178] D18 Committee, “Test Methods for Wetting and Drying Compacted Soil-Cement Mixtures,” ASTM International. doi: 10.1520/D0559-03.
[179] P. Turgut, “Limestone dust and glass powder wastes as new brick material,” *Materials and Structures*, vol. 41, no. 5, pp. 805–813, June 2008, doi: 10.1617/s11527-007-9284-3.
[180] M. Nodehi and F. Aguayo, “Ultra high performance and high strength geopolymer concrete,” *Journal of Building Pathology and Rehabilitation*, vol. 6, no. 1, p. 34, Dec. 2021, doi: 10.1007/s41024-021-00130-5.
[181] M. A. M. Ariffin, M. A. R. Bhutta, M. W. Hussin, M. Mohd Tahir, and N. Aziah, “Sulfuric acid resistance of blended ash geopolymer concrete,” *Construction and Building Materials*, vol. 43, pp. 80–86, June 2013, doi: 10.1016/j.conbuildmat.2013.01.018.
[182] T. A. Aiken, L. Gu, J. Kwasny, G. F. Huseien, D. McPolin, and W. Sha, “Acid resistance of alkali-activated binders: A review of performance, mechanisms of deterioration and testing procedures,” *Construction and Building Materials*, vol. 342, p. 128057, Aug. 2022, doi: 10.1016/j.conbuildmat.2022.128057.
[183] P. W. Ariyadasa *et al.*, “Macro and microstructural evolution of low-calcium fly ash-based geopolymer mortar exposed to sulphuric acid corrosion,” *Cement and Concrete Research*, vol. 178, p. 107436, Apr. 2024, doi: 10.1016/j.cemconres.2024.107436.
[184] W. Duan, Y. Zhuge, Y. Liu, C. W. K. Chow, A. Keegan, and G. Jiang, “Enhancing acid corrosion resistance in alkaline-activated materials with water treatment residue and blast-furnace slag,” *Construction and Building Materials*, vol. 447, p. 138105, Oct. 2024, doi: 10.1016/j.conbuildmat.2024.138105.

[185] J. P. Gevaudan, A. Caicedo-Ramirez, M. T. Hernandez, and W. V. Srubar, “Copper and cobalt improve the acid resistance of alkali-activated cements,” *Cement and Concrete Research*, vol. 115, pp. 327–338, Jan. 2019, doi: 10.1016/j.cemconres.2018.08.002.
[186] A. Hidalgo, C. Domingo, C. Garcia, S. Petit, C. Andrade, and C. Alonso, “Microstructural changes induced in Portland cement-based materials due to natural and supercritical carbonation,” *J Mater Sci*, vol. 43, no. 9, pp. 3101–3111, May 2008, doi: 10.1007/s10853-008-2521-5.
[187] J. Elsen, G. Mertens, and R. Snellings, “Portland Cement and other Calcareous Hydraulic Binders: History, Production and Mineralogy,” in *Advances in the characterization of industrial minerals*, G. Ferraris and G. E. Christidis, Eds., European Mineralogical Union, 2010, pp. 441–479. doi: 10.1180/EMU-notes.9.11.
[188] H. Levene, “Robust tests for equality of variances,” *Contributions to probability and statistics. Essays in honor of Harold Hotelling*, pp. 279–292, 1961.
[189] A. Rutherford, *Anova and Ancova*, Second Edi. Hoboken, New Jersey: John Wiley & Sons, Inc., 2011. doi: 10.1002/9781118491683.
[190] L. M. Lix, J. C. Keselman, and H. J. Keselman, “Consequences of assumption violations revisited: A quantitative review of alternatives to the one-way analysis of variance F test,” *Review of educational research*, vol. 66, no. 4, pp. 579–619, 1996, doi: 10.3102/00346543066004579.
[191] B. L. Welch, “On the comparison of several mean values: An alternative approach,” *Biometrika*, vol. 38, no. 3/4, pp. 330–336, 1951, doi: 10.2307/2332579.
[192] Kwiatkowski Construction Co., “Different Types of Concrete Strengths and Their Uses.” Accessed: Oct. 10, 2025. [Online]. Available: https://kwiatkowskiconcrete.com/2024/06/different-types-of-concrete-strengths-and-their-uses
[193] C15 Committee, *Specification for Loadbearing Concrete Masonry Units ASTM C90-24a*. doi: 10.1520/C0090-24A.
[194] M. Barnaure, S. Bonnet, and P. Poullain, “Earth buildings with local materials: Assessing the variability of properties measured using non-destructive methods,” *Construction and Building Materials*, vol. 281, p. 122613, Apr. 2021, doi: 10.1016/j.conbuildmat.2021.122613.
[195] M. N. O. Sadiku, A. J. Ajayi-Majebi, and P. O. Adebo, *Emerging Technologies in Manufacturing*. Cham: Springer International Publishing, 2023. doi: 10.1007/978-3-031-23156-8.
[196] Y. Zhang *et al.*, “3D printing technology in concrete construction,” *Nat. Rev. Clean Technol.*, vol. 1, no. 4, pp. 288–303, Apr. 2025, doi: 10.1038/s44359-025-00047-z.
[197] S. H. Khajavi *et al.*, “Additive Manufacturing in the Construction Industry: The Comparative Competitiveness of 3D Concrete Printing,” *Applied Sciences*, vol. 11, no. 9, p. 3865, Apr. 2021, doi: 10.3390/app11093865.
[198] M. P. Tinoco, É. M. De Mendonça, L. I. C. Fernandez, L. R. Caldas, O. A. M. Reales, and R. D. Toledo Filho, “Life cycle assessment (LCA) and environmental sustainability of cementitious materials for 3D concrete printing: A systematic literature review,” *Journal of Building Engineering*, vol. 52, p. 104456, July 2022, doi: 10.1016/j.jobe.2022.104456.
[199] A. Curth, N. Pearl, A. Castro-Salazar, C. Mueller, and L. Sass, “3D printing earth: Local, circular material processing, fabrication methods, and Life Cycle Assessment,”

Construction and Building Materials, vol. 421, p. 135714, Mar. 2024, doi: 10.1016/j.conbuildmat.2024.135714.
[200] A. Yousaf, A. Al Rashid, and M. Koç, "3D printing of alkali-activated geopolymers for sustainable and circular economy advancements," *Circular Economy*, vol. 3, no. 3, p. 100101, Sept. 2024, doi: 10.1016/j.cec.2024.100101.
[201] I. Bianco, B. Ap Dafydd Tomos, and R. Vinai, "Analysis of the environmental impacts of alkali-activated concrete produced with waste glass-derived silicate activator – A LCA study," *Journal of Cleaner Production*, vol. 316, p. 128383, Sept. 2021, doi: 10.1016/j.jclepro.2021.128383.
[202] P. S. Matheu, K. Ellis, and B. Varela, "Comparing the Environmental Impacts of Alkali Activated Mortar and Traditional Portland Cement Mortar using Life Cycle Assessment," *IOP Conf. Ser.: Mater. Sci. Eng.*, vol. 96, p. 012080, Nov. 2015, doi: 10.1088/1757-899X/96/1/012080.
[203] U. T. Bezerra, H. S. Ferreira, and N. P. Barbosa, Eds., "Current Developments and Future Needs for Natural Earth Construction: A State-of-the-Art Review," in *Bio-Inspired Materials*, vol. 6, in Frontiers in Biomaterials, vol. 6. , BENTHAM SCIENCE PUBLISHERS, 2019. doi: 10.2174/97898114068981190601.
[204] N. Hanratty, M. Khan, and C. McNally, "The Role of Different Clay Types in Achieving Low-Carbon 3D Printed Concretes," *Buildings*, vol. 14, no. 7, p. 2194, July 2024, doi: 10.3390/buildings14072194.
[205] Y. Li, H. Zhou, H. Liu, X. Ding, and W. Zhang, "Geotechnical properties of 3D-printed transparent granular soil," *Acta Geotech.*, vol. 16, no. 6, pp. 1789–1800, June 2021, doi: 10.1007/s11440-020-01111-7.
[206] C. Hong, X. Wang, K. Han, D. Su, and Z. Chen, "Performance investigation of 3D printed clay soil using fiber Bragg grating technology," *Acta Geotech.*, vol. 17, no. 2, pp. 453–462, Feb. 2022, doi: 10.1007/s11440-021-01250-5.
[207] N. Dal Ferro and F. Morari, "From Real Soils to 3D-Printed Soils: Reproduction of Complex Pore Network at the Real Size in a Silty-Loam Soil," *Soil Science Society of America Journal*, vol. 79, no. 4, pp. 1008–1017, July 2015, doi: 10.2136/sssaj2015.03.0097.
[208] M. A. DeRousseau, J. H. Arehart, J. R. Kasprzyk, and W. V. Srubar, "Statistical variation in the embodied carbon of concrete mixtures," *Journal of Cleaner Production*, vol. 275, p. 123088, Dec. 2020, doi: 10.1016/j.jclepro.2020.123088.
[209] L. Ben-Alon, V. Loftness, K. A. Harries, and E. Cochran Hameen, "Integrating Earthen Building Materials and Methods into Mainstream Construction Using Environmental Performance Assessment and Building Policy," *IOP Conf. Ser.: Earth Environ. Sci.*, vol. 323, no. 1, p. 012139, Aug. 2019, doi: 10.1088/1755-1315/323/1/012139.
[210] O. B. Carcassi, R. Salierno, P. A. Falcinelli, I. M. Paoletti, and L. Ben-Alon, "Upscaling Natural Materials in Construction: Earthen, Fast-Growing, and Living Materials," *Sustainability*, vol. 16, no. 18, p. 7926, Sept. 2024, doi: 10.3390/su16187926.
[211] F. Faleschini, D. Trento, M. Masoomi, C. Pellegrino, and M. A. Zanini, "Sustainable mixes for 3D printing of earth-based constructions," *Construction and Building Materials*, vol. 398, p. 132496, Sept. 2023, doi: 10.1016/j.conbuildmat.2023.132496.
[212] M. Xia and J. G. Sanjayan, "Methods of enhancing strength of geopolymer produced from powder-based 3D printing process," *Materials Letters*, vol. 227, pp. 281–283, Sept. 2018, doi: 10.1016/j.matlet.2018.05.100.

[213] Y. Yao, M. Hu, F. Di Maio, and S. Cucurachi, “Life cycle assessment of 3D printing geo-polymer concrete: An ex-ante study,” *J of Industrial Ecology*, vol. 24, no. 1, pp. 116–127, Feb. 2020, doi: 10.1111/jiec.12930.
[214] S. Muthukrishnan, S. Ramakrishnan, and J. Sanjayan, “Effect of alkali reactions on the rheology of one-part 3D printable geopolymer concrete,” *Cement and Concrete Composites*, vol. 116, p. 103899, Feb. 2021, doi: 10.1016/j.cemconcomp.2020.103899.
[215] J. Fernandes, M. Peixoto, R. Mateus, and H. Gervásio, “Life cycle analysis of environmental impacts of earthen materials in the Portuguese context: Rammed earth and compressed earth blocks,” *Journal of Cleaner Production*, vol. 241, p. 118286, Dec. 2019, doi: 10.1016/j.jclepro.2019.118286.
[216] A. Alsalman, L. N. Assi, R. S. Kareem, K. Carter, and P. Ziehl, “Energy and CO2 emission assessments of alkali-activated concrete and Ordinary Portland Cement concrete: A comparative analysis of different grades of concrete,” *Cleaner Environmental Systems*, vol. 3, p. 100047, Dec. 2021, doi: 10.1016/j.cesys.2021.100047.
[217] D. Glanz *et al.*, “Comparative environmental footprint analysis of ultra-high-performance concrete using Portland cement and alkali-activated materials,” *Front. Built Environ.*, vol. 9, p. 1196246, May 2023, doi: 10.3389/fbuil.2023.1196246.
[218] R. Bajpai, K. Choudhary, A. Srivastava, K. S. Sangwan, and M. Singh, “Environmental impact assessment of fly ash and silica fume based geopolymer concrete,” *Journal of Cleaner Production*, vol. 254, p. 120147, 2020, doi: 10.1016/j.jclepro.2020.120147.
[219] Astm:C138/C138M-13, “Standard Test Method for Density (Unit Weight), Yield, and Air Content (Gravimetric),” *ASTM International*, vol. i, pp. 23–26, 2013, doi: 10.1520/C0138.
[220] C. C. Test and B. Statements, “ASTM C143M, ‘Standard Test Method for Slump of Hydraulic Cement Concrete’, American Society for Testing and Materials, Vol. 04.02, pp.1-4, 2014,” vol. i, no. Reapproved, pp. 1–4, 2014, doi: 10.1520/C0143.
[221] ASTM C403, “Standard Test Method for Time of Setting of Concrete Mixtures by Penetration Resistance,” pp. 1–7, 2008, doi: 10.1520/C0403.
[222] C08 Committee, *Test Methods for Apparent Porosity, Water Absorption, Apparent Specific Gravity, and Bulk Density of Burned Refractory Brick and Shapes by Boiling Water*. doi: 10.1520/C0020-00R22.
[223] C01 Committee, *Test Method for Compressive Strength of Hydraulic Cement Mortars (Using 2-in. or [50mm] Cube Specimens)*. doi: 10.1520/C0109_C0109M-21.
[224] C496, *Test Method for Splitting Tensile Strength of Cylindrical Concrete Specimens*. doi: 10.1520/C0496_C0496M-17.
[225] ASTM C1425, *StandardTest Method for Interlaminar Shear Strength of 1–D and 2–D Continuous Fiber-Reinforced Advanced Ceramics at Elevated Temperatures*. [Online]. Available: https://www.astm.org/c1425-13.html
[226] Q. Wan, Y. Zhang, and R. Zhang, “The effect of pore behavior and gel structure on the mechanical property at different initial water content,” *Construction and Building Materials*, vol. 309, p. 125146, Nov. 2021, doi: 10.1016/j.conbuildmat.2021.125146.
[227] S. Chen *et al.*, “Pore structure of geopolymer materials and its correlations to engineering properties: A review,” *Construction and Building Materials*, vol. 328, p. 127064, Apr. 2022, doi: 10.1016/j.conbuildmat.2022.127064.
[228] T. Phoo-ngernkham, A. Maegawa, N. Mishima, S. Hatanaka, and P. Chindaprasirt, “Effects of sodium hydroxide and sodium silicate solutions on compressive and shear

bond strengths of FA–GBFS geopolymer," *Construction and Building Materials*, vol. 91, pp. 1–8, Aug. 2015, doi: 10.1016/j.conbuildmat.2015.05.001.
[229] M. S. Morsy, S. H. Alsayed, Y. Al-Salloum, and T. Almusallam, "Effect of Sodium Silicate to Sodium Hydroxide Ratios on Strength and Microstructure of Fly Ash Geopolymer Binder," *Arab J Sci Eng*, vol. 39, no. 6, pp. 4333–4339, June 2014, doi: 10.1007/s13369-014-1093-8.
[230] Vickers, Les, "Development of Geopolymer Systems for High Temperature Applications," Curtin University, 2015. Accessed: Dec. 18, 2024. [Online]. Available: http://hdl.handle.net/20.500.11937/1453
[231] A. Van Riessen, W. Rickard, and J. Sanjayan, "Thermal properties of geopolymers," in *Geopolymers*, Elsevier, 2009, pp. 315–342. doi: 10.1533/9781845696382.2.315.
[232] S. França, M. N. C. Oliveira, L. N. Sousa, M. V. De Moura Solar Silva, P. H. R. Borges, and A. C. Da Silva Bezerra, "The durability of alkali-activated mortars based on sugarcane bagasse ash with different content of Na2O," *J Build Rehabil*, vol. 8, no. 2, p. 74, Dec. 2023, doi: 10.1007/s41024-023-00319-w.
[233] A. Just and B. Middendorf, "Microstructure of high-strength foam concrete," *Materials Characterization*, vol. 60, no. 7, pp. 741–748, July 2009, doi: 10.1016/j.matchar.2008.12.011.
[234] J. E. Barralet, T. Gaunt, A. J. Wright, I. R. Gibson, and J. C. Knowles, "Effect of porosity reduction by compaction on compressive strength and microstructure of calcium phosphate cement," *J. Biomed. Mater. Res.*, vol. 63, no. 1, pp. 1–9, Jan. 2002, doi: 10.1002/jbm.1074.
[235] H. Chen, P. Feng, S. Ye, and W. Sun, "The coupling effect of calcium concentration and pH on early hydration of cement," *Construction and Building Materials*, vol. 185, pp. 391–401, Oct. 2018, doi: 10.1016/j.conbuildmat.2018.07.067.
[236] A. Kumar, G. Sant, C. Patapy, C. Gianocca, and K. L. Scrivener, "The influence of sodium and potassium hydroxide on alite hydration: Experiments and simulations," *Cement and Concrete Research*, vol. 42, no. 11, pp. 1513–1523, Nov. 2012, doi: 10.1016/j.cemconres.2012.07.003.
[237] H. Güllü, A. Cevik, K. M. A. Al-Ezzi, and M. E. Gülsan, "On the rheology of using geopolymer for grouting: A comparative study with cement-based grout included fly ash and cold bonded fly ash," *Construction and Building Materials*, vol. 196, pp. 594–610, Jan. 2019, doi: 10.1016/j.conbuildmat.2018.11.140.
[238] A. Favier, J. Hot, G. Habert, N. Roussel, and J.-B. d'Espinose De Lacaillerie, "Flow properties of MK-based geopolymer pastes. A comparative study with standard Portland cement pastes," *Soft Matter*, vol. 10, no. 8, p. 1134, 2014, doi: 10.1039/c3sm51889b.
[239] E. Negahban, A. Bagheri, and J. Sanjayan, "Pore gradation effect on Portland cement and geopolymer concretes," *Cement and Concrete Composites*, vol. 122, p. 104141, Sept. 2021, doi: 10.1016/j.cemconcomp.2021.104141.
[240] S. Yu, H. Bale, S. Park, J. Y. Hwang, and S. H. Hong, "Anisotropic microstructure dependent mechanical behavior of 3D-printed basalt fiber-reinforced thermoplastic composites," *Composites Part B: Engineering*, vol. 224, p. 109184, Nov. 2021, doi: 10.1016/j.compositesb.2021.109184.
[241] D. Heras Murcia, M. Genedy, and M. M. Reda Taha, "Examining the significance of infill printing pattern on the anisotropy of 3D printed concrete," *Construction and Building Materials*, vol. 262, p. 120559, 2020, doi: 10.1016/j.conbuildmat.2020.120559.

[242] C. Liu *et al.*, “Anisotropic mechanical properties of extrusion-based 3D printed layered concrete,” *Journal of Materials Science*, vol. 56, no. 30, pp. 16851–16864, 2021, doi: 10.1007/s10853-021-06416-w.
[243] E. Negahban, A. Bagheri, and J. Sanjayan, “Pore structure profile of ambient temperature-cured geopolymer concrete and its effect on engineering properties,” *Construction and Building Materials*, vol. 406, p. 133311, Nov. 2023, doi: 10.1016/j.conbuildmat.2023.133311.
[244] Z. Jiang, O. E. Ozbulut, G. Arce, and L. M. Colosi, “Accounting for decarbonization impacts across the full life cycle of alternative concrete materials: A case-study for graphene-amended cementitious composites,” *Journal of Cleaner Production*, vol. 482, p. 144186, Dec. 2024, doi: 10.1016/j.jclepro.2024.144186.
[245] Y. Liu *et al.*, “Advancing Sustainable Construction: Discrete Modular Systems & Robotic Assembly,” *Sustainability*, vol. 16, no. 15, p. 6678, Aug. 2024, doi: 10.3390/su16156678.
[246] D. A. Salas, A. D. Ramirez, N. Ulloa, H. Baykara, and A. J. Boero, “Life cycle assessment of geopolymer concrete,” *Construction and Building Materials*, vol. 190, pp. 170–177, Nov. 2018, doi: 10.1016/j.conbuildmat.2018.09.123.
[247] R. B. Meshram and S. Kumar, “Comparative life cycle assessment (LCA) of geopolymer cement manufacturing with Portland cement in Indian context,” *Int. J. Environ. Sci. Technol.*, vol. 19, no. 6, pp. 4791–4802, June 2022, doi: 10.1007/s13762-021-03336-9.
[248] J. Fořt, M. Mildner, and R. Černý, “Consequences of omitting some important factors in the environmental analyses of commercial sodium silicate/sodium hydroxide use for alkaline activation in the light of comparison with cement-based composites,” *Science of The Total Environment*, vol. 928, p. 172324, June 2024, doi: 10.1016/j.scitotenv.2024.172324.
[249] B. C. McLellan, R. P. Williams, J. Lay, A. Van Riessen, and G. D. Corder, “Costs and carbon emissions for geopolymer pastes in comparison to ordinary portland cement,” *Journal of Cleaner Production*, vol. 19, no. 9–10, pp. 1080–1090, June 2011, doi: 10.1016/j.jclepro.2011.02.010.
[250] W. Gao *et al.*, “The status, challenges, and future of additive manufacturing in engineering,” *Computer-Aided Design*, vol. 69, pp. 65–89, Dec. 2015, doi: 10.1016/j.cad.2015.04.001.
[251] I. Gibson, D. Rosen, B. Stucker, and M. Khorasani, *Additive Manufacturing Technologies*. Cham: Springer International Publishing, 2021. doi: 10.1007/978-3-030-56127-7.
[252] C. Buchanan and L. Gardner, “Metal 3D printing in construction: A review of methods, research, applications, opportunities and challenges,” *Engineering Structures*, vol. 180, pp. 332–348, Feb. 2019, doi: 10.1016/j.engstruct.2018.11.045.
[253] B. Khoshnevis and G. Bekey, “Automated Construction Using Contour Crafting -- Applications on Earth and Beyond,” presented at the 19th International Symposium on Automation and Robotics in Construction, Washington, DC, USA, Sept. 2002. doi: 10.22260/ISARC2002/0076.
[254] D. Hwang and B. Khoshnevis, “Concrete Wall Fabrication by Contour Crafting,” presented at the 21st International Symposium on Automation and Robotics in Construction, Jeju, Korea, Sept. 2004. doi: 10.22260/ISARC2004/0057.
[255] B. Khoshnevis and G. Bekey, “Centralized sensing and control of multiple mobile robots,” *Computers & Industrial Engineering*, vol. 35, no. 3–4, pp. 503–506, Dec. 1998, doi: 10.1016/S0360-8352(98)00144-2.

[256] B. Khoshnevis and R. Dutton, “Innovative Rapid Prototyping Process Makes Large Sized, Smooth Surfaced Complex Shapes in a Wide Variety of Materials,” *Materials Technology*, vol. 13, no. 2, pp. 53–56, Jan. 1998, doi: 10.1080/10667857.1998.11752766.
[257] M. Valente, A. Sibai, and M. Sambucci, “Extrusion-Based Additive Manufacturing of Concrete Products: Revolutionizing and Remodeling the Construction Industry,” *J. Compos. Sci.*, vol. 3, no. 3, p. 88, Sept. 2019, doi: 10.3390/jcs3030088.
[258] M. Nodehi, T. Ozbakkaloglu, and A. Gholampour, “Effect of supplementary cementitious materials on properties of 3D printed conventional and alkali-activated concrete: A review,” *Automation in Construction*, vol. 138, p. 104215, June 2022, doi: 10.1016/j.autcon.2022.104215.
[259] T. A. M. Salet, Z. Y. Ahmed, F. P. Bos, and H. L. M. Laagland, “Design of a 3D printed concrete bridge by testing,” *Virtual and Physical Prototyping*, vol. 13, no. 3, pp. 222–236, July 2018, doi: 10.1080/17452759.2018.1476064.
[260] T. Ooms *et al.*, “The Production of a Topology-Optimized 3D-Printed Concrete Bridge,” in *Third RILEM International Conference on Concrete and Digital Fabrication*, vol. 37, R. Buswell, A. Blanco, S. Cavalaro, and P. Kinnell, Eds., in RILEM Bookseries, vol. 37. , Cham: Springer International Publishing, 2022, pp. 37–42. doi: 10.1007/978-3-031-06116-5_6.
[261] F. P. Bos *et al.*, “The realities of additively manufactured concrete structures in practice,” *Cement and Concrete Research*, vol. 156, p. 106746, June 2022, doi: 10.1016/j.cemconres.2022.106746.
[262] V. Mechtcherine, J. Grafe, V. N. Nerella, E. Spaniol, M. Hertel, and U. Füssel, “3D-printed steel reinforcement for digital concrete construction – Manufacture, mechanical properties and bond behaviour,” *Construction and Building Materials*, vol. 179, pp. 125–137, Aug. 2018, doi: 10.1016/j.conbuildmat.2018.05.202.
[263] K. Zhang *et al.*, “Aerial additive manufacturing with multiple autonomous robots,” *Nature*, vol. 609, no. 7928, pp. 709–717, Sept. 2022, doi: 10.1038/s41586-022-04988-4.
[264] Z. Xu, D. Zhang, H. Li, X. Sun, K. Zhao, and Y. Wang, “Effect of FA and GGBFS on compressive strength, rheology, and printing properties of cement-based 3D printing material,” *Construction and Building Materials*, vol. 339, p. 127685, July 2022, doi: 10.1016/j.conbuildmat.2022.127685.
[265] N. Roussel, “Rheological requirements for printable concretes,” *Cement and Concrete Research*, vol. 112, pp. 76–85, Oct. 2018, doi: 10.1016/j.cemconres.2018.04.005.
[266] C. Liu *et al.*, “Influence of hydroxypropyl methylcellulose and silica fume on stability, rheological properties, and printability of 3D printing foam concrete,” *Cement and Concrete Composites*, vol. 122, p. 104158, Sept. 2021, doi: 10.1016/j.cemconcomp.2021.104158.
[267] T. Ding, J. Xiao, S. Zou, and X. Zhou, “Anisotropic behavior in bending of 3D printed concrete reinforced with fibers,” *Composite Structures*, vol. 254, no. July, p. 112808, 2020, doi: 10.1016/j.compstruct.2020.112808.
[268] M. Van Den Heever, A. Du Plessis, J. Kruger, and G. Van Zijl, “Evaluating the effects of porosity on the mechanical properties of extrusion-based 3D printed concrete,” *Cement and Concrete Research*, vol. 153, p. 106695, Mar. 2022, doi: 10.1016/j.cemconres.2021.106695.
[269] *Additive manufacturing — Material extrusion-based additive manufacturing of plastic materials — Part 1: Feedstock materials*, 2020.

[270] ISO/ASTM, *Additive manufacturing — Design — Part 2: Laser-based powder bed fusion of polymers*.
[271] F42 Committee, *Standard Guide for Additive Manufacturing General Principles Requirements for Purchased AM Parts*. doi: 10.1520/F3167-16.
[272] ISO/ASTM 52939:2023, *Additive manufacturing for construction — Qualification principles — Structural and infrastructure elements*, Dec. 2023.
[273] S. K. Kaliyavaradhan, P. S. Ambily, P. R. Prem, and S. B. Ghodke, "Test methods for 3D printable concrete," *Automation in Construction*, vol. 142, p. 104529, Oct. 2022, doi: 10.1016/j.autcon.2022.104529.
[274] L. Casagrande, L. Esposito, C. Menna, D. Asprone, and F. Auricchio, "Effect of testing procedures on buildability properties of 3D-printable concrete," *Construction and Building Materials*, vol. 245, p. 118286, June 2020, doi: 10.1016/j.conbuildmat.2020.118286.
[275] R. Buswell *et al.*, "Geometric quality assurance for 3D concrete printing and hybrid construction manufacturing using a standardised test part for benchmarking capability," *Cement and Concrete Research*, vol. 156, p. 106773, June 2022, doi: 10.1016/j.cemconres.2022.106773.
[276] J. Kruger, A. du Plessis, and G. van Zijl, "An investigation into the porosity of extrusion-based 3D printed concrete," *Additive Manufacturing*, vol. 37, no. November 2020, p. 101740, 2021, doi: 10.1016/j.addma.2020.101740.
[277] Z. Zhang, M. Shakoorioskooie, M. Griffa, P. Lura, and U. Angst, "A laboratory investigation of cutting damage to the steel-concrete interface," *Cement and Concrete Research*, vol. 138, p. 106229, Dec. 2020, doi: 10.1016/j.cemconres.2020.106229.
[278] N. Alanazi, J. T. Kolawole, R. Buswell, and L. Susmel, "The Theory of Critical Distances to assess the effect of cracks/manufacturing defects on the static strength of 3D-printed concrete," *Engineering Fracture Mechanics*, vol. 269, p. 108563, June 2022, doi: 10.1016/j.engfracmech.2022.108563.
[279] H.-J. Lee, E.-A. Seo, W.-W. Kim, J.-M. Yang, and J.-H. Moon, "X-ray CT Analysis of the Cross-Section of a 3D-Printed Deformed Layer," *Materials*, vol. 14, no. 24, p. 7764, Dec. 2021, doi: 10.3390/ma14247764.
[280] A. Aramburu, I. Calderon-Uriszar-Aldaca, and I. Puente, "3D printing effect on the compressive strength of concrete structures," *Construction and Building Materials*, vol. 354, p. 129108, Nov. 2022, doi: 10.1016/j.conbuildmat.2022.129108.
[281] P. Feng, X. Meng, J.-F. Chen, and L. Ye, "Mechanical properties of structures 3D printed with cementitious powders," *Construction and Building Materials*, vol. 93, pp. 486–497, Sept. 2015, doi: 10.1016/j.conbuildmat.2015.05.132.
[282] L. Casagrande, L. Esposito, C. Menna, D. Asprone, and F. Auricchio, "Effect of testing procedures on buildability properties of 3D-printable concrete," *Construction and Building Materials*, vol. 245, p. 118286, June 2020, doi: 10.1016/j.conbuildmat.2020.118286.
[283] L. Ma *et al.*, "Water loss and shrinkage prediction in 3D printed concrete with varying w/c and specimen sizes," *Cement and Concrete Composites*, vol. 149, p. 105523, May 2024, doi: 10.1016/j.cemconcomp.2024.105523.
[284] R. J. M. Wolfs, F. P. Bos, and T. A. M. Salet, "Correlation between destructive compression tests and non-destructive ultrasonic measurements on early age 3D printed

concrete," *Construction and Building Materials*, vol. 181, pp. 447–454, Aug. 2018, doi: 10.1016/j.conbuildmat.2018.06.060.
[285] P. Sikora *et al.*, "Insight into the microstructural and durability characteristics of 3D printed concrete: Cast versus printed specimens," *Case Studies in Construction Materials*, vol. 17, p. e01320, Dec. 2022, doi: 10.1016/j.cscm.2022.e01320.
[286] A. U. Rehman, A. Perrot, B. M. Birru, and J.-H. Kim, "Recommendations for quality control in industrial 3D concrete printing construction with mono-component concrete: A critical evaluation of ten test methods and the introduction of the performance index," *Developments in the Built Environment*, vol. 16, p. 100232, Dec. 2023, doi: 10.1016/j.dibe.2023.100232.
[287] Y. Mortada, M. Mohammad, B. Mansoor, Z. Grasley, and E. Masad, "Development of Test Methods to Evaluate the Printability of Concrete Materials for Additive Manufacturing," *Materials*, vol. 15, no. 18, p. 6486, Sept. 2022, doi: 10.3390/ma15186486.
[288] ICON, "House Zero." Accessed: Sept. 29, 2024. [Online]. Available: https://www.iconbuild.com/projects/house-zero
[289] https://www.fablabplymouth.org/, "WASP: 3D printing eco-homes with local clay." Accessed: Sept. 29, 2024. [Online]. Available: https://www.fablabplymouth.org/events/wasp/
[290] ASTM C31, *Practice for Making and Curing Concrete Test Specimens in the Field*. doi: 10.1520/C0031_C0031M-19.
[291] J. D. Malan, A. S. Van Rooyen, and G. P. A. G. Van Zijl, "Chloride Induced Corrosion and Carbonation in 3D Printed Concrete," *Infrastructures*, vol. 7, no. 1, p. 1, Dec. 2021, doi: 10.3390/infrastructures7010001.
[292] M. Fernand, Y. Li, Q. Qian, Y. Chi, and Z. Yang, "Effects of coarse aggregates on 3D printability and mechanical properties of ultra high performance fiber reinforced concrete," *Journal of Building Engineering*, vol. 96, p. 110516, Nov. 2024, doi: 10.1016/j.jobe.2024.110516.
[293] M. Colyn, G. Van Zijl, and A. J. Babafemi, "Fresh and strength properties of 3D printable concrete mixtures utilising a high volume of sustainable alternative binders," *Construction and Building Materials*, vol. 419, p. 135474, Mar. 2024, doi: 10.1016/j.conbuildmat.2024.135474.
[294] ASTM C39/C39M, "Standard Test Method for Compressive Strength of Cylindrical Concrete Specimens 1," *ASTM Standard Book*, vol. i, no. March, pp. 1–5, 2003, doi: 10.1520/C0039.
[295] ASTM C469, "Standard Test Method for Static Modulus of Elasticity and Poisson' s Ratio of Concrete in Compression," *ASTM International*, vol. i, pp. 1–5, 2014, doi: 10.1520/C0469.
[296] ASTM C496, "Standard Test Method for Splitting Tensile Strength of Cylindrical Concrete Specimens," pp. 545-545–3, 2008.
[297] A. Jain, M. J. Metzger, and B. J. Glasser, "Effect of particle size distribution on segregation in vibrated systems," *Powder Technology*, vol. 237, pp. 543–553, Mar. 2013, doi: 10.1016/j.powtec.2012.12.044.
[298] X. Gao, J. Zhang, and Y. Su, "Influence of vibration-induced segregation on mechanical property and chloride ion permeability of concrete with variable rheological performance," *Construction and Building Materials*, vol. 194, pp. 32–41, Jan. 2019, doi: 10.1016/j.conbuildmat.2018.11.019.

[299] D. Heras Murcia, M. Genedy, and M. M. Reda Taha, “Examining the significance of infill printing pattern on the anisotropy of 3D printed concrete,” *Construction and Building Materials*, vol. 262, p. 120559, Nov. 2020, doi: 10.1016/j.conbuildmat.2020.120559.
[300] N. Alanazi, J. T. Kolawole, R. Buswell, and L. Susmel, “The Theory of Critical Distances to assess the effect of cracks/manufacturing defects on the static strength of 3D-printed concrete,” *Engineering Fracture Mechanics*, vol. 269, p. 108563, June 2022, doi: 10.1016/j.engfracmech.2022.108563.
[301] A. V. Rahul, M. Santhanam, H. Meena, and Z. Ghani, “Mechanical characterization of 3D printable concrete,” *Construction and Building Materials*, vol. 227, p. 116710, 2019, doi: 10.1016/j.conbuildmat.2019.116710.
[302] J. N. Pacheco, J. De Brito, C. Chastre, and L. Evangelista, “Probabilistic Conversion of the Compressive Strength of Cubes to Cylinders of Natural and Recycled Aggregate Concrete Specimens,” *Materials*, vol. 12, no. 2, p. 280, Jan. 2019, doi: 10.3390/ma12020280.
[303] B. Khoshnevis, “Automated construction by contour crafting—related robotics and information technologies,” *Automation in Construction*, vol. 13, no. 1, pp. 5–19, Jan. 2004, doi: 10.1016/j.autcon.2003.08.012.
[304] J. J. Burger, “Robotically 3D Printed Formwork for Concrete Structures,” ETH Zurich, 2023. doi: 10.3929/ETHZ-B-000627524.
[305] A. A. Taqa, M. O. Mohsen, M. O. Aburumman, K. Naji, R. Taha, and A. Senouci, “Nano-fly ash and clay for 3D-Printing concrete buildings: A fundamental study of rheological, mechanical and microstructural properties,” *Journal of Building Engineering*, vol. 92, p. 109718, Sept. 2024, doi: 10.1016/j.jobe.2024.109718.
[306] S. T. Prathipati, J. Vardhan, D. Murali, C. Nithin, and C. Karthik Sai, “An experimental study on the effect of a Viscosity Modifying Agent on the rheological and strength behaviour of 3D Printed Concrete,” *J. Phys.: Conf. Ser.*, vol. 2779, no. 1, p. 012087, June 2024, doi: 10.1088/1742-6596/2779/1/012087.
[307] P. R. De Matos, T. Zat, M. M. Lima, J. D. S. Andrade Neto, M. T. Souza, and E. D. Rodríguez, “Effect of the superplasticizer addition time on the fresh properties of 3D printed limestone calcined clay cement (LC3) concrete,” *Case Studies in Construction Materials*, vol. 19, p. e02419, Dec. 2023, doi: 10.1016/j.cscm.2023.e02419.
[308] H. Gao, L. Jin, Y. Chen, Q. Chen, X. Liu, and Q. Yu, “Rheological behavior of 3D printed concrete: Influential factors and printability prediction scheme,” *Journal of Building Engineering*, vol. 91, p. 109626, Aug. 2024, doi: 10.1016/j.jobe.2024.109626.
[309] Y. Wu *et al.*, “Study on the rheology and buildability of 3D printed concrete with recycled coarse aggregates,” *Journal of Building Engineering*, vol. 42, p. 103030, Oct. 2021, doi: 10.1016/j.jobe.2021.103030.
[310] Y. Yin *et al.*, “Effect of Hydroxypropyl methyl cellulose (HPMC) on rheology and printability of the first printed layer of cement activated slag-based 3D printing concrete,” *Construction and Building Materials*, vol. 405, p. 133347, Nov. 2023, doi: 10.1016/j.conbuildmat.2023.133347.
[311] I. Harbouz, E. Roziere, A. Yahia, and A. Loukili, “Printability assessment of cement-based materials based on rheology, hydration kinetics, and viscoelastic properties,” *Construction and Building Materials*, vol. 325, p. 126810, Mar. 2022, doi: 10.1016/j.conbuildmat.2022.126810.

[312] V. N. Nerella and V. Mechtcherine, “Studying the Printability of Fresh Concrete for Formwork-Free Concrete Onsite 3D Printing Technology (CONPrint3D),” in *3D Concrete Printing Technology*, Elsevier, 2019, pp. 333–347. doi: 10.1016/B978-0-12-815481-6.00016-6.
[313] J. Mirza, M. S. Mirza, V. Roy, and K. Saleh, “Basic rheological and mechanical properties of high-volume fly ash grouts,” *Construction and Building Materials*, vol. 16, no. 6, pp. 353–363, Sept. 2002, doi: 10.1016/S0950-0618(02)00026-0.
[314] X. Shao *et al.*, “Study on Rheological and Mechanical Properties of Aeolian Sand-Fly Ash-Based Filling Slurry,” *Energies*, vol. 13, no. 5, p. 1266, Mar. 2020, doi: 10.3390/en13051266.
[315] M. F. Alnahhal, T. Kim, and A. Hajimohammadi, “Evolution of flow properties, plastic viscosity, and yield stress of alkali-activated fly ash/slag pastes,” *RILEM Tech Lett*, vol. 5, pp. 141–149, Dec. 2020, doi: 10.21809/rilemtechlett.2020.123.
[316] J. Mirza, M. S. Mirza, V. Roy, and K. Saleh, “Basic rheological and mechanical properties of high-volume fly ash grouts,” *Construction and Building Materials*, vol. 16, no. 6, pp. 353–363, Sept. 2002, doi: 10.1016/S0950-0618(02)00026-0.
[317] M. Nodehi, J. Ren, X. Shi, S. Debbarma, and T. Ozbakkaloglu, “Experimental evaluation of alkali-activated and portland cement-based mortars prepared using waste glass powder in replacement of fly ash,” *Construction and Building Materials*, vol. 394, p. 132124, Aug. 2023, doi: 10.1016/j.conbuildmat.2023.132124.
[318] Y. Chen, C. Romero Rodriguez, Z. Li, B. Chen, O. Çopuroğlu, and E. Schlangen, “Effect of different grade levels of calcined clays on fresh and hardened properties of ternary-blended cementitious materials for 3D printing,” *Cement and Concrete Composites*, vol. 114, p. 103708, 2020, doi: 10.1016/j.cemconcomp.2020.103708.
[319] N. Schiavone, V. Verney, and H. Askanian, “Pozzolan Based 3D Printing Composites: From the Formulation Till the Final Application in the Precision Irrigation Field,” *Materials*, vol. 14, no. 1, p. 43, Dec. 2020, doi: 10.3390/ma14010043.
[320] Y. K. Abdallah and A. T. Estévez, “3D-Printed Biodigital Clay Bricks,” *Biomimetics*, vol. 6, no. 4, p. 59, Oct. 2021, doi: 10.3390/biomimetics6040059.
[321] G. Beersaerts, T. Hertel, S. Lucas, and Y. Pontikes, “Promoting the use of Fe-rich slag in construction: Development of a hybrid binder for 3D printing,” *Cement and Concrete Composites*, vol. 138, p. 104959, Apr. 2023, doi: 10.1016/j.cemconcomp.2023.104959.
[322] G. Beersaerts, J. Soete, M. Giels, L. Eykens, S. Lucas, and Y. Pontikes, “3D printing of an iron-rich slag based hybrid mortar. A durable, sustainable and cost-competitive product?,” *Cement and Concrete Composites*, vol. 144, p. 105304, Nov. 2023, doi: 10.1016/j.cemconcomp.2023.105304.
[323] Ö. Çakir and F. Aköz, “Effect of curing conditions on the mortars with and without GGBFS,” *Construction and Building Materials*, vol. 22, no. 3, pp. 308–314, 2008, doi: 10.1016/j.conbuildmat.2006.08.013.
[324] B. Uzal, L. Turanlı, H. Yücel, M. C. Göncüoğlu, and A. Çulfaz, “Pozzolanic activity of clinoptilolite: A comparative study with silica fume, fly ash and a non-zeolitic natural pozzolan,” *Cement and Concrete Research*, vol. 40, no. 3, pp. 398–404, Mar. 2010, doi: 10.1016/j.cemconres.2009.10.016.
[325] S. Mousavinezhad, J. M. Garcia, W. K. Toledo, and C. M. Newtson, “A Locally Available Natural Pozzolan as a Supplementary Cementitious Material in Portland Cement Concrete,” *Buildings*, vol. 13, no. 9, p. 2364, Sept. 2023, doi: 10.3390/buildings13092364.

[326] K. Sobolev, M. Kozhukhova, K. Sideris, E. Menéndez, and M. Santhanam, “Alternative Supplementary Cementitious Materials,” in *Properties of Fresh and Hardened Concrete Containing Supplementary Cementitious Materials*, vol. 25, N. De Belie, M. Soutsos, and E. Gruyaert, Eds., in RILEM State-of-the-Art Reports, vol. 25. , Cham: Springer International Publishing, 2018, pp. 233–282. doi: 10.1007/978-3-319-70606-1_7.
[327] Y. Liu, L. Wang, Q. Yuan, and J. Peng, “Effect of coarse aggregate on printability and mechanical properties of 3D printed concrete,” *Construction and Building Materials*, vol. 405, p. 133338, Nov. 2023, doi: 10.1016/j.conbuildmat.2023.133338.
[328] A. A. Taqa, M. O. Mohsen, M. O. Aburumman, K. Naji, R. Taha, and A. Senouci, “Nano-fly ash and clay for 3D-Printing concrete buildings: A fundamental study of rheological, mechanical and microstructural properties,” *Journal of Building Engineering*, vol. 92, p. 109718, Sept. 2024, doi: 10.1016/j.jobe.2024.109718.
[329] S. Bhattacherjee, S. Jain, and M. Santhanam, “Developing 3D printable and buildable limestone calcined clay-based cement composites with higher aggregate content,” *Construction and Building Materials*, vol. 376, p. 131058, May 2023, doi: 10.1016/j.conbuildmat.2023.131058.
[330] M. Como, *Statics of Historic Masonry Constructions*, vol. 9. in Springer Series in Solid and Structural Mechanics, vol. 9. Cham: Springer International Publishing, 2017. doi: 10.1007/978-3-319-54738-1.
[331] A. M. Blakeway, “Experiments with 3D printing technologies in masonry construction,” 2014. [Online]. Available: http://hdl.handle.net/1721.1/103493
[332] J.-C. Morel, R. Charef, E. Hamard, A. Fabbri, C. Beckett, and Q.-B. Bui, “Earth as construction material in the circular economy context: practitioner perspectives on barriers to overcome,” *Phil. Trans. R. Soc. B*, vol. 376, no. 1834, p. 20200182, Sept. 2021, doi: 10.1098/rstb.2020.0182.
[333] A. Joshi, P. Poullain, F. Craveiro, and H. Bártolo, “Earth as a Construction Material for Sustainable 3D Printing: Rheological Aspect,” in *Progress in Digital and Physical Manufacturing*, J. O. Correia Vasco, H. De Amorim Almeida, A. Gonçalves Rodrigues Marto, C. A. Bento Capela, F. G. Da Silva Craveiro, H. M. Coelho Da Rocha Terreiro Galha Bárt, L. M. De Jesus Coelho, M. A. Simões Correia, M. M. Nogueira Vieira, and R. M. Barreiros Ruben, Eds., in Springer Tracts in Additive Manufacturing. , Cham: Springer International Publishing, 2023, pp. 270–280. doi: 10.1007/978-3-031-33890-8_24.
[334] Y. Maierdan *et al.*, “Rheology and 3D printing of alginate bio-stabilized earth concrete,” *Cement and Concrete Research*, vol. 175, p. 107380, Jan. 2024, doi: 10.1016/j.cemconres.2023.107380.
[335] Y. Maierdan, D. Zhao, P. H. Chokshi, M. Garmonina, and S. Kawashima, “Rheology, 3D printing, and particle interactions of xanthan gum-clay binder for earth concrete,” *Cement and Concrete Research*, vol. 182, p. 107551, Aug. 2024, doi: 10.1016/j.cemconres.2024.107551.
[336] Q. Lyu, P. Dai, M. Zong, P. Zhu, and J. Liu, “Plant-germination ability and mechanical strength of 3D printed vegetation concrete bound with cement and soil,” *Construction and Building Materials*, vol. 408, p. 133587, Dec. 2023, doi: 10.1016/j.conbuildmat.2023.133587.
[337] S. Kumar *et al.*, “Low-clay soil as fine aggregate in 3D printed concrete: insights into fresh and hardened properties,” *Journal of Sustainable Cement-Based Materials*, vol. 14, no. 7, pp. 1387–1403, July 2025, doi: 10.1080/21650373.2025.2505750.

[338] P. R. K. Soda, A. Dwivedi, S. C M, and S. Gupta, “Development of 3D printable stabilized earth-based construction materials using excavated soil: Evaluation of fresh and hardened properties,” *Science of The Total Environment*, vol. 924, p. 171654, May 2024, doi: 10.1016/j.scitotenv.2024.171654.
[339] S. Barnes, L. Kirssin, E. Needham, E. Baharlou, D. E. Carr, and J. Ma, “3D printing of ecologically active soil structures,” *Additive Manufacturing*, vol. 52, p. 102670, Apr. 2022, doi: 10.1016/j.addma.2022.102670.
[340] M. G. Arab, M. Omar, E. Alotaibi, O. Mostafa, M. Naeem, and O. Badr, “Bio-Inspired 3D-Printed Honeycomb for Soil Reinforcement,” in *Geo-Congress 2020*, Minneapolis, Minnesota: American Society of Civil Engineers, Feb. 2020, pp. 262–271. doi: 10.1061/9780784482834.029.
[341] J. Daher, J. Kleib, M. Benzerzour, N.-E. Abriak, and G. Aouad, “The Development of Soil-Based 3D-Printable Mixtures: A Mix-Design Methodology and a Case Study,” *Buildings*, vol. 13, no. 7, p. 1618, June 2023, doi: 10.3390/buildings13071618.
[342] P. R. K. Soda, A. Dwivedi, S. C M, and S. Gupta, “Development of 3D printable stabilized earth-based construction materials using excavated soil: Evaluation of fresh and hardened properties,” *Science of The Total Environment*, vol. 924, p. 171654, May 2024, doi: 10.1016/j.scitotenv.2024.171654.
[343] C. Liu *et al.*, “Influence of hydroxypropyl methylcellulose and silica fume on stability, rheological properties, and printability of 3D printing foam concrete,” *Cement and Concrete Composites*, vol. 122, p. 104158, Sept. 2021, doi: 10.1016/j.cemconcomp.2021.104158.
[344] M. V. Tran, Y. T. H. Cu, and C. V. H. Le, “Rheology and shrinkage of concrete using polypropylene fiber for 3D concrete printing,” *Journal of Building Engineering*, vol. 44, p. 103400, Dec. 2021, doi: 10.1016/j.jobe.2021.103400.
[345] R. Jayathilakage, P. Rajeev, and J. Sanjayan, “Rheometry for Concrete 3D Printing: A Review and an Experimental Comparison,” *Buildings*, vol. 12, no. 8, p. 1190, Aug. 2022, doi: 10.3390/buildings12081190.
[346] Anton Paar inc., “Rotational Viscometer: ViscoQC.” Accessed: Sept. 03, 2025. [Online]. Available: https://www.anton-paar.com/us-en/products/details/viscoqc/?sku=105025
[347] Astm:C138/C138M-13, “Standard Test Method for Density (Unit Weight), Yield, and Air Content (Gravimetric),” *ASTM International*, vol. i, pp. 23–26, 2013, doi: 10.1520/C0138.
[348] C. C. Test and B. Statements, “ASTM C143M, ‘Standard Test Method for Slump of Hydraulic Cement Concrete’, American Society for Testing and Materials, Vol. 04.02, pp.1-4, 2014,” vol. i, no. Reapproved, pp. 1–4, 2014, doi: 10.1520/C0143.
[349] ASTM C230, “Standard Specification for Flow Table for Use in Tests of Hydraulic Cement 1,” *Annual Book of ASTM Standards*, pp. 4–9, 2010, doi: 10.1520/C0230.
[350] D01 Committee, *Test Methods for Rheological Properties of Non-Newtonian Materials by Rotational Viscometer D2196-20*. doi: 10.1520/D2196-20.
[351] ISO14040, “Environmental Management - Life Cycle Assessment - Principles and Framework. International Standard ISO 14040.,” *International Organization for Standardization (ISO)*, 08, [Online]. Available: http://www.iso.org/iso/catalogue_detail.htm?csnumber=37456
[352] ACI 318-14, *ACI 318-14 - Building Code Requirements for Structural Concrete*. 2014.

[353] S. Antiohos and S. Tsimas, “Activation of fly ash cementitious systems in the presence of quicklime,” *Cement and Concrete Research*, vol. 34, no. 5, pp. 769–779, May 2004, doi: 10.1016/j.cemconres.2003.08.008.
[354] C. Shi and R. L. Day, “Pozzolanic reaction in the presence of chemical activators,” *Cement and Concrete Research*, vol. 30, no. 1, pp. 51–58, Jan. 2000, doi: 10.1016/S0008-8846(99)00205-7.
[355] A. Oner, S. Akyuz, and R. Yildiz, “An experimental study on strength development of concrete containing fly ash and optimum usage of fly ash in concrete,” *Cement and Concrete Research*, vol. 35, no. 6, pp. 1165–1171, 2005, doi: 10.1016/j.cemconres.2004.09.031.
[356] J. Kruger, A. du Plessis, and G. van Zijl, “An investigation into the porosity of extrusion-based 3D printed concrete,” *Additive Manufacturing*, vol. 37, no. November 2020, p. 101740, 2021, doi: 10.1016/j.addma.2020.101740.
[357] T. Ding, J. Xiao, S. Zou, and X. Zhou, “Anisotropic behavior in bending of 3D printed concrete reinforced with fibers,” *Composite Structures*, vol. 254, p. 112808, Dec. 2020, doi: 10.1016/j.compstruct.2020.112808.
[358] M. Nodehi, F. Aguayo, S. E. Nodehi, A. Gholampour, T. Ozbakkaloglu, and O. Gencel, “Durability properties of 3D printed concrete (3DPC),” *Automation in Construction*, vol. 142, p. 104479, Oct. 2022, doi: 10.1016/j.autcon.2022.104479.